ABSTRACT

Title of dissertation: DESIGN AND PERFORMANCE PREDICTION
OF SWASHPLATELESS HELICOPTER ROTOR
WITH TRAILING EDGE FLAPS AND TABS

Jaye Falls, Doctor of Philosophy, 2010

Dissertation directed by: Professor Inderjit Chopra
Department of Aerospace Engineering

This work studies the design of trailing edge controls for swashplateless helicopter primary control, and examines the impact of those controls on the performance of the rotor. The objective is to develop a comprehensive aeroelastic analysis for swashplateless rotors in steady level flight. The two key issues to be solved for this swashplateless control concept are actuation of the trailing edge controls and evaluating the performance of the swashplateless rotor compared to conventionally controlled helicopters. Solving the first requires simultaneous minimization of trailing flap control angles and hinge moments to reduce actuation power. The second issue requires not only the accurate assessment of swashplateless rotor power, but also similar or improved performance compared to conventional rotors. The analysis consists of two major parts, the structural model and the aerodynamic model. The inertial contributions of the trailing edge flap and tab are derived and added to the system equations in the structural model. Two different aerodynamic models are used in the analysis, a quasi-steady thin airfoil theory that includes arbitrary

hinge positions for the flap and the tab, and an unsteady lifting line model with airfoil table lookup based on wind tunnel test data and computational fluid dynamics simulation.

The design aspect of the problem is investigated through parametric studies of the trailing edge flap and tab for a Kaman-type conceptual rotor and a UH-60A swashplateless variant. The UH-60A model is not changed except for the addition of a trailing edge flap to the rotor blade, and the reduction of pitch link stiffness to imitate a soft root spring. Study of the uncoupled blade response identifies torsional stiffness and flap hinge stiffness as important design features of the swashplateless rotor. Important trailing edge flap and tab design features including index angle, aerodynamic overhang, chord and length are identified through examination of coupled trim solutions in wind tunnel conditions at high speed. Flap and tab configurations that minimize both the control angles and hinge moments required to trim are developed for both the Kaman-type and UH-60A models, and the rotors are successfully trimmed across the range of forward flight speed.

The conventionally controlled UH-60A rotor model is validated with data from the UH-60A Flight Test Program. Excellent correlation is obtained for rotor power in hover and in forward flight. It is shown that the magnitude of the predicted power, but not the trend versus forward speed, is affected by the calculation of inflow distribution. Both uniform inflow and a pseudo-implicit free wake model are used to calculate the inflow distribution for the swashplateless rotor. Using the free wake model, the predicted swashplateless rotor power is sensitive to the pattern of trailed vorticity from the rotor blade. Trailed vortices are added at the

inboard and outboard boundaries of the trailing edge flap, and the flap deflection is used to calculate an effective angle of attack for the calculation of the near and far wake. This wake model predicts the swashplateless rotor requires less main rotor power than the conventional UH-60A helicopter from hover to $\mu = 0.25$. As the forward flight speed increases, the swashplateless predicted power increases above the conventional rotor, and the rotor lift-to-drag ratio decreases below that of the conventional rotor.

Design and Performance Prediction of Swashplateless Helicopter
Rotor with Trailing Edge Flaps and Tabs

by

Jaye Falls

Dissertation submitted to the Faculty of the Graduate School of the
University of Maryland, College Park in partial fulfillment
of the requirements for the degree of
Doctor of Philosophy
2010

Advisory Committee:
Professor Inderjit Chopra, Chair/Advisor
Dr. Anubhav Datta, Co-Advisor
Professor Darryll Pines
Professor Norman Wereley
Associate Professor James Baeder
Professor Michael Coplan, Dean's Representative

Acknowledgments

I am pleased to acknowledge all those who have contributed to this work as I finally bring it to completion.

My deepest thanks to my advisor, Inderjit Chopra, for his many years of encouragement and support. He convinced me to add aerospace engineering to my education at a point when an easier topic might have been tempting for a young parent with a full complement of suburban distractions, and I have never regretted the undertaking. His contributions to my research, from the general to the detail level, have been large and greatly appreciated.

Dr. Anubhav Datta has acted as both my colleague and mentor in rotor dynamics. The excellence of his scholarship is well known, but his patience and kindness should also earn him fame. The thought-provoking discussions we had about rotor dynamics frequently clarified my thinking and bolstered my motivation.

I would also like to thank the other members of my advisory committee, Drs. Baeder, Coplan, Pines and Wereley, for their ongoing interest in and support for this work.

This work was supported in part by Kaman Aerospace Corporation. John Wei and Mike Bielefield provided useful discussion, guidance and data in the initial stages of the project. The Alfred P. Sloan Foundation and the Vertical Flight Foundation of the American Helicopter Society provided generous financial support for several years.

My colleagues from the Alfred Gessow Rotorcraft Center have been a welcome

Table of Contents

List of Figures

List of Abbreviations

α Angle of attack

β Blade flap angle

δT Variation of kinetic energy

δU Variation of potential energy

δW Virtual work

θ_0 Blade rigid pitch

θ_1 Blade twist

θ_{1c} Blade lateral cyclic pitch

θ_{1s} Blade longitudinal cyclic pitch

θ_{coll} Blade collective pitch

θ_{tw} Blade linear twist

λ Lock number

μ Advance ratio

σ Rotor solidity

$\hat{\phi}$ Blade elastic twist

ψ Azimuth angle

Ω Angular velocity

a Reference lift curve slope

c Blade nominal chord

c_b Blade chord

c_f Flap chord

C_T Rotor thrust coefficient

c_t Tab chord

d Distance from blade elastic axis to flap hinge

f Distance from flap hinge to tab hinge

i_a Flap second mass moment of inertia

i_t	Tab second mass moment of inertia
k_p	Flap hinge stiffness
k_q	Tab hinge stiffness
M	Mach number
m_0	Blade mass per unit length
M_p	Trailing edge flap hinge moment
M_q	Trailing edge tab hinge moment
M_β	Rigid blade flap hub moment
M_θ	Rigid blade pitch hub moment
p	Flap deflection (positive flap down)
q	Tab deflection (positive tab down)
s_a	Flap first mass moment of inertia
s_t	Tab first mass moment of inertia
t	Time
u	Blade elastic axial displacements
v	Blade elastic lag displacements
w	Blade elastic flap displacements
x	Blade spanwise position
C_Q	Rotor torque coefficient
C_W	Gross weight coefficient
GJ	Blade torsional rigidity
$(..)'$	First derivative with respect to x
$\ddot{(..)}$	Second derivative with respect to time
$\delta(.)$	Virtual variation
$\dot{(..)}$	First derivative with respect to time

Chapter 1

Introduction

1.1   Background

Conventional helicopter design includes the swashplate control mechanism, which although generally successful, is mechanically complex, highly loaded, heavy, and incurs a drag penalty. Therefore, alternative rotor pitch control concepts that enable swashplateless designs have been an active area of research. Individual blade control (IBC) is an active control concept developed for vibration control that can be adapted for the purpose of primary control; trailing edge flaps (TEFs) are one method for producing the changes in blade pitch required for trim. A tab actuated trailing edge flap is proposed for primary, swashplateless control of rotor systems. The purpose of the current work is to (1) develop a comprehensive analysis for rotors with flap-tab based primary control, (2) to understand the fundamental response of a flap-tab control system, identifying the key geometric and design parameters and (3) to accurately predict control angle requirements and the consequent changes in rotor performance in steady, level flight at a range of flight speeds.

1.2 Helicopter Primary Control

The defining characteristics of the helicopter are the abilities to hover and to take off and land vertically. These attributes combined with low-speed maneuvering permit the delivery and retrieval of valuable payloads in space restricted areas. Once helicopter technology matured, it was quickly perceived as an indispensable part of both military and civil air fleets. Unfortunately, the demand for reliable, affordable rotorcraft has stifled innovation that might jeopardize reliability or affordability, and for many decades technological development has tended to be evolutionary rather than revolutionary. Thus the rotor control system has changed incrementally, shedding parts and thus weight and complexity, but for most helicopters remains centered on the swashplate which is intrinsically heavy and complex.

The purpose of the helicopter control system is to manage the magnitude and direction of the thrust generated by the rotor. Typically, the magnitude of thrust is determined by the collective pitch of the rotor blades, and the direction of thrust is determined by the direction of the plane formed by the rotating blade tips, the tip-path-plane (TPP). The direction of the TPP is a function of the blade flapping angles, which occur in response to cyclic pitch inputs. The swashplate is a mechanism which allows control of blade pitch motions at the rotor hub.

Although the conventional hub and swashplate are mechanically complex and aerodynamically inefficient, the system provided a reliable solution to the problem of asymmetric aerodynamic loads on helicopters in forward flight. This solution permitted designers to concentrate on improving critical metrics of flight performance

such as range, speed and payload while reducing the vibration and noise resulting from the highly unsteady and complex aerodynamic flow over the rotor.

Design is cyclical however, and having made progress on the problems of vibration and noise [4], attention has returned to the hub, where the high part count, heavy and expensive components and exposed linkages add weight, cost and drag that can be remedied. New primary control concepts may eliminate the swashplate altogether. On-blade controls such as trailing edge flaps are used to indirectly control the blade pitch through the manipulation of pitching moment. The flaps are actuated, and flap deflection can change both the local aerodynamic properties of the blade and the distribution of lift, drag and pitch moment over the blade. By combining state-of-the-art hub design with swashplateless control, exposed linkages, bearings and hinges are removed from the aircraft profile, reducing the vehicle drag and weight. The result is that fabrication and maintenance become easier, reliability improves and the acquisition and operating costs of the mechanism may be reduced. To realize maximum benefit from the concept, it is important to assess the performance of the new hub configuration accurately. Then the designer will be able to weigh the definite advantages of reduced weight and drag against the possible disadvantages caused by changes in rotor performance.

Although the benefit of a new primary control concept can best be realized by including the concept from the initial stages of design, the exigencies of military and commercial cost restrictions may preclude such an effort. Instead, designers may be able to consider the concept in the context of retrofitting, where existing blade and fuselage designs are retained. The articulation and/or hinge arrangement

of the hub may also remain unchanged, with the main alteration being reduced torsional stiffness at the blade root to facilitate maximum blade twist in response to flap deflections on the blade. In this case, there is still a potential advantage to the swashplateless concept: the parasitic drag of the hub and the mechanical complexity and thus fabrication and repair costs can be reduced.

1.2.1   Swashplate Mechanism

The aerodynamic loads encountered by the helicopter blade in forward flight as it moves from the advancing side to the retreating side are unsteady and unequal. This asymmetry creates destabilizing loads on the aircraft. The solution to this problem was the implementation of cyclic pitch; the swashplate was invented by Hafner in the 1920's [5] and became the preferred way to produce cyclic pitch by the 1930's [6]. The mechanism consists of rotating and non-rotating plates connected through bearings, as shown in Figs. 1.1,1.2. Hydraulic actuators in the fixed frame move the fixed plate in accordance with pilot collective and cyclic inputs, forcing the rotating plate to move similarly. The rotating plate is connected to the blades with linkages, and as it moves vertically or tilts, the blade pitch collective and cyclic are changed. The collective is the steady pitch angle controlling the magnitude of thrust generated, and is produced by the vertical movement of the fixed plate. When the rotating plate is tilted, the pitch of each blade is altered as it moves around the azimuth, at a frequency of once per revolution. The cyclic pitch causes a change to the tilt of the tip-path-plane (TPP) which controls the direction of the thrust

vector. The system has proven to be so reliable that it has been in use for 70 years without major alteration.

The swashplate and rotor hub are sometimes covered by aerodynamic fairings which reduce the parasitic drag of the vehicle. Nevertheless, empirical data [3, 7] suggests that the swashplate can account for nearly half of the hub drag and the hub about 35% of the total parasitic drag.
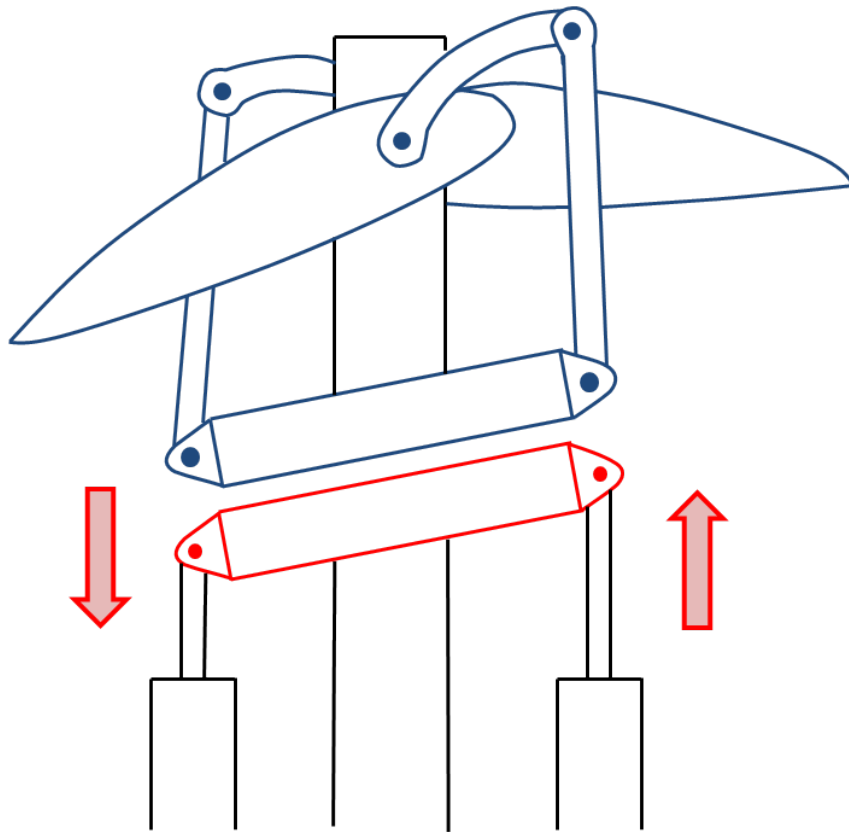
Figure 1.1: Schematic of Typical Swashplate

Figure 1.2: Hub and Swashplate of UH-60 Blackhawk

1.2.2   Swashplateless Control

Other attempts to solve the problem of asymmetric rotor lift followed the lead of Corradino d'Ascanio in 1930, who produced cyclic lift using trailing edge servo-tabs on the blades of his helicopter [7]. Blade twist is induced in response to the moment created by deflection of the servo-tab. Kaman put this system into production in the late 1940's with external servo-flaps, and Kaman Aerospace helicopters still use servo-flaps today.

Servo-flaps are separate airfoils located aft of the main blade in order to create large moment authority. These flaps are centered at the 75% radius of the blade, and are connected with linkages. The rotor is soft in torsion to maximize blade twist response to the aerodynamic moment created by the deflection of the servo-flap. Typically, the torsional frequency of servo-flap rotors is below 2/rev, compared to 3-5/rev for swashplate controlled rotors. Kaman uses two designs to produce

6

torsional softness: (1) a torsion bearing at the root in combination with a tension-torsion strap and (2) soft torsional rigidity (GJ) of the blade. To minimize the servo-flap deflection required to twist the blade into trim position, the blades are given a pre-collective called the index angle. This arrangement results in several advantages compared to the conventional swashplate control [8–11]. Although the servo-flap is small compared to the blade, the moment arm from the blade feathering axis to the flap is long, and the torsional softness of the blade means that the blade undergoes significant twist in response to small flap deflections. Consequently, the control forces required to deflect the servo-flaps with these designs are very low, and hydraulic actuation either may not be necessary or the requirement becomes minimal. In the Kaman rotors, the low control forces lead to clean hub designs through the lack of large bearings or hinges. The flap is controlled with push-pull rods in the rotating frame that connect to pilot collective and cyclic inputs in the fixed frame through a swashplate. The system tends to allow the pilot to have a good feel for the controls. The flaps on each blade are a decentralized control, which enhances vehicle survivability in the case of hub damage in flight.

There are also disadvantages to a flap-controlled rotor. The extra wetted area of external servo-flaps, plus the exposed linkages connecting the foils to the blades creates additional drag. Because the control mechanism is located in the rotating frame, it (the servo-flap) is subject to high rotational speeds and correspondingly high centrifugal loading. This affects not only the design of the servo-flap and the linkages, but also the interaction of multiple blades, where minor dissimilarities in mass or aerodynamic profile relating to the flap attachments are magnified into

major rotor imbalances. Thus the similitude of the blades, in mass and in profile, becomes even more important than for swashplate rotors, and the servo-flap rotor requires extra time and attention for proper tracking. The flap, the attachments linking the flap to the blade, and the actuator driving the flap add mass to the blade, and the center of that additional mass must be carefully located to avoid stability problems.

1.2.3 Kaman Helicopters

Kaman Aerospace Corporation has a long history with servo-flap rotors. Inspired by the successes of Pescara [12] and d"'Ascanio [13], Kaman created his own servo-flap helicopter [14] and put it into production. These rotors are characterized by low torsional stiffness and the use of index angles.

As the only industrial experts on servo-flap rotors, Kaman Aerospace has been historically the primary source of servo-flap research. Kaman [15–19] conducted a study with the U.S. Army on the controllable twist rotor (CTR), a dual control rotor with both a swashplate/pitch horn arrangement at the hub and servo-flaps on the blades. The swashplate was used for primary control and the servo-flaps controlled the blade twist. They found that with torsionally soft blades, they were able to reduce the diameter and solidity of the rotor while increasing performance in hover and forward flight. This was accomplished with high negative twist in the blades in hover, and less blade twist in forward flight. The concept was extended to include vibration reduction using multicyclic flap deflections. Full-scale wind tunnel

tests were conducted in support of the concept, but the complexity and weight of the dual control systems and the hydraulic actuation was an obstacle to production. The concept was modified by Lemnios and Jones [8], who proposed a system for simultaneous primary and vibration control, using a hydraulic actuation system in the rotating frame to provide multicyclic servo-flap deflections via a hydraulic slip ring.

Several investigations have addressed the analysis and improvement of Kaman's production rotors. An analysis was developed from the C81 rotorcraft simulation software that could model either conventional or servo-flap rotors, and used airfoil tables for aerodynamic properties [20]. The SH-2F model was validated against flight test data, and showed good correlation for flap deflection and rotor torque. Wei proposed variable indexing [21], which would allow the index angle to be changed in flight, producing performance improvements and hover and reduced vibration in high speed forward flight. Both of these effects are related to the alteration of blade airload distribution caused by trim position of the servo-flap. As the index angle is changed, the flap trim position also changes. Wei and Gallagher [9] observed that positive flap deflection or uploading, characterized by flap down deflection, improved the hover and forward flight performance on the SH-2G by redistributing the airloads over the blade, reducing the tip loading and making the total distribution more uniform. The switch to uploading from downloading on the Kaman rotors was achieved with significant modification of the fuselage and the introduction of composite blades. There have been investigations of the vibration characteristics of Kaman rotors [22–24]. Recently, spectral analysis has been used to identify the

9

primary servo-flap design features affecting vibration energy distributions [24].

Kaman Aerospace is examining the merits of integrated flaps [10, 25] compared to the external servoflaps that they have traditionally used. Integrating the flap into the airfoil section reduces the moment arm of the flap so that a larger flap and/or larger flap deflections are required for trim. The flapped section of the K-MAX intermeshing rotor blade was re-designed to integrate the external servo-flap into the main blade section. For the flapped section, the blade chord was increased so that the new chord length matched the original cross-sectional length of the main blade and servo-flap. The airfoil profile of the combined surfaces matched the original blade airfoil and the newly integrated trailing edge flap was hinged at its leading edge. The result of this reconfiguration was to improve performance, primarily through the increase of the lift-to-drag ratio. The elimination of the gap between the foils and the reduction of exposed linkages were the main sources of drag reduction. The lift of the new section increased significantly compared to the original blade section, for both positive and negative flap deflections. When the servo-flap is entirely integrated with the blade chord, it becomes a plain flap, and its pitching moment arm is significantly reduced. Consequently, the entire blade and rotor designs must be reconsidered to best take advantage of the strengths of the plain flap, and to reduce its disadvantages. Some of the most important design considerations are summarized in Ref. [25]. Despite positive results from this research, the current performance and potential advances of the trailing edge servo-flap rotor have been so satisfactory that major new designs do not appear to be in the immediate future of the company.

1.3 Active Controls and Helicopter Performance

Active controls have been proposed for helicopter rotors as methods for either vibration or noise reduction. These methods change the aerodynamic input to the vehicle system, rather than addressing the structural response like traditional passive controls, i.e., absorbers or isolators. The theory is to counteract the periodic aerodynamic excitation produced by the flight environment with periodic inputs from the blades. The input is optimally timed and phased to reduce one or more target loads. Such a periodic input is generally referred to as multicyclic control. As the primary studies in noise and vibration have matured, research focus has widened to include the effect of the active controls on rotor performance metrics like rotor torque and forward flight speed. This has occurred because it is important to ensure that improvements to the vibration and/or noise profiles do not carry concomitant penalties to rotor performance.

The term performance can cover a broad array of helicopter design terms including the classic metrics of speed, payload, range and general categories like specific productivity or environmental performance [3]. For the purpose of the current investigation, rotor performance refers exclusively to rotor shaft power and rotor lift-to-drag ratio. In this section, two major categories of active rotor control research, higher harmonic control and individual blade control, are reviewed in the context of rotor performance.

1.3.1 Higher Harmonic Control

Helicopter forward flight speed is limited by compressibility on the advancing blade and stall on the retreating blade. Agility and maneuverability require high rotor tip speed, which in turn is limited by consideration of rotor noise. These boundaries create a performance envelope (see Fig. 1.3) which constrains every helicopter design.
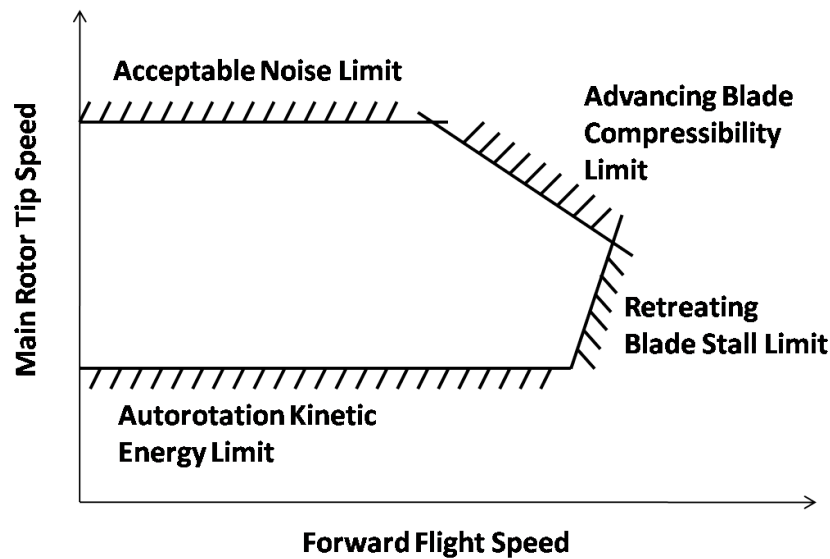
Figure 1.3: Limits of the Rotor Performance Envelope

It has been shown that helicopter performance can be enhanced with higher harmonic control (HHC). This is a control method by which small blade pitch inputs are added to the primary control inputs in the fixed frame, by including pitch frequencies above 1/rev. The additional actuation is usually applied through the existing swashplate, minimizing alteration to the vehicle but increasing weight with additional hydraulic actuators. The actuators must be capable of applying significant force at a wide range of frequencies. For a three or four bladed rotor, blade

pitch inputs at 3/rev and higher can push the stall limit beyond the compressibility limit of the advancing side [26]. Arcidiacono [27] found that 2/rev inputs could also be effective in delaying stall, and thus increasing the maximum forward flight speed. The concept was proven to be feasible in the early 1980s with wind tunnel tests of a model scale rotor [28, 29], which showed likely penalties for rotor torque across the range of forward flight speed. Nguyen *et al.* studied [30–32] expanding the performance envelope by delaying stall with HHC. A distinction was made between delaying stall and reducing rotor torque, as a multi-harmonic pitch schedule that reduces stall by 75% at cruise and high speed for the BO-105 only decreases rotor torque by 0.5%. In general, retreating side stall can be effectively suppressed with HHC for some rotors, but not usually in conjunction with a rotor performance improvement.

Comprehensive experimental studies of a 40% Mach-scaled BO-105 rotor was conducted to improve understanding of the effect of blade vortex interaction (BVI) on rotor noise and vibration, both with and without higher harmonic control. The Higher-harmonic-control Aeroacoustic Rotor Test (HART) and the subsequent series of tests on the same rotor (HART-II) produced a large database of test data, valuable for the examination of vibration and noise reduction, as well as detailed measurements of the rotor wake, blade pressure and rotor performance [33–36]. Most of the subsequent studies of the database have focussed on noise and vibration primarily, rather than performance.

Recently, Cheng has studied the effect of 2/rev HHC on rotor performance [37, 38], and found that adjusting the phase of the pitch input could produce small

reductions in power for a four-bladed, articulated rotor similar to the UH-60A Black-hawk. The major difference in the rotor model was the elimination of the UH-60A swept tip from the blade. Further gains can be realized by optimizing the pitch input schedule to minimize power, maximize thrust, or minimize rotor speed. Using a linear inflow model, an 11% increase in maximum thrust was realized at high speed, but a free wake model produced smaller improvements in all areas. It was shown that 2/rev HHC input changes lift distribution over the rotor disk, so more lift is generated at the front and rear of disk, as opposed to the advancing and retreating sides. It was indicated that the optimum input schedule was adequately predicted with linear inflow and rigid blades, followed by refinement with more refined aerodynamic and structural models.

Wachspress *et al.* [39] suggested that the most effective way to improve rotor performance is to reduce induced power. Induced power is the primary component of total power in hover, and a significant portion of the total power in forward flight. The result of using either 2/rev or 3/rev HHC on a 4-bladed rotor in forward flight was a 3 % to 4% reduction of induced power. It was also observed that the accuracy of predictions concerning the effect of HHC on rotor power is significantly affected by the fidelity of the wake model used.

1.3.2 Individual Blade Control

Individual Blade Control (IBC) describes a collection of rotor excitation methods that are located in the rotating frame, on each blade of the rotor. Many of the

systems that fall into this category were developed as an extension of HHC, and intended for application to similar problems, but eliminating the disadvantages of fixed frame actuation. Compared to HHC, the major advantages of IBC methods are the ability to operate at any desired frequency on each blade and the potential reduction in weight and power penalties. The frequency flexibility means not only an increase in potential applications (or simultaneous pursuit of multiple goals), but also the ability to operate with blades that are dissimilar.

Initial design concepts [15, 18, 40, 41] for IBC included hydraulic actuation in the rotating frame, which required complex sliprings and mechanical arrangements. The disadvantages of hydraulic actuation are being overcome by the recent advent of smart actuators characterized by low weight, compact size and high bandwidth [42]. Advances in smart materials and hybrid actuation schemes have allowed researchers in individual blade control to concentrate primarily on vibration reduction and noise reduction, with the hope that IBC suitable actuators will be available in the future.

The many different concepts that have been proposed for individual blade control can be divided into broad categories: blade pitch, blade twist, and active airfoils. Direct control of blade pitch is similar to swashplate control, but with the possibility of independent amplitude and phase control for each blade. Original concepts used active pitch links driven by hydraulic actuators, which required either a hydraulic slip ring or hydraulic pumps in the rotating frame. Guinn [40] described the design of a swashplateless control system of this type that used fly-by-light to integrate the hydraulic actuators, pumps and power supplies, and smart hydraulic pumps to vary pressure based on actuator load. The elimination of the swashplate and associated

linkages, and addition of mast fairing, was estimated to produce a 40% reduction in rotor profile drag. The estimated weight of the proposed control system was 40% less than the conventional fixed-frame system. Although higher harmonic control inputs were noted as a possible future advantage, the actuators were sized for 1/rev control. The study included only design and was not corroborated by experimental results, but highlighted some of the advantages of IBC. Ham [43] suggested that IBC could be used to control a variety of dynamic phenomena, including gust response and flutter. A BO105 helicopter fitted with hydraulic pitch link actuators was tested both in flight and in the wind tunnel [44, 45]. Although some improvement in vibration and noise were shown, significant improvements to rotor shaft power were not observed. Primary control was not part of this investigation. The last decade of advances in direct pitch IBC largely have been made in the development of control algorithms [46], rather than any major changes to the technology. An exception is the replacement of the hydraulic actuation system with hybrid piezohydraulic actuators [47]. These new actuators incorporate self-contained hydraulic pumps in each actuator unit, and are driven by electricity delivered through an electrical slip ring. Weight and complexity are greatly reduced, improving the potential of the direct pitch control concept.

Active twist blades control blade pitch through actuation of the entire blade, rather than just the root. Chen [48] designed, fabricated and tested a Froude scale rotor blade embedded with piezoceramic elements. The magnitude of blade twist was on the order of 0.5° at the tip, enough to offer some vibration control. A Mach-scaled model of a similar concept achieved 2° of blade twist in hover testing.

The blade was actuated up to 3/rev, and showed good thrust authority, which may indicate that this concept has potential for swashplateless control. The joint NASA/Army/MIT project on the active twist rotor (ATR) designed and fabricated a four-bladed rotor model to test in the NASA Langley Transonic Dynamics Tunnel. These model tests satisfy Mach, Froude and Lock number scaling simultaneously. Active fiber composite (AFC) actuators were embedded in the blades as part of the structure, layered through the thickness of the spar and oriented to produce maximum torsional control. These actuators had no failures during 40 hours of blade twisting, and demonstrated no loss of actuator authority during testing, which offers a promising indication of actuator robustness. Maximum blade twist was on the order of 1.52° [49–51]. Significant control authority for vibration reduction in hover and across the range of forward flight speed was demonstrated. There was little study of the effect of active twist on rotor performance, and primary control was outside the scope of the investigation. A brief design study by Kim *et al.* [52] proposed a piezoelectric tube actuator to twist the blade, and concluded that swashplateless primary control should be possible with active twist blades. However, required control moments were not compared to actuator capabilities to support the concept.

Active airfoils affect blade pitch indirectly, by causing the blade to twist in response to a change in the aerodynamic environment caused by the motion of the active part of the airfoil. The concept is frequently applied with additional airfoil elements like hinged trailing edge flaps, and may also be implemented with conformable airfoils or active camber control. One major advantage of this class of

active rotor concept is that the actuation power required is much less than for either the active pitch link or active twist concepts. This is because instead of moving the whole blade starting from the root, the actuated section is usually confined to only a fraction of the chord and span of the blade. A study of variable camber using trailing edge flaps in the early 1980s [53] found the potential for significant reduction of shaft power at high speed and thrust, but the concept was not pursued at the time for lack of suitable actuation. Advances in smart actuators increase the attractiveness of the active airfoil concepts [42], as their compact size allows them to fit within the blade profile, minimizing or eliminating exposed linkages and thus reducing associated profile drag.

Trailing edge flaps have been a popular research topic in the category of active airfoils. A drawback of trailing edge flaps is the discontinuity of airflow created at the flap boundaries. There are several sources of such discontinuity. Chordwise gaps that are difficult to seal occur if the flap is hinged aft of its leading edge, although aerodynamic overhang is useful in reducing hinge moment requirement and thus actuation power. Flaps with overhang protrude into the airflow when deflected. Spanwise gaps create the potential for trailed vorticity that adds to induced power losses and possibly to blade vortex interaction (BVI). Some of these issues will be examined more thoroughly in the following sections.

Conformable or variable camber airfoils work similarly to trailing edge flaps, with the advantage that there are no discrete flap boundaries that can cause aerodynamic penalties through increased profile drag or additional trailing vortices. The best airfoil design will have the flexibility and actuation to achieve maximum de-

flection at the trailing edge, while being stiff enough to maintain its shape under load. Anusonti and Gandhi have shown in a numerical investigation that actuator distribution and airfoil skin thickness are key design parameters [54]. The European aerospace agencies have started a joint project to investigate active trailing edges [55, 56]. The first phase of the project is actuator development and testing. Current smart actuator technology is sufficient to produce moderate deflections for a reasonable bandwidth, so this concept also may have some potential for both vibration and rotor primary control.

The focus of this investigation is the suitability of trailing edge flaps and tabs for helicopter primary control. Accordingly, the next section will review in detail prior trailing edge flap research.

1.4 Trailing Edge Flaps

A summary of the literature review of the trailing edge flaps may be found in Table 1, at the end of this chapter.

1.4.1 Vibration Control

The majority of current trailing edge flap research is directed to vibration and noise reduction through multicyclic deflections. This is in contrast to the early decades of helicopter development, when flaps were exclusively studied and used for primary control at 1/rev [12–14]. It wasn't until 1958 that a higher harmonic flap deflection was proposed by Payne [26], who noted that 3/rev blade pitch motions

can delay stall, and that multicyclic flap inputs might be applicable to vibration control. The first thorough study of the concept was carried out in the 1970s, when the Multicyclic Controllable Twist Rotor (MCTR) was designed, tested and analyzed in a joint Kaman Aerospace-US government project [15–19]. The multicyclic portion of the project was an extension of the original program, which studied a controllable twist rotor (CTR) for performance improvements. A 56 ft. diameter, 4-bladed, articulated rotor was fitted with servo-flaps 0.08R in length on the outboard section of the blade, and tested in a wind tunnel. The steady and 1/rev flap deflections were controlled by a swashplate in the fixed system, while the multicyclic deflections were produced by electro-hydraulic actuators in the rotating system. The servo-flaps were shown to have a significant effect on blade loads. The forces or moments most affected were determined by the weighting of different parameters in the control objective function. The analysis of the MCTR included a comprehensive aerodynamic model, including airfoil table look up, stall effects, and a prescribed wake. Although reduction of blade loads was demonstrated at 2/rev, the complexity and weight of the multiple control systems made this concept unattractive.

The creation of smart actuators with high bandwidth, low power requirements, light weight and compact size resurrected interest in trailing edge flaps for rotor applications in the 1990s. Because the actuators could fit inside the blade profile, plain flaps became a practical alternative to servo-flaps, offering a reduction in drag as exposed linkages and large hinge gaps are eliminated. Figure 1.4 offers plan and section views of a generic rotor blade with a servo-flap, a plain flap and a flap-tab.

A trailing edge flap system has been designed and installed on an MD-900

Rotor Blade with Servo-Flap

Leading Edge

Trailing Edge

Rotor Blade with Trailing Edge Flap

Rotor Blade with Trailing Edge Flap and Tab
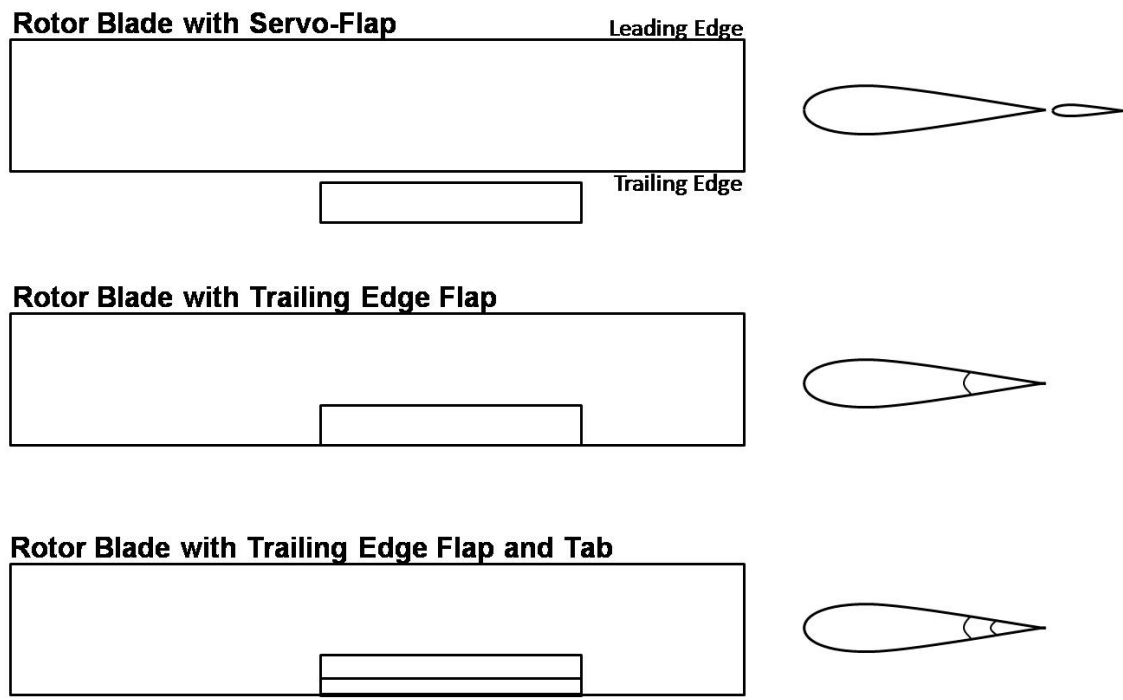
Figure 1.4: Schematic Diagram of Generic Rotor Blade with Varying Trailing Edge Flap Configurations

helicopter as part of the DARPA sponsored Smart Material Actuated Rotor Technology (SMART) program [57–60] at Boeing. The 5-bladed rotor is composite and bearingless, and has diameter 34 ft, with one flap per blade. The trailing edge flap has 0.25c chord, span of 0.18R and an overhang of $0.40c_f$. The first phase of this long-term program developed the smart actuators that can provide both large displacement and high force in the demanding flight environment [59]. In the next phase, the full-scale rotor with flaps and piezoelectric actuators was whirl-tower tested to demonstrate the reliable operation of the flaps [60]. Parameters including blade loads, pitch link loads, flap loads and flap actuator displacements were measured. The flaps were actuated at harmonics up to 6/rev, and also given static deflections. Flap damage was simulated by giving one flap static deflections while the remaining flaps received dynamic input. The flaps were observed to produce approximately 10% oscillatory thrust at medium actuation voltage, indicating that the flap system as designed could meet the requirements for vibration reduction in forward flight. The wind tunnel testing of the rotor reached speeds of at least 155 knots, and tested different deflection schedules for the flap. Preliminary reports suggest that measured noise was reduced by 50%. Comprehensive analysis of the SMART rotor proceeded concurrently with experiments [57, 58]. CAMRAD/JA is based on a mode shape approach and was modified for trailing edge flaps. The aerodynamic model of the flap uses either thin airfoil theory or airfoil table lookup. The structural model includes a flap hinge spring and damper, but does not include the inertial effects of the flap on the blade. CAMRAD II is a higher level code that is based on the finite element method. It includes unsteady aerodynamics and varying

22

wake models. In this code, the flap inertial effects are included, and the flap motion can either be prescribed or a degree of freedom. It was found that the lower level analysis adequately captured rotor response and flap loads to permit initial design studies. The higher level analysis becomes necessary to predict blade and flaps loads with greater accuracy, and to assess the coupled blade-flap dynamics.

Eurocopter also has a full-scale active flap rotor [61–63]. The Advanced Technology Rotor (ATR) was modified with one 0.15c trailing edge flap per blade. The flap span is 0.10R, located at the 75% radius of the blade. This 4-bladed hingeless rotor is 11m in diameter and fits the BK117 helicopter. In the first phase of the project, different acutation concepts were designed and tested on the bench, in rotation for centrifugal load and in the wind tunnel. A piezoelectric actuator was developed that fits within the blade section and maintains the CG near the quarter-chord. Whirl tower tests in the next phase of the program demonstrated the robustness of the rotor and flap components. The flaps were controlled in two different ways: 1)voltage inputs were given that corresponded to the desired flap deflection, or 2)the flap deflection was monitored and voltage adjusted to match the desired prescribed deflection. The second method was tested extensively: measurements were taken of blade and flap loads which compared well to predicted values. The flight tests which began in 2005 collected vibration data at the gearbox for 60 and 100 kts flight speeds, using open-loop control of the flaps. Subsequent flight testing with a closed-loop controller has demonstrated significant simultaneous reduction of the vertical force and pitch and roll moments at the hub, for a wide range of speeds in steady level flight. The flap design for this effort was produced with

numerical predictions from CAMRAD II, with airfoil lookup tables and flap inertia included. The aerodynamic properties for flapped airfoils were obtained from a combination of CFD studies and thin airfoil theory.

The Japanese Aerospace Exploration Agency (JAXA) has also undertaken a research and development program for the active flap [64, 65]. The primary focus of this project is noise reduction. Having developed a piezoelectric actuation system, the flapped section of the blade was recently tested in a transonic wind tunnel where flap deflection and surface pressure were measured. Test cases simulated landing, hover and maximum cruise speed conditions. The flap system achieved adequate deflection at a range of harmonics from 2/rev to 5/rev. Whirl tower and wind tunnel tests of the complete rotor are planned.

Many experimental investigations at the model scale have also been carried out. Hall *et al.* [66] developed the piezoceramic bimorph actuator to fit within a model scale blade. The refined design produced flap deflections of $\pm11°$ at 100 Hz on the bench, and was predicted to be able to produce at least $\pm5°$ at typical helicopter operating speeds. Fulton and Ormiston [67] and Koratkar and Chopra [68] used wind tunnel tests of Mach-scaled rotors in hover and in forward flight to demonstrate sufficient flap authority for multi-function vibration suppression. Roget and Chopra [69] developed and tested a control algorithm for dissimilar blades with trailing edge flaps. Using individual control input for each blade, instead of phase-shifted identical inputs for all blades, allowed significant reduction of vibration loads.

Numerical analysis of rotors with trailing edge flaps has been seriously studied since the early 1990s. Millott and Friedmann [70, 71] started their investigation

of servoflaps on a hingeless rotor using rigid blades, an aerodynamic model based on thin airfoil theory and uniform inflow. Flap inertia was included in the structural model, and the hinge gap was considered with the inclusion of an efficiency factor applied to the hinge moment. The analysis was then enhanced with the inclusion of flexible blades, which significantly changed vibrations predictions, but not overall flap behavior in the system. Parameter studies of flap size, spanwise location and blade torsional stiffness at the root showed that flap effectiveness was affected significantly by blade torsional stiffness and by spanwise location. Locating the flap near the node of the second flap mode of the blade resulted in maximum flap authority. A comparison to other vibration active control methods indicated that the flap could be as effective as IBC, while requiring less power [71]. Milgram and Chopra built a comprehensive analysis based on the University of Maryland Advanced Rotorcraft Code (UMARC), that included an unsteady, indicial aerodynamic model and a free wake model. The wake model did not include the effects of trailed vorticity at the flap boundaries. A parametric design study with a multicyclic controller examined the effect of flap chord, length, spanwise location and controller parameters. In general, the flap effectiveness at vibration reduction was found to be insensitive to flap size or location, since the controller compensated for differences in performance by varying the flap amplitude within the boundaries of $\pm 5°$. One exception is flap length which could not be reduced below a certain minimum, beyond which the required flap inputs would exceed the prescribed maximum. The flap was predicted to be effective at all advance ratios. The results were compared to both CAMRAD/JA and experimental data from wind tunnel

testing [72]. Although both analyses showed fair agreement with the baseline rotor for blade loads, the trailing edge flap predictions varied from fair to poor. Myrtle and Friedmann [73] proposed a new aerodynamic model for the active flap called the rational function approach (RFA) which used two-dimensional unsteady effects and compressibility in the time domain. Compared to a quasisteady model based on Theodorsen's thin airfoil theory [74], similar vibration control was achieved, but flap actuation power increased. Zhang *et al.* [75] studied active and passive vibration reduction by combining optimum blade structural design with active flap control. The goal was to reduce vibration with minimum control input and to identify the key design features for a rotor blade with integrated flap, so as to stay within the stroke limitations of current smart actuators. By using simultaneous optimization of the blade structure and the flap design, it was found that similar vibration reduction could be achieved compared to a rotor blade retrofitted with a flap, but with 30% to 60% less flap deflection across the range of forward flight speed. The effectiveness of the flap actuated at 3/rev, 4/rev and 5/rev was enhanced by a blade tuned to have its second flap mode at 3/rev and its third flap mode at 5/rev. Depailler and Friedmann [76] concentrated on reducing vibration when dynamic stall is also present, at forward flight speeds ranging from $\mu = 0.3$ to $\mu = 0.45$. The study used both single and dual flaps, and limited the total flap deflection to $\pm 4°$. The single flap was 0.12 of the blade length, located at 0.75R. The dual flaps were each 0.06 long, located at 0.72R and 0.92R. The dual flaps seemed to be more effective at controlling vibration due to dynamic stall, but both configurations could reduce vibration to acceptable levels. The US Army and NASA developed an active elevon rotor (AER) in a joint

project [77]. Both dual and single flap systems were studied on an Apache blade model modified to reduce torsional stiffness. Patt, Liu and Friedmann [78] used dual flaps to examine the simultaneous reduction of noise and vibration, and validated results with experimental data. The simultaneous solution requires compromised results for both vibration and noise, with neither being as successfully controlled as they can be with a dedicated solution.

1.4.2 Primary Control

Subsequent to the renewed interest in trailing edge flaps as active control devices Ormiston [79], conducted a feasibility study of flaps for primary control. The analytical model used rigid blades, quasi-steady thin airfoil theory and uniform inflow. Elevon (trailing edge flap) reversal was identified as a key phenomenon for the flap controlled swashplateless rotor. Reversal is defined as the point at which the lift directly produced by flap deflection is equal to or less than the opposing lift caused by the induced elastic twist. Since the range of operation for a moment flap is predicted to be larger than for a lift flap, a flap controlled helicopter should typically operate beyond flap reversal speed. The conclusion drawn from this observation was that the torsional frequency should be low enough to maximize the twist induced by the flap. It was also noted that blade pitch indexing would have the effect of reducing the total required flap deflections.

Shen *et al.* [80–84] conducted the first in-depth, methodical investigation of trailing edge flaps for swashplateless primary control. A series of numerical stud-

ies were carried out with UMARC on an ultralight teetering rotor, the bearingless McDonnell-Douglas Advance Rotor Technology (MDART) rotor, and a heavy utility rotor. The aerodynamic model included thin airfoil theory and an unsteady model for flaps without aerodynamic balance. Flap drag was estimated with the unsteady model. Simultaneous primary and vibration control was examined with a multicyclic controller, and the stability of the flapped rotor was determined with eigenanalysis. Results for the baseline, unflapped MDART rotor were compared to wind tunnel test data and predictions from CAMRAD II and showed fair agreement. The primary design parameters for the swashplateless rotor were found to be index angle and torsional frequency. The blade pitch angles of the conventional and swashplateless rotor were compared, with both rotors at 2.1/rev torsional frequency. It was observed that the blade collective, longitudinal cyclic and lateral cyclic pitch angles induced by the trailing edge flap deflections on the swashplateless rotor were similar to the conventional rotor pitch control angles in both magnitude and trend. When positive flap deflections contributed additional lift, the swashplateless rotor had a slightly lower blade collective pitch angle than the conventional rotor. The swashplateless MDART rotor could be trimmed across the range of forward flight speeds with mean flap angles of $\pm 5°$ and half peak-to-peak angles less that $6°$, and 99% reduction of vibration loads was predicted with small additional deflections. Investigation of the heavy utility rotor proceeded with linear inflow and quasi-steady thin airfoil theory for the aerodynamic model. A parametric study of the flap configuration examined flap overhang, chord, span, spanwise location and blade index angle in to minimize flap control angles and hinge moment at high speed. It was

shown that flap control angles can be reduced significantly with the selection of index angle and flap length. Flap hinge moment was sensitive to the size of the flap overhang. Overall, the parameters that were most effective at reducing flap control angles and hinge moment were similar for all of the examined rotors, regardless of weight-class. Improving the flap geometry and location with the results of the parametric studies resulted in moderate flap collective and half peak-to-peak angles, and moderate actuation power required.

Ganguli *et al.* [85, 86] have also studied the swashplateless rotor concept, and have proposed various enhancements to improve feasibility. The primary control inputs of a swashplateless rotor with individual blade control are typically predicted to be higher than the inputs required for vibration or noise control. This larger requirement conflicts with the limited stroke capabilities of smart actuators. It was suggested that the blade cyclic deflections could be reduced or eliminating by shifting the location of the vehicle center of gravity (cg). Sensitivity studies indicated that optimal location of the cg in combination with blade pitch indexing could reduce the maximum required half peak-to-peak blade deflections by almost 50%. It was further recommended that active cg positioning be investigated for micro- and unmanned rotorcraft. For small vehicles, the active cg could reduce blade cyclics to zero across the range of forward flight speed. Survivability is a concern with the swashplateless rotor, as any damage to a blade automatically compromises the control system. Damage was simulated on one blade of a BO105 rotor model in UMARC by suppressing pitch collective, longitudinal cyclic and lateral cyclic, both individually and in combination. In the event of partial or complete damage

29

to one blade, the individual blade control deflections of the remaining blades are reconfigured to maintain trim. In hover, loss of collective control for one blade results in increased collective for the three undamaged blades, and 1/rev forces and moments. In forward flight, it was predicted that the rotor could still be trimmed at low and moderate advance ratios, but at high advance ratio, either a collective failure or a collective and lateral cyclic failure leads to difficulty in trimming. The difficulty in trimming is directly related to the magnitude of longitudinal cyclic deflection in the damaged blade. Damage in forward flight also produces large 1/rev and 2/rev loads.

1.4.3 Experimental and Numerical Characterization of Flapped Airfoils

Although plain flaps have long been in use on fixed wing aircraft, they do not have a similarly long rotorcraft history. Consequently, the experiments conducted and published tend to include flight conditions, aerodynamic properties and Reynolds numbers most suitable to fixed wing aircraft. Early wind tunnel tests of plain flaps were sometimes conducted at Reynolds numbers below 1×10^6, meaning that viscous effects such as flow separation might be more influential in the test results than they would at the higher Reynolds numbers at which helicopters typically operate. Most frequently, the goal of the experiment had been to identify incremental changes in lift and pitching moment coefficients due to flap and/or tab deflections, and drag was not considered in these studies. Occasionally, when

both flap and tab were installed on an airfoil, only positive flap deflections were tested, even when both positive and negative tab deflections were included in the test matrix.

Abbott and von Doenhoeff [87] describe a variety of high-lift devices for fixed wing airfoils and reviewed the state of the art up to 1950. Plain flaps were observed to act as a change of camber, and for unseparated flow and no gaps the resulting change in lift and pitching moment could be well predicted by thin airfoil theory. Hinge moment and flap lift predictions were less accurate due to increased viscosity effects over the aft section of the airfoil. The changes to aerodynamic properties can be calculated for either symmetric or cambered airfoils as increments that add to the baseline properties of the unflapped section. From experiments with plain flaps on a selection of cambered airfoils [88, 89], it is shown that although significant increases in maximum lift coefficient can be achieved, the angle of maximum lift coefficient decreases with positive flap deflection. For unstalled, unseparated flow, at positive angles of attack a positive flap deflection produces an increase in airfoil lift, and increase in drag and a nose-down pitching moment. Conversely, in the same conditions, negative flap deflections produce opposite changes. Wenzinger *et al.* [90, 91] compared different flap types to identify the configuration producing the maximum increase in lift. Tests were conducted at Reynolds numbers up to 8.0e6, and measurements of airfoil lift, drag, pitching moment and flap hinge moment were taken. Slotted flaps and split flaps were the primary focus. Similar to the plain flap, the slotted flap increases lift by increasing effective camber, but it also delays flow separation over the flap by ducting air from the lower surface to the upper surface

31

of the airfoil. The split flap allows deflection only of the lower surface of the flap, and like the slotted flap, is designed to deflect only in one direction (positive). Wenzinger's results showed that the best combination of high lift and low drag is produced by the slotted flap.

Ames, with co-authors Street [92] and Sears [93, 94], conducted a series of wind tunnel tests on NACA 0009 airfoils with plain flap and tab. For each case, the total chord size of the flap and tab combined $(c_f + c_t)$ was fixed, and three tabs of 10, 20 and 30 percent flap chord were studied. In the case of a 50 percent flap [92], $c_f + c_t = 0.5c$, and this results in the following pairings: 10% tab, 40% flap $(0.10c_t, 0.40c_f)$; 20% tab, 30% flap; 30% tab, 20% flap. The purpose of the tests was to generate 2-D sectional aerodynamic data for the design of airplane tail surfaces. The gaps at the leading edges of both the flap and the tab were sealed to prevent airflow between the top and bottom surfaces of the airfoil. The section angles of attack covered the range from $-15°$ to $10°$, while the flap angle was varied from $0°$ to $45°$ (positive flap angle is flap down), and the tab angles were varied from $-30°$ to $30°$. The section was fitted with pressure tubes in a single row on both the upper and lower surfaces of the airfoil, the flap, and the tab, and tested at $R_e = 3.4e6$. The properties measured were airfoil normal force and pitching moment, flap normal force and hinge moment, and tab normal force and hinge moment; drag is not reported. These tests produced a fundamental description of the airfoil-flap-tab system. Positive tab deflection produces an increase in airfoil normal force, and the slope of the normal force increment is not very sensitive to tab chord size or deflection. The tab loses its effectiveness against airfoil pitching moment and flap

hinge moment as tab deflections increase in either direction, and also as tab chord increases. Airfoil normal force and pitching moment are significantly and linearly affected by flap deflection, until stall is reached. The experimental data were used to produce parameterized design curves [95] for the estimation of changes to airfoil lift and pitching moment and flap hinge moment based on flap and tab chord and flap and tab deflections. These curves are compared to the results of thin airfoil theory, and show fair agreement for unstalled conditions. When the flap or tab are stalled, agreement is poor. Other NACA investigations of the plain flap and tab indicated that the most increase in lift with the least increase in drag was achieved when the tab was large compared to the flap [96]. This result was found when the flap and tab deflected in the same direction and hinge gaps were sealed. Liddell [97] showed that the inclusion of aerodynamic balance or overhang on the flap, where the flap hinge is behind the leading edge, significantly reduces flap hinge moment while protecting the gains to lift. However, profile drag is increased, especially as the flap deflection increases.

As flapped airfoils recently have been considered for helicopter applications, researchers have used both tests and simulations to evaluate airfoils and flap configurations. Hassan, Straub and Noonan [2] conducted two-dimensional wind tunnel tests of flapped versions of the HH-06 and HH-10 airfoils. The intention was to create airfoil lookup tables suitable for use in comprehensive analysis codes, and thus the test matrix covered a wide range of Mach numbers, angles of attack and flap deflection, which varied from $\pm 8°$. The flaps all had aerodynamic balance or flap overhang. This is an important parameter for helicopter applications, since flap

hinge moment requirement can be reduced with the use of overhang. Reducing flap hinge moment leads to lower actuation power required, which is key for lightweight, compact, on-blade actuation. The flap hinge was fixed at 0.75c on the airfoil, and the overhang, measured with respect to the flap chord, varied from $0.35c_f$ to $0.45c_f$. Gaps between the airfoil and flap were not sealed. The aerodynamic properties measured included airfoil lift, drag and pitching moment, flap lift and hinge moment, at Mach numbers from 0.45 to 0.75, and Reynolds numbers from 2.7e6 to 5e6. The wind tunnel tests were followed by computational fluid dynamics (CFD) predictions, for which the airfoil-flap system was modeled as one piece, with no gap. From these tests, it was observed that the size of the flap overhang had a significant effect on airfoil pitching moment, airfoil drag and flap hinge moment coefficients. The flap overhang also tended to cause a slight decrease in airfoil lift coefficient, due to flow through the hinge gap. The flap hinge moment coefficients also were shown to be sensitive to airfoil thickness ratio. Accuracy of the CFD predictions was greatly affected by the configuration of the grid at the flap leading edge. Previously observed effects of flap deflection on aerodynamic properties were noted again, showing that for positive angles of attack, positive flap deflection increases airfoil lift and drag coefficients and negative flap deflections decreases airfoil lift and drag coefficients compared to the baseline value measured at neutral flap position.

The time and expense required to wind tunnel test a flapped airfoil through the range of conditions necessary to construct an airfoil lookup table is considerable, and difficulty increases as the Mach numbers become transonic. However, accuracy and computational expense prevented simulation from being a viable substitute for the

wind tunnel. Recently, improvements in methodology and advances in computing speed have made automated generation of airfoil lookup tables with CFD feasible. Mayda and van Dam [98] generated tables for the UH-60A airfoils, SC1095 and SC1094R8, for Mach numbers from 0.4 to 0.8. Good agreement with experimental data is shown at M=0.4, but agreement is only fair at M=0.8, where solutions are more difficult to obtain [99, 100]. Ongoing research in refining CFD turbulence models may lead to prediction improvements for stalled and separated flow [101]. Automating the table generation seems not to degrade the accuracy of the data, and greatly improves the feasibility of studies using novel airfoil modifications.

Jose and Baeder conducted CFD investigations of flapped airfoils to predict basic aerodynamic properties of flapped airfoils [102], and to develop improved techniques for modeling flap overhang and hinge gap [103]. In both cases, the goal is to characterize flapped airfoils for rotorcraft applications. For subsonic Mach numbers, CFD predictions show good agreement with thin airfoil theory for airfoil lift, pitching moment and flap hinge moment. As the flow becomes transonic, the prediction captures flow phenomena that causes it to diverge from the predictions of thin airfoil theory. The major discernible effect of airfoil thickness is to reduce flap hinge moment. It was shown for several airfoils that the effect of flap deflection on airfoil drag can be estimated using an effective angle of attack. The effective angle of attack serves to convert drag from a function of angle of attack and flap deflection to solely a function of angle of attack. This is a powerful conclusion, suggesting that for any airfoil, the aerodynamic properties, including drag, of a flapped alternative in subsonic and unstalled flow can be well approximated using the properties of the

original section and an effective angle of attack.

The effect of flap overhang was also examined using CFD, comparing the resulting predictions to the wind tunnel tests conducted by Hassan *et al.* on the HH-06 airfoil [2]. The gap between the airfoil and the flap was modeled using two different CFD mesh techniques. Gap averaging simulates the gap by averaging the flow over the upper and lower surfaces of the airfoil, thus setting the density, pressure and velocity equal on either side of the gap. The gap is not directly modeled, resulting in a single, continuous mesh that can be the same as the mesh used with no gap. The patched mesh method uses an additional mesh in the gap, which has a high number of grid points in both the chordwise and through thickness directions. Although the gap is constrained to be no more than 0.01c, the high grid point density is required to accurately model the boundary layer and the flow through the gap. It was seen that the gap averaging method, which is simpler to model and computationally less expensive, produces aerodynamic predictions that compare well to experimental data. One effect of the gap is to reduce flap authority by decreasing lift and pitching moment while increasing drag and hinge moment. Current CFD results on the effect of the hinge gap are supported by older wind tunnel tests conducted for fixed-wing investigations [96, 97, 104].

The combination of advanced simulation techniques and partial validation with experimental data allows the exploration of many flap configurations, with some confidence in the accuracy of the results.

1.4.4   Wake of Flapped Airfoils

An important addition to the aerodynamic model of the comprehensive analysis used in the current investigation is the effect of the trailing edge flap on the blade wake. Accordingly, current flap wake research is reviewed here.

Johnson [6] describes the fundamental physics of the rotor vortex wake. The bound circulation due to the lift on the rotor blade is trailed into the wake from the tip and the root. The radial variation of the bound circulation leads to trailed vorticity, while the the azimuthal variation leads to shed vorticity. The combination of shed and trailed vorticity forms a vortex sheet behind the rotating blade. The bound circulation reaches a maximum strength on the outboard section of the blade, then drops to zero over a short distance. This abrupt decrease in circulation strength produces a large vorticity strength at the blade tip, which attracts the other vortices and causes them to roll up into a concentrated tip vortex. The strength of the tip vortex grows to match the maximum bound circulation. At the blade root, the bound circulation also decreases to zero, but more gradually so that the strength of the trailed vortex at the root is much lower than at the tip. It is common to analyze the wake thus described using a vortex lattice model, which is computationally intensive. A simplified vortex lattice model neglects the inboard shed and trailed vorticity, leaving only the trailed vorticity on the outboard section or the single concentrated tip vortex. This approach captures the essential behavior of the wake and is computationally efficient.

The introduction of a trailing edge flap on the outboard section of the blade

requires a reassessment of the tip vortex wake model. Lee *et al.* measured tip vortex position and strength on an oscillating NACA 0015 wing with no twist, taper or tip shaping [105, 106]. Models with both full and partial span flaps were fitted with endplates to ensure two-dimensional flow, and 48 pressure taps were distributed over both surfaces of the wing. A triple hot-wire probe was used to measure the velocities of the tip vortex, and was computer controlled to follow the movement of the vortex. The maximum flap deflection in either direction was 7.5°, and the flap was deflected at varying start times, for an actuation period corresponding to one-half of the wing oscillating cycle. It was observed that negative (flap up) deflections instigated at the onset of flow reversal mitigate the nose down pitching moment that results from dynamic stall. This effect was attributed to suction pressure on the lower surface of the flap, and a reduction in suction pressure (with an accompanying loss of lift) on the upper surface of the wing. Flap deflection in either direction changed the radial position, strength and shape of the tip vortex. For the full span flap, positive (flap down) deflection moved the vortex centroid outboard, increased the strength of the vortex while decreasing peak vorticity compared to baseline, and diffused the vortex. Negative flap deflection moved the centroid inboard, concentrated the vortex, and reduced its strength. The results for the partial span flap were similar, except the negative flap deflections resulted in a more diffuse tip vortex than the baseline wing. Further tests on the partial span flap examined the effect of higher harmonic actuation on the tip vortex [107]. The maximum flap deflection was ±8°, at 2, 3, and 4/rev harmonics. Harmonic flap motion significantly decreased peak vorticity, while increasing core radius. The general conclusion of the all the tests

was that trailing edge flap deflections have an effect on the strength, concentration and location of the tip vortex, but further tests on a rotating wing are required.

1.4.5 Performance Improvement

In hover, rotor induced drag is reduced by off-loading blade tip (weakening tip vortex) with taper, swept tips, anhedral, and primarily, large negative blade twist. All of these blade design features help to redistribute blade lift more evenly across the span. However, highly twisted blades are a disadvantage in forward flight. One way to reconcile the conflict between high performance in hover and in forward flight is to achieve good hover performance with low blade twist. The HIMARCS (High Maneuverability and Agility Rotor and Control System) rotor [108] is a test platform for evaluating lift enhancement devices such as leading edge slats and trailing edge flaps. Slats and flaps at fixed deployments were studied at a range of rotor lift coefficients, advance ratios and vehicle parasite areas. It was concluded that for a low blade twist of $-8°$, a leading edge slat with a moderate $6°$ deflection produced the best improvement in rotor performance (reduction in rotor torque) compared to the baseline blade, a $10°$ slat and a $3°$ flap. Further studies of the rotor using 3D viscous CFD analysis [109] found that trailing edge flaps at fixed deflections in combination with low twist rotor blades allow good performance in both hover and high speed flight. A blade with $-7°$ twist and an inboard flap matches the performance of an unflapped blade with $-13°$ twist.

Glaz and Friedmann [110] combined active/passive optimization with the RFA

aerodynamic model to study both vibration reduction and rotor performance at high advance ratios. The flap aerodynamics were represented by thin airfoil theory augmented with a semi-empirical model which assumed positive and negative flap deflection produced the same increase in drag, and did not consider the effects of blade angle of attack or Mach number. Considering the baseline blade without a flap, the optimization was able to achieve either a 23% reduction in vibration with a 4% increase in rotor power, or a 5% reduction in power with a 5% increase in vibration. A multi-objective function design without a flap showed an 11% reduction in vibration and a 5% reduction in rotor power. An active/passive configuration with optimized structural design and an active flap, controlled for both vibration and rotor power reduction, achieved about 25% vibration reduction and 5% power reduction. Liu *et al.* [111] extended the study to include dynamic stall at high advance ratios.

Yeo compared seven active controls in their effect on rotor performance: IBC, trailing edge flap, active twist, oscillatory jet, Gurney flap, leading edge droop, leading edge slat [112]. The rotor model was based on an Apache with updated airfoils, modified as necessary to implement each control. The aerodynamic model in CAMRAD II was enhanced with airfoil tables specific to each type of active control. Each set of tables was generated with different combinations of wind tunnel testing and numerical simulation, with at least four different baseline airfoils. Calculated increments in lift, drag and pitching moment were added to the baseline for the investigation. The performance metrics used were rotor lift-to-drag ratio at one thrust and a range of advance ratios and blade loading sweeps at two airspeeds. It

was shown that IBC, active twist and trailing edge flaps improved the rotor lift-to-drag ratio when controlled at 2/rev, but did not increase maximum blade loading. The other active controls increased the maximum blade loading when deployed over the retreating side, but did not improve the lift-to-drag ratio.

1.4.6   Gurney Flaps

A Gurney flap is a thin plate perpendicular to the pressure surface of the airfoil, devised as a control for the separation of trailing edge flow. Depending on chord size and placement, the Gurney flap offers an increase in maximum lift coefficient, a slight delay in stall angle, and an increase in nose-down pitching moment for small increase in drag. Gai and Palfrey [113] conducted wind tunnel tests with flow visualization to show that the Gurney flap reduces or eliminates separation on the upper surface of the airfoil, with a small region of separation upstream of the flap on the lower surface. One of the most important parameters determining the effectiveness of the Gurney flap is its size relative to the airfoil chord. As long as the flap remains within the boundary layer, the drag penalty remains small. As the size of the flap increases, the drag penalty increases as unsteady wake effects increase. By moving the flap forward of the trailing edge some small amount, it is possible to add an actuation system that fits within the profile of the airfoil, and enabling the Gurney flap to be deployed at advantageous flight conditions and retracted at other times. This retains the improvements to lift while reducing the drag penalty [114]. Chandrasekhara *et al.* [115] proposed using a Gurney flap to recover lift lost by a

variable droop airfoil. The variable droop controls compressible dynamic stall at the cost of a significant decrease in $C_{l_{max}}$. Combining the two controls retained the improvement to dynamic stall while reducing drag and moment coefficients. Kinzel *et al.* [116] numerically examined the effectiveness of Gurney flaps for improving rotor performance. Increases in maximum flight speed, rotor lift-to-drag ratio and achievable thrust were predicted. It was suggested that deployable Gurney flaps could be used for vibration control in addition to performance enhancement.

1.4.7 Tab Actuated Flaps

The tab actuated flap was suggested by Loewy and Tseng [117] as a type of aeroelastic amplification for smart actuators. Amplification is required to boost the limited stroke capabilities of the typical smart actuator, but the desire to locate the actuator on the rotor blade severely constrains the size and weight envelope. By actuating the tab instead of the flap, and using amplification, relatively small inputs of actuator power and stroke can result in larger flap deflections than would be achieved with direct flap actuation. The investigation used a one degree of freedom system with a fixed wing, prescribed tab and free floating flap. The design variables of the system were the flap hinge position and the hinge stiffness. A feedback loop was used to control static instability in the system. It was predicted that the design variables would control both the system gain (ratio of flap deflection to tab deflection) and its frequency response. Heinze and Karpel [118] tested the concept on a high aspect ratio wing in a low speed wind tunnel. The piezoceramic

bimorph actuator mounted in the flap produced no more than ±3° tab deflection at frequencies up to 20 Hz; the maximum gain measured was 1.8. At low frequency, the flap deflection was 180° out of phase with the tab, but as actuation frequency increased, the phase difference decreased. The key parameters for performance were found to be flap hinge stiffness and flap inertia, so that a light weight flap with low stiffness yields the best gain and frequency response to tab deflection.

1.5   Objective of Current Research

The objective of this research is to examine the feasibility of using tab actuated flaps and trailing edge flaps as primary control systems for swashplateless helicopters. In doing so, an understanding of the fundamental physics of the system is established.

There are two key barriers to the successful design and implementation of such a system. First, the magnitude of the control angles and hinge moments required to trim the swashplateless rotor must be compatible with the stroke, force and bandwidth capabilities of an actuator that fits within the profile of the helicopter airfoil. Second, the effect of the flap and tab deflections on the performance of the swashplateless helicopter, as measured by rotor torque and rotor lift-to-drag ratio, must be predicted accurately for comparison to the performance achieved by the conventional swashplate system.

A state of the art, comprehensive analysis is refined to include a trailing edge flap and a tab-actuated flap. In analyzing a conventional rotor, blade pitch angles

are used to produce a coupled trim solution. For the swashplateless variation, trim procedure is modified so that the control angles are provided by either flap (for a trailing edge flap system)or tab (for a tab-actuated flap system) deflections.

To accurately predict the control requirements and performance effects of the flaps and tabs, aerodynamic models are developed which include the incremental effect of the trailing edge controls on the sectional airfoil properties. Then the inflow model is expanded to include both the near and far wake effects of the deflected controls.

An initial goal is to understand the control requirements and key design parameters of the tab actuated flap system using a simplified, rigid blade model and a conceptual rotor with torsionally soft blades. A parametric study examines the effect on primary control of design variables such as index angle, blade root and flap spring stiffness, flap and tab radial length, chord length, midspan location, and overhang.

Next, a thorough investigation of an existing helicopter, the UH-60A, is carried out with the comprehensive analysis. A parametric study using key design variables is conducted to minimize the control angles and hinge moments required to trim the swashplateless rotor at high speed, in steady level flight.

Finally, the consequences of replacing the swashplate with on-blade, trailing edge controls are evaluated. The performance of the swashplateless rotor is calculated and compared to the baseline rotor at various levels of thrust and for different values of parasite drag.

In the present work, a helicopter model with a swashplate is referred through-

out as conventional, or as baseline. When making comparisons between a conventional and swashplateless helicopter, the modifications to the swashplateless model have been limited to the addition of trailing edge flaps and tabs, and the reduction of the pitch spring stiffness at the blade root. This is because the analysis does not include an explicit structural representation of the swashplate; instead the mechanism is represented through the stiffness and damping characteristics of the pitch links.

1.6 Scope of Current Research

The focus of the current research is the development of a comprehensive aeroelastic analysis of swashplateless helicopter rotors with trailing edge flaps and tabs for primary control. The kinetic and potential energy expressions, and governing equations, are derived using Hamilton's Principle and solutions are produced using finite element methods in space and in time. The beam finite elements of the blade have fifteen degrees of freedom, allowing the continuity of deflection and slope of axial extension, flap, lag and torsion. For this investigation only one flap deflection and one tab deflection are permitted per blade, but the flap and the tab can extend over multiple blade elements. Two aerodynamic models are used in the investigation. The first is a quasi-steady model developed from thin airfoil theory by Theodorsen and Garrick [119]. This model includes a trailing edge flap and a tab with arbitrary hinge locations. The second model uses airfoil table lookup to obtain sectional aerodynamic coefficients for the control surfaces. The coefficients

are based on blade angle of attack, Mach number, flap deflection and tab deflection, and are compared to the baseline airfoil (either unflapped or with control surfaces at zero deflection) to calculate an incremental change to the blade lift, drag and pitch moment. Uniform inflow is generally used for studies in hover. The Bagai-Leishman pseudo-implicit free wake model was used in forward flight. The free wake model was modified to include the effect of the trailing edge flap in the near and the far wake by adding vorticity trailers to the blade at the radial bounds of the flap. The solution of the structural response is coupled with an aerodynamic model and a trim procedure using the vehicle equilibrium equations. This allows the rotor to be examined either in isolation or as part of a vehicle in free flight. The wind tunnel trim analysis conditions prescribe longitudinal and lateral shaft angles, and tail rotor collective. Trim solutions can be produced for targeted thrust and hub moments, or for targeted thrust and first harmonic blade flapping.

First, a swashplateless conceptual rotor similar to servo-flap rotors produced by Kaman Aerospace is studied with a rigid blade analysis. The rotor has blades that are very soft in torsion, and the flaps and tabs are integral to the blade profile. The purpose of the study is to establish the feasibility of using tab actuated flaps for primary control of the rotor. The rigid blade model includes degrees of freedom for blade flap, blade torsion, trailing edge flap and tab. A forward differencing scheme is used to calculate a steady state, wind tunnel solution for the rotating system, where the control inputs to the system are provided by the tab angles. A parametric design study reveals the sensitivity of the rotor system to design variables such as index angle, span, chord length, midspan location and hinge position of the flap and tab.

The purpose of the study is to reduce both control angles and hinge moments so that the actuation power required for the tab is minimized.

Then a second swashplateless rotor model is created as a variant of the UH-60A helicopter by adding a trailing edge flap and a tab to each blade, and reducing the torsional stiffness of the root spring. All other properties of the rotor are unchanged. The control angles and hinge moments required to trim the rotor are evaluated with parameter studies. These studies were conducted in two parts: (1) uncoupled blade response in hover, and (2) wind tunnel trim in forward flight and at high speed. The uncoupled blade response study illuminates the fundamental physics of the system by testing the effect of such variables as blade torsional stiffness and trailing edge flap spring stiffness. This study used uniform inflow and the thin airfoil aerodynamic model. Key design variables were identified in the second part of the parameter study, where properties such as index angle, flap and tab span, flap and tab chord length, midspan position of the flap/tab, and hinge position of the flap and tab were examined for their effect on the control angles and hinge moments. This study used non-uniform inflow distribution with the free wake model, and thin airfoil aerodynamics.

The comprehensive analysis is used to validate the structural and aerodynamic models of a baseline UH-60A rotor. This rotor was selected for examination because it has been extensively studied in the NASA/Army UH-60A Airloads Program. Predicted blade pitch angles, rotor shaft angles and rotor performance are compared to flight test data in hover and in forward flight.

Next, the drag of flapped airfoils is examined, using both experimental and

47

numerical data. A general empirical model is developed for the drag of flapped airfoils. This model can be used in analyses of trailing edge flap airfoils, in the absence of detailed test or numerical data. A set of airfoil tables are generated for a flapped SC1094r8 airfoil, using computational fluid dynamics analysis. These tables are employed in all performance predictions for the swashplateless rotor.

The performance of the swashplateless rotor is compared to the baseline helicopter. The behavior of the baseline rotor as the torsional frequency is reduced is investigated for insight into the behavior of the swashplateless rotor. Performance in hover for the swashplateless and baseline rotors in wind tunnel trim with uniform inflow is methodically studied for the figure of merit, main rotor power and twist distribution. In forward flight, the rotors are first examined in wind tunnel trim, using a free wake model with a single tip vortex. The effect of the inflow model upon the main rotor power prediction is explored through close study of the blade angle of attack distribution and operating envelopes for the Mach number, lift and drag coefficients. The inflow model is refined to include the effect of the trailing edge flap in the near and far wake, and the power prediction is re-evaluated for the swashplateless rotor. Vehicle trim solutions are calculated for the swashplateless and baseline rotors, and the power and rotor shaft angle are compared.

Finally, a systematic performance study compares the swashplateless rotor to the baseline through rotor power and rotor lift-to-drag ratio at several levels of thrust and for incremental reduction of parasite drag.

1.7 Overview of Dissertation

Chapter 1 reviews the history and evolution of helicopter primary control systems. Alternatives to the swashplate system are examined, and their strengths and disadvantages are described. The various trailing edge controls are discussed, including flaps, tab actuated flaps and gurney flaps, and a survey is made of numerical and experimental research with these controls for vibration reduction and primary control. The objective and scope of the current work are presented.

In chapter 2, the details of the aeroelastic formulation of the comprehensive analysis are described through the derivation of the governing equations of the tab actuated flap system; the aerodynamic, inertial and structural contributions of the flap and tab are given. The wind tunnel and vehicle trim procedures are outlined for the swashplateless rotor. The development and improvement of the trailing edge flap aerodynamic model is outlined.

Chapters 3 and 4 present the results of this investigation. First the parameter studies of a Kaman-type rotor with torsionally soft blades and the UH-60A are described, where the purpose is to minimize the control angles and hinge moments required to trim the rotors. Next, the impact of the trailing edge flap on rotor performance is studied in hover and in forward flight.

Chapter 5 discusses the key conclusions of the current work, and offers recommendations for future work.

Table 1: Summary of Trailing Edge Flap Literature by Category

Description	Vibration		Primary	Performance
	Experimental	Numerical		
Full-scale	Straub et al. [2], Straub and Kennedy [3] Toulmay et al. [10], Dieterich et al. [11], Konstanzer et al. [12] Noburu et al. [18], Noboru and Saito [19]	Straub and Hassan [4], Straub and Charles [5]	Pescara [6], d'Ascanio [7], Kaman [8]	Payne [9] Lemnios and Smith [13], McCloud [14], Lemnios and Dunn [15], McCloud and Weisbrich [16], Wei and Weisbrich [17]
Model-scale	Spangler and Hall [20], Fulton and Ormiston [22], Koratkar and Chopra [23], Roget and Chopra [24]			Noonan et al. [21]
Analytical		Millott and Friedmann [25], Friedmann and Millott [28], Milgram et al. [31], Myrtle and Friedmann [34], Zhang et al. [37], Depailler and Friedmann [39],	Ormiston [26], Shen [29], Shen et al. [32], Shen and Chopra [35], Shen and Chopra [38], Shen et al. [40],	Glaz et al. [27], Liu et al. [30], Yeo [33], Gagliardi and Barakos [36]
			Continued on next page	

Table 1 – continued from previous page

Description	Vibration		Primary	Performance
	Experimental	Numerical		
		Fulton [41], Patt et al. [43]	Ganguli et al. [42], Ganguli et al. [44]	
Airfoils				Wenzinger and Ames [45], Wenzinger and Harris [46], Street and Ames [47], Ames and Sears [48], Ames and Sears [49], Ames and Sears [50], Sears and Purser [51], Liddell [52], Hassan et al. [53], Jose and Baeder [54], Jose et al. [55]
Wake				Gerontakos and Lee [56], Panagakos and Lee [57], Lee and Pereira [58]
Gurney	Gai and Palfrey [59], Standish and van Dam [61]			Chandrasekhara et al. [60], Kinzel et al. [62]

Description	Vibration		Primary	Performance
	Experimental	Numerical		
Flap-Tabs	Heinze and Karpel [65]			Theodorsen and Garrick [63], Loewy and Tseng [64]

Chapter 2

Analytic Model

This chapter describes the aeroelastic analysis of a swashplateless helicopter rotor controlled with trailing edge flaps and tabs. For such rotors, the swashplate and pitch links that directly control blade pitch in typical rotors have been replaced with a soft torsion spring at the root. The blade pitch control is achieved indirectly, by inducing the blade response to aerodynamic loads generated by the deflections of the tab and flap. When both a flap and a tab are present, deflection of the tab generates aerodynamic forces and a moment about the tab hinge which cause the flap to respond by deflecting about its hinge in the opposite direction. The blade in turn is induced to twist in the direction opposite to the flap so that equilibrium with the new aerodynamic environment is achieved. The actuator chosen for this application must have sufficient stroke to meet the required deflection angle and must generate enough force to overcome the hinge moment. Therefore, the magnitude of the control angles and hinge moments required to trim the rotor determine the characteristics of the actuator chosen to drive the control surface. The control angles are also significant for their effect on the aerodynamic properties of the rotor blades, since the changes to the rotor lift, drag and pitch moment will change the power required to trim the rotor. Accordingly, the purpose of this investigation is twofold: first, to predict the control angles and hinge moments required for trim, and second, to

assess the effect of the trailing edge controls on rotor performance.

The analysis is based on the blade equations of motion and their solution using finite element methods in space and in time. This solution is coupled with an aerodynamic model and a trim procedure using the vehicle equilibrium equations. This allows the rotor to be examined either in isolation or as part of a vehicle in free flight.

The derivation of the governing equations is described in Section 2.1, and their implementation is discussed in Section 2.2. The aerodynamic models and the specific steps taken to incorporate the flap and tab are presented in Section 2.3.

2.1   Governing Equations

The equations of motion have been derived for a rigid blade model and for an elastic blade model, using Hamilton's Principle, with the assumption of steady level flight. In the rigid model, the rotor has four degrees of freedom: blade flap, torsion, trailing edge flap deflection and tab deflection. This provides a simple approximation of the tab control angles required in hover and forward flight and a basic understanding of the rotor response to tab inputs. In the elastic model, the long slender blades are discretized into one dimensional beam elements capable of flap and lag bending, elastic torsion and axial deformation. In addition, each elastic blade has been modified to include degrees of freedom for the trailing edge flap and tab deflections, which includes the structural and inertial contributions of the flap and tab.

2.1.1 Coordinate Systems

2.1.1.1 Rigid Blade Frames

In the rigid blade rotor system, the four degrees of freedom are blade flap, β, blade pitch, θ, trailing edge flap deflection, p, and trailing edge tab deflection, q. Four rotating coordinate frames are used. The undeformed frame is defined by the unit vectors $(\hat{i}_1, \hat{j}_1, \hat{k}_1)$. $\hat{i}_1$ is aligned with the pitch axis and is positive radially outward. $\hat{j}_1$ is positive toward the leading edge. $\hat{k}_1$ is along the shaft $\hat{k}_1 = \hat{i}_1 \times \hat{j}_1$. The frame $(\hat{i}_2, \hat{j}_2, \hat{k}_2)$ has origin at the flap hinge and follows the flap deformation. The frame $(\hat{i}_3, \hat{j}_3, \hat{k}_3)$ has origin at the flapped pitch axis and follows nose up torsion. The frames $(\hat{i}_4, \hat{j}_4, \hat{k}_4)$ and $(\hat{i}_5, \hat{j}_5, \hat{k}_5)$ have origins at the aileron and tab hinge respectively, and rotate with the aileron and the tab. The transformations are given below.

$$
\begin{Bmatrix} \hat{i}_2 \\ \hat{j}_2 \\ \hat{k}_2 \end{Bmatrix} = \begin{bmatrix} \cos\beta & 0 & \sin\beta \\ 0 & 1 & 0 \\ -\sin\beta & 0 & \cos\beta \end{bmatrix} \begin{Bmatrix} \hat{i}_1 \\ \hat{j}_1 \\ \hat{k}_1 \end{Bmatrix} \tag{2.1}
$$

$$
\begin{Bmatrix} \hat{i}_3 \\ \hat{j}_3 \\ \hat{k}_3 \end{Bmatrix} = \begin{bmatrix} 1 & 0 & 0 \\ 0 & \cos\theta & \sin\theta \\ 0 & -\sin\theta & \cos\theta \end{bmatrix} \begin{Bmatrix} \hat{i}_2 \\ \hat{j}_2 \\ \hat{k}_2 \end{Bmatrix} \tag{2.2}
$$

$$
\begin{Bmatrix} \hat{i}_4 \\ \hat{j}_4 \\ \hat{k}_4 \end{Bmatrix} = \begin{bmatrix} 1 & 0 & 0 \\ 0 & \cos(\theta+p) & \sin(\theta+p) \\ 0 & -\sin(\theta+p) & \cos(\theta+p) \end{bmatrix} \begin{Bmatrix} \hat{i}_2 \\ \hat{j}_2 \\ \hat{k}_2 \end{Bmatrix} \tag{2.3}
$$

$$
\left\{ \begin{array}{c} \hat{i_5} \\ \hat{j_5} \\ \hat{k_5} \end{array} \right\} = \left[\begin{array}{ccc} 1 & 0 & 0 \\ 0 & \cos(\theta + p + q) & \sin(\theta + p + q) \\ 0 & -\sin(\theta + p + q) & \cos(\theta + p + q) \end{array} \right] \left\{ \begin{array}{c} \hat{i_2} \\ \hat{j_2} \\ \hat{k_2} \end{array} \right\} \tag{2.4}
$$

2.1.1.2 Elastic Blade Frames

There are six rotating coordinate frames used for the elastic blade equations with the flap and tab. These are the hub fixed frame, the hub rotating frame, the blade undeformed frame, the blade deformed frame, and the flap and tab coordinate frames, denoted by H, R, U, D, f and t, respectively. The hub rotating frame (X,Y,Z), unit vectors $(\hat{i}_R, \hat{j}_R, \hat{k}_R)$, rotates at constant angular velocity $\Omega \hat{k}_R$ with respect to the fixed frame, with the origin defined at the intersection of the rotor shaft axis and the blade elastic axis. $\hat{i}_R$ is aligned with the pitch axis and is positive radially outward. $\hat{j}_R$ is in the plane of rotation, and positive toward the leading edge. $\hat{k}_R$ is along the shaft $\hat{k}_R = \hat{i}_R \times \hat{j}_R$. The transformation between the hub rotating frame and the hub fixed frame is

$$
\left\{ \begin{array}{c} \hat{i_R} \\ \hat{j_R} \\ \hat{k_R} \end{array} \right\} = \left[\begin{array}{ccc} \cos\psi & \sin\psi & 0 \\ -\sin\psi & \cos\psi & 0 \\ 0 & 0 & 1 \end{array} \right] \left\{ \begin{array}{c} \hat{i_H} \\ \hat{j_H} \\ \hat{k_H} \end{array} \right\} = T_{RH} \left\{ \begin{array}{c} \hat{i_H} \\ \hat{j_H} \\ \hat{k_H} \end{array} \right\} \tag{2.5}
$$

where the azimuth angle, ψ is Ωt. Given a point P on the elastic axis of the undeformed blade, the coordinate system of the cross section at that point is (x, y, z), with axes along and normal to the principal axes of the cross section. The blade undeformed frame, unit vectors $(\hat{i}_U, \hat{j}_U, \hat{k}_U)$, is rotated by the precone angle, β_p, about $\hat{j}_R$. The transformation between the blade undeformed frame and the hub rotating

56

frame is

$$
\left\{ \begin{array}{c} \hat{i_U} \\ \hat{j_U} \\ \hat{k_U} \end{array} \right\} = \left[\begin{array}{ccc} \cos\beta_p & 0 & \sin\beta_p \\ 0 & 1 & 0 \\ -\sin\beta_p & 0 & \cos\beta_p \end{array} \right] \left\{ \begin{array}{c} \hat{i_R} \\ \hat{j_R} \\ \hat{k_R} \end{array} \right\} = T_{UR} \left\{ \begin{array}{c} \hat{i_R} \\ \hat{j_R} \\ \hat{k_R} \end{array} \right\} \tag{2.6}
$$

As the blade deforms, the arbitrary point P moves to P', where the coordinate system corresponding to the cross section at that point is (ξ, η, ζ). In the undeformed frame, the x-axis is aligned with the undeformed blade elastic axis; in the deformed frame, the ξ-axis is aligned with the deformed elastic axis. By assuming an Euler-Bernoulli beam, where plane sections remain plane, the deformed blade and the movement of point P to P' can be described by three elastic translations (u,v,w) and the blade rotation (θ_1). The transformation from the blade undeformed frame to the blade deformed frame $(\hat{i}_D, \hat{j}_D, \hat{k}_D)$ is

$$
\left\{ \begin{array}{c} \hat{i_D} \\ \hat{j_D} \\ \hat{k_D} \end{array} \right\} = T_{DU} \left\{ \begin{array}{c} \hat{i_U} \\ \hat{j_U} \\ \hat{k_U} \end{array} \right\} \tag{2.7}
$$

The transformation matrix T_{DU} from the undeformed to the deformed frame can be assembled using rotations about the three axes of the (x, y, z) system to move to the (ξ, η, ζ) coordinate system. The rotations are $\theta_1, \bar{\beta}, \bar{\zeta}$ about $(\hat{i}, \hat{j}, \hat{k})$, resulting in the matrix:

$$
\begin{bmatrix}
\cos\bar{\beta}\cos\bar{\zeta} & \cos\bar{\beta}\sin\bar{\zeta} & \sin\bar{\beta} \\
-\sin\theta_1\sin\bar{\beta}\cos\bar{\zeta}-\cos\theta_1\sin\bar{\zeta} & -\sin\theta_1\cos\bar{\beta}\sin\bar{\zeta}-\cos\theta_1\cos\bar{\zeta} & \sin\theta_1\cos\bar{\beta} \\
-\cos\theta_1\cos\bar{\beta}\cos\bar{\zeta}+\sin\theta_1\sin\bar{\zeta} & -\cos\theta_1\sin\bar{\beta}\sin\bar{\zeta}-\sin\theta_1\cos\bar{\zeta} & \cos\theta_1\sin\bar{\beta}
\end{bmatrix}
$$

$$(2.8)$$

By defining the rotations in terms of the elastic deformations (u, v, w) and the blade twist θ_1, the transformation from the undeformed frame to the deformed frame can be approximated with the following :

$$
\begin{bmatrix}
1-\frac{1}{2}v'^2-\frac{1}{2}w'^2 & v' & w' \\
-v'\cos\theta_1-w'\sin\theta_1 & (1-\frac{1}{2}v'^2)\cos\theta_1-w'v'\sin\theta_1 & (1-\frac{1}{2}w'^2)\sin\theta_1 \\
v'\sin\theta_1-w'\cos\theta_1 & -(1-\frac{1}{2}v'^2)\sin\theta_1-w'v'\cos\theta_1 & (1-\frac{1}{2}w'^2)\cos\theta_1
\end{bmatrix}
\left\{
\begin{array}{c}
\hat{i_U} \\
\hat{j_U} \\
\hat{k_U}
\end{array}
\right\}
$$

$$(2.9)$$

where the blade twist $\theta_1 = \theta_0 + \hat{\phi}$, and includes rigid blade pitch control and pre-twist, plus elastic twist. The rigid blade pitch $\theta_0 = \theta_{tw} + \theta_c oll + \theta_{1c}cos\psi + \theta_{1s}sin\psi$. The blade elastic twist $(\hat{\phi})$ is about the deformed elastic axis.

The frames $(\hat{i}_f,\hat{j}_f,\hat{k}_f)$ and $(\hat{i}_t,\hat{j}_t,\hat{k}_t)$ have origins at the aileron and tab hinge respectively, and rotate with the aileron and the tab. The hinge lines of each control surface are defined as parallel to the blade elastic axis. The transformations between the the aileron and blade deformed frames, and between the tab and aileron

deformed frames are given below.

$$
\left\{ \begin{array}{c} \hat{i}_f \\ \hat{j}_f \\ \hat{k}_f \end{array} \right\} = d\hat{i}_D + \left[\begin{array}{ccc} 1 & 0 & 0 \\ 0 & \cos p & \sin p \\ 0 & -\sin p & \cos p \end{array} \right] \left\{ \begin{array}{c} \hat{i}_D \\ \hat{j}_D \\ \hat{k}_D \end{array} \right\} = T_{fD} \left\{ \begin{array}{c} \hat{i}_D \\ \hat{j}_D \\ \hat{k}_D \end{array} \right\} \tag{2.10}
$$

$$
\left\{ \begin{array}{c} \hat{i}_t \\ \hat{j}_t \\ \hat{k}_t \end{array} \right\} = t\hat{i}_f + \left[\begin{array}{ccc} 1 & 0 & 0 \\ 0 & \cos q & \sin q \\ 0 & -\sin q & \cos q \end{array} \right] \left\{ \begin{array}{c} \hat{i}_f \\ \hat{j}_f \\ \hat{k}_f \end{array} \right\} = T_{tf} \left\{ \begin{array}{c} \hat{i}_f \\ \hat{j}_f \\ \hat{k}_f \end{array} \right\} \tag{2.11}
$$

The origin of each frame is at the control surface hinge line. The flap coordinate frame is offset by a distance d from the elastic axis of the blade. The tab coordinate frame is offset by a distance t from the hinge line of the flap.

2.1.2 Nondimensionalization and Ordering Scheme

The derivation and implementation of the equations of motion are nondimensional, both to keep the analysis generally applicable and to minimize scaling issues. The physical properties of the system are nondimensionalized by reference parameters as shown in Table 2.1. These reference parameters are used throughout the formulation.

As the equations of motion are derived using Hamilton's Principle, many higher order terms occur that complicate the expressions without adding significant precision. Accordingly, an ordering scheme has been consistently followed to simplify the analysis. Terms of the third order or higher have been discarded unless

Physical Property	Reference Parameter
Length	R
Time	$1/\Omega$
Mass/Length	m_0
Velocity	ΩR
Acceleration	$\Omega^2 R$
Force	$m_0 \Omega^2 R^2$
Moment	$m_0 \Omega^2 R^3$
Energy or Work	$m_0 \Omega^2 R^3$

Table 2.1: Nondimensionalization of Physical Properties

they are necessary to maintain the symmetry of the mass and stiffness matrices of the system. In addition, higher order terms that contribute to the gyroscopic couplings from the Coriolis effect are retained. The parameter ε is defined, such that $\varepsilon << 1$, of the same order as the nondimensional blade flap, w, or lag, v, deflections. The orders of magnitude of the nondimensional physical quantities of the system are listed in Table 2.2.

In this listing, a is the reference lift curve slope, and m_0 is the reference mass per unit length. m_0 is defined as the mass per unit length of an equivalent uniform blade having the same flap inertia of the blade modeled, such that

$$m_0 = \frac{3I_\beta}{R^3} = \frac{3 \int_0^R mr^2 dr}{R^3} \tag{2.12}$$

The small angles $\hat{\phi}, p, q$ are approximated with Taylor series so that $\sin\phi \approx$

Nondimensional Quantity	Order
$\frac{EA}{m_0\Omega^2 R^2}$	$O(\varepsilon^{-2})$
$\frac{M_{xF}}{m_0 R}, \frac{M_{yF}}{m_0 R}, \frac{M_{zF}}{m_0 R}$	$O(\varepsilon^{-1})$
$\frac{x}{R}, \frac{h}{R}, \frac{x_{CG}}{R}, \frac{y_{CG}}{R}, \frac{m}{m_0}, \frac{\partial}{\partial\psi}, \frac{\partial}{\partial x}$	$O(1)$
$\mu, \cos\psi, \sin\psi, \theta_0, \theta_{tw}, \theta_{75}, \theta_{1c}, \theta_{1s}, \frac{c_1}{a}, \frac{d_2}{a}$	$O(1)$
$\frac{EI_y}{m_0\Omega^2 R^4}, \frac{EI_z}{m_0\Omega^2 R^4}, \frac{GJ}{m_0\Omega^2 R^4}, \frac{I_{xF}}{m_0 R^3}, \frac{I_{yF}}{m_0 R^3}$	$O(1)$
$\frac{v}{R}, \frac{w}{R}, \frac{\eta}{R}, \frac{\zeta}{R}, \phi, \beta_p, \frac{k_A}{R}, \frac{k_{m1}}{R}, \frac{k_{m2}}{R}$	$O(\varepsilon)$
$p, q, \alpha_s, \phi_s, \lambda, \frac{\eta_c}{R}, \frac{c_0}{a}, \frac{d_1}{a}, \frac{f_0}{a}$	$O(\varepsilon)$
$\frac{EB_2}{m_0\Omega^2 R^5}, \frac{EC_2}{m_0\Omega^2 R^5}$	$O(\varepsilon)$
$\frac{e_d}{R}, \frac{e_g}{R}, \frac{e_A}{R}, \dot{x}_F, \dot{y}_F, \dot{z}_F, \dot{\alpha}_s, \dot{\phi}_s$	$O(\varepsilon^{3/2})$
$\lambda_T, \frac{u}{R}, \frac{d_0}{a}, \frac{f_1}{a}$	$O(\varepsilon^2)$
$\frac{EB_1}{m_0\Omega^2 R^6}, \frac{EC_1}{m_0\Omega^2 R^6}$	$O(\varepsilon^2)$

Table 2.2: Ordering Assumptions for Nondimensional Quantities

$\phi - \frac{\phi^2}{2}$ and $\cos\phi \approx 1 - \frac{\phi^3}{6}$. In most cases, the ordering scheme described here reduces these expressions to those obtained with the small angle assumption, but some of the additional terms are retained for symmetry.

2.1.3   Using Hamilton's Principle to Derive the Equations of Motion

The governing equations for the rigid model and the finite element energy expressions for the elastic model are derived using the generalized Hamilton's principle. This principle states that for a conservative system, the true motion of a

system, between prescribed initial conditions at time t_1 and final conditions at time t_2, is that particular motion for which the time integral of the difference between the potential and kinetic energies is a minimum. For rotor systems, there are noncon-servative forces which are not derivable from a potential function. The generalized principle for nonconservative systems is given as

$$\delta \Pi_b = \int_{t_1}^{t_2} (\delta U - \delta T - \delta W) dt = 0 \qquad (2.13)$$

where δU, δT, and δW represent virtual work from conservative forces (variation of potential energy), inertial forces (variation of kinetic energy), and non-conservative forces. The current investigation considers the rotor alone, and neglects any dis-cussion of the fuselage. The external forces are discussed in Section 2.3, under Aerodynamic Modeling.

2.1.4 Rigid Blade Equations

In order to prevent confusion in notation for the aileron deflection δ and the variational parameter δ, the aileron and tab deflections are denoted by p and q radians. The flap and torsion deflections are β and θ. The aileron spans from r_{a_1} to r_{a_2}. The tab spans from r_{t_1} to r_{t_2}. The main blade section extends from the leading edge LE_b to the trailing edge TE_b, and has chord c. Over the aileron span, the main blade extends from the LE_b to a shorter trailing edge up to the aileron TE_{ba}, so that its chord is c_b. The aileron extends from LE_a to TE_a with chord c_f, except over the tab span, where it extends from LE_a to TE_{at}. The tab extends from LE_t to the TE_t, with chord c_t. In general, TE_t or TE_a need not be the same point as

TE_b. TE_{ba} need not be same as LE_a and TE_{at} need not be the same as LE_t because of the gaps between the main blade and aileron and the aileron and flap.

The variation of potential energy is given by

$$\delta U = k_\beta \delta\beta + k_\theta \delta\theta + k_p \delta p + k_q \delta q \tag{2.14}$$

The virtual work from non-conservative forces is given by

$$\delta W = M_\beta \delta\beta + M_\theta \delta\theta + M_p \delta p + M_q \delta q \tag{2.15}$$

where M_β, M_θ, M_p, and M_q are the aerodynamic moments about the flap hinge, pitch bearing, aileron hinge, and tab hinge. The variation of kinetic energy is given by

$$\delta T = \int_b \rho_b \mathbf{v}_b . \delta\mathbf{v}_b + \int_a \rho_a \mathbf{v}_a . \delta\mathbf{v}_a + \int_t \rho_t \mathbf{v}_t . \delta\mathbf{v}_t \tag{2.16}$$

Each integral denotes the separate contributions of the blade (b), aileron (a), and tab (t). Each has appropriate spatial variables and limits.

The derivation follows the standard procedure of expressing the position vector $\mathbf{r}$ and velocity $\mathbf{v}$ of a generic point on the blade, aileron, or tab in the undeformed rotating frame coordinates.

$$\mathbf{r} = x_1 \hat{i}_1 + y_1 \hat{j}_1 + z_1 \hat{k}_1 \tag{2.17}$$

The angular velocity vector, $\Omega = \Omega \hat{k}_1$, then leads to

$$\mathbf{v} = \frac{\partial \mathbf{r}}{\partial t} + \Omega \times \mathbf{r} = (\dot{x}_1 - \Omega x_1)\hat{i}_1 + (\dot{y}_1 + \Omega y_1)\hat{j}_1 + \dot{z}_1 \hat{k}_1 \tag{2.18}$$

The variational expression is then

$$\mathbf{v} \cdot \delta\mathbf{v} = (-\ddot{x}_1 + \Omega^2 x_1)\delta x_1 + (-\ddot{y}_1 + \Omega^2 y_1)\delta y_1 - \ddot{z}_1 \delta z_1 \tag{2.19}$$

63

where, anticipating definite integral over time, terms of the form $\dot{x}_1 \delta \dot{x}_1$, $x_1 \delta \dot{x}_1$, etc, have been replaced with $-\ddot{x}_1 \delta x_1$, $-\dot{x}_1 \delta x_1$, etc. For example,

$$\int_{t1}^{t2} \dot{x}_1 \delta x_1 = \dot{x}_1 \delta x_1 \big|_{t1}^{t2} - \int_{t1}^{t2} \ddot{x}_1 \delta x_1 = 0 - \int_{t1}^{t2} \ddot{x}_1 \delta x_1 \tag{2.20}$$

The contribution to kinetic energy variation from the blade is obtained by integrating over the blade alone. This also holds for the aileron and tab, i.e. the parts

$$\int_b \rho \mathbf{v}_b \cdot \delta \mathbf{v}_b \, d\eta_b \, dr, \quad \int_a \rho \mathbf{v}_a \cdot \delta \mathbf{v}_a \, d\eta_a \, dr, \quad \text{and} \quad \int_t \rho \mathbf{v}_t \cdot \delta \mathbf{v}_t \, d\eta_t \, dr$$

have the following integration limits

$$\int_b = \int_e^{r_{a1}} \int_{TE_b}^{LE_b} + \int_{r_{a1}}^{r_{a2}} \int_{TE_{ba}}^{LE_b} + \int_{r_{a2}}^{R} \int_{TE_b}^{LE_b} \tag{2.21}$$

$$\int_a = \int_{r_{a1}}^{r_{t1}} \int_{TE_a}^{LE_a} + \int_{r_{t1}}^{r_{t2}} \int_{TE_{at}}^{LE_a} + \int_{r_{t2}}^{r_{a2}} \int_{TE_a}^{LE_a} \tag{2.22}$$

$$\int_t = \int_{r_{t1}}^{r_{t2}} \int_{TE_t}^{LE_t} \tag{2.23}$$

where η_b, η_a and η_t are the local chordwise coordinate directions of the main blade, aileron, and tab. η_b is zero at the blade elastic axis and is positive forward. η_a and η_t are zero at the aileron and tab hinges and positive forward. For example, if d is the distance of the aileron hinge lying behind the elastic axis, and f is the distance of the tab hinge lying behind the aileron hinge, then generic points on the main blade, aileron, and tab are given by the following expressions.

$$\mathbf{r}_b = e\hat{i}_1 + (r - e)\hat{i}_2 + \eta_b \hat{j}_3$$

$$\mathbf{r}_a = e\hat{i}_1 + (r - e)\hat{i}_2 - d\hat{j}_3 + \eta_a \hat{j}_4 \tag{2.24}$$

$$\mathbf{r}_t = e\hat{i}_1 + (r - e)\hat{i}_2 - d\hat{j}_3 - f\hat{j}_4 + \eta_t \hat{j}_5$$

e is the flap hinge offset. Assuming small deformations and neglecting non-linear terms, a straight-forward application of the above procedure leads to the following form of the generalized Hamilton's principle (eqn. 2.13)

$$\int_{t_1}^{t_2} \left[(\dots)\delta\beta + (\dots)\delta\theta + (\dots)\delta p + (\dots)\delta q\right] dt = 0$$

Putting the terms $(\dots) = 0$ generates the inertial contributions to the four governing equations for flap, torsion, aileron and tab.

Note that while gathering the $\delta\beta$ terms, some of the contributing terms from the aileron and the tab (via kinetic energy) will be identical to the main blade terms, except for their integration limits. For these particular terms, the integration limits are merged using eqs. 2.21– 2.23. Thus, the properties of the blade include the aileron and the tab properties. The properties of the aileron include the tab properties. The reason behind these identical terms is that the aileron deflection is defined with respect to the main blade and similarly the tab deflection is defined with respect to the aileron.

The rigid blade flap, torsion, aileron, and tab equations are as follows.

Flap equation β :

$$
\begin{aligned}
I_\beta \ddot{\beta} + \Omega^2 I_\beta &\left[1 + \frac{eS_\beta}{I_\beta} + \frac{k_\beta}{I_\beta \Omega^2}\right]\beta \\
&+ \bar{S}_\theta \ddot{\theta} + \Omega^2 \bar{S}_\theta \left(1 + \frac{eS_\theta}{\bar{S}_\theta}\right)\theta \\
&+ \bar{S}_a \ddot{p} + \Omega^2 \bar{S}_a \left(1 + \frac{eS_a}{\bar{S}_a}\right)p \\
&+ \bar{S}_t \ddot{q} + \Omega^2 \bar{S}_t \left(1 + \frac{eS_t}{\bar{S}_t}\right)q = M_\beta
\end{aligned}
\tag{2.25}
$$

Torsion equation β :

$$\bar{S}_\theta \ddot{\beta} + \Omega^2 \bar{S}_\theta \left(1 + \frac{eS_\theta}{\bar{S}_\theta}\right) \beta$$
$$+ I_\theta \ddot{\theta} + \Omega^2 I_\theta \left[1 + \frac{k_\theta}{I_\theta \Omega^2}\right] \theta$$
$$+ [I_a - dS_a] \ddot{p} + \Omega^2 I_a \left[1 - \frac{dS_a}{I_a}\right] p$$
$$+ (I_t - (d+t)S_t) \ddot{q} + \Omega^2 I_t \left[1 - \frac{(d+t)S_t}{I_t}\right] q = M_\theta$$

(2.26)

Aileron equation β :

$$\bar{S}_a \ddot{\beta} + \Omega^2 \bar{S}_a \left(1 + \frac{eS_a}{\bar{S}_a}\right) \beta$$
$$+ [I_a - dS_a] \ddot{\theta} + \Omega^2 I_a \left[1 - \frac{dS_a}{I_a}\right] \theta$$
$$+ I_a \ddot{p} + \Omega^2 I_a \left[1 - \frac{dS_a}{I_a} + \frac{k_a}{I_a \Omega^2}\right] p$$
$$+ (I_t - tS_t) \ddot{q} + \Omega^2 I_t \left[1 - \frac{(d+t)S_t}{I_t}\right] q = M_p$$

(2.27)

Tab equation q :

$$\bar{S}_t \ddot{\beta} + \Omega^2 \bar{S}_t \left(1 + \frac{eS_t}{\bar{S}_t}\right) \beta$$
$$+ [I_t - (d+t)S_t] \ddot{\theta} + \Omega^2 I_t \left[1 - \frac{(d+t)S_t}{I_t}\right] \theta$$
$$+ (I_t - tS_t) \ddot{p} + \Omega^2 I_t \left[1 - \frac{(d+t)S_t}{I_t}\right] p$$
$$+ I_t \ddot{q} + \Omega^2 I_t \left[1 - \frac{(d+t)S_t}{I_t} + \frac{k_t}{I_t \Omega^2}\right] q = M_q$$

(2.28)

The structural properties are defined as follows.

Blade properties:

$\rho =$ area density $\; kg/m^2$

$$\int_{LE_b}^{TE_b} \rho d\eta = m_b \;\; \text{mass per unit span} \;\; kg/m$$

$$\int_{LE_b}^{TE_b} \eta \rho d\eta = x_I m_b = s_\theta \;\; \text{first moment of mass per unit span} \;\; kg - m/m$$

$$\int_{LE_b}^{TE_b} \eta^2 \rho d\eta = i_\theta \;\; \text{second moment of mass per unit span} \;\; kg - m^2/m$$

(2.29)

For each we have the following radial moments

$$\int_e^R m_b dr = M_b \;\; \text{zero-th radial moment} = \text{blade mass} \;\; kg$$

$$\int_e^R (r-e)m_b dr = S_\beta \;\; \text{first radial moment} = \text{first flap moment} \;\; kg - m$$

$$\int_e^R (r-e)^2 m_b dr = I_\beta \;\; \text{second radial moment} = \text{flap moment of inertia} \;\; kg - m^2$$

(2.30)

Then

$$\int_e^R s_\theta dr = \int_e^R x_I m_b dr = S_\theta \;\; \text{zero-th radial moment} \;\; kg - m$$

$$\int_e^R (r-e)s_\theta dr = \int_e^R (r-e)x_I m_b dr = \bar{S}_\theta \;\; \text{first radial moment} \;\; kg - m^2$$

$$\int_e^R (r-e)^2 s_\theta dr = \int_e^R (r-e)^2 x_I m_b dr = \bar{\bar{S}}_\theta \;\; \text{second radial moment} \;\; kg - m^2$$

(2.31)

And finally

$$\int_e^R i_\theta dr = I_\theta \;\; \text{zero-th radial moment} \;\; kg - m$$

$$\int_e^R (r-e)i_\theta dr = \bar{I}_\theta \;\; \text{first radial moment} \;\; kg - m^2$$

(2.32)

$$\int_e^R (r-e)^2 i_\theta dr = \bar{\bar{I}}_\theta \;\; \text{second radial moment} \;\; kg - m^2$$

Aileron properties:

$$\int_{LE_a}^{TE_a} \rho d\eta = m_a \quad \text{mass per unit span} \quad kg/m$$

$$\int_{LE_a}^{TE_a} \eta \rho d\eta = x_p m_a = s_a \quad \text{first moment of mass per unit span} \quad kg - m/m \quad (2.33)$$

$$\int_{LE_a}^{TE_a} \eta^2 \rho d\eta = i_a \quad \text{second moment of mass per unit span} \quad kg - m^2/m$$

For each we have the following radial moments

$$\int_{r_{a1}}^{r_{a2}} m_a dr = M_a \quad \text{zero-th radial moment = aileron mass} \quad kg$$

$$\int_{r_{a1}}^{r_{a2}} (r - e) m_a dr = S_{\beta a} \quad \text{first radial moment} \quad kg - m \quad (2.34)$$

$$\int_{r_{a1}}^{r_{a2}} (r - e)^2 m_a dr = I_{\beta a} \quad \text{second radial moment} \quad kg - m^2$$

Then

$$\int_{r_{a1}}^{r_{a2}} s_a dr = \int_{r_{a1}}^{r_{a2}} x_p m_a dr = S_a \quad \text{zero-th radial moment} \quad kg - m$$

$$\int_{r_{a1}}^{r_{a2}} (r - e) s_a dr = \int_{r_{a1}}^{r_{a2}} (r - e) x_p m_a dr = \bar{S}_a \quad \text{first radial moment} \quad kg - m^2$$

$$\int_{r_{a1}}^{r_{a2}} (r - e)^2 s_a dr = \int_{r_{a1}}^{r_{a2}} (r - e)^2 x_p m_a dr = \bar{\bar{S}}_a \quad \text{second radial moment} \quad kg - m^2$$

$$(2.35)$$

And finally

$$\int_{r_{a1}}^{r_{a2}} i_a dr = I_a \quad \text{zero-th radial moment} \quad kg - m$$

$$\int_{r_{a1}}^{r_{a2}} (r - e) i_a dr = \bar{I}_a \quad \text{first radial moment} \quad kg - m^2 \quad (2.36)$$

$$\int_{r_{a1}}^{r_{a2}} (r - e)^2 i_a dr = \bar{\bar{I}}_a \quad \text{second radial moment} \quad kg - m^2$$

Tab properties:

$$\int_{LE_t}^{TE_t} \rho \, d\eta = m_t \quad \text{mass per unit span} \quad kg/m$$

$$\int_{LE_t}^{TE_t} \eta \rho \, d\eta = x_q m_t = s_t \quad \text{first moment of mass per unit span} \quad kg - m/m \quad (2.37)$$

$$\int_{LE_t}^{TE_t} \eta^2 \rho \, d\eta = i_t \quad \text{second moment of mass per unit span} \quad kg - m^2/m$$

For each we have the following radial moments

$$\int_{r_{t1}}^{r_{t2}} m_t \, dr = M_t \quad \text{zero-th radial moment} = \text{tab mass} \quad kg$$

$$\int_{r_{t1}}^{r_{t2}} (r - e) m_t \, dr = S_{\beta t} \quad \text{first radial moment} \quad kg - m \quad (2.38)$$

$$\int_{r_{t1}}^{r_{t2}} (r - e)^2 m_t \, dr = I_{\beta t} \quad \text{second radial moment} \quad kg - m^2$$

Then

$$\int_{r_{t1}}^{r_{t2}} s_t \, dr = \int_{r_{t1}}^{r_{t2}} x_q m_t \, dr = S_t \quad \text{zero-th radial moment} \quad kg - m$$

$$\int_{r_{t1}}^{r_{t2}} (r - e) s_t \, dr = \int_{r_{t1}}^{r_{t1}} (r - e) x_q m_t \, dr = \bar{S}_t \quad \text{first radial moment} \quad kg - m^2$$

$$\int_{r_{t1}}^{r_{t2}} (r - e)^2 s_a \, dr = \int_{r_{t1}}^{r_{t2}} (r - e)^2 x_q m_t \, dr = \bar{\bar{S}}_t \quad \text{second radial moment} \quad kg - m^2$$

$$(2.39)$$

And finally

$$\int_{r_{t1}}^{r_{t2}} i_t \, dr = I_t \quad \text{zero-th radial moment} \quad kg - m$$

$$\int_{r_{t1}}^{r_{t2}} (r - e) i_t \, dr = \bar{I}_t \quad \text{first radial moment} \quad kg - m^2 \quad (2.40)$$

$$\int_{r_{t1}}^{r_{t2}} (r - e)^2 i_t \, dr = \bar{\bar{I}}_t \quad \text{second radial moment} \quad kg - m^2$$

where LE stands for leading edge, TE stands for trailing edge. The subscript b denotes the non aileron tab part of the blade, a denotes the aileron, and t denotes the tab. e is the flap hinge offset.

2.1.5 Elastic Blade Equations

The flap and tab are rigid elements that share the identical motions of the blade in axial extension, flapwise and chordwise bending and elastic twist. The flap is connected to the blade by a torsion spring at a hinge located at an arbitrary location on the flap chord. The tab is connected to the flap in a similar fashion. In this investigation, the tab motions are prescribed with the assumption of harmonic motion at rotor speed (1/rev). Flap motion is generated in response to tab deflections. The strain and kinetic energy expression of the baseline blade include all terms that are independent of the flap and tab motions, so the structural properties of each blade element describe the entire section, including the flap and tab. Although the mass properties of the flap and tab can be defined, these values are used to calculate the shear forces and moments due to the control surfaces alone, rather than an additional mass contribution to the blade.

The variation of potential energy is given in three parts, for the blade, aileron and tab

$$\delta U = \delta U_b + \delta U_f + \delta U_t \tag{2.41}$$

where the blade potential is expressed by

$$\delta U_b = \int_0^R \iint E_x \epsilon_{xx} \delta \epsilon_{xx} + G \epsilon_{x\eta} \delta \epsilon_{x\eta} + G \epsilon_{x\zeta} \delta \epsilon_{x\zeta} d\eta d\zeta dx \tag{2.42}$$

and the variation of potential energy for the aileron and tab is

$$\delta U_f + \delta U_t = k_p p \delta_p + k_q q \delta_q \tag{2.43}$$

k_p and k_q are the springs located at the hinges of the inelastic aileron and

tab.   The non-conservative forces and moments contributing to the virtual work correspond to the system degrees of freedom

$$\delta W = \int_0^R (L_u \delta u + L_v \delta v + L_w \delta w + M_{\hat\phi} \delta\hat\phi + M_p \delta p + M_q \delta q)dx \qquad (2.44)$$

where L_u, L_v and L_w are the airloads in the x, y and z and $M_{\hat\phi}$, M_p, and M_q are the aerodynamic moments about the blade elastic axis, the aileron hinge and the tab hinge, respectively. These forces and moments are calculated either from unsteady thin airfoil theory, or by using airfoil tables. The variation of kinetic energy for the elastic blade is similar to that of the rigid blade, where the integration limits follow the spanwise and chordwise boundaries of the blade, aileron and tab:

$$\delta T = \int_b \rho \mathbf{v}_b \cdot \delta \mathbf{v}_b d\eta_b dx + \int_f \rho \mathbf{v}_f \cdot \delta \mathbf{v}_f d\eta_f dx + \int_t \rho \mathbf{v}_t \cdot \delta \mathbf{v}_t d\eta_t dx \qquad (2.45)$$

As for the rigid blade equations, this derivation expresses the position vector $\mathbf{r}$, and velocity $\mathbf{v}$ of an arbitrary point on the blade, aileron or tab in the blade undeformed frame.

The position vector of the arbitrary point $\mathbf{r}$ on the deformed blade is

$$\mathbf{r}_b = x_d \hat{i} + y_d \hat{j} + z_d \hat{k} = \begin{bmatrix} (x+u) & v & w \end{bmatrix} \begin{Bmatrix} \hat{i} \\ \hat{j} \\ \hat{k} \end{Bmatrix} + \begin{bmatrix} -\lambda\hat\phi' & \eta & \zeta \end{bmatrix} \begin{Bmatrix} \hat{i}_\xi \\ \hat{j}_\eta \\ \hat{k}_\zeta \end{Bmatrix} \qquad (2.46)$$

which in the blade undeformed frame becomes

$$\mathbf{r}_b = [x + u - \lambda\hat\phi' - v'(y_d - v) - w'(z_d - w)]\hat{i} + [v + (y_d - v)]\hat{j} + [w + (z_d - w)]\hat{k} \qquad (2.47)$$

71

where

$$(y_d - v) = \eta \cos \theta_1 - \zeta \sin \theta_1 \ \text{ and } \ (z_d - w) = \eta \sin \theta_1 + \zeta \cos \theta_1$$

The arbitrary point $\mathbf{r}$ on the deflected aileron is expressed in the blade deformed frame

$$\mathbf{r}_f = y_f \cos p \, \hat{j}_D + y_f \sin p \, \hat{k}_D - d \, \hat{j}_D \tag{2.48}$$

where d is the distance from the blade elastic axis to the aileron hinge. The expression is transformed to the blade undeformed frame and reduced to the second order:

$$\mathbf{r}_f = \{(y_f \cos p - d)(-v' \cos \theta_1 - w' \sin \theta_1) + y_f \sin p(v' \sin \theta_1 - w' \cos \theta_1) + u\} \, \hat{i}$$

$$+\{(y_f \cos p - d) \cos \theta_1 - y_f \sin p \sin \theta_1 + v\} \, \hat{j}$$

$$+\{(y_f \cos p - d) \sin \theta_1 + y_f \sin p \cos \theta_1 + w\} \, \hat{k}$$

$$\tag{2.49}$$

Similarly, the arbitrary point $\mathbf{r}$ on the deflected tab, is expressed in the blade deformed frame as

$$\mathbf{r}_t = [(y_t \cos q - f) \cos p - y_t \sin q \sin p] \, \hat{j}_D + [(y_t \cos q - f) \sin p + y_t \sin q \cos p] \, \hat{k}_D - d \, \hat{j}_D \tag{2.50}$$

where f is the distance from the aileron hinge to the tab hinge. The expression is transformed also to the blade undeformed frame and reduced to the second order:

72

$$
\mathbf{r}_t = \{[(y_t \cos q - f) \cos p](-v' \cos \theta_1 - w' \sin \theta_1)
$$

$$
+ [(y_t \cos q - f) \sin p + y_t \sin q \cos p](v' \sin \theta_1 - w' \cos \theta_1) + u\}\,\hat{i}
$$

$$
+ \{[(y_t \cos q - f) \cos p - y_t \sin q \sin p] \cos \theta_1 - [(y_t \cos q - f) \sin p + y_t \sin q \cos p] \sin \theta_1 + v\}\hat{j}
$$

$$
+ \{[(y_t \cos q - f) \cos p - y_t \sin q \sin p] \sin \theta_1 + [(y_t \cos q - f) \sin p + y_t \sin q \cos p] \cos \theta_1 + w\}\hat{k}
$$

(2.51)

The velocity vector in the blade undeformed frame is

$$
\mathbf{v} = \frac{\partial \mathbf{r}}{\partial t} + \Omega \times \mathbf{r} = (\dot{x}_d - y_d \Omega \cos \beta_p)\hat{i} + (\dot{y}_d + x_d \Omega \cos \beta_p - z_d \Omega \sin \beta_p)\hat{j} + (\dot{z}_d + y_d \Omega \sin \beta_p)\hat{k}
$$

(2.52)

Following the integration limits as defined by eqs. 2.21 - 2.23 and using integration by parts, the variational expression yields

$$
\int \mathbf{v} \cdot \delta \mathbf{v} = (-\ddot{x}_d + 2\dot{y}_d + x_d - z_d\beta_p)\delta x_d + (-\ddot{y}_d - 2\dot{x}_d + 2\dot{z}_d\beta_p + y_d)\delta y_d
$$
$$
+ (-\ddot{z}_d - 2\dot{y}_d\beta_p + z_d\beta_p^2 - x_d\beta_p)\delta z_d
$$

(2.53)

Assuming small deformations and reducing to the second order, the above procedure leads to the following form of the generalized Hamilton's principle (eq. 2.13), where the expressions for strain energy, kinetic energy and virtual work are integrated by parts:

$$
\int_{t_1}^{t_2} \Big[(\ldots)\delta u + (\ldots)\delta v + (\ldots)\delta w + (\ldots)\delta\hat{\phi} + (\ldots)\delta\hat{\phi}' + (\ldots)\delta p + (\ldots)\delta q \Big]\, dt = 0
$$

73

By collecting the terms for δu, δv, δw, $\delta \hat{\phi}$, δp and δq, the governing equations are generated for extension, chord bending, flap bending, torsion, aileron and tab. The first 4 of these equations are refinements of the blade equation. The last two are new hinge moment equations for the flap and tab.

Elastic extension equation u_e :

$$
\left[EAu'_e + EAK_A^2 \left(\theta' \hat{\phi}' + \theta' w' v'' + \frac{\hat{\phi}'^2}{2} \right) \right.
$$

$$
\left. - EAe_A v''(\cos\theta - \hat{\phi}\sin\theta) + EAw''(\sin\theta + \hat{\phi}\cos\theta) \right]'
$$
(2.54)

$$
+ m(\ddot{u}_e - u_e - x - 2\dot{v}) = L_u
$$

Chord bending equation v :

$$
\Big[v''(EI_Z \cos^2\theta + EI_Y \sin^2\theta) + w''(EI_Z - EI_Y)\cos\theta\sin\theta
$$

$$
- v''\hat{\phi}\sin 2\theta(EI_Z - EI_Y) + w''\hat{\phi}\cos 2\theta(EI_Z - EI_Y)
$$

$$
- v''\hat{\phi}^2 \cos 2\theta(EI_Z - EI_Y) - w''\hat{\phi}^2 \sin 2\theta(EI_Z - EI_Y)
$$

$$
- EB_2\theta'\hat{\phi}'\cos\theta - EAe_A u'_e(\cos\theta - \hat{\phi}\sin\theta) + EAK_A^2 u'_e w'\theta'
$$

$$
+ (GJ + EB_1\theta'^2)\hat{\phi}'w' - EC_2\hat{\phi}''\sin\theta \Big]''
$$

$$
- m \Big[-\ddot{v} + e_g\ddot{\theta}\sin\theta + e_g\cos\theta + v - \hat{\phi}\sin\theta + 2\dot{w}\beta_p + 2e_g\dot{v}'\cos\theta
$$

$$
+ 2e_g\dot{w}'\sin\theta + \ddot{\hat{\phi}}e_g\sin\theta - 2\dot{u}_e + 2\int_0^x (v'\dot{v}' + w'\dot{w}')dx \Big]
$$

$$
- me_g \left(x\cos\theta - \hat{\phi}x\sin\theta + 2\dot{v}\cos\theta \right)' + \left\{ mv' \int_x^1 (-\ddot{u}_e + u_e + x + 2\dot{v}) \right\}'
$$

$$
- m_p e_p \left(\ddot{p}\sin\theta + p\ddot{\theta}\cos\theta + 2\dot{\theta}\dot{p}\cos\theta - p\dot{\theta}^2\sin\theta - p\sin\theta \right) - m_p e_p p\, (x\sin\theta)'
$$

$$
- m_q e_q \left(\ddot{q}\sin\theta + q\ddot{\theta}\cos\theta + 2\dot{\theta}\dot{q}\cos\theta - q\dot{\theta}^2\sin\theta - q\sin\theta \right) = L_v
$$

(2.55)

Flap bending equation w :

$$\Big[w''(EI_Z \sin^2\theta + EI_Y \cos^2\theta) + v''(EI_Z - EI_Y)\cos\theta\sin\theta$$

$$+w''\hat{\phi}\sin 2\theta(EI_Z - EI_Y) + v''\hat{\phi}\cos 2\theta(EI_Z - EI_Y)$$

$$+w''\hat{\phi}^2\cos 2\theta(EI_Z - EI_Y) - v''\hat{\phi}^2\sin 2\theta(EI_Z - EI_Y)$$

$$-EAe_A u'_e(\sin\theta + \hat{\phi}\cos\theta) - EB_2\hat{\phi}'\theta'\sin\theta + EC_2\hat{\phi}''\cos\theta\Big]''$$

$$- m\left(-\ddot{w} - e_g\ddot{\theta}\cos\theta - e_g\ddot{\hat{\phi}}\cos\theta - 2\dot{v}\beta_p - x\beta_p\right)$$

$$- me_g\left(x\sin\theta + \hat{\phi}x\cos\theta + 2\dot{v}\sin\theta\right)' + \left\{mw'\int_x^1(-\ddot{u}_e + u_e + x + 2\dot{v})\right\}'$$

$$- m_p e_p\left(-\ddot{p}\cos\theta + p\ddot{\theta}\sin\theta + 2\dot{\theta}\dot{p}\sin\theta + p\dot{\theta}^2\cos\theta\right) - m_p e_p p\,(x\cos\theta)'$$

$$- m_q e_q\left(-\ddot{q}\cos\theta + q\ddot{\theta}\sin\theta - 2\dot{\theta}\dot{q}\sin\theta + q\dot{\theta}^2\cos\theta\right) = L_w$$

(2.56)

Torsion equation $\hat{\phi}$:

$$(w''^2 - v''^2)\cos\theta\sin\theta(EI_Z - EI_Y) + v''w''\cos 2\theta$$

$$\hat{\phi}(w''^2 - v''^2)\cos 2\theta(EI_Z - EI_Y) - 2\hat{\phi}v''w''\sin 2\theta$$

$$+ \Big[GJ(\hat{\phi}' + w'v'') + EAK_A^2(\theta' + \phi')u'_e$$

$$+EB_1\theta'^2\hat{\phi}' - EB_2\theta'(v''\cos\theta + w''\sin\theta)\Big]'$$

$$- \Big[-k_m^2\ddot{\hat{\phi}} - \hat{\phi}(k_{m_2}^2 - k_{m_1}^2)\cos 2\theta - (k_{m_2}^2 - k_{m_1}^2)\cos\theta\sin\theta - x\beta_p e_g\cos\theta$$

$$-ve_g\sin\theta + xv'e_g\sin\theta - xw'e_g\cos\theta + \ddot{v}e_g\sin\theta - \ddot{w}e_g\cos\theta - k_m^2\ddot{\theta}\Big]$$

$$+ m_p k_p^2\ddot{p} - m_p e_p\left(d\ddot{p} + dp\cos 2\theta\right)$$

$$+ m_q k_q^2\ddot{q} - m_q e_q\left[(t+d)\ddot{q} + (t+d)q\cos 2\theta\right] = L_{\hat{\phi}}$$

(2.57)

Aileron equation p :

$$m_p k_p^2 \left[-\ddot{\theta} - (\ddot{\hat{\phi}} + \ddot{p}) + (\phi + p) - 2\dot{w}' - (1 + 2\dot{v}') \sin\theta\cos\theta + \left(2\dot{w}' - 2(\dot{\hat{\phi}} + p)\right)\cos^2\theta \right]$$

$$+ m_p e_p \left[d(\ddot{\hat{\phi}} + \ddot{\theta} + p\dot{\theta}^2 + 2\dot{w}' - \dot{\hat{\phi}}) + d(1 + 2\dot{v}')\sin\theta\cos\theta + d(p + 2\dot{\hat{\phi}} - 2\dot{w}')\cos^2\theta \right.$$

$$+ \left((\ddot{v} - v + xv') + (\ddot{w} + xw' + x\beta_p)(\dot{\hat{\phi}} + p) + 2(\dot{u} + \dot{v}v' - \dot{w}\beta_p) \right)\sin\theta$$

$$\left. + \left(-(\ddot{w} + xw' + x\beta_p) + (\ddot{v} - v + xv')(\dot{\hat{\phi}} + p) - 2(\dot{v}w' + \dot{v}\beta_p) \right)\cos\theta \right]$$

$$+ m_q k_q^2 \left[-\ddot{\theta} - (\ddot{\hat{\phi}} + \ddot{p} + \ddot{q}) + (\hat{\phi} + q) - 2\dot{w}' - (1 + 2\dot{v}')\sin\theta\cos\theta \right.$$

$$\left. + (2\dot{w}' - 2(\dot{\hat{\phi}} + q)\cos^2\theta) \right]$$

$$+ m_q e_q \left[(t + d)(\ddot{\theta} + \ddot{\hat{\phi}} + q\dot{\theta}^2 + 2\dot{w}' - \dot{\hat{\phi}}) + t(\ddot{p} + \ddot{q} - p) + ((t + d)(1 + 2\dot{v}'))\sin\theta\cos\theta \right.$$

$$+ \left((t + d)(p + q + 2\dot{\hat{\phi}} - 2\dot{w}') + t\left((p + q)\dot{\theta}^2 + p\dot{q}^2 + p \right) \right)\cos^2\theta$$

$$+ \left((\ddot{v} - v + xv') + (\ddot{w} + xw' + x\beta_p)(\dot{\hat{\phi}} + p) + 2(\dot{u} + \dot{v}v' - \dot{w}\beta_p) \right)\sin\theta$$

$$\left. + \left(-(\ddot{w} + xw' + x\beta_p) + (\ddot{v} - v + xv')(\dot{\hat{\phi}} + p) - 2(\dot{v}w' + \dot{v}\beta_p) \right)\cos\theta \right] + k_p p = M_p$$

$$(2.58)$$

Tab equation q :

$$m_q k_q^2 \left[-\ddot{\theta} - (\ddot{\hat{\phi}} + \ddot{p} + \ddot{q}) + (\hat{\phi} + p + q) - 2\dot{w}' - (1 + 2\dot{v}')\sin\theta\cos\theta \right.$$

$$\left. + (2\dot{w}' - 2(\dot{\hat{\phi}} + p + q)\cos^2\theta) \right]$$

$$+ m_q e_q \left[(t + d)(\ddot{\theta} + \ddot{\hat{\phi}} + 2\dot{w}' - \dot{\hat{\phi}}) + t(\ddot{p} - p) + ((t + d)(1 + 2\dot{v}'))\sin\theta\cos\theta \right.$$

$$+ \left((t + d)(p + q + 2\dot{\hat{\phi}} - 2\dot{w}') + tp \right)\cos^2\theta$$

$$+ \left((\ddot{v} - v + xv') + (\ddot{w} + xw' + x\beta_p)(\dot{\hat{\phi}} + p) + 2(\dot{u} + \dot{v}v' - \dot{w}\beta_p) \right)\sin\theta$$

$$\left. + \left(-(\ddot{w} + xw' + x\beta_p) + (\ddot{v} - v + xv')(\dot{\hat{\phi}} + p) - 2(\dot{v}w' + \dot{v}\beta_p) \right)\cos\theta \right] + k_q q = M_q$$

$$(2.59)$$

The sectional properties are defined as follows. The blade properties include

the aileron and tab. They are assumed to remain nominally constant in presence of aileron and tab deflections. The aileron properties include the tab. They are assumed to remain nominally constant in presence of tab deflections. The blade properties are as follows.

$$\int\int_A d\eta d\zeta = A$$

$$\int\int_A \eta d\eta d\zeta = Ae_A$$

$$\int\int_A \zeta d\eta d\zeta = 0$$

$$\int\int_A \lambda_T d\eta d\zeta = 0$$

$$\int\int_A (\eta^2 + \zeta^2) d\eta d\zeta = AK_A^2$$

$$\int\int_A (\eta^2 + \zeta^2)^2 d\eta d\zeta = B_1$$

$$\int\int_A \eta(\eta^2 + \zeta^2)^2 d\eta d\zeta = B_2$$

$$\int\int_A \eta^2 d\eta d\zeta = I_Z$$

$$\int\int_A \zeta^2 d\eta d\zeta = I_Y$$

$$\int\int_A \lambda_T^2 d\eta d\zeta = EC_1$$

$$\int\int_A \zeta \lambda_T d\eta d\zeta = EC_2$$

$$\int\int_A \rho d\eta d\zeta = m$$

$$\int\int_A \rho\eta d\eta d\zeta = me_g$$

$$\int\int_A \rho\zeta^2 d\eta d\zeta = mk_{m_1}^2$$

$$\int\int_A \rho\eta^2 d\eta d\zeta = mk_{m_2}^2$$

$$\int\int_A \rho(\eta^2 + \zeta^2) d\eta d\zeta = mk_m^2$$

$$\int\int_A \rho\zeta d\eta d\zeta = 0$$

$$\int\int_A \rho\eta\zeta d\eta d\zeta = 0$$

$$\int\int_A \rho\lambda_T d\eta d\zeta = 0$$

$$(2.60)$$

where A is the sectional area, e_A is the tension axis offset positive in front of the elastic axis, E is the Young's modulus of the blade material, m is mass per unit span, e_g is the center of gravity offset positive in front of the elastic axis, and k_m, k_{m1} and k_{m2} are the radii of gyration.

The aileron and tab properties are as follows. They are the same, aileron

properties are denoted with the subscript p, the tab properties with q.

$$\int\int_{A_q} \rho d\eta d\zeta = m_q \qquad\qquad \int\int_{A_p} \rho d\eta d\zeta = m_p$$

$$\int\int_{A_q} \rho\eta d\eta d\zeta = me_q \qquad\qquad \int\int_{A_p} \rho\eta d\eta d\zeta = me_p \qquad (2.61)$$

$$\int\int_{A_q} \rho(\eta^2 + \zeta^2)d\eta d\zeta = m_q k_q^2 \qquad \int\int_{A_p} \rho(\eta^2 + \zeta^2)d\eta d\zeta = m_p k_p^2$$

m_p and m_q are the aileron and tab mass per unit span, k_p and k_q are the radii of gyration and e_p and e_q are the local c.g. offsets with respect to aileron and tab hinge axes. The c.g. offsets are positive forward.

Effect of Trailing Edge Controls on Strain Energy

The inertial contributions of the trailing edge controls to the equations of motion are detailed below and in the following section. As noted previously, the variation of the strain energy for the main blade includes all terms that are independent of the flap and tab deflection, and the blade sectional properties describe the entire blade section, including the flap and the tab. Accordingly, adding the flap and tab to the system does not change the formulation of the strain energy except for the presence of torsional springs at the flap and tab hinges. The variation of the potential energy of the trailing edge control surfaces is:

$$\delta U_f + \delta U_t = k_p p\delta_p + k_q q\delta_q \qquad (2.62)$$

where k_p and k_q are the springs located at the hinges of the flap and tab.

Effect of Trailing Edge Controls on Kinetic Energy

Flap and tab motions create incremental changes to the kinetic energy of the blade. The total incremental change to the kinetic energy from the flap and tab motion for each of the degrees of freedom for the blade element is expressed as the following variation:

$$\delta T_f + \delta T_t = \int (\Delta T_v \cdot \delta v + \Delta T_w \cdot \delta w + \Delta T_{\hat{\phi}} \cdot \delta \hat{\phi} + \Delta T_v' \cdot \delta v' + \Delta T_w' \cdot \delta w')dx \quad (2.63)$$

The individual components of this variational for the flap contribution alone are:

$$\Delta T_u = 0 \quad (2.64)$$

$$\Delta T_v = - m_p e_p \left[\left(\ddot{p} - \dot{\theta}^2 p - p \right) \sin \theta + \left(2\dot{\theta}\dot{p} + \ddot{\theta}p \right) \cos \theta \right]$$
$$- m_p e_p \left[\left(\ddot{p}(\hat{\phi} + p) + \dot{p}^2 \right) \cos \theta \right] \quad (2.65)$$

$$\Delta T_w = - m_p e_p \left[- \left(\ddot{p} - \dot{\theta}^2 p \right) \cos \theta + \left(2\dot{\theta}\dot{p} + \ddot{\theta}p \right) \sin \theta \right]$$
$$- m_p e_p \left[\left(\ddot{p}(\hat{\phi} + p) + \dot{p}^2 \right) \sin \theta \right] \quad (2.66)$$

$$\Delta T_\phi = m_p k_p^2 \ddot{p}$$
$$- m_p e_p \left[d \left(\ddot{p} - p \right) + 2dp \cos^2 \theta + p \left(\ddot{w} + x\beta_p \right) \sin \theta + p \left(\ddot{v} - v \right) \cos \theta \right] \quad (2.67)$$

$$\Delta T_{v'} = m_p e_p x p \sin \theta_0 \quad (2.68)$$

$$\Delta T_{w'} = m_p e_p x p \cos \theta_0 \quad (2.69)$$

The incremental inertial changes from the flap and tab combined are:

$$\Delta T_u = 0 \tag{2.70}$$

$$
\begin{aligned}
\Delta T_v = &- m_p e_p \left[\left(\ddot{p} - \dot{\theta}^2 p - p \right) \sin\theta + \left(2\dot{\theta}\dot{p} + \ddot{\theta}p \right) \cos\theta \right] \\
&- m_p e_p \left[\left(\ddot{p}(\hat{\phi} + p) + \dot{p}^2 \right) \cos\theta \right] \\
&- m_q e_q \left[\left(\ddot{q} - \dot{\theta}^2 q - q \right) \sin\theta + \left(2\dot{\theta}\dot{q} + \ddot{\theta}q \right) \cos\theta \right] \\
&- m_q e_q \left[\left(\ddot{q}(\hat{\phi} + p + q) + (\dot{p} + \dot{q})^2 + q\ddot{p} \right) \cos\theta \right]
\end{aligned} \tag{2.71}
$$

$$
\begin{aligned}
\Delta T_w = &- m_p e_p \left[- \left(\ddot{p} - \dot{\theta}^2 p \right) \cos\theta + \left(2\dot{\theta}\dot{p} + \ddot{\theta}p \right) \sin\theta \right] \\
&- m_p e_p \left[\left(\ddot{p}(\hat{\phi} + p) + \dot{p}^2 \right) \sin\theta \right] \\
&- m_q e_q \left[- \left(\ddot{q} - \dot{\theta}^2 q \right) \cos\theta + \left(2\dot{\theta}\dot{q} + \ddot{\theta}q \right) \sin\theta \right] \\
&- m_q e_q \left[\left(\ddot{q}(\hat{\phi} + p + q) + (\dot{p} + \dot{q})^2 + q\ddot{p} \right) \sin\theta \right]
\end{aligned} \tag{2.72}
$$

$$
\begin{aligned}
\Delta T_\phi = &m_p k_p^2 \ddot{p} \\
&- m_p e_p \left[d \left(\ddot{p} - p \right) + 2dp\cos^2\theta + p \left(\ddot{w} + x\beta_p \right) \sin\theta + p \left(\ddot{v} - v \right) \cos\theta \right] \\
&+ m_q k_q^2 \ddot{q} \\
&- m_q e_q \left[(t + d)(\ddot{q} - q) + 2(t + d)q\cos^2\theta + q \left(\ddot{w} + x\beta_p \right) \sin\theta + q \left(\ddot{v} - v \right) \cos\theta \right]
\end{aligned} \tag{2.73}
$$

$$\Delta T_{v'} = m_q e_q x(q + p) \sin\theta_0 \tag{2.74}$$

$$\Delta T_{w'} = m_q e_q x(q + p) \cos\theta_0 \tag{2.75}$$

80

Effect of Trailing Edge Controls on External Work

The motion of the flap and the tab creates a change in the aerodynamic environment of the blade that results in altered blade lift, L^A and pitching moment, $M_{\hat{\phi}}^A$. The resulting change in the variational term for the external work of the blade is

$$\delta(\Delta W_b) = \int (\Delta L^A \cdot \delta w + \Delta D^A \cdot \delta w + \Delta M_{\hat{\phi}}^A \cdot \delta \hat{\phi}) dx \qquad (2.76)$$

In addition, the flap and the tab each have aerodynamic hinge moments which contribute to the total external work:

$$\delta(\Delta W_f + \Delta W_t) = \int (M_p^A \cdot \delta p + M_q^A \cdot \delta q) dx \qquad (2.77)$$

The flap hinge moment, M_p^A, the tab hinge moment, M_q^A, and the changes to the blade lift, drag and pitch moment are described in the discussion of the aerodynamic model in 2.2.

Although the change to the blade drag caused by the motion of the flap and tab is also a factor in the external work, this change is not predicted by thin airfoil theory. Instead, it can be calculated with computational fluid dynamics (CFD) or extracted from wind tunnel test data. These methods are discussed in 2.2.3.

2.2   Aerodynamic Model

The aerodynamic model in the comprehensive analysis is in two parts: one for the airfoil sections of the main blade, and the second for the flapped airfoil sections. Within the section of the blade that includes trailing edge flaps and/or tabs, total

aerodynamic properties for each two dimensional airfoil section are calculated by adding the incremental change caused by the deflection of the flap to the lift, drag and pitch moment of the main blade. By dividing the analysis in this way, different models for the unflapped and flapped airfoils can be combined as desired. However, a note of caution must be introduced, because differences in the drag divergence Mach number between the flapped and unflapped airfoils (at a given angle of attack) can introduce a large drag increment that is not physical and will produce potentially misleading results. Two models have been used for the flapped airfoils in this investigation. The first is a quasi-steady model developed from thin airfoil theory by Theodorsen and Garrick [119]. This model includes a trailing edge flap and a tab. Both control surfaces may include aerodynamic balance (also known as overhang), which is defined as the offset from the leading edge of the control to the hinge of the control. Overhang is included in the geometric configuration to reduce hinge moment, which in turn reduces the power required to actuate the control. The model is an extension of the general potential flow theory [74] for an oscillating airfoil. Although compressibility is not included in the theory, the Prandtl-Glauert correction is used in the comprehensive analysis. An indicial model which does include compressibility and unsteady effects was developed by Hariharan and Leishman [120] and implemented within the comprehensive analysis; this model does not allow aerodynamic balance and is not used in the current investigation. The second model uses airfoil table lookup to obtain section aerodynamic coefficients for the control surfaces. The coefficients are based on blade angle of attack, Mach number, flap deflection and tab deflection, and are compared to the baseline airfoil (with

control surfaces at zero deflection) to calculate an incremental change to the blade lift, drag and pitch moment.

The aerodynamic model for the main blade, with various refinements, has been thoroughly described [121], [122]. It is a lifting line model which combines the following elements: sectional angle of attack based on blade deformations and control angles, a Weissinger-L (W-L) lifting line near wake, a far wake model (in this case, the Bagai-Leishman pseudo-implicit model) and two dimensional airfoil properties. In the case of the baseline (swashplate) rotor, control angles used to calculate sectional angle of attack include blade collective and lateral and longitudinal cyclics. In contrast, the swashplateless rotor uses an index angle and zero cyclics with blade deformations to calculate the sectional angle of attack. The airfoil properties are obtained either from airfoil lookup tables or from quasi-steady thin airfoil theory. The near and far wake models have been refined to include the effects of the trailing edge flap.

2.2.1 Quasi-steady Flapped Airfoil Model

Theodorsen developed a general aerodynamic theory for an airfoil with a trailing edge flap [74]. The theory uses potential flow and the Kutta condition to establish the lift, pitching moment and flap hinge moment for a thin airfoil, oscillating in pitch and plunge. The unsteadiness of the flow is captured with the lift deficiency function C(k), which is a function of the reduced frequency, $k = \frac{\omega c}{2v}$. In reduced frequency, ω is the frequency of oscillation, c is the chord, and v is the speed of air

flow. This function is a measure of the effect of the shed wake on the magnitude

and phase of the circulatory aerodynamic loads generated by the oscillating foil. For

high frequencies, the value of C(k) approaches 0.5, thus reducing the circulatory lift

to one-half of the quasi-steady value. For low frequencies, C(k) approaches 1.0. In

this investigation, the swashplateless rotor is controlled by flap and/or tab deflec-

tions at 1/rev, or low frequency. Thus the effect of shed wake on loads and rotor

performance may be neglected without significantly diminishing the accuracy of the

calculations. The noncirculatory forces and moments are apparent mass terms, and

do not depend on wake vorticity. In the general theory, the flap hinge is located

at the leading edge of the flap, so there is no gap between the body of the airfoil

and the flap and flow leakage between the flap and airfoil is not considered. The

flap deflection is measured with respect to the airfoil. The theory was extended by

Theodorsen and Garrick [119] to include a flap hinge that is not necessarily located

at the flap leading edge, and a tab that is similarly connected to the flap. The tab

deflection is measured with respect to the flap. The distance from the leading edge

to the hinge is the overhang for the flap or tab. Again, there is no flow between

the flap and the blade, or between the tab and the flap, as the gap is assumed

to be sealed. The major deficiency of this model is the absence of a drag model.

This precludes any evaluation of the effect of flap and tab deflections on rotor shaft

power.

The nondimensional incremental lift and pitching moment, and the moments

about the flap and tab hinges, are expressed as functions of the azimuthal derivatives

of the blade motions. The notation is $\overset{\star}{()} = \frac{\partial ()}{\partial \psi} = \frac{\partial}{\partial t} \times \frac{1}{\Omega}$. The expressions are as

follows:

$$\Delta L = \frac{\gamma}{6a}[C_{lp}pU_t^2 + C_{l\overset{\star}{p}}\overset{\star}{p}\,U_t + C_{l\overset{\star\star}{p}}\overset{\star\star}{p} + C_{lq}qU_t^2 + C_{l\overset{\star}{q}}\overset{\star}{q}\,U_t + C_{l\overset{\star\star}{q}}\overset{\star\star}{q}] \qquad (2.78)$$

$$\Delta M = \frac{\gamma}{6a}[C_{mp}pU_t^2 + C_{m\overset{\star}{p}}\overset{\star}{p}\,U_t + C_{m\overset{\star\star}{p}}\overset{\star\star}{p} + C_{mq}qU_t^2 + C_{m\overset{\star}{q}}\overset{\star}{q}\,U_t + C_{m\overset{\star\star}{q}}\overset{\star\star}{q}] \quad (2.79)$$

$$\begin{aligned}
H_p = \frac{\gamma}{6a}[&C_{hpp}pU_t^2 + C_{hp\overset{\star}{p}}\overset{\star}{p}\,U_t + C_{hp\overset{\star\star}{p}}\overset{\star\star}{p} \\
&+C_{hpq}qU_t^2 + C_{hp\overset{\star}{q}}\overset{\star}{q}\,U_t + C_{hp\overset{\star\star}{q}}\overset{\star\star}{q} \\
&-C_{hp\overset{\star}{w}}\overset{\star}{w}\,U_t - C_{hp\overset{\star\star}{w}}\overset{\star\star}{w} \\
&+C_{hp\alpha}(\theta_0 + \hat{\phi})U_t^2 + C_{hp\overset{\star}{\alpha}}(\overset{\star}{\theta}_0 + \overset{\star}{\phi})U_t + C_{hp\overset{\star\star}{\alpha}}(\overset{\star\star}{\theta}_0 + \overset{\star\star}{\phi})]
\end{aligned} \qquad (2.80)$$

$$\begin{aligned}
H_q = \frac{\gamma}{6a}[&C_{hqp}pU_t^2 + C_{hq\overset{\star}{p}}\overset{\star}{p}\,U_t + C_{hq\overset{\star\star}{p}}\overset{\star\star}{p} \\
&+C_{hqq}qU_t^2 + C_{hq\overset{\star}{q}}\overset{\star}{q}\,U_t + C_{hq\overset{\star\star}{q}}\overset{\star\star}{q} \\
&-C_{hq\overset{\star}{w}}\overset{\star}{w}\,U_t - C_{hq\overset{\star\star}{w}}\overset{\star\star}{w} \\
&+C_{hq\alpha}(\theta_0 + \hat{\phi})U_t^2 + C_{hq\overset{\star}{\alpha}}(\overset{\star}{\theta}_0 + \overset{\star}{\phi})U_t + C_{hq\overset{\star\star}{\alpha}}(\overset{\star\star}{\theta}_0 + \overset{\star\star}{\phi})]
\end{aligned} \qquad (2.81)$$

In these expressions, λ is Lock number, $\lambda = \frac{\rho a c R^4}{I_b}$ blade flap inertia $I_b = \frac{m_0 R^3}{3}$. The aerodynamic partials in the above equations are calculated using Theodorsen coefficients:

Lift Coefficients:

$$C_{lp} = 2\left(T_{10} - lT_{21}\right)$$

$$C_{l\overset{\star}{p}} = \frac{c}{2}\left(T_{11} - T_4\right) + lc\left(-T_{10} - \sqrt{1 - c_p^2}\right)$$

$$C_{l\overset{\star\star}{p}} = \frac{c^2}{4}\left(-T_1 + lT_4\right)$$

$$C_{lq} = 2\left(T_{10q} - mT_{21q}\right)$$ (2.82)

$$C_{l\overset{\star}{q}} = \frac{c}{2}\left(T_{11q} - T_{4q}\right) + mc\left(-T_{10q} - \sqrt{1 - d_q^2}\right)$$

$$C_{l\overset{\star\star}{q}} = \frac{c^2}{4}\left(-T_{1q} + mT_{4q}\right)$$

Pitch Moment Coefficients:

$$C_{mp} = -\frac{1}{2}\left(T_{15} + lT_{22}\right)$$

$$C_{m\overset{\star}{p}} = -\frac{c}{4}\left(T_{16} + lT_{23}\right)$$

$$C_{m\overset{\star\star}{p}} = -\frac{c^2}{8}\left(2T_{13} + lT_{24}\right)$$

$$C_{mq} = -\frac{1}{2}\left(T_{15q} + lT_{22q}\right)$$ (2.83)

$$C_{m\overset{\star}{q}} = -\frac{c}{4}\left(T_{16q} + lT_{23q}\right)$$

$$C_{m\overset{\star\star}{q}} = -\frac{c^2}{8}\left(2T_{13q} + lT_{24q}\right)$$

Flap Hinge Moment Coefficients:

$$C_{hpp} = -\frac{1}{2\pi}\left[T_{18} + T_{12}T_{10} + l(T_{26} - T_{12}T_{21} - 2T_{10}T_{20}) + l^2(T_{28} + 2T_{20}T_{21})\right]$$

$$C_{hp\overset{\star}{p}} = -\frac{c}{4\pi}\left[T_{19} + \frac{1}{2}T_{11}T_{12} + l(T_{27} - T_{10}T_{12} - T_{20}T_{11}) + l^2(T_{29} + 2T_{10}T_{20})\right]$$

$$C_{hp\overset{\star\star}{p}} = -\frac{c^2}{8\pi}\left(-T_3 + 2lT_2 - l^2T_5\right)$$

$$C_{hpq} = -\frac{1}{2\pi}\left[Y_9 + T_{10}T_{12} + l(Y_{11} - 2T_{10}T_{20}) + lm(Y_{15} + 2T_{20}T_{21}) + m(Y_{13} - T_{12}T_{21})\right]$$

$$C_{hp\overset{\star}{q}} = -\frac{c}{4\pi}\left[Y_{10} + \frac{1}{2}T_{11}T_{12} + l(Y_{12} + T_{11}T_{20}) + lm(Y_{16} + 2T_{10}T_{20}) + m(Y_{14} - T_{10}T_{12})\right]$$

$$C_{hp\overset{\star\star}{q}} = -\frac{c^2}{8\pi}\left(-Y_6 + lY_3 - lmY_1 + mY_4\right)$$

$$C_{hp\overset{\star}{w}} = -\frac{1}{2}(T_{12} - 2lT_{20})$$

$$C_{hp\overset{\star\star}{w}} = -\frac{c}{4}(-T_1 + lT_4)$$

$$C_{hp\alpha} = -\frac{1}{2}(T_{12} - 2lT_{20})$$

$$C_{hp\overset{\star}{\alpha}} = -\frac{c}{4}\left[T_{17} + T_{12} + l(T_{25} - 2T_{20})\right]$$

$$C_{hp\overset{\star\star}{\alpha}} = -\frac{c^2}{8}(2T_{13} + lT_{24})$$

(2.84)

Tab Hinge Moment Coefficients:

$$C_{hqp} = -\frac{1}{2\pi}\left[Y_{17} + T_{10q}T_{12q} + l(Y_{21} - T_{12q}T_{21q}) + lm(Y_{23} + 2T_{20q}T_{21q}) + m(Y_{19} - 2T_{10q}T_{20q})\right]$$

$$C_{hq\overset{\star}{p}} = -\frac{c}{4\pi}\left[Y_{18} + \frac{1}{2}T_{11q}T_{12q} + l(Y_{22} - T_{10q}T_{12q}) + lm(Y_{24} + 2T_{10q}T_{20q}) + m(Y_{20} - T_{11q}T_{20q})\right]$$

$$C_{hq\overset{\star\star}{p}} = -\frac{c^2}{8\pi}\left(-Y_6 + lY_3 - lmY_1 + mY_4\right)$$

$$C_{hqq} = -\frac{1}{2\pi}\left[T_{18q} + T_{12q}T_{10q} + m(T_{26q} - T_{12q}T_{21q} - 2T_{10q}T_{20q}) + m^2(T_{28q} + 2T_{20q}T_{21q})\right]$$

$$C_{hq\overset{\star}{q}} = -\frac{c}{4\pi}\left[T_{19q} + \frac{1}{2}T_{11q}T_{12q} + m(T_{27q} - T_{10q}T_{12q} - T_{20q}T_{11q}) + m^2(T_{29q} + 2T_{10q}T_{20q})\right]$$

$$C_{hq\overset{\star\star}{q}} = -\frac{c^2}{8\pi}\left(-T_{3q} + 2mT_{2q} - m^2T_{5q}\right)$$

$$C_{hq\overset{\star}{w}} = -\frac{1}{2}(T_{12q} - 2mT_{20q})$$

$$C_{hq\overset{\star\star}{w}} = -\frac{c}{4}(-T_{1q} + mT_{4q})$$

$$C_{hq\alpha} = -\frac{1}{2}(T_{12q} - 2mT_{20q})$$

$$C_{hq\overset{\star}{\alpha}} = -\frac{c}{4}\left[T_{17q} + T_{12q} + m(T_{25q} - 2T_{20q})\right]$$

$$C_{hq\overset{\star\star}{\alpha}} = -\frac{c^2}{8}(2T_{13q} + mT_{24q})$$

$$(2.85)$$

where in the above equations, $T_1, ..., T_{29}$ are Theodorsen coefficients entirely dependent on the geometry of the airfoil and flap, while the set $T_{1q}, ..., T_{29q}$ is dependent on airfoil and tab. The Theodorsen coefficients $Y_1, ..., Y_24$ are calculated using both flap and tab geometry.

2.2.2 Table Lookup

The table lookup model allows nonlinear aerodynamic data to be easily retrieved and interpolated for use in comprehensive analysis. Measured airfoil data

are arranged in tables for specific angles of attack and Mach number so that sectional aerodynamic coefficients for lift, drag and pitch moment can be produced for the blade. The procedure is identical for all blade airfoil sections, flapped or unflapped: the angle of attack used to retrieve aerodynamic coefficients does not consider the flap deflection; in other words, the flap is considered to be at the zero deflection, or neutral position. The blade tables are in C81 format, and a two dimensional, linear interpolation algorithm is used to calculate the aerodynamic coefficients.

The effect of the flap is included through additional tables for flapped airfoils. Flap hinge moment and flap lift are retrieved directly from these tables, through linear interpolation of angle of attack, Mach number, and flap deflection. The effect of the flap on lift, drag and pitching moment is calculated as an increment which is added to the baseline value of the unflapped airfoil. C81 tables are created for a range of flap deflections, including a table for zero flap deflection; coefficients can be interpolated between the zero flap position and a flap deflection, or between two different flap deflections. Once the coefficients have been determined, the increment is calculated by subtraction from the identified flap baseline.

The primary limitation of the table lookup method is the paucity of data for flapped airfoils. Although wind tunnel tests have been conducted for airfoils with flaps and/or tabs, most published data are focused on lift and pitch moment, and do not include drag data, which hinders the evaluation of the flap effect on rotor performance. In addition, much of the published data for flapped airfoils was produced for subsonic, fixed wing aircraft, with testing envelopes that do not cover the normal range of helicopter operations. For this reason, the current investigation

confines the scope of lookup tables to airfoils with flaps only, and does not include tables for a deflected tab. In the following sections, the drag of flapped airfoils is studied using not only the limited test data that has been published, but also computational fluid dynamics (CFD) analysis.

2.2.3 Drag of Flapped Airfoils

Published aerodynamic data for airfoils with trailing edge flaps is limited, especially drag data. For flapped airfoils, there is insufficient published data to construct a full C81 aerodynamics table. Within the comprehensive analysis, airfoil tables for the SC1095 and SC1095R8 sections [99] are used to calculate the performance baseline. CFD analysis is used to provide additional aerodynamic data for the SC1095R8 with flaps; the CFD predictions for zero flap deflection will be compared to test data for validation of the baseline airfoil. The SC1095R8 as the template for the flapped airfoil because it is used for the much of the outboard section of the UH-60A blade, where a flap is most likely to be located. Secondarily, the existing measured TEF data are used to develop a drag model which can be generalized to other flapped airfoils. For cases where neither measured test data nor CFD analysis is available for a flapped airfoil, this empirical model may be used to estimate drag.

2.2.3.1 Experimental Data

Ames and Sears conducted a series of wind tunnel tests on NACA airfoils that included drag measurement for cambered, flapped airfoils at very low Reynolds

numbers. Recent tests of flapped airfoils with overhang (with accompanying CFD predictions for a limited number of cases), have been performed by Hassan et al. [2], for the Apache HH-06 and HH-10 airfoils. A sample of data points is shown in Figure 2.1, where data from and have been compiled. In Figure 2.2, the data for the HH-06 airfoil at Mach number 0.6 shows the general effect of flap deflections. At positive angles of attack, positive TEF deflections cause an increase in drag, which reflects the increase in effective angle of attack. Negative TEF deflections create a decrease in effective angle of attack, and a corresponding decrease in drag. The opposite trend occurs for negative angles of attack. Based on this observation, a simply shifted drag coefficient can be written as:

$$c_d = d_0 + d_2 \left(\alpha + \delta/n\right)^2 \tag{2.86}$$

where the shift depends on the direction of the flap deflection. In the above equation, α is the blade angle of attack and δ is the TEF deflection. While fitting the expression to the data, it became clear that the drag polar shifts with the TEF deflection, divided by the term n; n is chosen to best fit the data for the limited angle of attack range of $\pm 2°$. Note the expression can be generalized to any other airfoil by substituting the appropriate d_0 and d_2 coefficients. For example, in Figure 2.3 the HH-06 data are approximated with:

$$c_d = 0.01 + 2 \left(\alpha + \delta/3\right)^2 \tag{2.87}$$

while the SC1095 airfoil drag at Mach of 0.3 may be modeled using:

$$c_d = 0.0092 + 0.2403 \left(\alpha + \delta/3\right)^2 \tag{2.88}$$

The SC1095R8 drag model is shown in Figure 2.4, for TEF deflections of $\pm 10°$. These TEF deflections were chosen as the expected bounds of the control flap angles for the range of flight speeds. However, compared to the measured test data for the unflapped airfoil, it can be seen that the airfoil drag cannot be described by the quadratic equation for angles of attack below -2° or above 12°. At 12°, the drag departs from a generally quadratic trend, and can better be described as linear to 20°. The same trend can be seen for negative angles of attack, starting at -2°. The angles of attack at which the transition to separated flow occurs are specific to the airfoil under examination, and are an important detail when considering flapped airfoils. Figure 2.2 shows that the transition for the HH-06 airfoil occurs near 4° angle of attack, almost 10° earlier than the SC1095R8. Accordingly, when drag is in the separated flow region, beyond the description of d_0 and d_2, the model is extended empirically, to follow the slope of the baseline drag curve at higher angles of attack. Figure 2.5 shows the results of this extension for the SC1095R8. In the model, the point at which the transition is made to occur is a function of both angle of attack and Mach number.

2.2.3.2 CFD Analysis

The SC1095R8 airfoil is examined using a two dimensional Navier-Stokes CFD code (TURNS) to produce aerodynamic properties over a range of angles of attack, Mach number, and flap deflection. The CFD computations are performed using the overset structured mesh solver OVERTURNS. This code solves the compress-

ible RANS equations using a diagonal form of the implicit approximate factorization method developed by Pulliam and Chaussee. The Spalart-Allmaras turbulence model is employed for the RANS closure. The code was validated against test data and other CFD analyses for the SC1095 airfoil. The trailing edge flap is hinged at the leading edge, and is modeled with no gap. The flap chord length is 0.15c. The baseline airfoil is the SC1095R8 with zero flap deflection.

The lift, drag and pitch moment coefficients for the baseline prediction are compared to test data at Mach number of 0.3 (See Fig. 2.7). At positive angles of attack, the CFD prediction of drag matches the test data within 5%, except for the region from 12° to 16°. For the negative angles of attack, accuracy is within 5% from 0° to -4°. Beyond -4°, the slope of the prediction follows the test data closely, but the magnitude differs significantly. The CFD prediction of lift matches test data within 5%, for angles of attack between -10° and 14°. For positive angles of attack, the trend of the prediction follows the data closely. On the negative side, the prediction diverges from test data at -10°. The pitch moment prediction follows the trends of the test data closely within the angle of attack bounds defined for lift.

The drag prediction for the flapped airfoil follows the trends established in the wind tunnel tests of the HH-06 [2]: at positive angles of attack, a negative (upward) TEF deflection reduces the airfoil drag, while positive (downward) TEF deflection increases the drag. The reverse occurs for negative angles of attack. Figure 2.8 shows the drag predictions for TEF deflections of ±10°. The CFD results are compared to the empirical model in Figure 2.9. The drag prediction for −10° TEF deflection follows the empirical model very closely, for the range of angles of attack

from -20° to 20°. The maximum difference between the CFD and the empirical model is 5% at -20° (See Figure 2.9a). Drag prediction for +10° TEF deflection is shown in Figure 2.9b; at positive angles of attack, the CFD prediction follows the empirical model through 16°. At negative angles of attack, the prediction matches the model exactly through -4°. Beyond -4°, the slopes of the prediction and the model correlate well, but there is significant difference in magnitude. The major source of the discrepancy is the angle of attack at which the the drag prediction enters the separated flow region. Referring to Figure 2.8, it can be observed that the initial angle of attack for separated flow shifts with the TEF deflection. For negative angles of attack, as the TEF deflection increases from -10° to +10°, the nonlinear initiation shifts left, to more negative angles. Overall, the comparison of the empirical model to the CFD predictions shows that the model can serve as a good prediction of flapped airfoil drag in the absence of either test data or CFD prediction. This is helpful considering the relative scarcity of such data.

2.2.4   Inflow and Wake Model

A refined wake roll-up is proposed which includes the trailing edge flap in the near and far wake calculations by assuming small interruptions to the flow at the inboard and outboard bounds of the flap. The baseline wake model uses a fully rolled-up free tip vortex, developed by Bagai and Leishman [123]. An iterative procedure is used to calculate bound circulation strengths for the near and far wake. The near wake model is based on the Weissinger-L lifting line theory. Initially,

94

sectional angles of attack along the blade are calculated using blade deformations and uniform inflow, and are used to extract lift coefficients from 2D airfoil tables. The first estimate of the bound circulation strengths is derived from the lift using the Kutta-Joukowski theorem. The far wake is based on the bound circulation strengths, and produces a non-uniform inflow distribution which is used to re-calculate the sectional angles of attack. The new angles of attack enter the near wake model and result in revised bound circulation strengths for the far wake. A converged wake solution results in bound circulations strengths that are consistent for the airfoil tables, the near wake and the far wake. The strength across each element is assumed constant. The shed vortex at the blade tip is assigned a circulation strength corresponding to the maximum bound circulation outboard of 0.5R on the blade. This is based on the assumption that all of the circulation outboard of that point rolls up into the tip vortex.

Thin airfoil theory is used to calculate equivalent blade angles of attack that include the effect of the trailing edge flap as follows:

$$\alpha_{eff} = \alpha + c_{l_\delta} \delta \tag{2.89}$$

where c_{l_δ} depends on the chord length of the flap:

$$c_{l_\delta} = \frac{1}{\pi}(acos(c) + \sqrt{1 - c^2}) \tag{2.90}$$

and c is the location of the leading edge of the flap on the airfoil. The effective angles of attack are now used to extract lift coefficients from the airfoil tables for the flapped sections of the blade. Bound circulation strengths are calculated in the near wake model as before. Instead of using a single tip vortex however, trailers at

95

the radial bounds of the flap are included in the model. With the periodic oscillation of the flap, gaps appear at the inboard and outboard flap edges. It is suggested that these gaps cause interruptions in the flow that can produce small trailers at the flap bounds. The three trailed vortices (at blade tip, outboard flap bound and inboard flap bound) on each of four blades are shown at low advance ration $\mu = 0.11$ in figures 2.12, 2.13 and 2.14. These figures show the strong interaction between wake and blade that is typically found at low speed. The strength of each flap trailer is calculated as the difference between the strengths of the elements neighboring the gap. The circulation strength of the tip vortex is the peak circulation outboard of 0.5R, less the contribution of the two flap trailers. Figure 2.11 shows a schematic of the new wake model. The effect of the trailing edge flap on the bound circulation strengths is shown in Figure 2.15. In this plot, the radial bounds of the flap are marked, and discontinuities can be seen at those points in the circulation strengths where an effective angle of attack has been used to account for the flap deflection.

2.3   Solution Procedure

The comprehensive analysis is based on the University of Maryland Advanced Rotorcraft Code (UMARC), which uses finite element analysis in space (FEM or FEA) and in time (FET) to analyze rotors either in isolation or in conjunction with a fuselage. An important part of this procedure is coupled trim, which simultaneously solves the blade response and vehicle trim equations; these equation sets are interdependent and require iteration to converge to a solution.

Two categories of trim are used in this investigation: free flight and wind tunnel. Free flight is a six degree of freedom problem, where trim is achieved through the equilibrium of 3 forces and 3 moments on the rotor system, and the variables are the lateral and longitudinal rotor shaft positions, the tail rotor collective, and the control angle collective, longitudinal and lateral cyclic. The wind tunnel trim is a three degree of freedom problem and is further divided into two types: zero flapping and zero hub moment. Both of these have targeted thrust and prescribed rotor shaft angles and tail rotor collective, and use the same variables to achieve trim: control angle collective, longitudinal and lateral cyclic. For zero flapping trim, the control angles are varied to produce zero first blade flap harmonics, while for the zero hub moment trim, the object is to produce zero hub pitch and roll moments. These trim solutions are referred to as coupled because the blade response depends on the airloads, and as the blade response is updated, the loads on the rotor system change also.

The trim procedure and equations are the same for conventional and swash-plateless rotors. The only difference is the type of control used on the rotor: blade pitch angles for the conventional system, and either flap or tab angles for the swash-plateless system.

2.3.1 Free Flight Trim

The rotor trim equations are nonlinear equilibrium equations for the three forces (vertical, longitudinal and lateral) and three moments (pitch, roll and yaw)

97

on the system. These equations are shown below:

$$F_1 = W - T\cos(\alpha_s)\cos(\phi_s) + D\sin(\theta_{FP}) - H\sin(\alpha_s)$$

$$+Y\sin(\phi_s) + Y_F\sin(\phi_s) \tag{2.91}$$

$$F_2 = D\cos(\theta_{FP}) + H\cos(\alpha_s) - T\sin(\alpha_s)\cos(\phi_s) \tag{2.92}$$

$$F_3 = Y\cos(\phi_s) + Y_F\cos(\phi_s) + T\cos(\alpha_s)\sin(\phi_s) \tag{2.93}$$

$$F_4 = M_y + M_{yF} + W\left(h\sin(\alpha_s) - X_{cg}\cos(\alpha_s)\right)$$

$$-D\left(x_{cg}\sin(\alpha_s) + h\cos(\alpha_s)\right) \tag{2.94}$$

$$F_5 = M_x + M_{xF} + Y_F h + W(h\sin(\phi_s) - Y_{cg}\cos(\phi_s)) \tag{2.95}$$

$$F_6 = Q - Y_F l_T \tag{2.96}$$

They form a vector, $\boldsymbol{F}$, which is a function of the trim parameters so that

$$\mathbf{F}(\theta) = 0 \tag{2.97}$$

and the residuals of the equations describe the vehicle equilibrium. For these six equations, there are six trim variables, where θ is defined for the conventional rotor

$$\{\theta_0 \quad \theta_{1c} \quad \theta_{1s} \quad \alpha_s \quad \phi_s \quad \theta_{tr}\} \tag{2.98}$$

for the flap-controlled swashplateless rotor

$$\{p_0 \quad p_{1c} \quad p_{1s} \quad \alpha_s \quad \phi_s \quad \theta_{tr}\} \tag{2.99}$$

and for the tab-controlled swashplateless rotor

$$\{q_0 \quad q_{1c} \quad q_{1s} \quad \alpha_s \quad \phi_s \quad \theta_{tr}\} \tag{2.100}$$

θ is varied to minimize the residuals in 2.97 by means of a Newton-Raphson algorithm.

2.3.2 Wind Tunnel Trim

The goal for the zero flapping wind tunnel trim solution is to achieve a target thrust and zero first harmonic blade flapping. The equations which describe this goal are

$$\mathbf{F}(\theta) = \beta - \beta_{target} = 0 \tag{2.101}$$

$$\beta = \left\{ \frac{C_T}{\sigma} \quad \beta_{1c} \quad \beta_{1s} \right\} \tag{2.102}$$

The second type of wind tunnel trim used in this investigation is similar in that the solution is obtained by varying the control angles until the residuals approach zero, but instead of using zero flapping as the target, zero hub moments are the goal, as shown:

$$\mathbf{F}(\theta) = M - M_{target} = 0 \tag{2.103}$$

$$M = \left\{ \frac{C_T}{\sigma} \quad M_x \quad M_y \right\} \tag{2.104}$$

2.3.3 Blade Response Calculations Using Finite Elements in Time and Space

The blade response is calculated using discretized equations of motion which are derived using the finite element method. The method uses the energy expressions

from eq. 2.13, and is discretized as follows for a blade b :

$$\delta \Pi_b = \int_{\psi_I}^{\psi_F} \left[\sum_{i=1}^{N} (\delta U_i - \delta T_i - \delta W_i) \right]_b d\psi = 0 \qquad (2.105)$$

where there are N discrete elements in the blade, considered from an initial azimuth ψ_I, to a final azimuth ψ_F. In this investigation, the blades are considered identical. The equations of motion used for the finite element analysis assume the general form:

$$M \overset{\star\star}{q} + C(\psi) \overset{\star}{q} + K(\psi)q = F(\psi, q) \qquad (2.106)$$

Finite Element Method in Space

The blade beam elements have fifteen degrees of freedom, regardless of the presence of flaps and/or tabs. The degrees of freedom ensure displacement and slope continuity for blade flap and lag, and displacement continuity for blade elastic twist and extension at the element boundaries. At each boundary node there are six degrees of freedom $(u, v, v', w, w', \hat{\phi})$, describing extension, lag, lag slope, flap, flap slope and elastic twist. In addition to these twelve, there are two internal nodes for axial extension, u, and one internal node for elastic twist $\hat{\phi}$. This arrangement produces linear variations for the bending and torsional moments, and a quadratic variation for axial force. For each beam element, the deflections are distributed using interpolating polynomials and elemental nodal displacements, $\mathbf{q}$. For an individual beam element, i, the blade deflections are

$$\mathbf{u(s)} = \left\{ \begin{array}{c} u(s) \\ v(s) \\ w(s) \\ \hat{\phi}(s) \end{array} \right\} = \left[\begin{array}{cccc} H_u & 0 & 0 & 0 \\ 0 & H & 0 & 0 \\ 0 & 0 & H & 0 \\ 0 & 0 & 0 & H_{\hat{\phi}} \end{array} \right] q_i \qquad (2.107)$$

where $\mathbf{q}$ is the vector of elemental nodal displacements

$$\left[\begin{array}{ccccccccccccccc} u_1 & u_2 & u_3 & u_4 & v_1 & v_1' & v_2 & v_2' & w_1 & w_1' & w_2 & w_2' & \hat{\phi}_1 & \hat{\phi}_2 & \hat{\phi}_3 \end{array} \right] \qquad (2.108)$$

The Hermite polynomials which constitute the flap and lag shape functions allow the abovementioned continuity of displacement and slope. The shape functions for elastic twist and axial extension are Lagrange polynomials, for displacement continuity. In the shape functions which follow, $s = x_i/l_i$, and l_i is the length of beam element i

$$\mathbf{H_u^T} = \left\{ \begin{array}{c} H_{u1} \\ H_{u2} \\ H_{u3} \\ H_{u4} \end{array} \right\} = \left\{ \begin{array}{c} -4.5s^3 + 9s^2 - 5.5s + 1 \\ 13.5s^3 - 22.5s^2 + 9s \\ -13.5s^3 + 18s^2 - 4.5s \\ 4.5s^3 - 4.5s^2 + s \end{array} \right\} \qquad (2.109)$$

$$\mathbf{H^T} = \left\{ \begin{array}{c} H_1 \\ H_2 \\ H_3 \\ H_4 \end{array} \right\} = \left\{ \begin{array}{c} 2s^3 - 3s^2 + 1 \\ l_i(s^3 - 2s^2 + s) \\ -2s^3 + 3s^2 \\ l_i(s^3 - s^2) \end{array} \right\} \qquad (2.110)$$

101

$$\mathbf{H_{\hat{\phi}}^{T}} = \left\{ \begin{array}{c} H_{\hat{\phi}_1} \\ H_{\hat{\phi}_2} \\ H_{\hat{\phi}_3} \end{array} \right\} = \left\{ \begin{array}{c} 2s^2 - 3s + 1 \\ -4s^2 + 4s \\ -2s^2 - s \end{array} \right\} \tag{2.111}$$

The shape functions are then used to express the elemental energy expressions in matrix form

$$\Delta_i = \delta U_i - \delta T_i - \delta W_i = \delta q_i^T (M_b \overset{\star\star}{q} + C_b \overset{\star}{q} + K_b q - F_b)_i \tag{2.112}$$

The mass, damping and stiffness matrices contain only the linear terms from the equations of motion, while the nonlinear terms are moved to the force matrix, and are linearized using a Taylor series expansion. Then the force can be described as the sum of the linear and nonlinear parts as follows:

$$(F_b)_i = (F_0)_i + (F_{NL})_i = (F_0)_i + (F_{NL})_i|_{q_{0_i}} + \frac{\partial F_{NL}}{\partial q_i} q_i \tag{2.113}$$

The individual beam elements are added together with displacement and slope conditions enforced at adjoining element nodes. At this point, after assembly, additional degrees of freedom are added for the trailing edge flap and the tab. The inertial properties as derived previously are added to the mass, damping and stiffness matrices, and nonlinear terms are added to the force expressions as described above. The variational energy equation for the system is then

$$\delta \Pi = \int_{\psi_I}^{\psi_F} \delta q_T (M_b \overset{\star\star}{q} + C_b \overset{\star}{q} + K_b q - F_b) d\psi = 0 \tag{2.114}$$

and the equations of motion for the total system assume the form shown in Eq. 2.106.

Boundary conditions are applied at the root during assembly. The exact conditions applied depend on the type of rotor: articulated, hingeless or bearingless.

There are as many finite element equations as there are global degrees of freedom; to improve computational efficiency, the system is transformed into normal modes using the blade natural vibration modes. The natural vibration modes about the mean deflected position are obtained using the linear terms of the mass and stiffness matrices; these modes are used to reduce the entire nonlinear system. The normal mode equations resemble the original set shown in 2.106

$$\bar{M} \, \overset{\star\star}{p}_b + \bar{C} \, \overset{\star}{p}_b + \bar{K} p_b = \bar{F}_b \tag{2.115}$$

where the global displacement vector, q_b, is now represented by m modes:

$$q_b = \Phi p_b \tag{2.116}$$

and Φ is the matrix of m normal modes. The mass, damping, stiffness and force matrices in normal space are

$$
\begin{aligned}
\bar{M} &= \Phi^T M_b \Phi \\
\bar{C} &= \Phi^T C_b \Phi \\
\bar{K} &= \Phi^T K_b \Phi \\
\bar{F} &= \Phi^T F_b
\end{aligned}
\tag{2.117}
$$

Finite Element Method in Time

The finite element in time (FET) method is appropriate for steady level flight, which is the assumption for this investigation. The method is based on the Hamilton's principle in weak form, and uses a temporal discretization of the blades. The

normal mode, $\mathbf{p_b}$, is approximated around the azimuth using shape functions. The temporal nodes, ξ, are assumed to have displacement continuity between elements. Then the normal mode equations, 2.115, can be written as

$$\int_0^{2\pi} \delta p_b^T (\bar{M} \overset{\star\star}{p}_b + \bar{C} \overset{\star}{p}_b + \bar{K} p_b - F)d\psi = 0 \qquad (2.118)$$

noting that the integration is over the entire azimuth, 2π, and both the damping and stiffness matrices contain periodic terms. This equation can be restated so that

$$\int_0^{2\pi} \delta y^T Q d\psi = 0 \qquad (2.119)$$

where the y contains the normal modes

$$y = \left\{ \begin{array}{c} p_b \\ \overset{\star}{p}_b \end{array} \right\} \qquad (2.120)$$

and

$$Q = \left\{ \begin{array}{c} \bar{F} - \bar{C} \overset{\star}{p}_b - \bar{K} p_b \\ \bar{M} \overset{\star}{p}_b \end{array} \right\} \qquad (2.121)$$

The discretized form of 2.119 is

$$\sum_{i=1}^{N_t} \int_{\psi_i}^{\psi_{i+1}} \delta y_i^T Q_i d\psi = 0 \qquad (2.122)$$

where N_t is the number of time elements in one revolution. Q is linearized about the steady state value of the normal modes

$$y_0 = [p_b^T \ \overset{\star}{p}_b^T] \qquad (2.123)$$

so that the equation becomes

104

$$\sum_{i=1}^{N_t} \int_{\psi_i}^{\psi_{i+1}} \delta y_i^T Q_i(y_0 + \Delta y) d\psi = \sum_{i=1}^{N_t} \delta y_i^T [Q_i() y_0 + K_t(y_0) \Delta y] d\psi = 0 \qquad (2.124)$$

In this form,

$$K_t = \begin{bmatrix} \frac{\partial \bar{F}}{\partial p_b} - \bar{K} & \frac{\partial \bar{F}}{\partial p_b} - \bar{C} \\ & \\ 0 & \bar{M} \end{bmatrix} \qquad (2.125)$$

For the *ith* time element, the time variation of the modal displacement vector can be expressed in terms of shape function, **H$_t$**, and the temporal nodal displacement vector, ξ_i, as

$$\left. \begin{aligned} p_{b_i}(\psi) &= H_t(s) \xi_i \\ \delta p_{b_i}(\psi) &= H_t(s) \delta \xi_i \end{aligned} \right\} \qquad (2.126)$$

where the local temporal coordinate for the *ith* time element is

$$s = \frac{\psi - \psi_i}{\psi_{i+1} - \psi_i} \qquad (2.127)$$

$0 \le s \le 1$, and $\psi_{i+1} - \psi_i$ is the time span of the time element. The temporal shape function matrix, $H_t(s)$ has the form

$$H_t = [H_t I_m, \cdots, H_{t_{n_t+1}} I_m] \qquad (2.128)$$

in which I_m is an $m \times m$ identity matrix, m being the dimension of the modal displacement vector. By substituting 2.126 into 2.124, the following appears

$$\sum_{i=1}^{N_t} \int_{\psi_i}^{\psi_{i+1}} \delta \xi_i^T N^T [Q_i + K_{t_i} N \Delta \xi_i] d\psi = 0 \qquad (2.129)$$

in which

$$N = \left\{ \begin{array}{c} H_t(\psi) \\[2ex] \overset{\star}{H}_t(\psi) \end{array} \right\} \tag{2.130}$$

Because the $\delta\xi_i$ are arbitrary for $i = 1, \cdots, N_t$, Eq. 2.129 becomes for the global matrices

$$Q^G + K_t^G \Delta\xi^G = 0 \tag{2.131}$$

which has the boundary conditions

$$\begin{aligned} \xi(0) &= \xi(2\pi) \\ \overset{\star}{\xi}(0) &= \overset{\star}{\xi}(2\pi) \end{aligned} \tag{2.132}$$

2.3.4   System Solution

A coupled solution consists of converged solutions for blade response, trim control angles and rotor wake. The trim control angles may involve blade pitch settings for a swashplate configuration, flap or tab deflections for a swashplateless configuration, and shaft position angles depending on wind tunnel or free flight trim. To accomplish this simultaneous convergence within the comprehensive analysis, the solution procedure is divided into stages.

First, the initial conditions are established for the control angles. These can be either user input or the result of a rigid blade analysis. The rigid blade analysis used to estimate initial conditions uses flap dynamics and uniform inflow with a linearized set of trim equations. When user input is used, it can be based on the final trim settings of previously converged cases. Because of the nonlinear nature of

the system, the initial conditions must be a good estimate of the final settings.

Next, a Jacobian matrix is calculated, using the initial trim settings as a baseline. The initial blade air loads, blade response and hub loads are calculated. The steady part of the hub loads provides the rotor forces and moments in the trim equations. The trim equations (see eqs. 2.91 - 2.96) are linearized about the baseline established with the initial conditions using a Taylor's series expansion

$$F(\theta_i + \Delta\theta_i) = F(\theta_i) + \frac{\partial F}{\partial \theta}|_{\theta=\theta_0}\Delta\theta_i = 0 \tag{2.133}$$

The Jacobian, $\frac{\partial F}{\partial \theta}$, is assembled by perturbing each of the control settings one at a time and using the resulting hub loads to calculate the residuals of the trim equations:

$$\frac{\partial F}{\partial \theta} \approx \frac{F(\theta + \Delta\theta) - F(\theta)}{\Delta\theta} \tag{2.134}$$

where the controls θ are given in eqs. 2.98, 2.99, and 2.100, and $\Delta\theta$ are the set of control perturbations, on the order of 1%, 5% or 10%. During the calculation of the Jacobian, the quasi-steady aerodynamic model with uniform inflow is used to calculate the airloads.

Finally, the Jacobian matrix is used to move the analysis from the initial control settings to the final trim solution. At each iteration, the residuals of the trim equations are calculated for the current control settings, and the trim settings are updated using a forward difference formula

$$\left[\frac{\partial F}{\partial \theta}\right]_{\theta=\theta_i}\Delta\theta_i = F(\theta_i) \tag{2.135}$$

$$\theta_{i+1} = \theta_i + \Delta\theta_i \tag{2.136}$$

Trim convergence is achieved when the trim convergence criteria, ϵ_1, reaches the user-defined limit. Typically, this is 0.001 or less. The blade response convergence criteria, ϵ_2, is typically closer to 0.01. This value implies that the blade response at the final iteration is within 1% of its value at the penultimate iteration.

The free wake model is initiated after the blade response has begun to converge. This usually occurs between the 10th and 20th iterations. Until the free wake is turned on, a linear or uniform inflow model is used. After free wake initiation, an additional 10 or 20 iterations may be necessary to achieve a trim solution.

2.3.5   Rotor Models

For any rotor model, the structural properties of the blade are applied to discrete beam elements. The properties, such as mass, center of gravity, bending stiffness or torsional stiffness, may differ between elements, but are held constant within the element.

Kaman Conceptual Rotor

The baseline properties are based on a typical Kaman-type rotor with very low blade torsional stiffness, and the baseline configuration is presented in Table 1. The root pitch spring is soft to enable maximum blade twist in response to tab deflections. The resulting torsional frequency is 1.8/rev. The flap-tab configuration is described in terms of total blade chord. The flap chord does not include the tab. Therefore in the baseline configuration, where the flap chord is 20% of total blade

chord, and the tab chord is 10% of the total, the flap and tab together occupy the trailing 30% of the total chord. The flap and tab do not necessarily have the same span; in the case where the flap is longer than the tab, outside of the tab boundaries, the flap alone occupies the trailing 30% of the total chord. The thrust level for this rotor is set to $\frac{c_T}{\sigma} = 0.062$.

UH-60A Rotor

In order to implement swashplateless control, the pitch link is removed and replaced with a soft torsion spring. The rotor properties, and fuselage properties needed for trim, are the same as the UH-60A helicopter, except that the first torsion frequency is now reduced from 4.4/rev (baseline) to 1.9/rev (swashplateless). The helicopter used for the analysis is modeled in UMARC with a single main rotor and a tail rotor. Each blade has coincident flap and lag hinges at 4.66% span, and a 26.83 ft radius with an aerodynamic root cutout of 20%. The nominal chord of the blades is 1.73 ft. The rotor speed is 258 RPM. The blades are discretized into 20 finite elements with flap, lag, torsion and axial degrees of freedom. The tip sweep in the outer 6.9% of the blade span (reaching a maximum of 20∘ at 94.5% span) is modeled as structural (center of gravity) and aerodynamic (lift) offsets from a straight, undeformed elastic axis. The baseline aerodynamic, trim and structural models have been validated against flight test data.

2.4 Concluding Remarks

An analysis methodology was developed for swashplateless helicopters controlled by trailing edge flaps and tabs. Initially, a linear, rigid blade model was developed to examine the effects of the flap and the tab on the rotor response in isolation. The parent-child relationships of the flap to the tab, and the blade to the flap were identified in the equations of motion. From these, it became clear that each control at the airfoil trailing edge may be considered a child to the parent section immediately before it, and additional dependent sections can be added to the system of equations without extensive derivation. Having established the governing equations of a system with two nested trailing edge controls, the equations for additional nested trailing edge controls on the rigid blade can be assumed with some confidence, and only the aerodynamics require further exploration.

In the next phase, a state of the art comprehensive analysis was refined to include the contributions of the trailing edge controls in the structural, aerodynamic and coupled trim models. The analysis is based on finite element methods in space and time. Each rotor blade is divided into multiple elements, and each blade element includes 15 degrees of freedom for the blade flap, lag, torsion and axial deformations. The trailing edge flap and tab are each represented by additional single degrees of freedom attached to the blade as a whole. The nonlinear inertial contributions of the flap and the tab were added to the structural model, along with the ability to include blade index angle, which is important for trailing edge flap effectiveness. Another key design parameter, blade torsional softness, can be modeled at the root

with a soft pitch spring, or along the blade with low torsional rigidity, GJ. There are two primary aerodynamic models for the flapped airfoils in this investigation: quasi-steady thin airfoil theory, and airfoil table lookup. Both of these models can accommodate aerodynamic balance in the flap and the tab. Each was implemented to calculate the incremental change to airfoil section lift and pitching moment produced by deflection of the trailing edge flap and/or tab. The increment can then be added to the properties of the baseline airfoil section. It is possible to use flap airfoil section data that does not match the baseline airfoil section. The likelihood of this is increased by the limited availability of flapped airfoil data. In such cases, the airfoil angles of attack and flap deflections at which separated flow and shock formation occur may vary significantly, and the incremental changes calculated for lift, drag and pitching moment may lead to inaccurate or misleading predictions. Recent advances in analysis methodology and computing speed have made CFD a more practical method for the generation of airfoil lookup tables. For this investigation, CFD was used to generate tables for an SC1094R8 airfoil with a trailing edge flap. The flap was 0.15c in size and was hinged at its leading edge (having no aerodynamic balance). The gap between the flap and the airfoil was sealed. The tab was not included in this simulation. For the tables generated, the range of angle of attack was $\pm 20°$, Mach numbers from 0.3 to 0.8, and flap deflections of $\pm 15°$. The predicted aerodynamic properties showed good agreement to wind tunnel test data for the unflapped airfoil. The drag of the flapped airfoil section can also be estimated with an empirical model that is a function of section angle of attack and flap deflection. This type of model provides a fast approximation of drag when more precise

111

information is not available. Drag predicted from the empirical model showed fair agreement to wind tunnel tests and to CFD results. The coupled trim procedure of the comprehensive analysis was modified to allow swashplateless rotors. Collective, longitudinal cyclic and lateral cyclic remain trim variables, but the primary control may be either blade pitch, flap deflection or tab deflection. The two primary types of trim solution have either three or six degrees of freedom, resulting in conditions that are termed isolated rotor trim or vehicle trim in this investigation. For isolated rotor trim, the shaft angles and tail rotor collective are fixed, and three constraints are given. The constraints are typically in the form of thrust, longitudinal and later cyclic blade flapping or thrust, hub pitch and roll moments. Converged solutions for blade response and trim are found quickly, typically with less than 60 iterations. Finally, calculation of the inflow distribution was examined to understand its influence on rotor trim conditions and rotor power. Uniform inflow is compared to the nonlinear distribution created by a free wake model with a single tip vortex. The effect of the trailing edge flap was included in the free wake model by the addition of vortex trailers at the radial bounds of the flap.
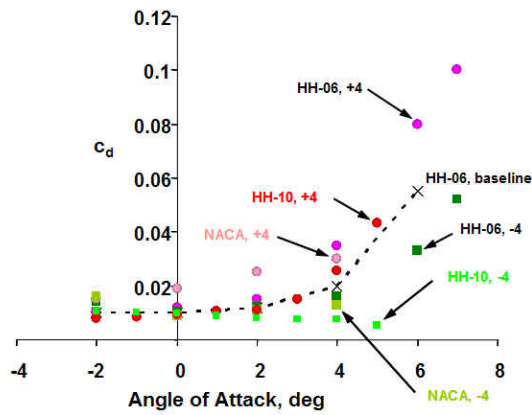
Figure 2.1: Measured Drag for the NACA 23012 (Ames and Sears [1]) and Apache HH-06 and HH-10 (Hassan et al. [2]) Flapped Airfoils. Positive ($4°$) and Negative ($-4°$) Flap Deflections Shown.
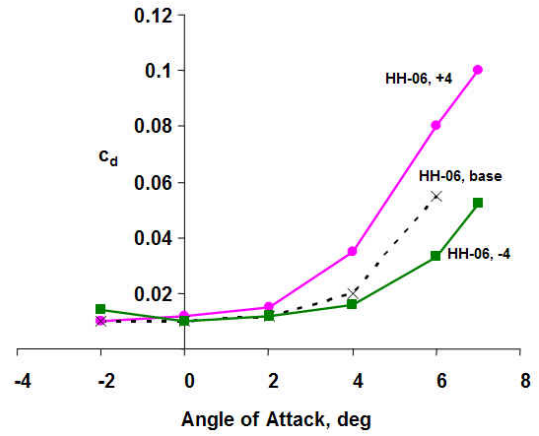
Figure 2.2: Measured Drag for Flapped HH-06 Airfoil, M $= 0.6$
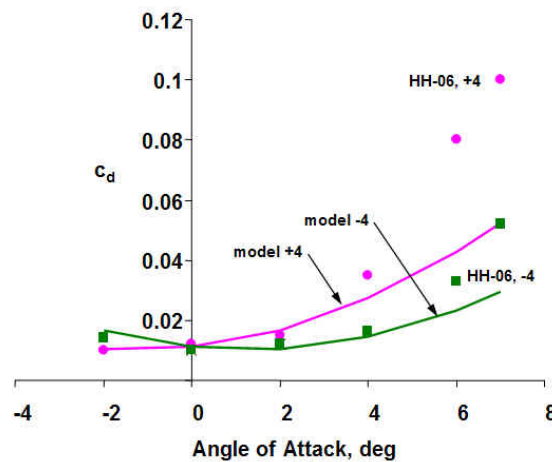
Figure 2.3: Empirical Model of Drag for Flapped HH-06 Airfoil, Showing $\pm 4°$ TEF Deflections
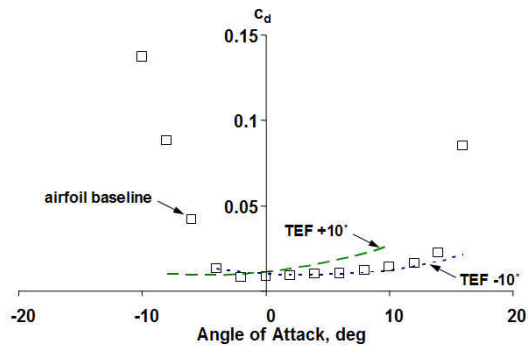
Figure 2.4: Empirical Model of Drag for Flapped SC1095R8 Airfoil, M = 0.3, Showing ±10° TEF Deflections
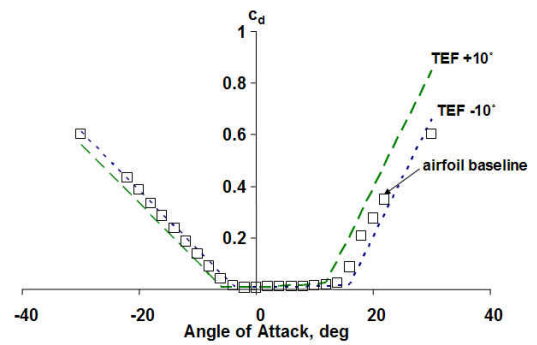
Figure 2.5: Extended Empirical Model of Drag for Flapped SC1095R8 Airfoil, Showing ±10° TEF Deflections
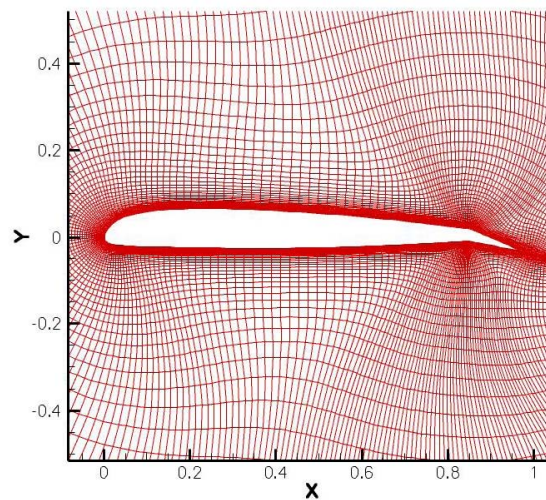
Figure 2.6: Grid for 2-D CFD Analysis of Flapped SC1095R8 Airfoil. Shown with Flap Chord $c_f = 0.15c$, Positive Flap Deflection.
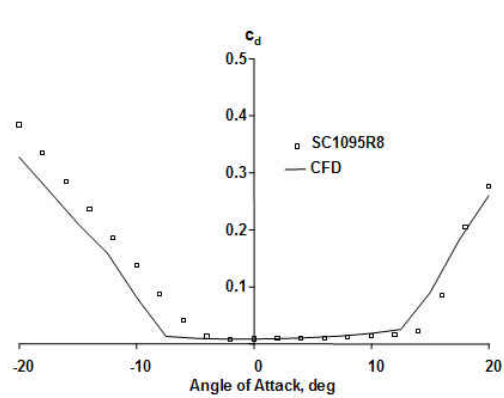
(a) Drag Coefficient
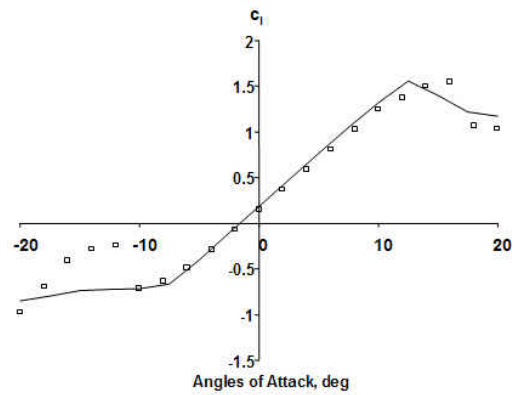
(b) Lift Coefficient
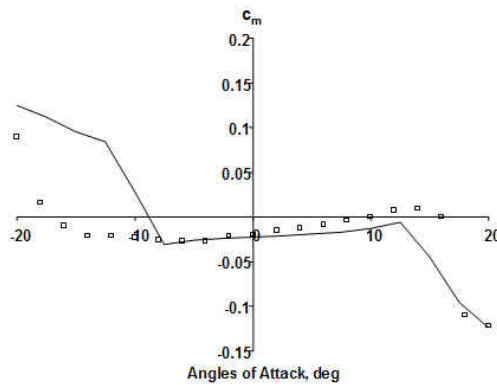
(c) Pitch Moment Coefficient

Figure 2.7: Comparison of CFD Predicted and Measured Baseline SC1095R8 Airfoil

Properties at M = 0.3, No Flap.
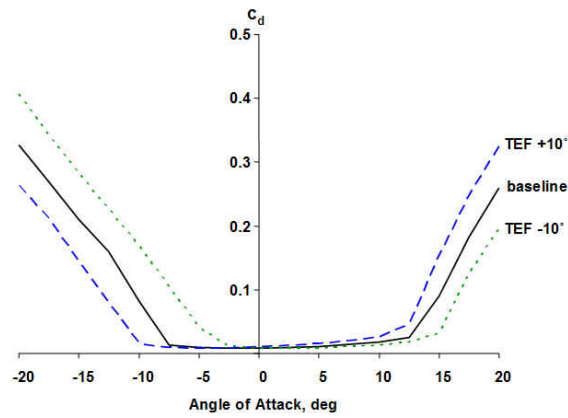
Figure 2.8: CFD Drag Prediction for $\pm 10°$ TEF Deflection for Flapped SC1095R8, $c_f = 0.15c$, No Overhang, M = 0.3

(a) -10° TEF Deflection

(b) 10° TEF Deflection
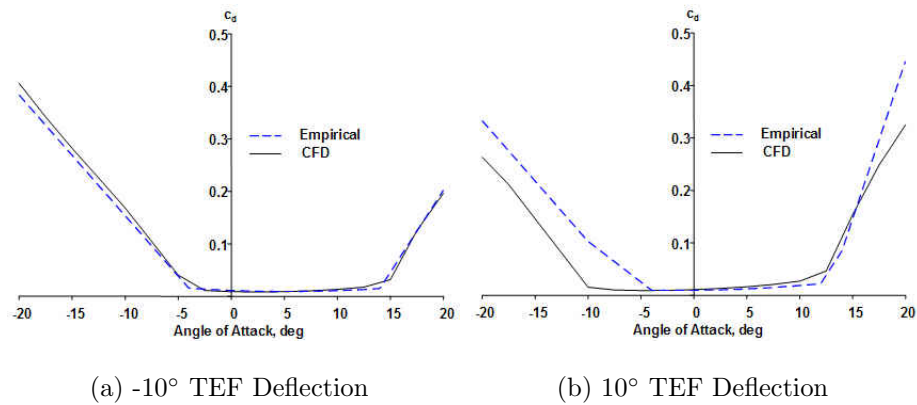
Figure 2.9: Comparison of CFD Drag Prediction and Empirical Model for Flapped SC1095R8, $c_f = 0.15c$, No Overhang, M = 0.3
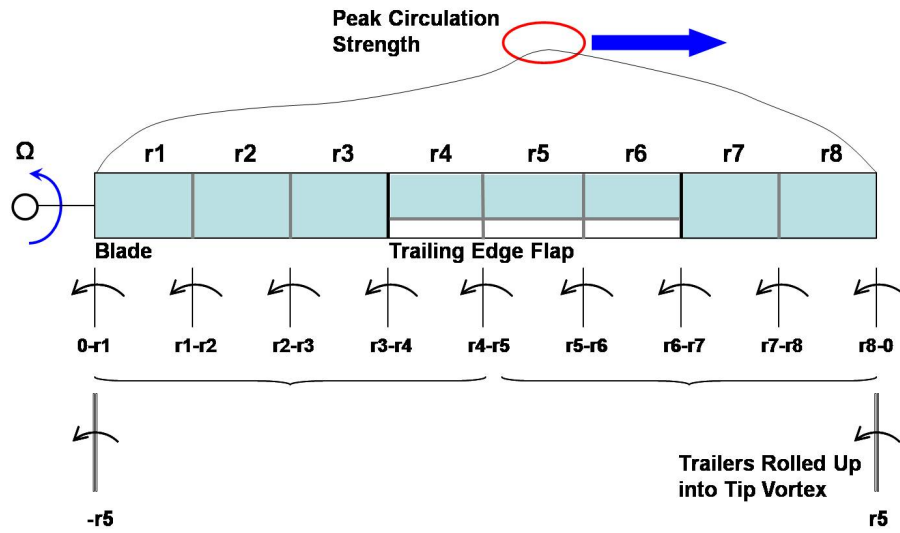
Figure 2.10: Plan View of Rotor Blade Schematic with Trailed Near Wake and Tip Vortex Free Wake
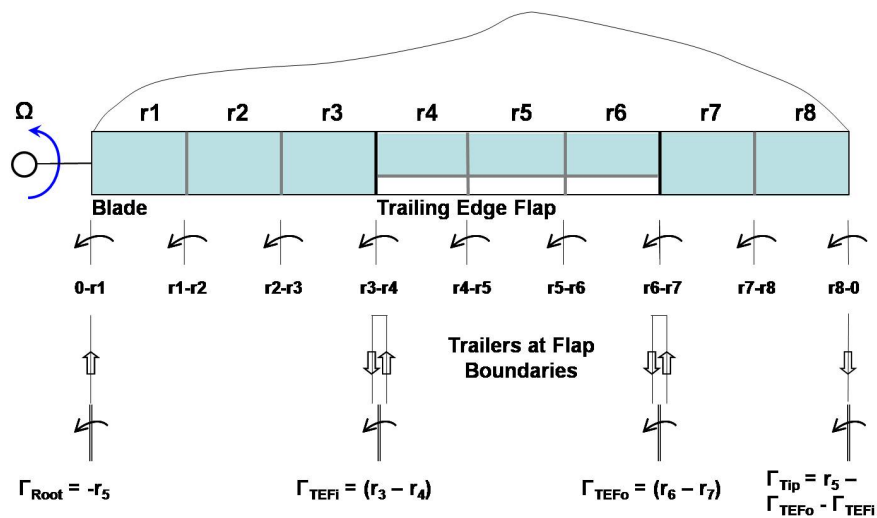
Figure 2.11: Schematic of Trailed Near Wake and TEF Trailers Free Wake
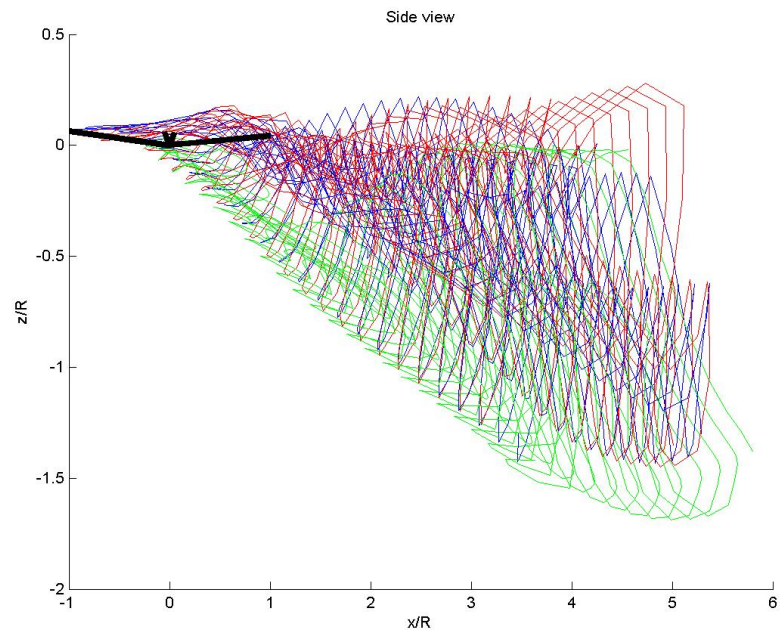
Figure 2.12: Side View of Swashplateless Rotor Wake with Flap Trailers at $\mu = 0.11$, 6 Turns. Illustration of Wake Formed By Three Trailers on Each Blade.
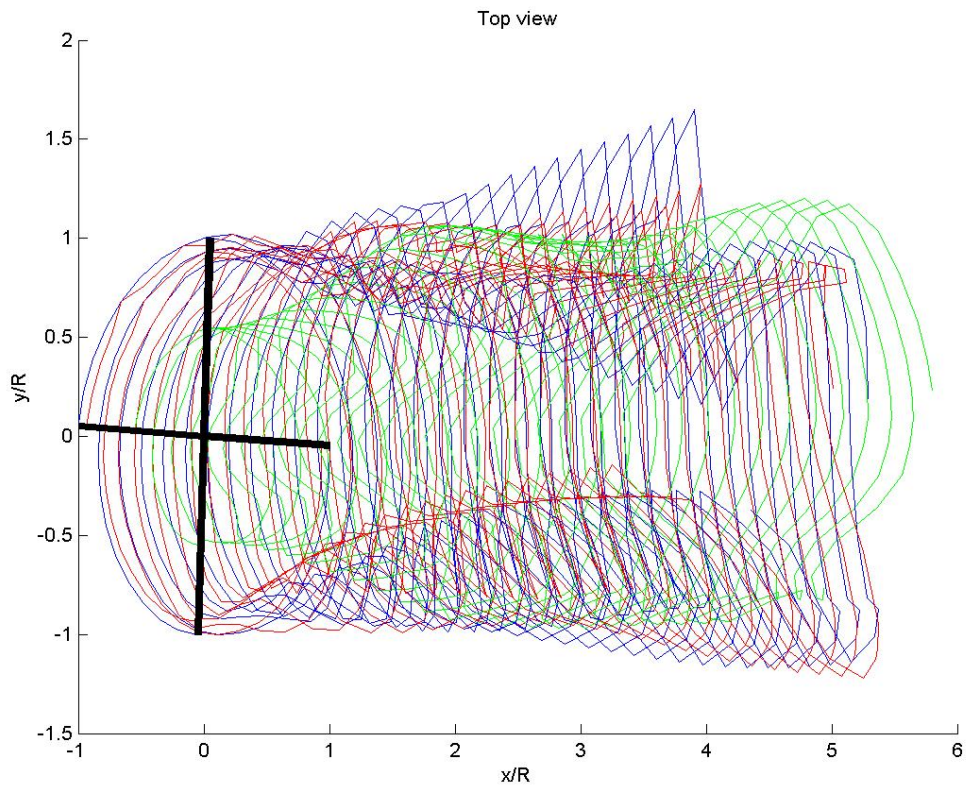
Figure 2.13: Top View of Swashplateless Rotor Wake with Flap Trailers at $\mu = 0.11$, 6 Turns. Illustration of Wake Formed By Three Trailers on Each Blade.
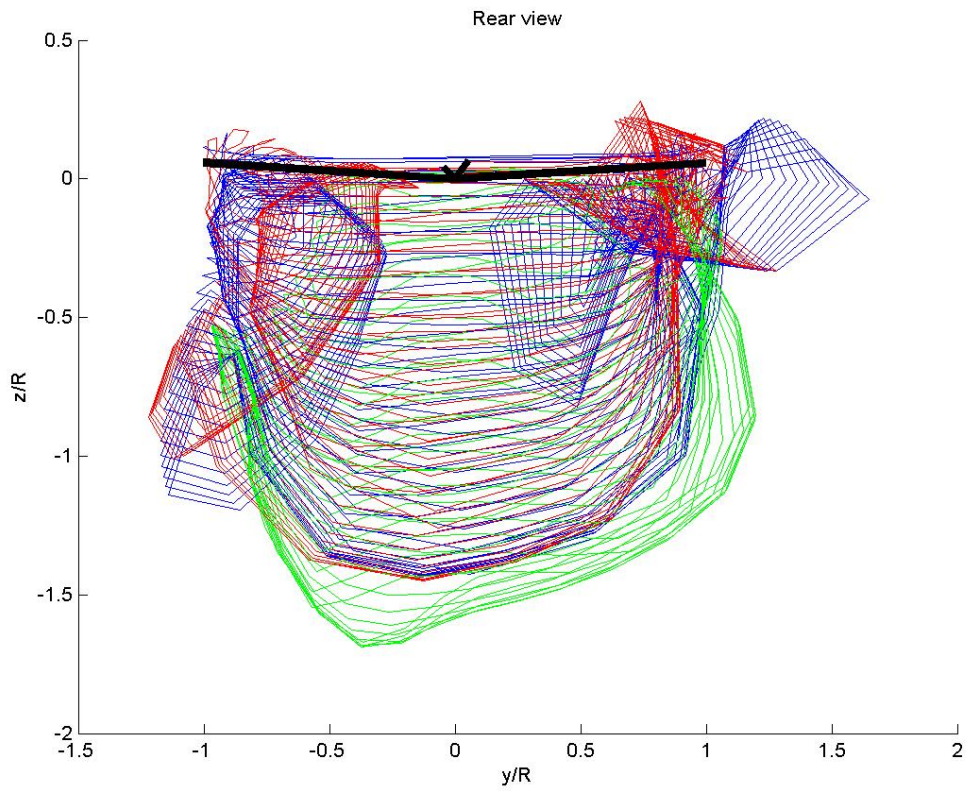
Figure 2.14: Rear View of Swashplateless Rotor Wake with Flap Trailers at $\mu =$ 0.11, 6 Turns. Illustration of Wake Formed By Three Trailers on Each Blade.
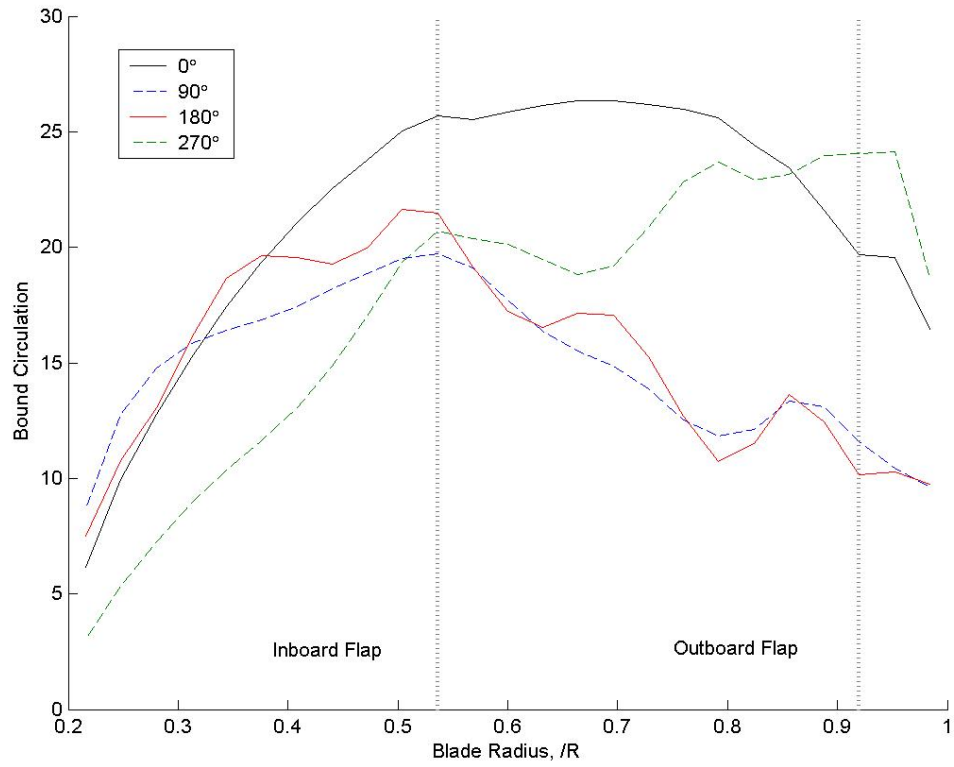
Figure 2.15: Radial Distribution of Bound Circulation at 0°, 90°, 180° and 270° Azimuth Angles, $\mu = 0.11$.

Chapter 3

Design Studies of Swashplateless Rotor

The swashplateless rotor concept under investigation is controlled indirectly by trailing edge flaps and tabs. The two key obstacles to this concept are:

1. the flap and/or tab deflections and hinge moments required to achieve rotor trim, and

2. the effect of the flap and/or tab deflections on the main rotor performance.

This chapter addresses the first issue by studying two different types of rotor and attempting to minimize the control angles and hinge moments required to trim the rotors in forward flight. The general approach is to conduct a study for each rotor which determines the sensitivity of the rotor to a design parameter. The parameters chosen represent aspects of the design geometry which can be modified in isolation. The chapter is divided into two sections. First, a conceptual rotor for a light utility helicopter with very low torsional rigidity (Kaman-type) is examined in a swashplateless configuration with trailing edge flaps and tabs, using a rigid blade, linear analysis model. The flap is a degree of freedom in the system while the tab is a prescribed deflection. The parametric study determines the effect of each design variable on the tab authority through required control angles and on actuation power through required hinge moment. The analysis model permits the initial rotor design and configuration of the swashplateless flap and tab control system. The

control angles and hinge moments of the conceptual rotor are minimized to show the feasibility of on-blade actuation with existing actuators of limited force and stroke.

Second, the rotor of an existing heavy utility helicopter (UH-60A) is examined in two swashplateless configurations: one with trailing edge flaps only, and the other with both trailing edge flaps and tabs. This study is further subdivided into sections for uncoupled blade response and coupled trim. The purpose of this part of the investigation is to examine the feasibility of retro-fitting an existing rotor with a swashplateless, flap and/or tab driven primary control system, without significant alteration to the blades or the general rotor description. This capability is desirable because retaining an existing rotor and blade configuration significantly reduces the time and expense involved in a new vehicle design. The integrated flap and tab maintain the profiles of the existing airfoil sections in use on the blade, which means that molds and machining arrangements can be re-used. New sections containing a flap, tab and actuator can be mass-balanced so that the center of gravity is not changed and undesirable pitch-flap couplings and instabilities do not arise. Although the torsion frequency must be reduced to facilitate blade twist, this can be done at the root with some combination of springs and linkages, allowing the flap and lag modes of the blade to remain largely unchanged. The UH-60A blade also has a swept tip, which is designed to mitigate compressibility effects at high speed. The flap and tab are located on the blade to avoid overlap with this tip. This rotor is made swashplateless for analysis by replacing the pitch links with soft root springs, and locating the flap and tab on the blade so as to avoid overlap with the swept tip.

The purpose of the uncoupled study is to develop understanding of the fundamental physics of the blade response to flap or tab deflections. This understanding can aid design by revealing the lift and moment mechanisms which contribute to the authority of the control. The coupled trim parameter studies gauge the minimum deflections and hinge moments which can be used to trim the rotor. These results define the mechanical characteristics required from the actuation system which will drive the flap or tab. One benefit of using the UH-60A rotor is the extensive flight test data that allows validation of the baseline rotor analysis. This validation permits some confidence in the following results for the swashplateless variant of the rotor.

3.1   Rigid Blade Linear Model

This section describes the development of a rigid blade aeroelastic trim model to predict the required tab control angles in forward flight. In this model, the trailing edge flap deflections are produced in response to the aerodynamic hinge moments created by the deflections of the tab. The system is described by four degrees of freedom, where blade flap (β), torsion (θ), trailing edge flap (p), and tab deflection (q) are the independent degrees. The equations of motion for a fixed wing are given by Theodorsen in Ref. [119]. Here, the equations have been derived for a rotary wing. Only the linear terms have been retained because the blades are assumed to be rigid, and the lag degree of freedom is neglected. A forward differencing method is used to calculate the trim solution in steady, level flight.

The geometric parameters of the flap and tab are shown in Fig 3.1. The total

chord of the section is the sum of c_b, c_f and c_t, but although the size (as a percentage of the total) of each section may vary during the course of analysis, the total chord remains constant. The aerodynamic formulation [119] is a thin airfoil model which includes arbitrary hinge axes for the flap and tab, but the gaps are assumed to be sealed. The rotor trim targets are thrust and zero hub roll and pitch moments. For the trim solution, the tab motion is a trim variable, and is no longer considered a dynamic degree of freedom. The trim solution is taken after sufficient revolutions to ensure that the steady state has been achieved.

3.2   Swashplateless Conceptual Rotor in Wind Tunnel Trim

This section contains the results of a parametric sensitivity study which produced an optimal trailing flap and tab design for a conceptual rotor. The design process has the objective of simultaneously minimizing control angles and hinge moments. Since the rotor is conceptual, many properties can be varied, but some of the general parameters of the rotor are kept constant. These properties are listed in Table 3.1. The thrust level for this rotor is set to $C_T/\sigma = 0.062$ for all advance ratios. The longitudinal and lateral shaft angles are zero. The inflow model is linear, and no fuselage characteristics (such as parasite drag) are considered.

3.2.1   Rotor Properties

The baseline properties are based on a typical rotor (Kaman-type) with very low blade torsional stiffness, and the baseline flap and tab configuration is presented

Parameter	Value
Radius, R	16 ft
Blade Chord, c	1.25 ft
Lock Number, γ	10.0
Rotor Speed	460 RPM

Table 3.1: Principal Characteristics of Kaman-type Conceptual Rotor

in Table 3.2. The root pitch spring is soft to enable maximum blade twist in response to tab deflections. The resulting torsional frequency is 1.8/rev. The flap-tab configuration is described in terms of total blade chord. The flap chord does not include the tab. Therefore in the baseline configuration, where the flap chord is 20% of total blade chord, and the tab chord is 10% of the total, the flap and tab together occupy the trailing 30% of the total chord. The flap and tab do not necessarily have the same span; in the case where the flap is longer than the tab, outside of the tab boundaries, the flap alone occupies the trailing 30% of the total chord.

3.2.2 Parametric Study of Trailing Edge Flap and Tab

The study examines the tab control angles and hinge moments over a range of design parameters. They are: (i) the index angle, (ii) blade chord ratio, (iii) flap radial location, and (iv) flap and tab overhang (hinge position). The effect of advance ratio on the required tab deflections is studied in Fig. 3.4. As the advance ratio increases from 0.15 to 0.35, the collective tab angle decreases slightly, while

Parameter	Value
Flap Chord, c_f	0.20c
Tab Chord, c_t	0.10c
Flap Span	0.24R
Tab Span	0.18R
Index Angle	5°
Flap Overhang	$0.25c_f$
Tab Overhang	$0.25c_t$
Flap Midspan Position	0.75R
Blade Pre-twist	$-10°$

Table 3.2: Baseline Configuration of Kaman-type Rotor for Parametric Study

the half peak-to-peak value increases. The half peak-to-peak (hpp) angle represents the magnitude of the lateral and longitudinal cyclic flap deflections, and is defined as $\sqrt{\delta_{1c}^2 + \delta_{1s}^2}$. Figure 3.5 shows the hinge moment values increase as advance ratio increases.

Index Angle

The index angle is the pre-collective applied to the blade to minimize the total torsional deflection required to achieve the equilibrium trim position for a given flight condition ([79]). The effect of index angle on the required tab deflections and hinge moments are shown in Fig. 3.2. As index angle increases from 5° to 13.5°,

the tab collective decreases from 32° to 0°. The hpp value of the control angle decreases steadily as the index angle increases. The plot shows that the mean and half peak-to-peak values of tab hinge moment reach a minimum at 15° index angle (Fig. 3.3). At this index angle, the tab control angles are $-5°$ mean, and 8° hpp, while the mean and hpp tab hinge moments are 0.5 ft-lbs.

Combined Chord

The effect of combined flap and tab chord (c_f+c_t) is shown in Fig. 3.6. The proportion of tab chord to combined chord is held constant at 33% (identical to the baseline configuration), as the combined chord length of the flap and tab together is changed relative to the total chord. The tab collective is approximately constant as the combined chord increases from 30% to 50% of total chord. Required tab collective increases sharply when the combined chord is less than 30% of the total. The very high magnitude of the control angles below 30% indicates an infeasible design region, perhaps requiring more detailed investigation. It can be seen that tab hinge moment decreases as the combined chord increases from 20% to 30% (Fig. 3.7), before beginning to increase in magnitude as the combined chord becomes larger than 30% of the total chord. These results are a direct reflection of the tradeoff between hinge moment and moment arm.

Midspan Location

The flap radial location refers to the midspan of the flap, and in this study is the same for both the flap and the tab. Both the tab collective and half peak-to-peak value decrease as the midspan position moves from 0.65R to 0.85R (Fig. 3.8). The region between 0.65R and 0.75R (the baseline position) appears to be an infeasible design region where the required control angles are extremely high; outboard of 0.75R, the decrease in collective is gradual. The tab hinge moment follows a similar trend to the control angles (Fig. 3.9).

Flap Overhang

The effect of variation in flap overhang is shown in Fig. 3.10. The overhang describes the position of the flap hinge relative to the leading edge of the flap, so that the baseline $0.25c_f$ overhang places the hinge at the flap quarter-chord. The parameter is also known as the aerodynamic balance. It can be seen that varying flap overhang from 1% to 25% decreases the tab deflections required in both collective and half peak-to-peak value. The tab hinge moment decreases steadily as the overhang is increased (Fig. 3.10). These results must be balanced by the consideration of drag increase caused by protrusion into the flow. Overhang is beneficial in terms of hinge moment, but the gains provided by larger values may be negated by increases in drag [2], especially at higher Mach numbers. Current research with computational fluid dynamics (CFD) [103] has shown that flap overhang has little effect on blade lift and pitch moment, but increases drag. In addition, the gap

produced by overhang between the flap and the blade section tends to reduce the effectiveness of the flap by reducing lift and pitch moment and increasing flap drag and hinge moment. These effects can be included in future investigations by means of airfoil tables generated by wind tunnel testing or by computational methods.

Tab Overhang

The effect of tab overhang is similarly investigated in Fig. 3.12. As the tab overhang increases from 1% to 25%, the required tab collective decreases steadily. The tab cyclic angles are not significantly affected by the tab overhang. Again, the tab hinge moment decreases steadily as the tab overhang increases in Fig. 3.13.

Improved Flap and Tab Configuration

This parametric study enables the determination of an improved configuration for the case of the typical rotor. The parameters are chosen to minimize both required control angles and tab hinge moments and are listed in Table 3.3. The major differences from the baseline configuration are in the sizes of the tab and flap chords, relative to both the blade and to each other, the 10 degree increase in index angle, and the decrease in flap and tab overhang from 25% to 10% of their respective chords.

Figure 3.14 compares the effect of advance ratio on both the optimized and the baseline configurations. The results for the optimized configuration are shown as a solid line; the baseline results are connected by a dashed line. The magnitude

Parameter	Value
Flap Chord, c_f	0.29c
Tab Chord, c_t	0.06c
Flap Span	0.30R
Tab Span	0.30R
Index Angle	15°
Flap Overhang	$0.10c_f$
Tab Overhang	$0.10c_t$
Flap Midspan Position	0.75R
Blade Pre-twist	$-10°$

Table 3.3: Improved Configuration of Flap and Servotab for Kaman-type Rotor

of the mean tab angle decreases from 32° for the baseline to 6° for the optimized configuration at advance ratio 0.35. The half peak-to-peak angle decreases from 29° for the baseline to 8.6° for the optimum. Fig. 3.15 also shows a significant reduction in the tab hinge moment for the improved configuration. At advance ratio 0.35, the mean tab hinge moment decreases from 12 ft-lb to 0.7 ft-lb. The half peak-to-peak value of hinge moment decreases from 12 ft-lb for the baseline to 1.5 ft-lb for the new configuration. These improvements in required control angles and hinge moments imply reduced stroke and force requirements for an actuator for the system.

3.3 Comprehensive Analysis

The next section describes the development of a refined comprehensive analysis to predict the tab control angles and hinge moments. The analysis is performed on a representative rotor with all characteristics similar to the UH-60A rotor, except those that must be changed for the swashplateless rotor. First, the rotor model is described, including the details of the structural model, and the modifications made to accommodate the swashplateless control. Then, the results of the analysis are described, with a discussion on minimization of the tab angles and hinge moments. As before, a new trailing edge flap and tab configuration is developed from a baseline by means of a simple parametric sensitivity study.

3.3.1 Description of Model

In order to implement swashplateless control, the pitch link is removed and replaced with a soft torsion spring. The rotor properties, and fuselage properties needed for trim, are the same as the UH-60A helicopter, except that the first torsion frequency is now reduced from 4.4/rev (baseline) to 1.9/rev (swashplateless). The helicopter used for the analysis is modeled in UMARC with a single main rotor and a tail rotor. Each blade has coincident flap and lag hinges at 4.66% span, and a 26.83 ft radius with an aerodynamic root cutout of 20%. The nominal chord of the blades is 1.73 ft. The rotor speed is 258 RPM. The blades are discretized into 20 finite elements with flap, lag, torsion and axial degrees of freedom. The tip sweep in the outer 6.9% of the blade span (reaching a maximum of 20° at 94.5% span)

132

is modeled as structural (center of gravity) and aerodynamic (lift) offsets from a straight, undeformed elastic axis. The baseline aerodynamic, trim and structural models have been validated against flight test data in Refs. [122] and [124]. The natural frequencies of the baseline blade are shown in fan plot form in Fig. 3.16. Reducing the torsional frequency of the rotor for the swashplateless configuration produces the alteration to the modes seen in Fig. 3.17. The primary change is to the first torsional mode, while the first lag and flap modes are essentially unchanged. The second flap mode is very similar for both the swashplateless and conventional rotors, from 0.6 to 1.3 of the normalized rotor speed, but the third flap mode is only unchanged from 0.90 to 1.3 of the rotor speed. As the rotor speed is reduced to low RPM, the modification of the torsional stiffness causes more change to the natural frequencies. Natural frequencies for the baseline and swashplateless rotors rotating at the operating speed are listed in Table 3.4.

The second order nonlinear beam formulation, based on Refs. [125] and [126], is modified to integrate the structural, inertial and aerodynamic contributions of the trailing edge flap and tab. The flap and tab are modeled as additional, but single, degrees of freedom. Note that for the trim problem, either the tab or flap motions are trim variables. Although the flap and tab can be defined across multiple elements with varying properties, the motion of each is described by a single deflection. The unsteady aerodynamic formulation for the trailing edge flap and tab is that used earlier, the thin airfoil model developed by Theodorsen and Garrick. For consistency, thin airfoil theory is used for both the main blade and the flap-tab sections. The inflow is calculated using a refined Bagai-Leishman pseudo-implicit

Mode	Baseline Freq.	Swashplateless Freq.
1st Lag	0.276	0.276
1st Flap	1.037	1.037
2nd Flap	2.833	2.844
1st Torsion	4.302	1.990
3rd Flap	4.692	4.682
4th Flap	5.200	5.188
5th Flap	7.914	7.874
6th Flap	11.412	11.704
2nd Lag	12.431	12.434
2nd Torsion	13.536	9.881

Table 3.4: Calculated Natural Frequencies (per rev) for UH-60A Baseline and Swash-plateless Rotors at Normal Operating Speed, 258 RPM

free wake model, modified for flexible blades [122]. This is a single tip vortex model with no corrections for the flap edge gaps. The trim solution is for a thrust level of $C_T/\sigma = 0.084$, and targeted hub pitch and roll moments. The shaft angles are fixed at longitudinal tilt of 7.31° nose down pitch and lateral tilt of 1.5° right wing down. These values are based on the high speed flight C8534 of the UH-60A Airloads Program. This corresponds to a vehicle gross weight of 17500 lbs ($C_W/\sigma = 0.0783$) and forward speed of 155 knots ($\mu=0.368$). The same thrust level and shaft angles are maintained for all flight speeds. The hub moments for flight C8534 are 6040

ft-lbs roll left and 4169 ft-lbs nose down. Here, the rotor is trimmed to zero hub moments at all flight conditions, in the absence of available data at lower speeds. In real flight, these conditions vary with speed, and are in general less stringent at lower speeds.

3.4 Swashplateless UH-60A Rotor with Trailing Edge Flap

The parameter study of design variables is conducted twice for the swashplateless rotor, first for the swashplateless rotor controlled by a trailing edge flap, and again with trailing edge flaps and tabs. This investigation allows the designs of the flap only and the flap/tab configurations to be configured for minimum control angles and hinge moments, and then those designs can be compared to each other. Such a comparison will show the advantages and disadvantages of each configuration for the UH-60A rotor, and provide general insight for any rotor of similar size and characteristics.

3.4.1 Uncoupled Blade Response to Flap in Hover

The uncoupled blade response to trailing edge flap deflection shows how blade pitch and thrust generation depend on the key design parameter of torsional stiffness. There are two primary changes that flap deflection can make to the aerodynamic environment of the rotor blade: (i)the blade twist is induced by a pitching moment which is an equilibrium response to the flap hinge moment and (ii)the blade lift is directly altered along the span which contains the flap. The torsional stiffness of

the blade (either at the root or along the span) determines the contribution of each of these two modes to the total blade response.

Parameter	Value
Flap Chord, c_f	0.15c
Flap Span	0.39R
Index Angle	15°
Flap Overhang	$0.0c_f$
Flap Midspan Position	0.75R
Torsional Frequency	2.0/rev

Table 3.5: Baseline Configuration of UH-60A type Swashplateless Rotor with Trailing Edge Flaps

The torsional frequency is varied from 1.5/rev to 4.3/rev by adjusting the stiffness of the blade root spring. The uncoupled blade pitch response to steady flap deflection in hover is shown in Fig. 3.18a. The index angle is 15°. Downward flap deflection is considered positive, and produces blade nose down twist. As the flap deflection increases from -10° to 10°, the blade twists nose down. The response is strictly linear for the higher torsional frequencies, and becomes slightly nonlinear as the root spring softens. At torsional frequencies below 2/rev, the maximum flap deflection for which a converged blade response could be calculated decreases. As expected, softening the spring allows the blade pitch response to increase for the same trailing edge flap input. This can also be seen in the rate at which the blade

pitches in response to the flap deflection, in Fig. 3.18b.

The blade loading (a non-dimensional thrust measurement) is also calculated as a function of flap deflection and torsional frequency. In Fig. 3.19a as the root spring is softened, for the same flap deflection, the blade loading decreases. This is a result of the nose down blade twist which increases with the decreasing torsional frequency. The blade loading has a linear response to flap deflection, which is seen in the pointwise derivative of the blade loading with respect to flap deflection in Fig. 3.19b. Only when the torsional frequency is reduced below 2/rev does the blade loading become slightly nonlinear as the flap deflection increases.

3.4.2 Coupled Wind Tunnel Trim Solution with Flap in Forward Flight

A range of geometric parameters was studied to minimize the flap control angles and hinge moments at high speed ($\mu = 0.368$). The baseline rotor has a 0.15c flap hinged at its leading edge, with 15° index angle applied to the blade. The baseline configuration for this study is identical to that described in Table 3.5. The parameters are (i) index angle, (ii) flap span, (iii) flap chord and (iv) flap overhang. Flap deflection and hinge moment are examined for each parameter. The deflections are reported as the flap collective, which is the steady deflection, and the flap half peak-to-peak (hpp). The half peak-to-peak (hpp) angle represents the magnitude of the lateral and longitudinal cyclic flap deflections, and is defined as $\sqrt{\delta_{1c}^2 + \delta_{1s}^2}$.

The baseline flap configuration is examined across the range of forward flight

speed. From $\mu = 0.10$ to $\mu = 0.15$, the collective and hpp angles decrease to their respective minimums so that the flap collective is -7.5° and the hpp is 8.5°. From $\mu = 0.15$ to $\mu = 0.368$, the flap deflections required to trim increase in Fig. 3.20a until the flap collective has reached -13° and the hpp is 17°. In Fig. 3.20b, the hpp of the flap hinge moment similarly increases with advance ratio to a maximum of 33.16 ft-lb at $\mu = 0.368$. The mean of the flap hinge moment does not change much with forward flight speed, and remains between 14 to 16 ft-lbs across the range. The hpp flap angle is considerably larger than the stroke capabilities of current smart actuator technology. This capability is considered a boundary because smart actuators have the high bandwidth, low weight and compactness to fit within the blade profile and drive the flap without also adding excessive mass. However, other actuator types are also being considered which might expand these flap deflection and hinge moment boundaries in the future.

Index Angle

The purpose of the index angle is to give a pre-collective that moves the blade close to its final trim position in pitch. This positioning means that the blade pitch does not have to be changed very much to achieve trim, and thus the required flap deflection is reduced. Unfortunately, just as the pitch collective required to trim changes with the flight condition, the bes index angle also changes with flight condition. Since index angle is not a degree of freedom in this investigation, the index is selected to suit the most challenging flight condition within the scope of

the investigation, and remains constant for all other conditions. This parameter study is designed to select the index angle that best minimizes flap angle and hinge moment at $\mu = 0.368$ in steady level flight.

The magnitude of both the flap collective and the hpp angle are above $15°$ at $13°$ of index angle in Fig. 3.21a. These decrease gradually and nonlinearly as index angle increases, until flap deflections reaches a minimum of -9° collective and $12°$ hpp at $20°$ index. The mean flap hinge moment decreases steadily as index angle increases from $13°$ to $20°$ in Fig. 3.21b, following the steady decrease in flap collective angle. The hpp variation in the hinge moment decreases as the index increases from $13°$ to $15°$, but then shows only small change as the index increases from $15°$ to $20°$, with a slight increase showing at the highest index angle. The decrease in flap deflections and in mean hinge moment indicate that high index angle is beneficial, and $20°$ index is selected.

Flap Chord

The effectiveness of the flap is not sensitive to the size of the flap chord, so as the flap chord size is increased from 0.10c to 0.25c in Fig 3.22a, neither the collective nor the hpp flap deflections change very much. There is a slight decrease in the magnitude of the flap deflections at 0.15c. In Fig. 3.22b, the mean and the hpp of the hinge moment increase significantly with flap chord length. Selecting the best flap chord is thus a compromise between minimizing the deflections and the hinge moment. For this investigation, a chord of 0.15c was selected.

Flap Overhang

Overhang describes the distance of the flap hinge as a percentage of the flap chord, aft of the flap leading edge. Increasing the overhang from $0.0c_f$ to $0.50c_f$ (moving the hinge to 50% of the flap chord) causes first a small increase in flap deflections at $0.17c_f$, then a decrease as the hinge continues to move aft in Fig. 3.23a. The hinge moments show a similar trend in Fig. 3.23b, but the changes in both the mean and hpp hinge moments are more significant than those seen for the flap angles. Although both flap deflections and hinge moment reach a minimum at the largest overhang, or aftmost position of the hinge, the overhang selected for this study is $0.33c_f$. This choice is a compromise between the results of this parameter study and other work [103] that has shown an increase in profile drag due to flap overhang.

Flap Span

As the length of the flap increases along the blade radius, it gains authority as seen in Fig. 3.24a and the flap deflections required to achieve trim at high speed decrease. As the flap span increases from 0.20R to 0.40R, the flap collective decreases from -18° to -13°. The hpp decreases similarly as the span increases, from 20° at 0.20R to 15° at 0.40R. Figure 3.24b shows that the flap hinge moment increases with the flap length. The change in both the mean and hpp hinge moment is more significant from 0.30R to 0.40R, although the increase in the mean hinge moment in that range is small, while the increase in the hpp is larger. This study indicates

that the best length for the flap is 0.30R, so that flap angles are reduced without incurring too large a penalty in flap hinge moment.

Before making a final selection of the flap geometry, the parameter study was repeated for an index angle of 20°. This produced no change in the optimal value for any parameter except for flap length. After the index angle is increased from 15° to 20°, the optimal flap span changes from 0.30R to 0.40R. The flap angles in Fig. 3.25a show a similar trend to that seen in Fig. 3.24a, where the collective and hpp angles decrease as the flap length increases. At the higher index angle, the decrease in flap deflection is larger, so that at 0.40R, the collective is -10° and the hpp is 14°; this compares to -13° collective and 15° hpp for the same flap span at 15° index angle. Figure 3.25b shows that the trend of the hinge moments changes for the higher index angle: as the span increases from 0.20R to 0.40R, both the mean and hpp of the hinge moment decreases steadily. The new minimum of the hinge moment hpp is 26 ft-lb at 0.40R, whereas at 15° index angle, the minimum was 25 ft-lb at 0.20R. Based on this re-examination of the flap span, the final value for the flap length is 0.40R.

Improved Flap Configuration

The geometry of the trailing edge flap for the swashplateless rotor was configured for minimum flap angles and hinge moments at high speed ($\mu = 0.368$) in steady level flight. The primary changes to the configuration are index angle and flap overhang. The properties of this configuration are listed in Table 3.6.

Parameter	Value
Flap Chord, c_f	0.15c
Flap Span	0.39R
Index Angle	20°
Flap Overhang	$0.33c_f$

Table 3.6: Improved Configuration of UH-60A type Swashplateless Rotor with Trailing Edge Flaps

Altering the baseline flap parameters to the new values results in a reduction in the flap deflections required to trim across the range of forward flight speed. In Fig. 3.26a the flap collective has decreased by at least 2° at every speed across the range, while the hpp angle decreases 23%, from 17° to 13°, at $\mu = 0.368$. Figure 3.26b shows the significant decreases in flap hinge moment as a result of the configuration change. At high speed, $\mu = 0.368$, the mean hinge moment is reduced by 96%, and the hpp by 90%.

3.5   Swashplateless UH-60A Rotor with Trailing Edge Flap and Tab

The motivation for the investigation of tab-actuated trailing edge flaps for swashplateless rotors is to produce a primary control system which requires minimal actuation power.

3.5.1 Uncoupled Blade Response to Flap and Tab in Hover

The uncoupled blade response to tab input offers insight to the fundamental physics of the trailing edge flap-tab system. The torsional frequency and the TEF (also called aileron) frequency are the two major design properties used to examine the nature of the blade response to the tab. The blade pitch and trailing edge flap deflections are examined for the direction and rate of response; from these conclusions are drawn about the influence of these properties on the rotor response in hover. The baseline case for the uncoupled study is described in Table 3.7: an index angle of 15° is applied to the blade; the combined flap and tab chord is 0.40c (flap = 0.25c, tab = 0.15c). Blade pitch is positive nose up. Downward flap or tab deflection is considered positive (i.e., nose up is positive for the control surfaces).

The blade deflections are calculated in response to tab input for torsional frequencies from 1.6/rev to 3.5/rev (Fig. 3.27), while the aileron hinge stiffness is adjusted to keep the aileron frequency constant at 2.15/rev. Blade pitch is defined at 75%R, and includes elastic twist deflection and the index angle. The built-in pre-twist is zero at this location. At the lowest torsional frequency, 1.6/rev, the blade moves nose up in response to positive tab input (tab down). For positive tab deflection, the flap is negative, and vice versa. At zero tab input, q=0, there is a twist deflection due to the offset elastic axis resulting from tip sweep. As the torsional frequency increases, indicating a stiffer torsional spring at the root, the blade pitch continues to increase with increasing tab input, but at a slower rate. This is reflected in the blade pitch derivative, $\frac{\partial \theta}{\partial q}$, which decreases as torsional frequency increases

Parameter	Value
Flap Chord, c_f	0.25c
Tab Chord, c_t	0.15c
Flap Span	0.39R
Tab Span	0.39R
Index Angle	15°
Flap Overhang	$0.0c_f$
Tab Overhang	$0.0c_t$
Flap Midspan Position	0.75R
Torsional Frequency	2.0/rev
Aileron Frequency	2.15/rev

Table 3.7: Baseline Configuration of UH-60 type Rotor

(Fig. 3.27b).

The flap, shown in Fig. 3.28, always deflects in the opposite direction to tab input, with little variation due to torsional frequency. The derivative of the flap response, $\frac{\partial p}{\partial q}$, shows that the flap response rate is only slightly changed by increasing torsional frequency (Fig. 3.28b). There are two competing mechanisms at work: (1) the positive tab results in a lift increase due to the blade twisting nose up, but (2) the negative flap causes a decrease in lift over the span of the flap. If the net effect is an increased blade lift due to positive tab deflection, then moment (blade twisting nose up) is dominant. If the net effect of positive tab deflection is a decrease in lift

(flap lift decrement), then lift is dominant.

This is clarified in Fig. 3.29a. At a torsion frequency of 1.6/rev, the blade loading, C_T/σ, follows the blade pitch (as shown in Fig. 3.27a), and increases with positive tab input (Fig. 3.29a); the dominant effect is therefore moment. At an increased torsional frequency of 3.5/rev, blade loading decreases as tab input increases, as a consequence of the negative lift increment provided by the trailing edge flap. This effect overrides the twist effect because the stiffer torsional spring reduces blade twist response; the dominant effect is therefore lift. In between these extremes the mechanisms are mixed, and at 1.9/rev the tab acts with both lift and moment effect, depending on the magnitude of tab input. The derivative of blade loading (Fig. 3.29b) quantifies the lift and moment mechanisms by showing the moment mode has a positive rate of change with tab input, while the lift mode has a negative rate of change with tab input. Thus, such a plot can be used to determine the primary mechanism of control for the swashplateless control system.

Although torsion frequency has the dominant effect only on pitch response, the aileron frequency affects both aileron and pitch response. As aileron hinge stiffness increases, the blade pitch response is reduced until at 4.8/rev, blade pitch is constant for the range of tab input (Fig. 3.30a). Here, the moments from the flap and tab are equal and opposite. Above 4.8/rev, the aileron ceases to deflect substantially, and the tab behaves as a flap. The derivative shows the rate of pitch response decreases with increasing aileron frequency (Fig. 3.30b).

As expected, the flap response increases in magnitude as tab input becomes larger, while the flap moves in opposition to the tab. The effect of aileron hinge

stiffness is that flap response decreases as the hinge spring is stiffened (Fig. 3.31a). The flap derivative begins to increase sharply as the aileron frequency approaches 1.5/rev (Fig. 3.31b).

The rotor thrust shows the transition from dominant moment effect at low aileron frequency to dominant lift effect at high aileron frequency (Fig. 3.32a). As the aileron stiffness increases, the flap deflection steadily decreases until the tab is effectively acting as a flap. In this case, the thrust decreases with increasingly positive tab input, as the blade twists nose down (as it would for a positive flap deflection). The derivative in Fig. 3.32b demonstrates again the dominance of moment or lift effect in response to tab input.

3.5.2 Coupled Wind Tunnel Trim Solution with Flap and Tab in Forward Flight

A range of geometric parameters was studied to minimize the tab control angles and hinge moments at high speed ($\mu = 0.368$). The baseline rotor has a 0.25c flap and 0.15c tab (0.40c combined) both hinged at their leading edges, with 15° index angle applied to the blade. The baseline configuration for this study is identical to that described in Table 3.7, except for the aileron frequency, which was increased to 3.7/rev to facilitate trim convergence. The parameters are (i) index angle, (ii) tab chord as percentage of combined flap-tab, (iii) combined flap-tab chord as percentage of blade chord and (iv) flap overhang and tab overhang. Tab deflection and hinge moment are examined for each parameter.

Index Angle

The range of index angle is from 12° to 20°. As the index angle increases, the required tab collective decreases from -5° at 12° index to -3° at 18° index; the tab cyclic angle (hpp) is relatively insensitive to index angle (Fig. 3.33a). The mean hinge moment decreases from 9 ft-lb to 4 ft-lb as the index angle increases, while the hpp decreases until the index angle is 18°, then increases slightly; both the mean and hpp portions of the moment reach a minimum at 18° index angle (Fig. 3.33b).

Tab Chord Ratio

Tab chord ratio is the ratio of the tab chord to the combined flap and tab chords ($c_t/(c_t + c_f)$). The combined flap and tab chord ($c_f + c_t$) is kept constant at 0.40c. As the the tab chord is increased from 30% to 65%, the tab control angles are reduced by one-third (Fig. 3.34a), but the tab hinge moment hpp is doubled (from 22 ft-lb to 42 ft-lb in Fig. 3.34b), indicating that increasing tab chord carries the disadvantage of simultaneously increasing tab hinge moment.

Combined Chord Ratio

Next, the combined chords are examined as a parameter, where the tab is kept at a constant 38% of the total. In this case, increasing the combined chord from 25% to 50% of the airfoil can reduce the required tab control angle, both in collective and cyclics (Fig. 3.35a); however, the major effect is on tab hinge moment, as seen in Fig. 3.35b, where the hpp value of the moment increases from 3 ft-lb to 25 ft-

lb. Similar to the tab chord, these trends indicate that increasing combined chord size reduces tab angles but the benefit is more than offset by the increase in hinge moment.

Flap Overhang

The hinge moment can be significantly reduced by using overhang on either the flap, or tab, or both. First, increasing the flap overhang causes the tab hpp angles to double (from 2.5° to 5°) as the flap hinge moves from $0.0c_f$ to $0.50c_f$ (Fig. 3.36a), although the absolute magnitude of the control angles remains moderate. However, the hpp value of the tab hinge moment is reduced by 60%, from 22 ft-lb to 9 ft-lb as the hinge moves aft from the leading edge, thus offsetting the small increase in control angle (Fig. 3.36b).

Tab Overhang

The tab overhang acts similarly: in Fig. 3.37a, the tab control angles increase only slightly as the tab hinge varies from $0.0c_t$ to $0.50c_t$, but in Fig. 3.37b the tab hinge moment is strongly affected by the location of the tab hinge.

Improved Flap and Tab Configuration

The preceding results are used to select a flap-tab configuration that minimizes both tab control angles and hinge moment for coupled trim at μ=0.368. The flap chord is reduced to 0.22c from 0.25c, and the tab chord is reduced from 0.15c to

0.13c. The index angle is increased by 3° to 18°, the flap overhang is set to $0.30c_f$, and the tab overhang to $0.33c_t$. Across a range of forward flight speeds, the tab hpp angle now remains between 5° to 6° (Fig. 3.38a). The hpp tab hinge moment decreases from 5 ft-lb at μ=0.368 to 3ft-lb at μ=0.1 (Fig. 3.38b). The improved configuration is summarized in Table 3.8.

Parameter	Value
Flap Chord, c_f	0.22c
Tab Chord, c_t	0.13c
Flap Span	0.39R
Tab Span	0.39R
Index Angle	18°
Flap Overhang	$0.3c_f$
Tab Overhang	$0.33c_t$
Flap Midspan Position	0.75R
Torsional Frequency	2.0/rev
Aileron Frequency	3.7/rev

Table 3.8: Final Trailing Edge Flap and Tab Configuration of UH-60 type Rotor

3.6   Concluding Remarks

Swashplateless rotors controlled with trailing edge flaps or tab actuated trailing edge flaps were designed using parameter studies to identify key design variables.

Then the rotors were trimmed across the range of forward flight speed and designs were configured to simultaneously minimize both control angles and hinge moments. Both a new, conceptual rotor and an existing, production rotor were fitted with tab actuated trailing edge flaps. For comparison, the existing, production rotor also was fitted with trailing flaps only. The uncoupled blade response of the UH-60A type rotor to tab or flap deflection was examined with varying torsional stiffness at the blade root and with varying stiffness at the flap hinge. Finally, the two different control schemes are compared.

3.6.1   Swashplateless Rotors with Tab Actuated Trailing Edge Flap

The isolated rotors are trimmed to a prescribed thrust and zero hub moments, with shaft angles fixed. The quasi-steady thin airfoil aerodynamic model is used for both blade and flap sections. Inflow is distributed uniformly for the Kaman-type conceptual rotor analyzed with the linear, rigid blade model. A free wake model with a single tip vortex calculates the inflow distribution for the swashplateless rotor derived from the UH-60A, when a trim solution is calculated.

The Kaman-type conceptual rotor has blades with rectangular planform and moderate linear twist. It has a nominal thrust level of $c_T/\sigma = 0.062$, and has not been designed in detail for any specific mission. The result of a parametric design study was that the swashplateless rotor could be trimmed across the range of forward flight speed from $\mu = 0.15$ to 0.35 with tab collective angles between $7°$ to $9°$ and tab half peak-to-peak angles below $9°$. The corresponding hinge moments

in forward flight remain below 2.0 ft-lb mean, and 1.5 ft-lb half peak-to-peak. The index angle is 15°, and the flap and tab are located at the blade 0.75 radius. The flap chord is 0.29c and the tab chord is 0.06c, for a total combined chord of 0.35c. The flap hinge is located at $0.10c_f$ and the tab hinge is at $0.10c_t$. The very low hinge moments can be attributed in part to the aerodynamic balance given to both the flap and the tab.

The UH-60A rotor has significant nonlinear twist and a swept tip; at $\mu = 0.368$, the thrust level is $c_T/\sigma = 0.083$. The complex rotor was designed to achieve demanding military missions. The swashplateless variant differs from the conventional rotor by the addition of trailing edge flap and tabs and the reduction of the torsional frequency from 4.3/rev to 2.0/rev by softening the pitch spring at the blade root. The swashplateless rotor resulting from the parametric study could be trimmed across the range of forward flight speed from hover to $\mu = 0.368$. From high speed down to transition speed at $\mu = 0.10$, the tab collective angle is between $-4.5°$ to $-6.0°$, and the tab half peak-to-peak angles remain below 6.2°. In the same speed range, the mean tab hinge moment is between 2.5 ft-lb to 6.5 ft-lb, while the half peak-to-peak hinge moment is between 3.5 ft-lb to 5.0 ft-lb. The flap chord is 0.22c and the tab chord is 0.13c, for a total combined chord of 0.35c. The blade pitch index angle of 18°, the flap overhang of $0.3c_f$ and the tab overhang of $0.33c_t$ were all significant design features that minimized both tab control angles and hinge moment.

Examination of the uncoupled blade response of the UH-60A swashplateless rotor showed that the deflection of the trailing edge tab causes change in both blade lift and blade twist response. Positive tab deflection leads to positive lift increment

along the tab span, negative lift increment along the flap span, and blade nose-up pitch. The torsional stiffness of the blade determines the contribution of the lift and moment modes to the total blade response. Both blade pitch and thrust responses are governed by blade torsional stiffness. The stiffness of the flap hinge spring also affects blade pitch, trailing edge flap and thrust responses. Depending on the spring stiffness at the blade root and at the flap hinge, positive tab deflection may result in either an increase or decrease of the thrust.

3.6.2 Swashplateless Rotor with Trailing Edge Flap Only

The comprehensive analysis used to examine the swashplateless rotor with trailing edge flap is identical to that used in the previous design studies. In this case, the UH-60A rotor is fitted with a trailing edge flap, and the torsional stiffness is reduced to 2.0/rev by softening the root pitch spring. When controlled by a trailing edge flap, the swashplateless rotor can be trimmed across the range of forward flight speed with a flap collective between 6.5° to 10.5°, and flap half peak-to-peak angles ranging from 7.5° to 13.5°. The corresponding hinge moment from $\mu = 0.10$ to 0.368 has a mean less than 1 ft-lb, and half peak-to-peak value less than 3.0 ft-lb. Compared to the same rotor with both flaps and tabs, the flap only swashplateless design has a higher index angle at 20°, and similar flap overhang of $0.33c_f$. The flap chord at 0.15c is much smaller than the flap-tab combination at 0.35c.

In this case, the uncoupled blade response showed that positive flap deflection leads to a positive lift increment along the flap span and blade nose-down pitch.

The stiffness of the blade root pitch spring controls the blade twist response to flap deflection. Positive flap deflection always results in a decrease of thrust, across the range of torsional frequency from 1.5/rev to 4.3/rev.

The key conclusions of the design study are summarized here:

1. A swashplateless derivative of a modern heavy utility (UH-60A) rotor can be trimmed across the range of forward flight speed with tab-actuated trailing edge flaps. Compared to controlling the rotor with trailing edge flaps only, at high speed ($\mu = 0.368$) with fixed shaft angles and zero hub moments, the required tab control angles are less than half the deflections required by a flap only system. The tab hinge moment is larger than the flap hinge moment of an equivalent system, but it still small in absolute magnitude. The low stroke and force required for the tab-actuated trailing edge flap concept make it a good candidate for on-blade smart actuators.

2. The effectiveness of the trailing edge flap in inducing blade twist response is enhanced by a low torsional frequency near 2.0/rev. The tab actuated flap requires a combination of low torsional frequency near 2.0/rev and low aileron frequency near 2.0/rev to effectively induce blade twist. As spring stiffness at the blade root and flap hinge is reduced, the moment contribution outweighs the lift contribution of the trailing edge deflection.

3. Index angle improves the feasibility of swashplateless rotors with trailing edge controls. The pre-collective acts to reduce the blade travel required to achieve trim, and thus reduces the deflections required from the trailing edge control.

4. Aerodynamic balance reduces required hinge moment for trailing edge controls. The parameter studies suggest flap overhang of $0.30c_f$ and similar tab overhang of $0.30c_t$ are beneficial. However, the hinge moment reduction resulting from aerodynamic balance is offset by a slight increase in required control angles, an increase in airfoil profile drag, and a decrease in airfoil lift and pitching moment. These competing effects must be carefully considered in final design.

5. The combined chord of the flap and the tab has a significant effect on the tab hinge moment required to trim. The increase in tab hinge moment that results with an increase in the combined chord is much larger than the corresponding decrease in tab deflection. Similarly, when the combined chord is held constant, increasing the tab chord results in a slight decrease of control angle, but a large increase in tab hinge moment.

6. Increasing the length of the trailing edge control increases its effectiveness, so the required control angles are reduced. The effect on hinge moment can vary with other parameters however, and must be examined before length is chosen.
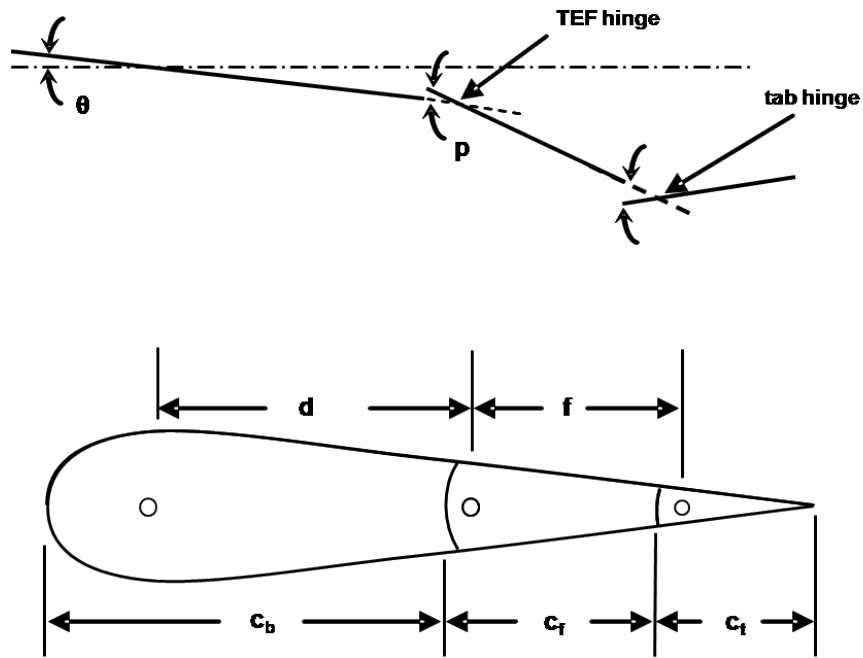
Figure 3.1: Schematic of Airfoil with Flap and Tab, Showing Hinges, Deflections and Geometry
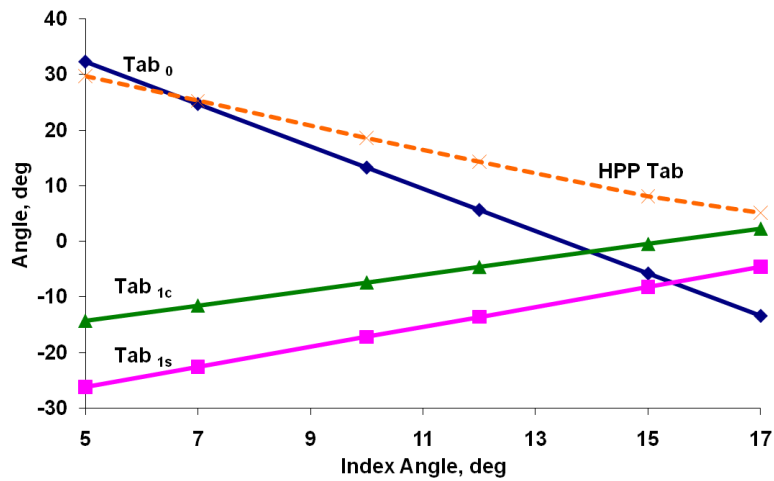
Figure 3.2: Effect of Index Angle on Tab Control Angles for Kaman-type Rotor, $\mu = 0.35$, $C_T/\sigma = 0.062$, Rigid Blades
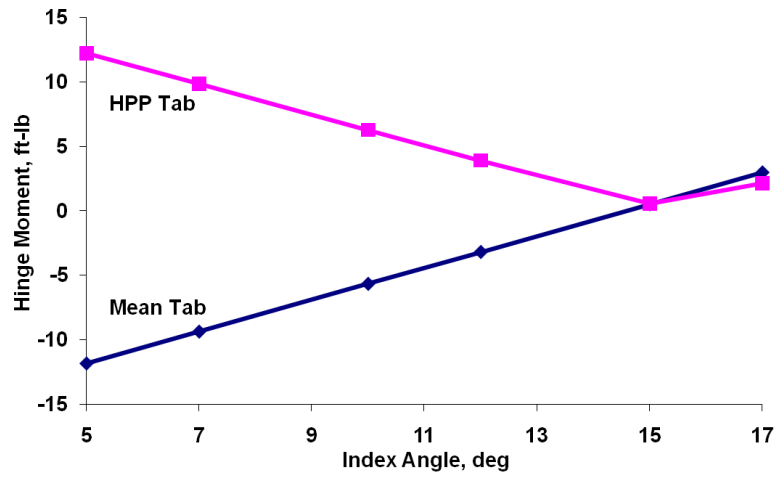
Figure 3.3: Effect of Index Angle on Tab Hinge Moments for Kaman-type Rotor, $\mu = 0.35$, $C_T/\sigma = 0.062$, Rigid Blades
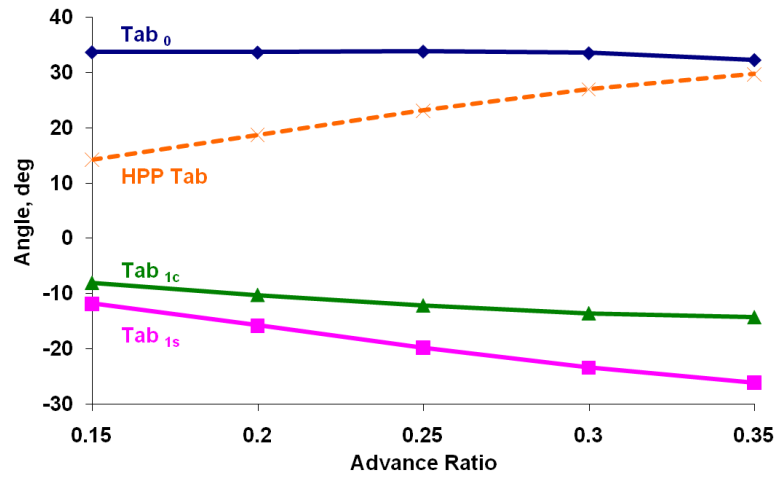
Figure 3.4: Effect of Advance Ratio on Tab Control Angles for Kaman-type Rotor, $\theta_{idx} = 5°$, $C_T/\sigma = 0.062$, Rigid Blades
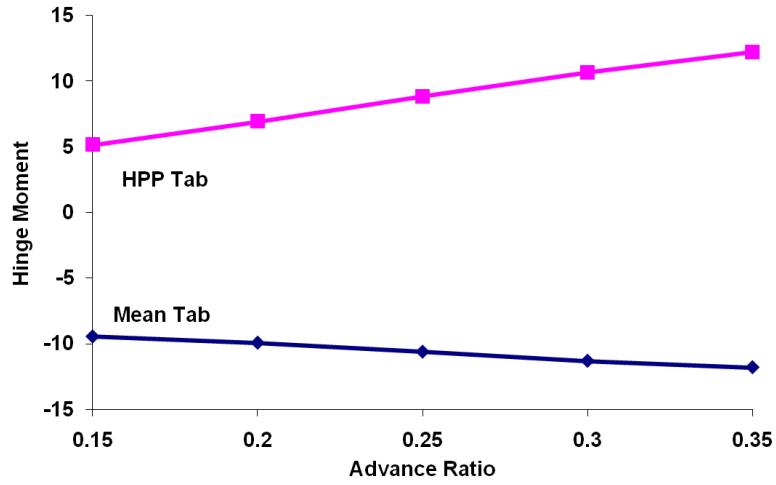
Figure 3.5: Effect of Advance Ratio on Tab Hinge Moments for Kaman-type Rotor, $\theta_{idx} = 5°$, $C_T/\sigma = 0.062$, Rigid Blades
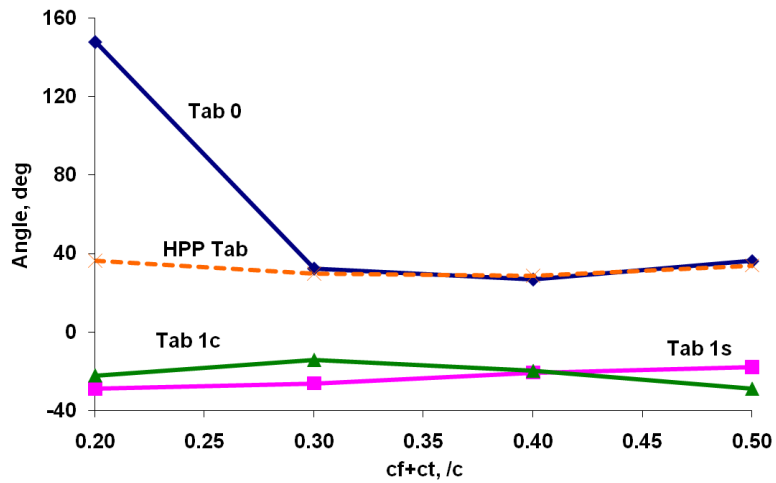
Figure 3.6: Effect of Combined Chord on Tab Control Angles for Kaman-type Rotor, $\mu = 0.35$, $\theta_{idx} = 5°$, $C_T/\sigma = 0.062$, Rigid Blades
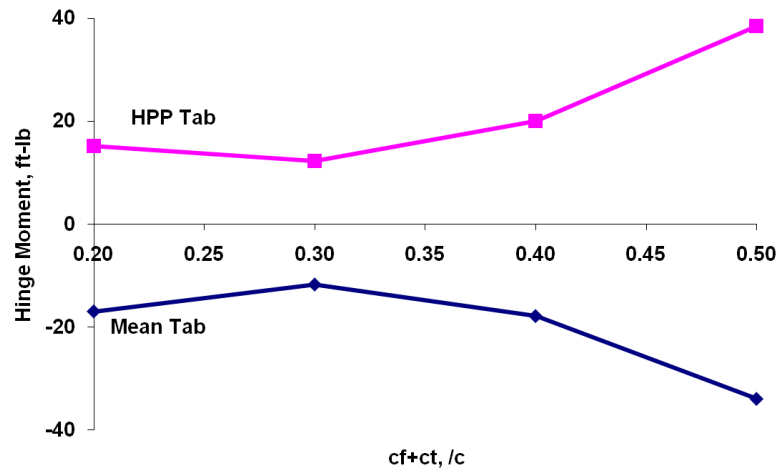
Figure 3.7: Effect of Combined Chord on Tab Hinge Moments for Kaman-type Rotor, $\mu = 0.35$, $\theta_{idx} = 5°$, $C_T/\sigma = 0.062$, Rigid Blades
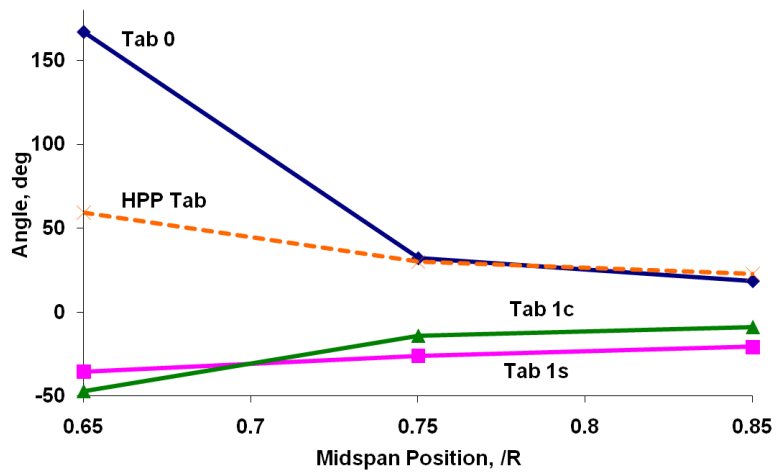
Figure 3.8: Effect of Radial Position on Tab Control Angles for Kaman-type Rotor, $\mu = 0.35$, $\theta_{idx} = 5°$, $C_T/\sigma = 0.062$, Rigid Blades
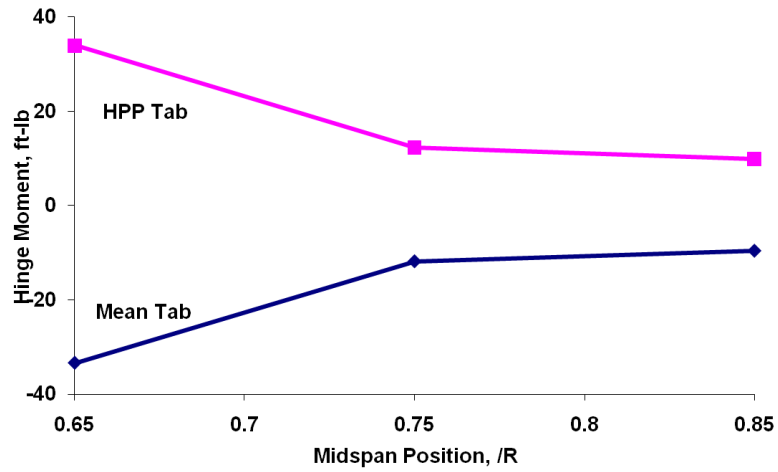
Figure 3.9: Effect of Radial Position on Tab Hinge Moments for Kaman-type Rotor, $\mu = 0.35$, $\theta_{idx} = 5°$, $C_T/\sigma = 0.062$, Rigid Blades
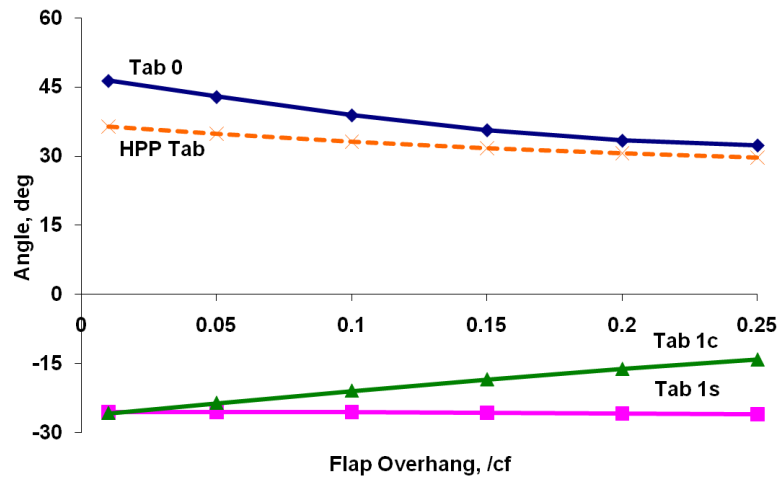
Figure 3.10: Effect of Flap Overhang on Tab Control Angles for Kaman-type Rotor, $\mu = 0.35$, $\theta_{idx} = 5°$, $C_T/\sigma = 0.062$, Rigid Blades

159
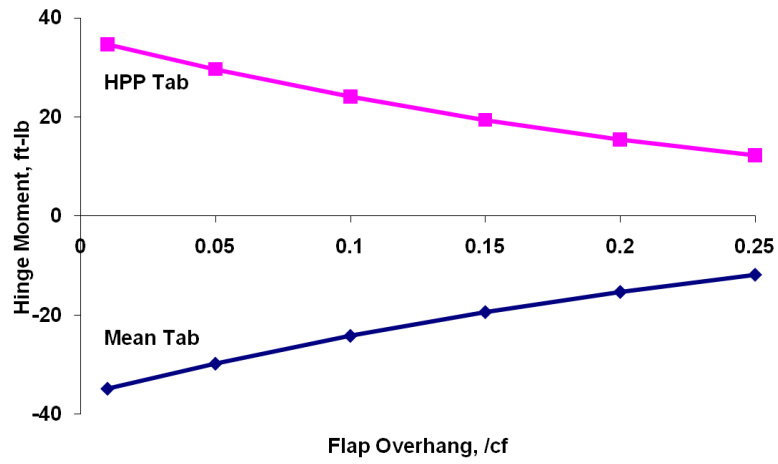
Figure 3.11: Effect of Flap Overhang on Tab Hinge Moments for Kaman-type Rotor, $\mu = 0.35$, $\theta_{idx} = 5°$, $C_T/\sigma = 0.062$, Rigid Blades
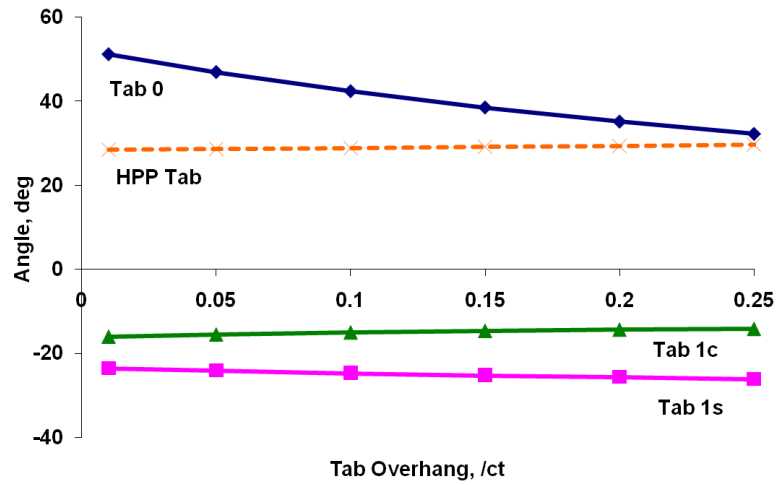
Figure 3.12: Effect of Tab Overhang on Tab Control Angles for Kaman-type Rotor, $\mu = 0.35$, $\theta_{idx} = 5°$, $C_T/\sigma = 0.062$, Rigid Blades
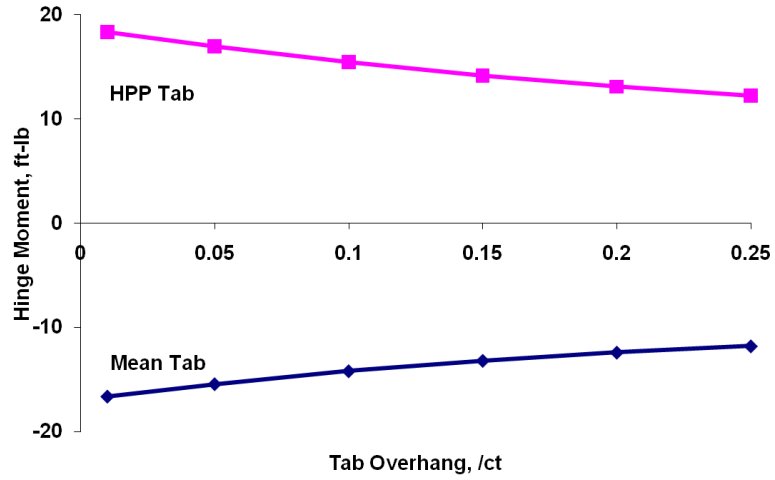
Figure 3.13: Effect of Tab Overhang on Tab Hinge Moments for Kaman-type Rotor, $\mu = 0.35$, $\theta_{idx} = 5°$, $C_T/\sigma = 0.062$, Rigid Blades
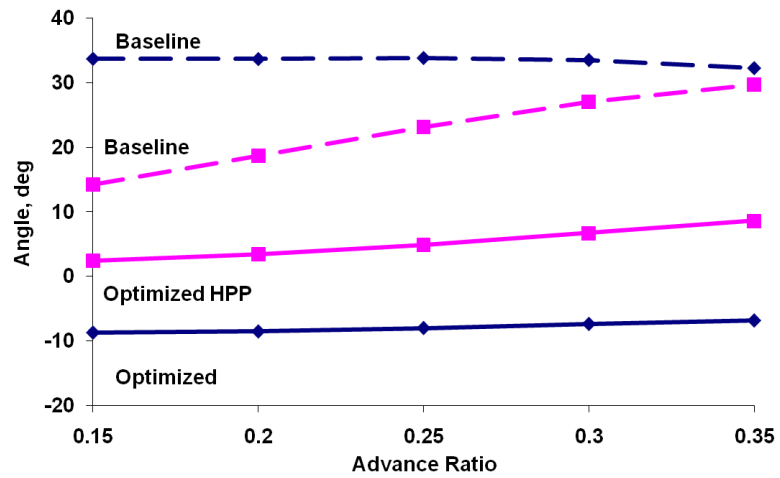
Figure 3.14: Comparison of Baseline and Improved Tab Control Angles for Kaman-type Rotor, $C_T/\sigma = 0.062$, Rigid Blades
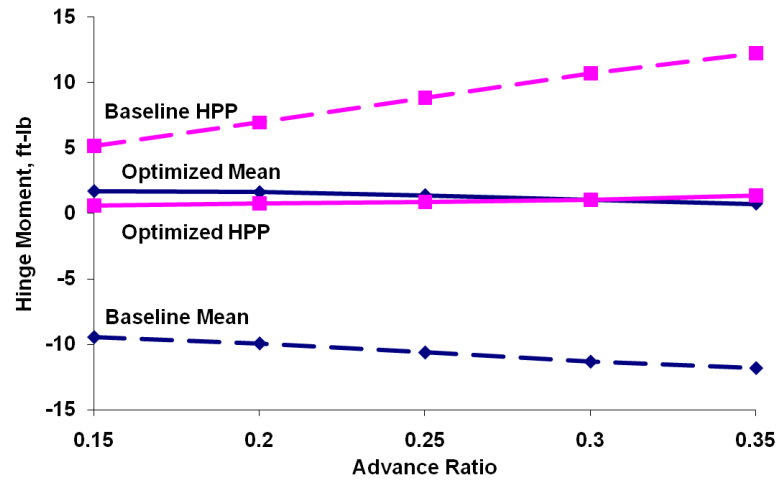
Figure 3.15: Comparison of Baseline and Improved Tab Hinge Moments for Kaman-type Rotor, $C_T/\sigma = 0.062$, Rigid Blades
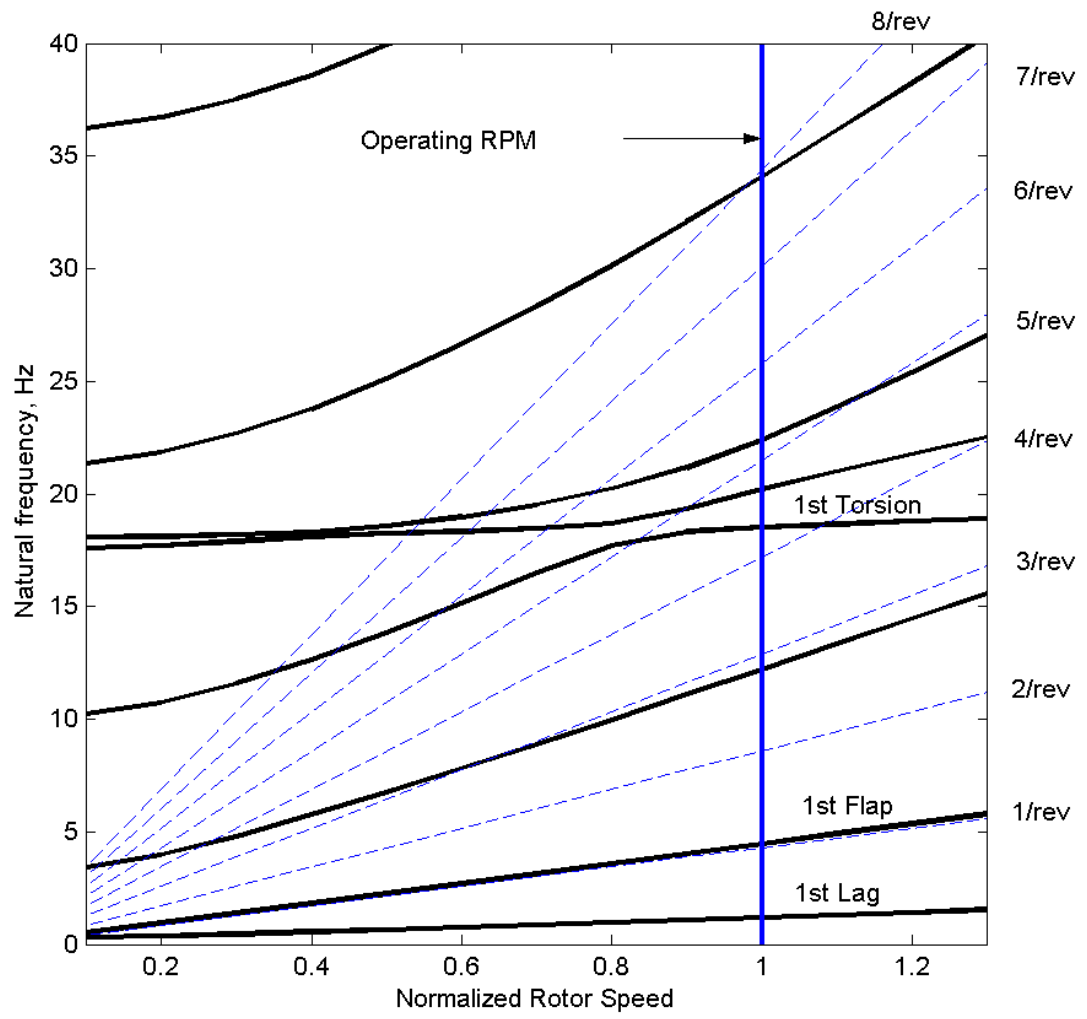
Figure 3.16: Fan Plot of UH-60A Baseline Rotor Model
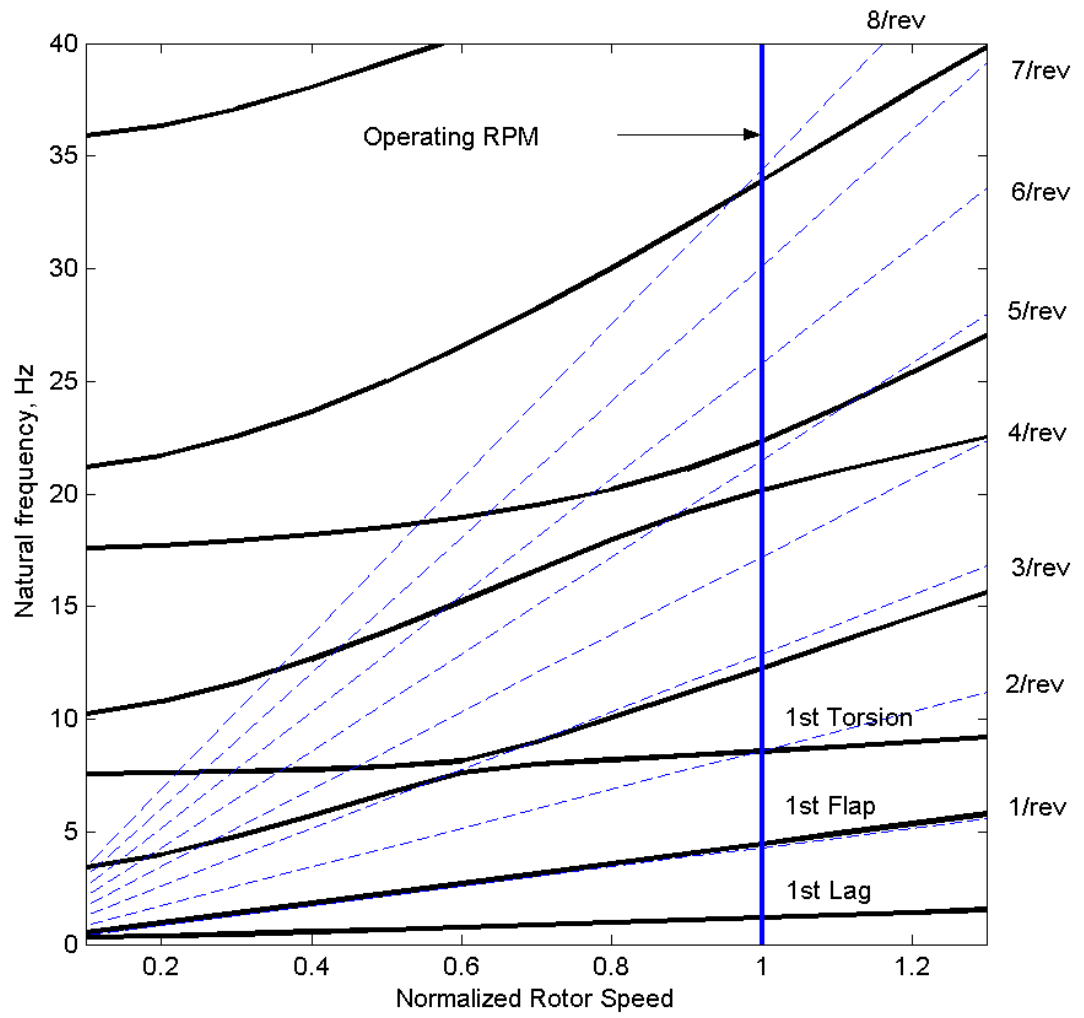
Figure 3.17: Fan Plot of Swashplateless Rotor Model
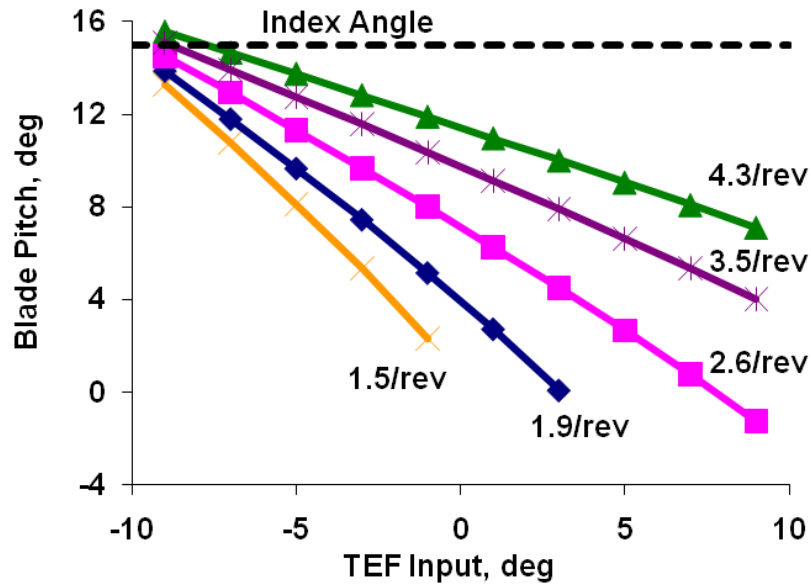
(a) Pitch Response
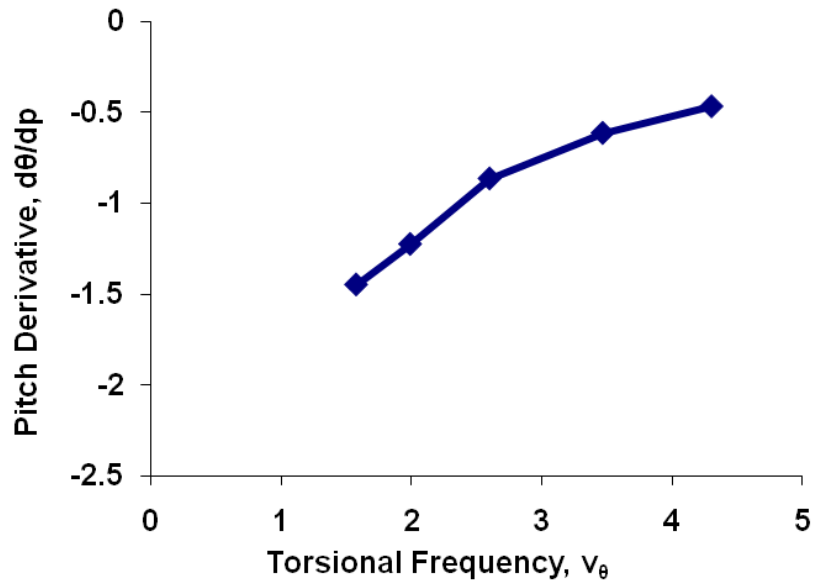
(b) Pitch Derivative

Figure 3.18: Uncoupled Blade Pitch Response to TEF Input for Varying Torsional Frequency, UH-60A type Rotor $\mu = 0.0$, $\theta_{idx} = 15°$
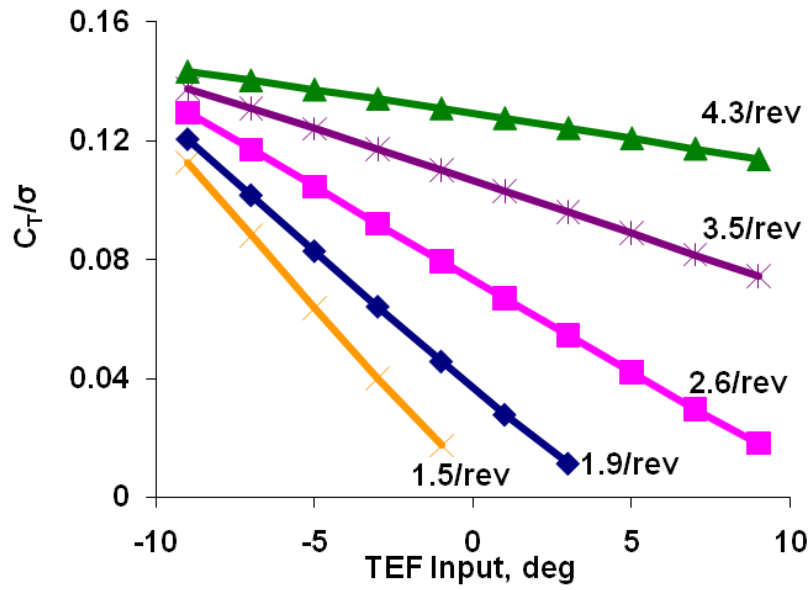
(a) Thrust Response
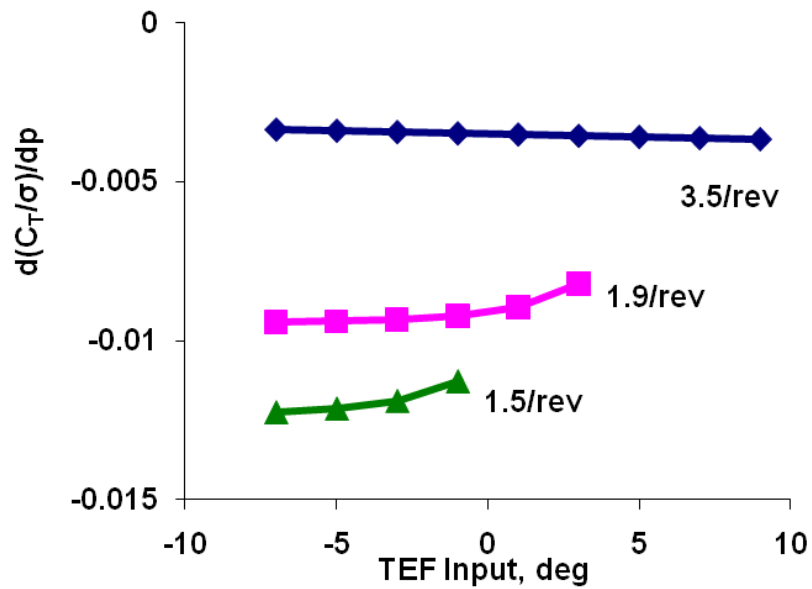
(b) Thrust Derivative

Figure 3.19: Uncoupled Blade Loading Response to TEF Input for Varying Torsional

Frequency, UH-60A type Rotor $\mu = 0.0$, $\theta_{idx} = 15°$
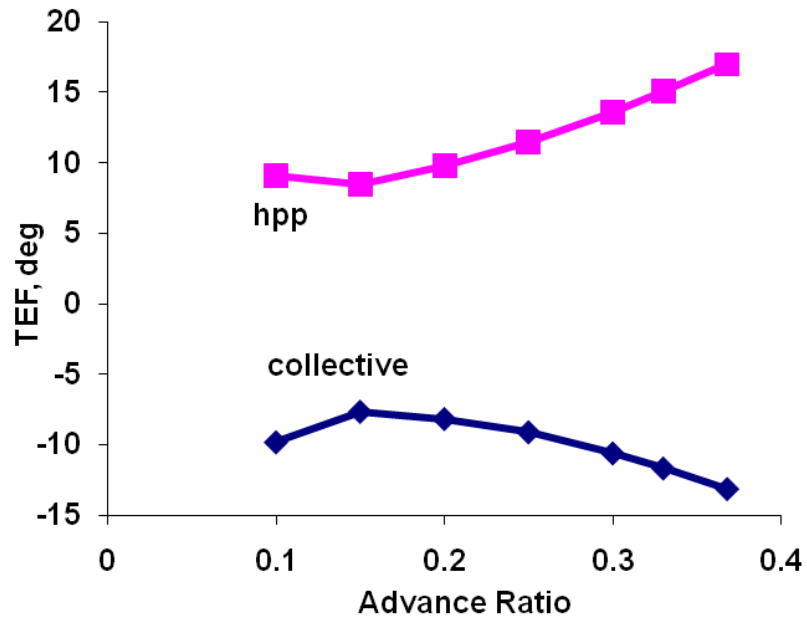
(a) Flap Control Angles
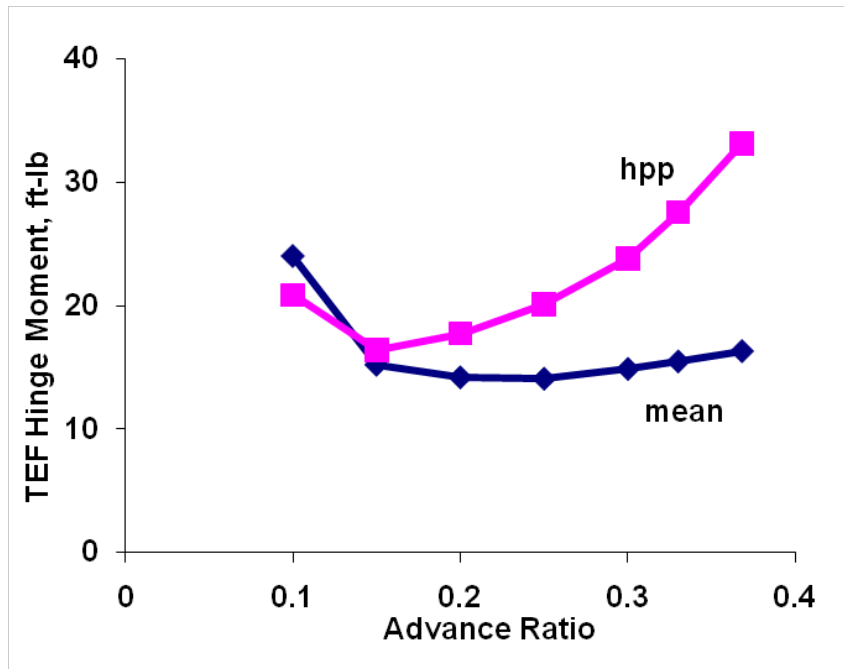
(b) Flap Hinge Moment

Figure 3.20: Effect of Advance Ratio on Flap Control Angles and Hinge Moment, UH-60A Type Rotor, $\theta_{idx} = 15°$, $C_T/\sigma = 0.084$
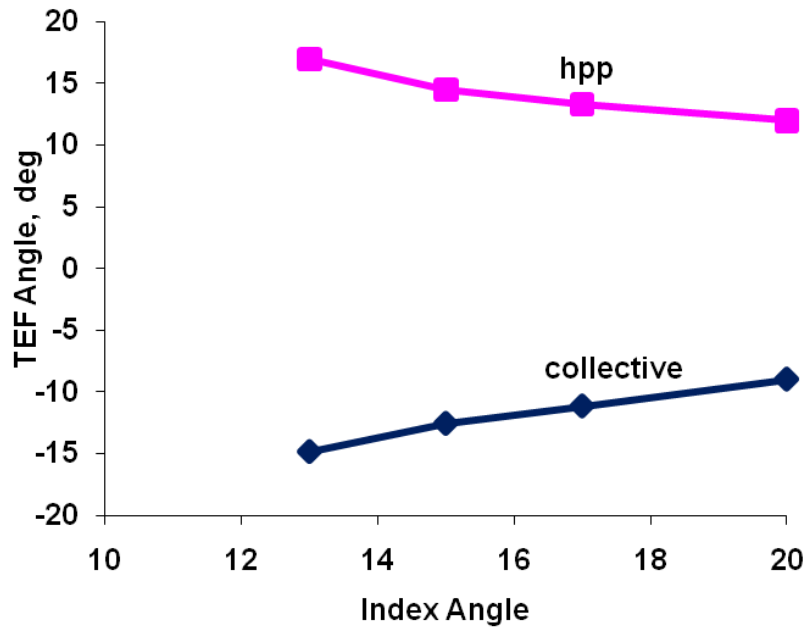
(a) Flap Control Angles
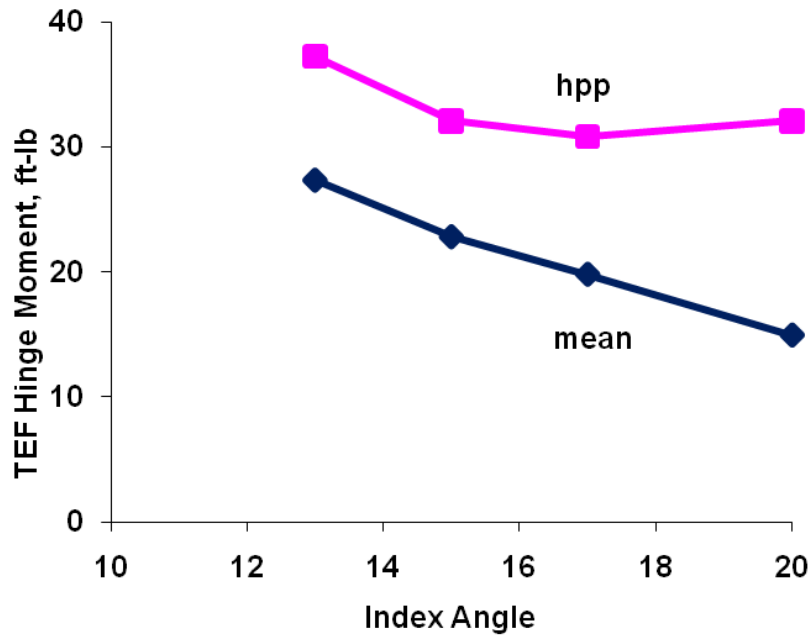
(b) Flap Hinge Moment

Figure 3.21: Effect of Index Angle on Flap Control Angles and Hinge Moment, UH-60A Type Rotor, $overhang = 0.0c_f$, $\mu = 0.368$, $C_T/\sigma = 0.084$
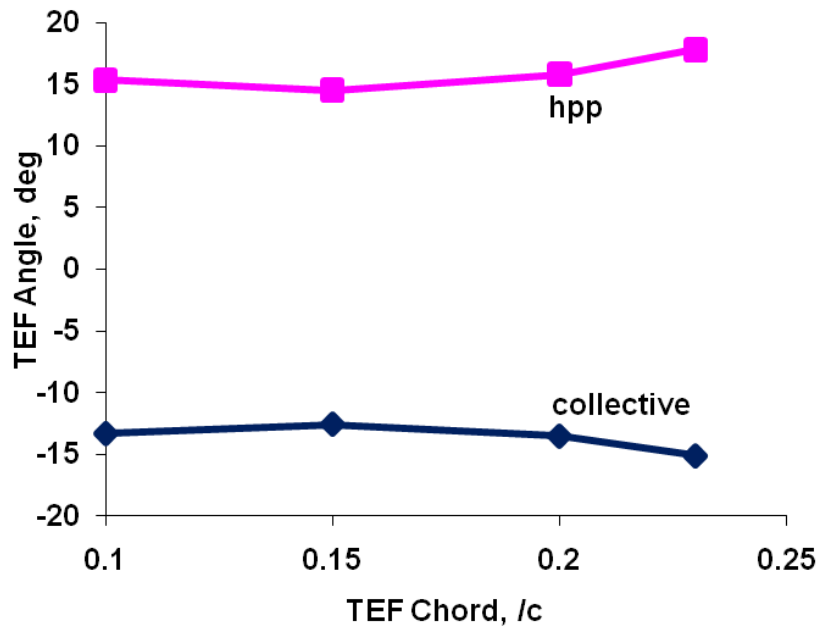
(a) Flap Control Angles
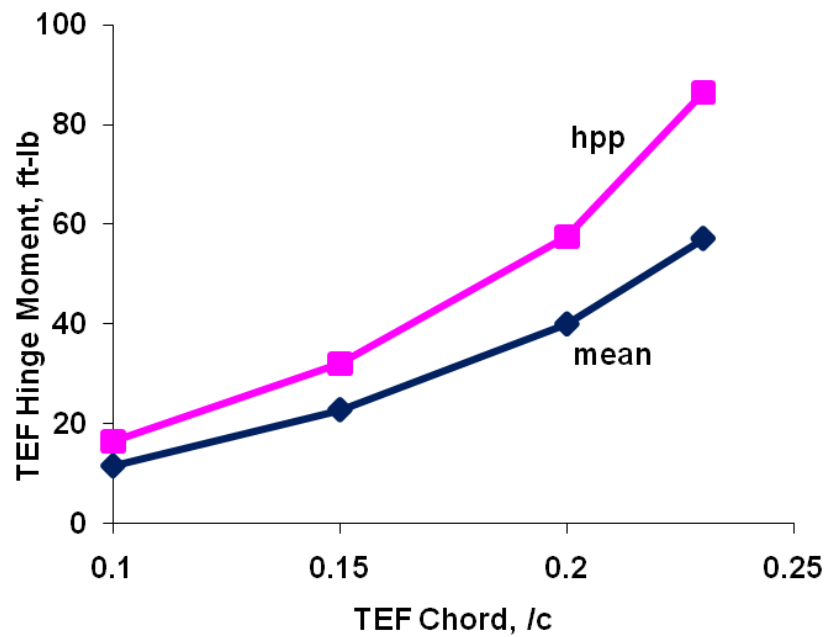
(b) Flap Hinge Moment

Figure 3.22: Effect of Flap Chord on Flap Control Angles and Hinge Moment, UH-60A Type Rotor, $\theta_{idx} = 15°$, $overhang = 0.0c_f$, $\mu = 0.368$, $C_T/\sigma = 0.084$
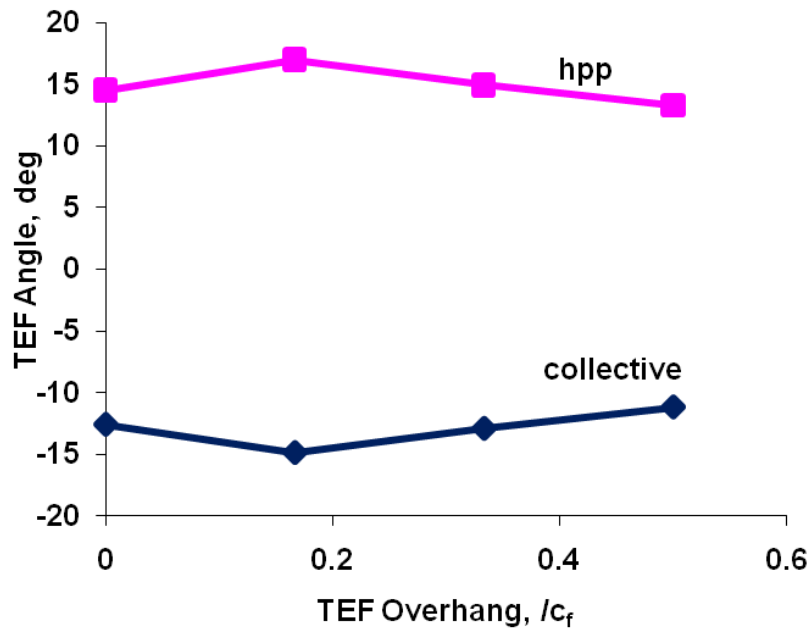
(a) Flap Control Angles
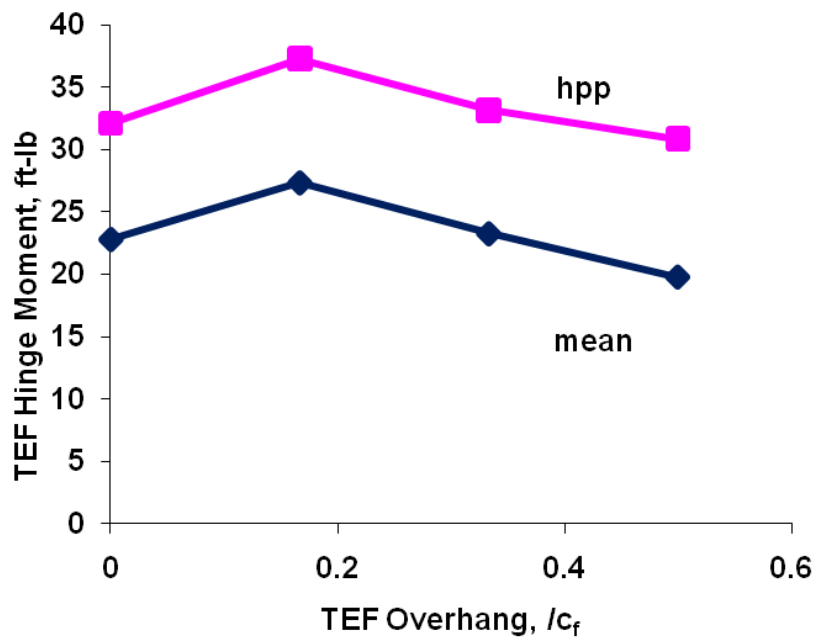
(b) Flap Hinge Moment

Figure 3.23: Effect of Flap Overhang on Flap Control Angles and Hinge Moment, UH-60A Type Rotor, $\theta_{idx} = 15°$, $\mu = 0.368$, $C_T/\sigma = 0.084$
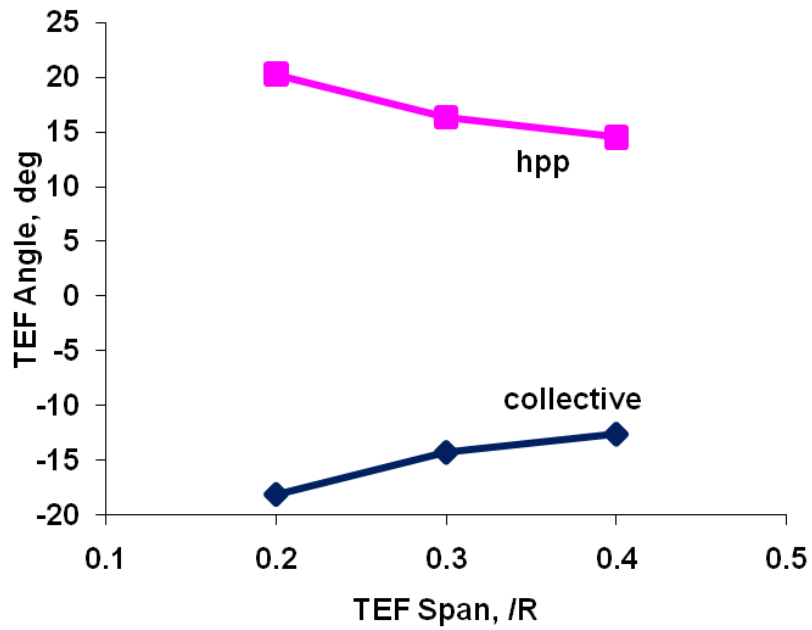
(a) Flap Control Angles
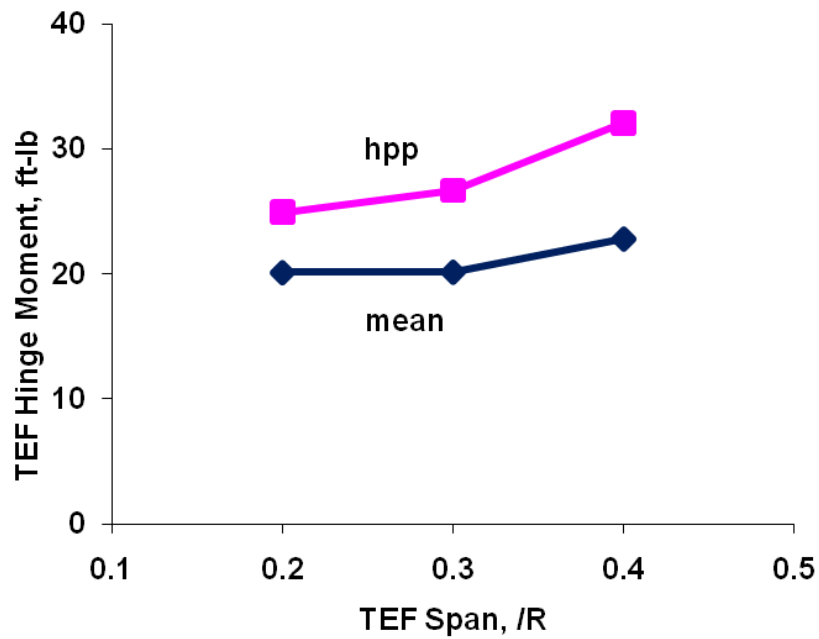
(b) Flap Hinge Moment

Figure 3.24: Effect of Flap Span on Flap Control Angles and Hinge Moment, UH-60A Type Rotor, $\theta_{idx} = 15°$, $overhang = 0.0c_f$, $\mu = 0.368$, $C_T/\sigma = 0.084$

171
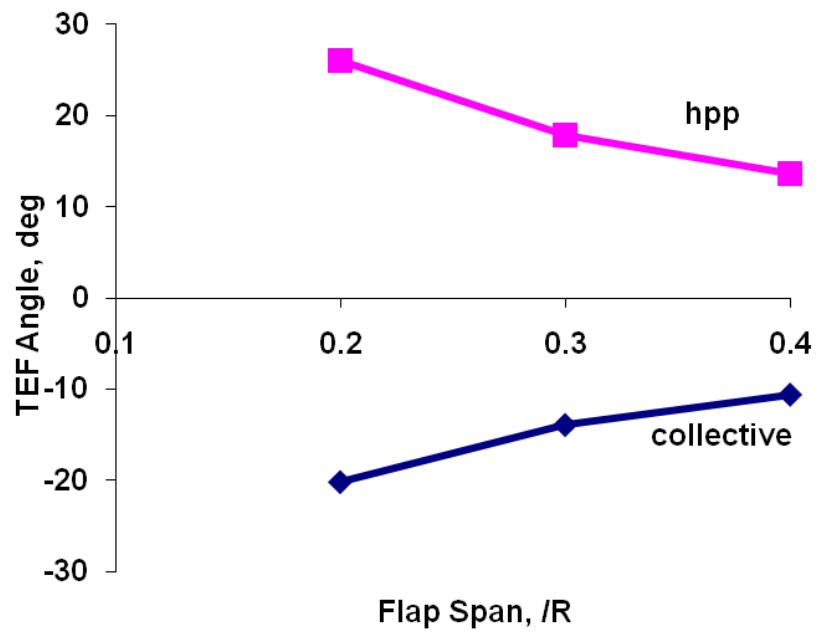
(a) Flap Control Angles
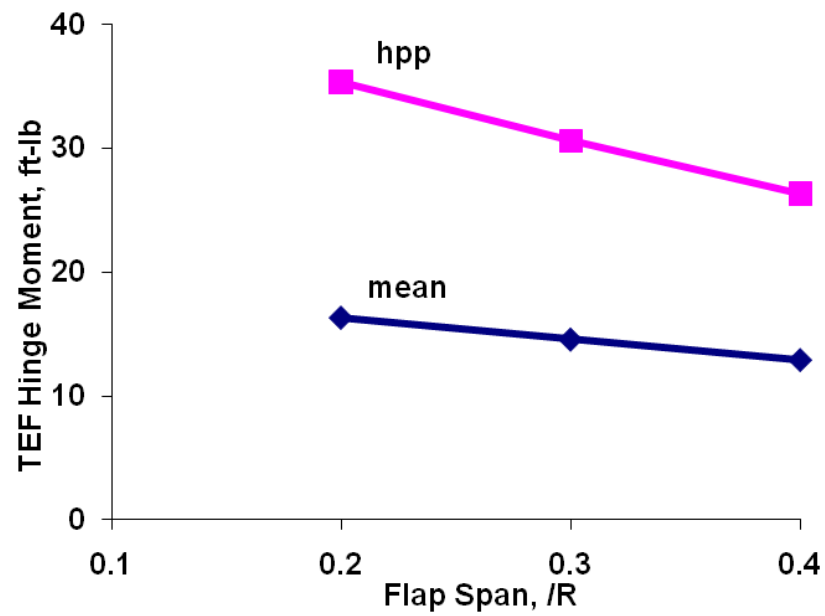
(b) Flap Hinge Moment

Figure 3.25: Effect of Flap Span on Flap Control Angles and Hinge Moment, UH-60A Type Rotor, $\theta_{idx} = 20°$, $overhang = 0.0c_f$, $\mu = 0.368$, $C_T/\sigma = 0.084$
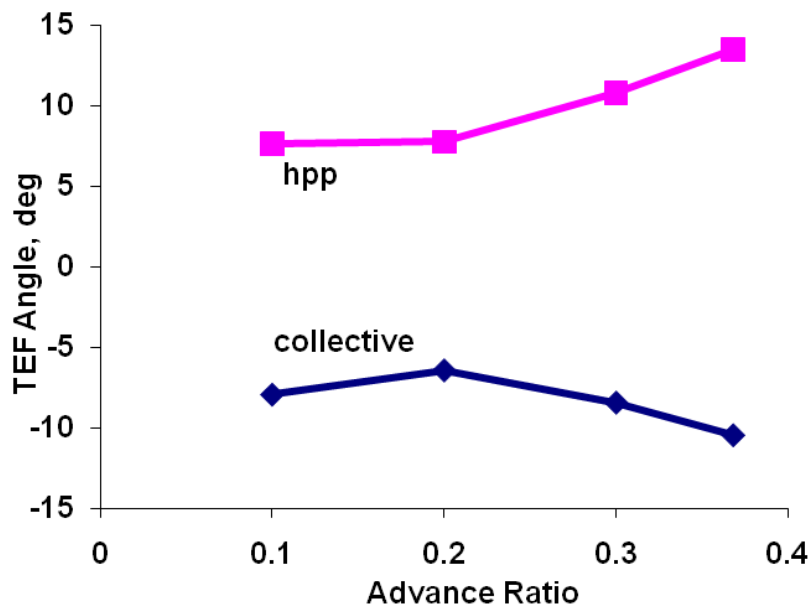
(a) Flap Control Angles
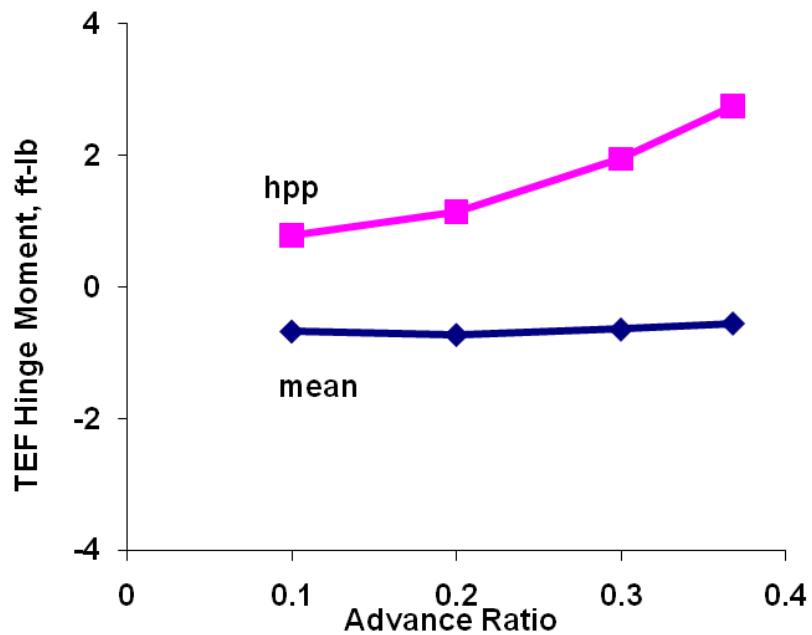
(b) Flap Hinge Moment

Figure 3.26: Effect of Advance Ratio on Improved Flap Configuration, UH-60A

Type Rotor, $\theta_{idx} = 20°$, $ovh = 0.33c_f$, $C_T/\sigma = 0.084$
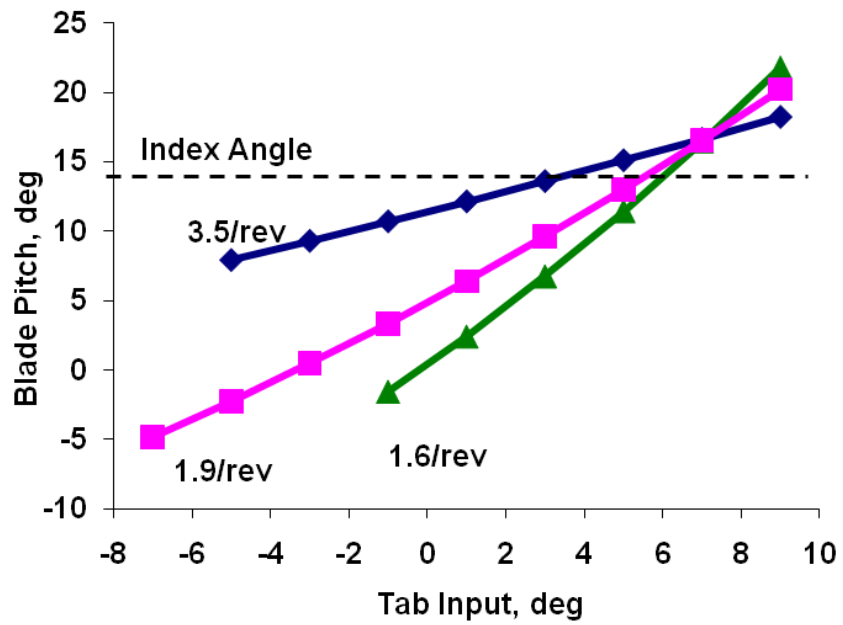
(a) Pitch Response
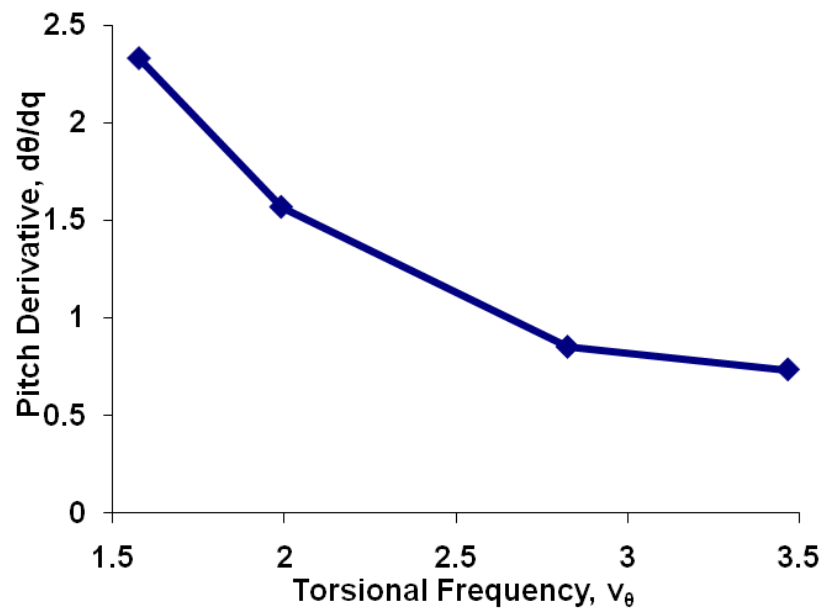
(b) Pitch Derivative

Figure 3.27: Uncoupled Blade Pitch Response to Tab Input for Varying Torsional Frequency, UH-60A type Rotor $\mu = 0.0$, $\theta_{idx} = 15°$, Aileron Frequency $= 2.15$/rev
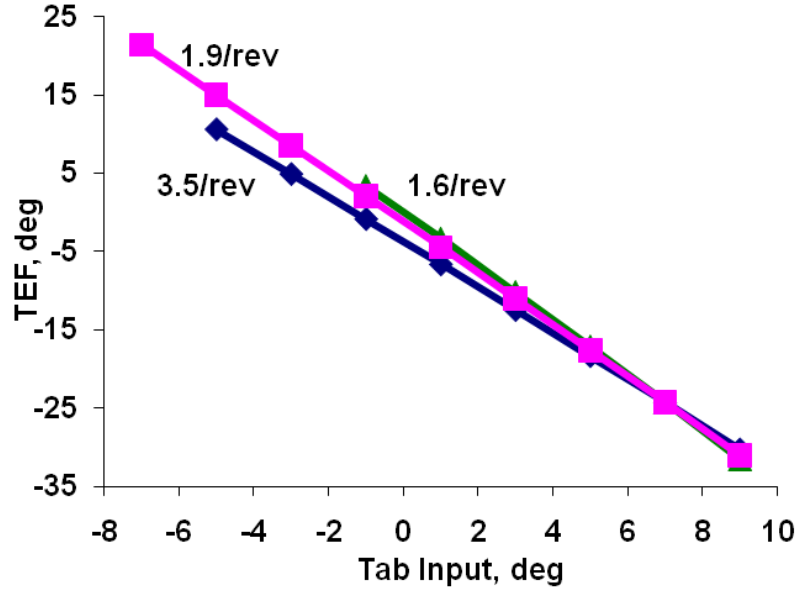
(a) TEF Response
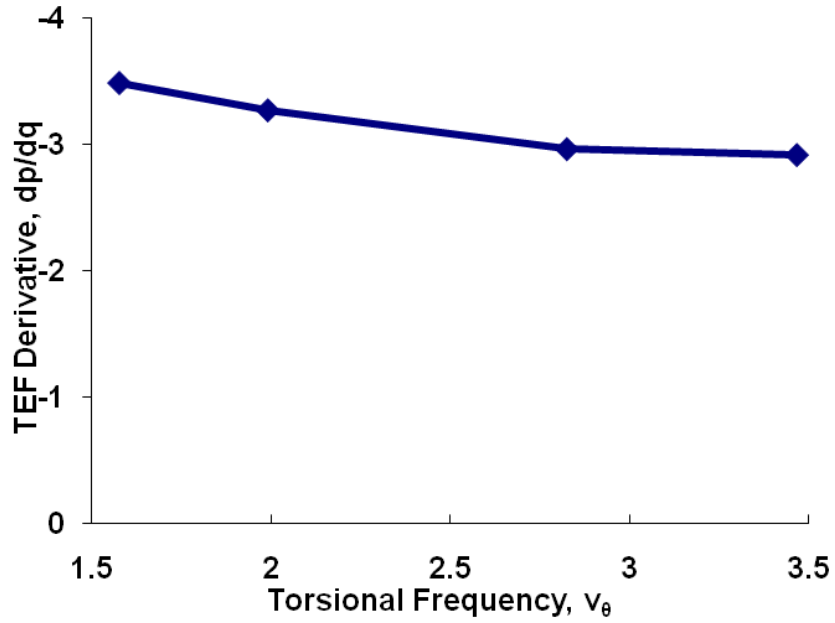
(b) TEF Derivative

Figure 3.28: Uncoupled TEF Response to Tab Input for Varying Torsional Frequency, UH-60A type Rotor $\mu = 0.0$, $\theta_{idx} = 15°$, Aileron Frequency = 2.15/rev
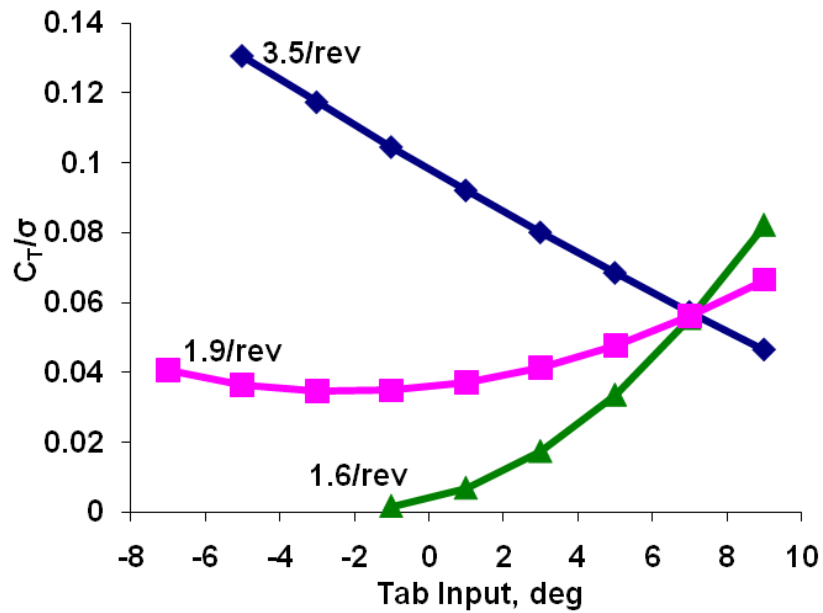
(a) Thrust Response
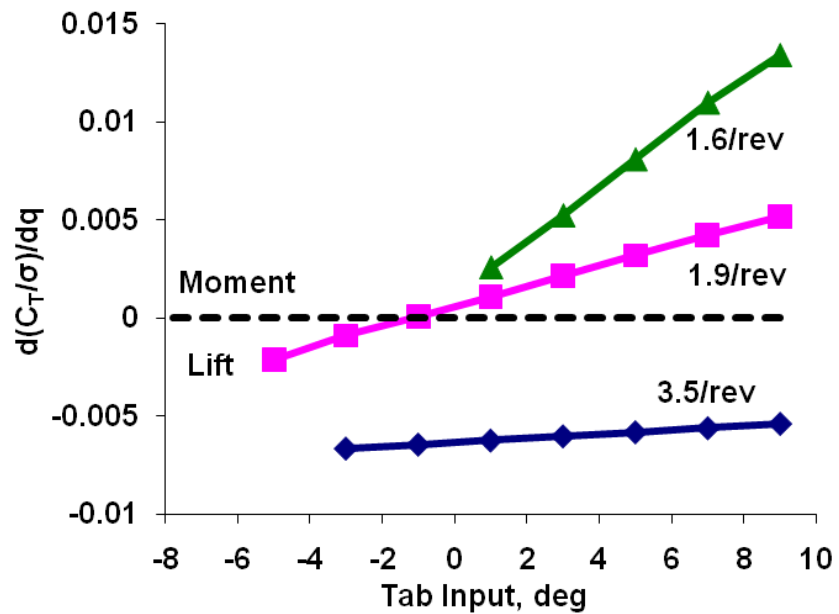
(b) Thrust Derivative

Figure 3.29: Uncoupled Blade Loading Response to Tab Input for Varying Torsional

Frequency, UH-60A type Rotor $\mu = 0.0$, $\theta_{idx} = 15°$, Aileron Frequency = 2.15/rev
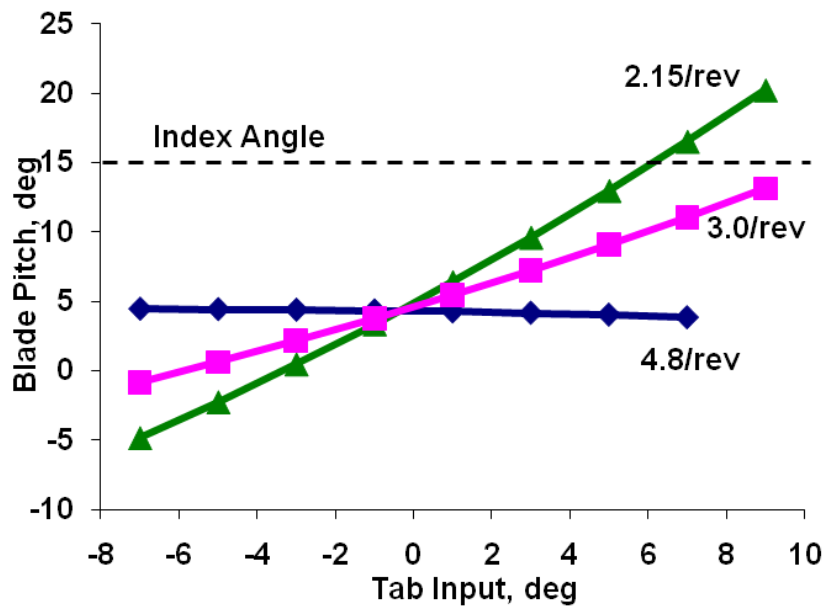
(a) Pitch Response
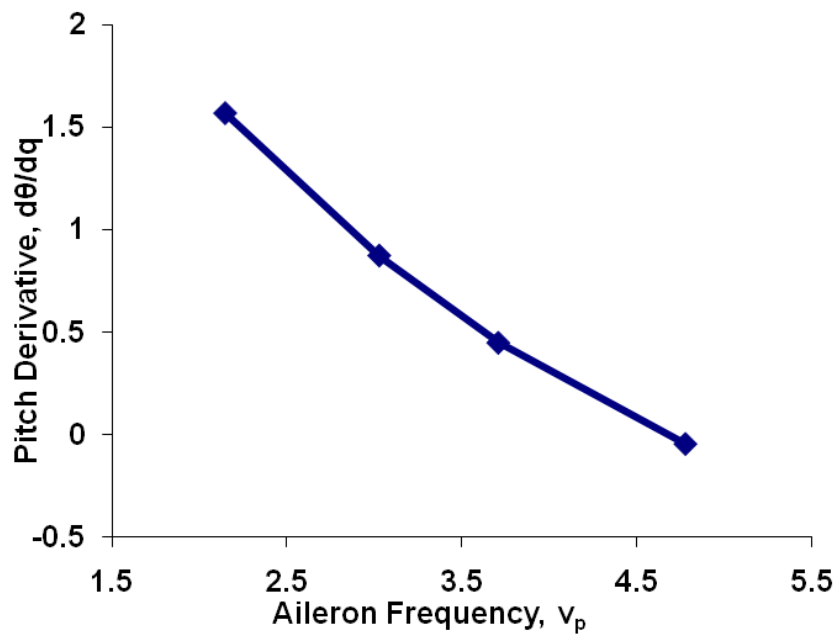
(b) Pitch Derivative

Figure 3.30: Uncoupled Blade Pitch Response to Tab Input for Varying Aileron Frequency, UH-60A type Rotor $\mu = 0.0$, $\theta_{idx} = 15°$, Torsional Frequency = 1.9/rev
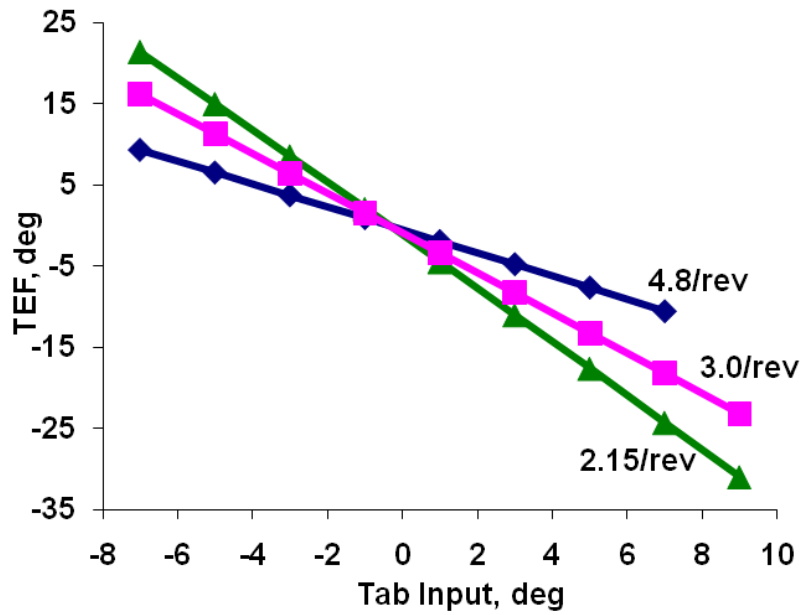
(a) TEF Response
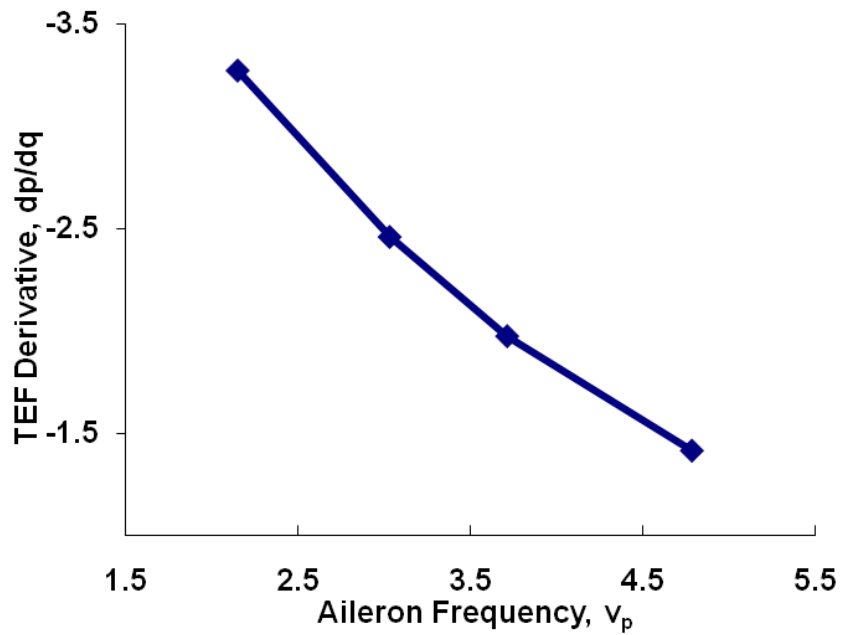
(b) TEF Derivative

Figure 3.31: Uncoupled TEF Response to Tab Input for Varying Aileron Frequency, UH-60A type Rotor $\mu = 0.0$, $\theta_{idx} = 15°$, Torsional Frequency = 1.9/rev
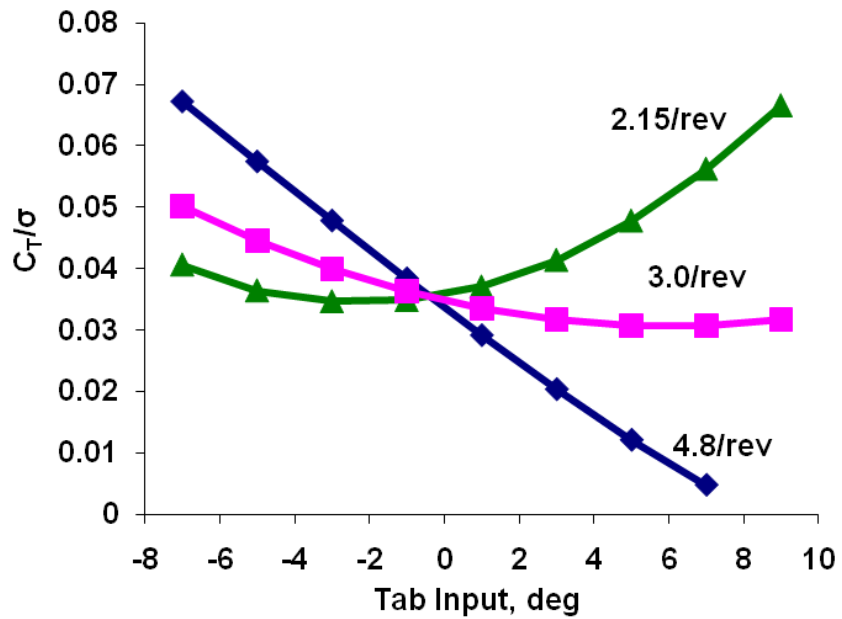
(a) Thrust Response
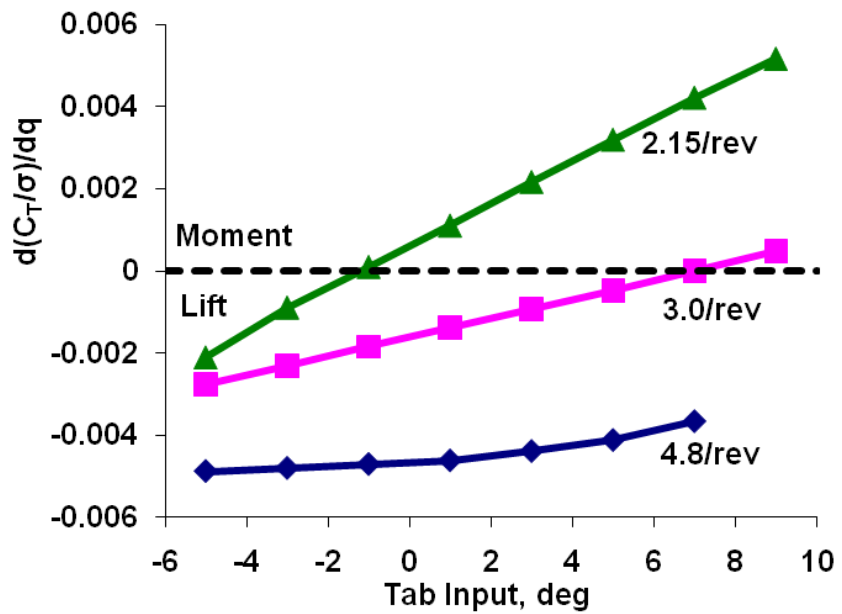
(b) Thrust Derivative

Figure 3.32: Uncoupled Blade Loading Response to Tab Input for Varying Aileron

Frequency, UH-60A type Rotor $\mu = 0.0$, $\theta_{idx} = 15°$, Torsional Frequency $= 1.9$/rev
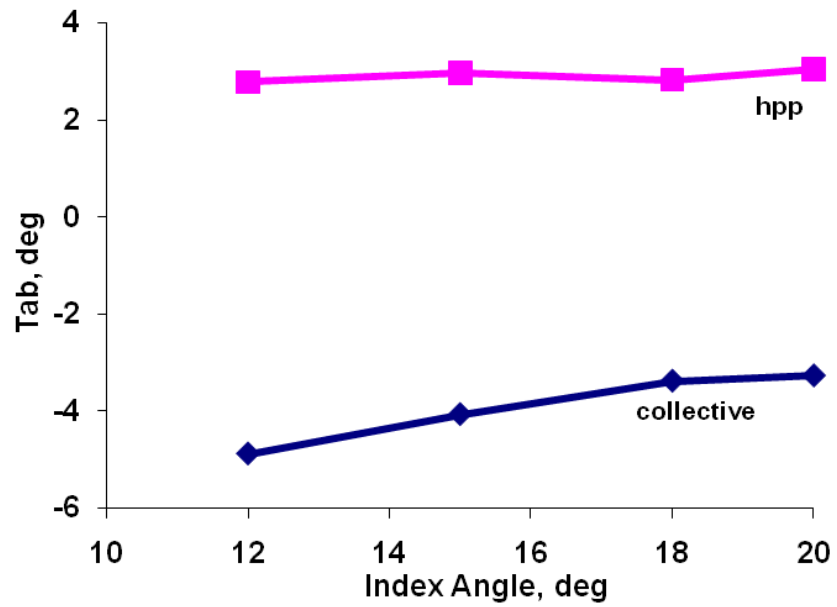
(a) Tab Control Angles
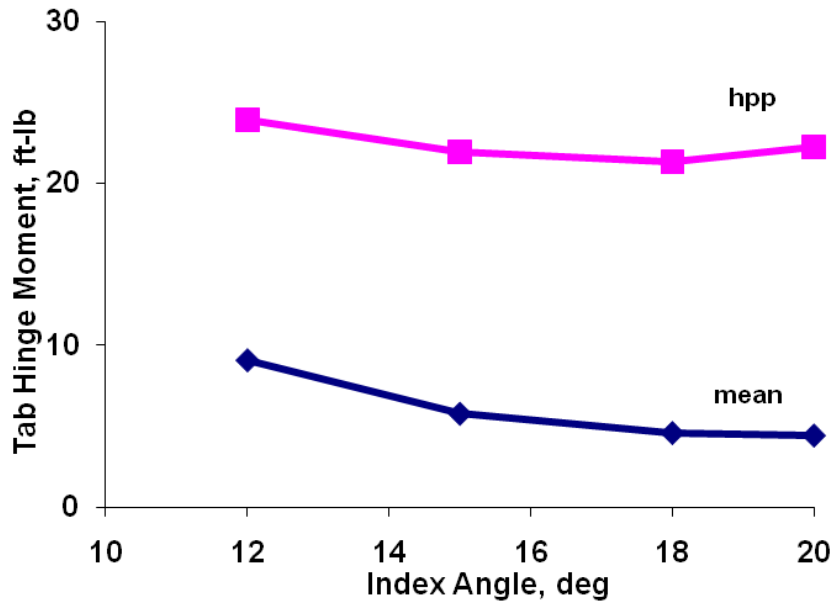
(b) Tab Hinge Moment

Figure 3.33: Effect of Index Angle on Tab Control Angles and Hinge Moment, UH-60A Type Rotor, $\mu = 0.368$, $C_T/\sigma = 0.084$
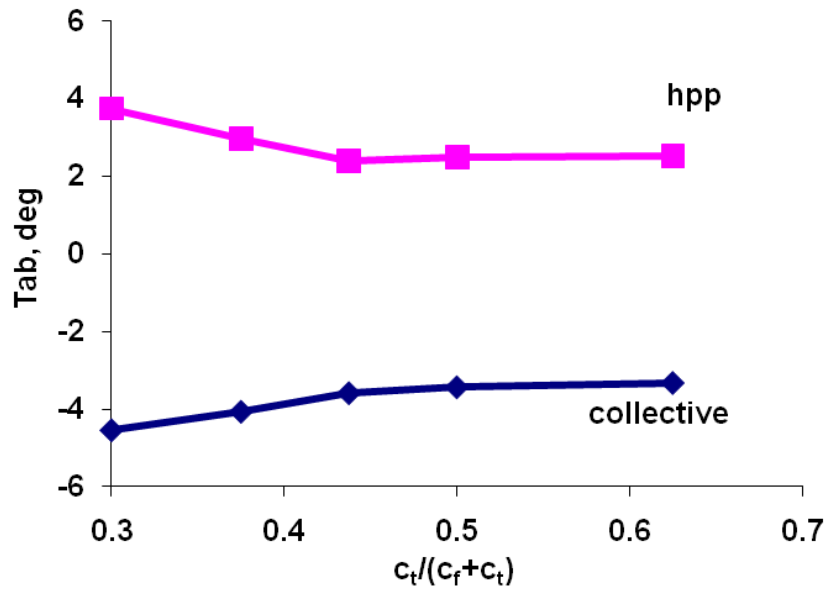
(a) Tab Control Angles
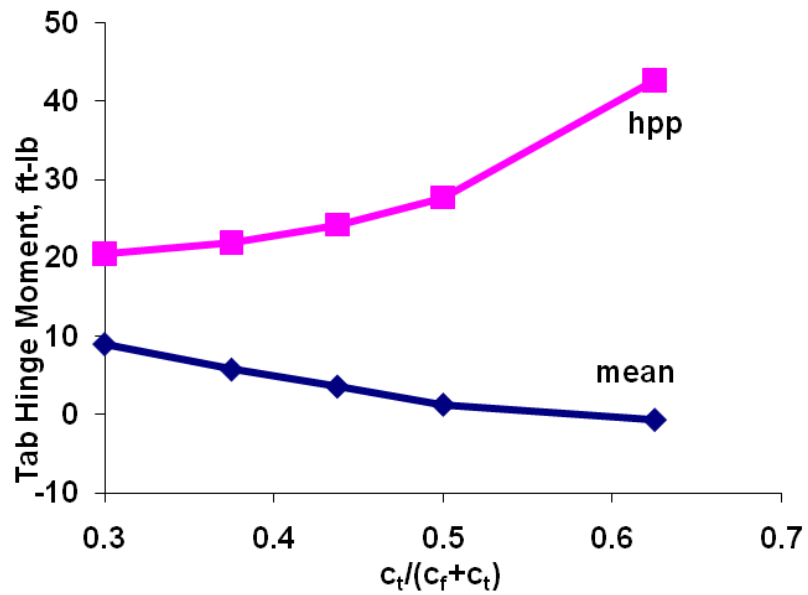
(b) Tab Hinge Moment

Figure 3.34: Effect of Tab Chord Ratio on Tab Control Angles and Hinge Moment, UH-60A Type Rotor, $\mu = 0.368$, $\theta_{idx} = 15°$, $C_T/\sigma = 0.084$
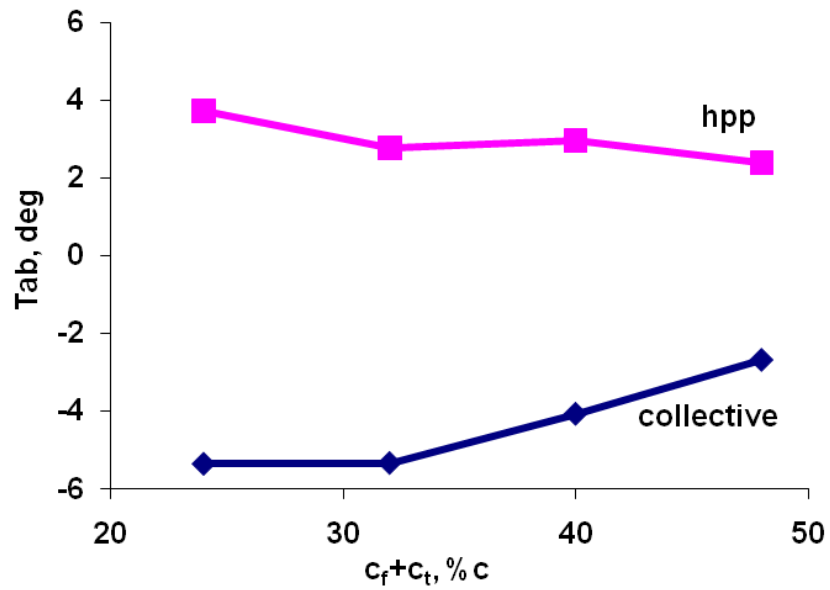
(a) Tab Control Angles
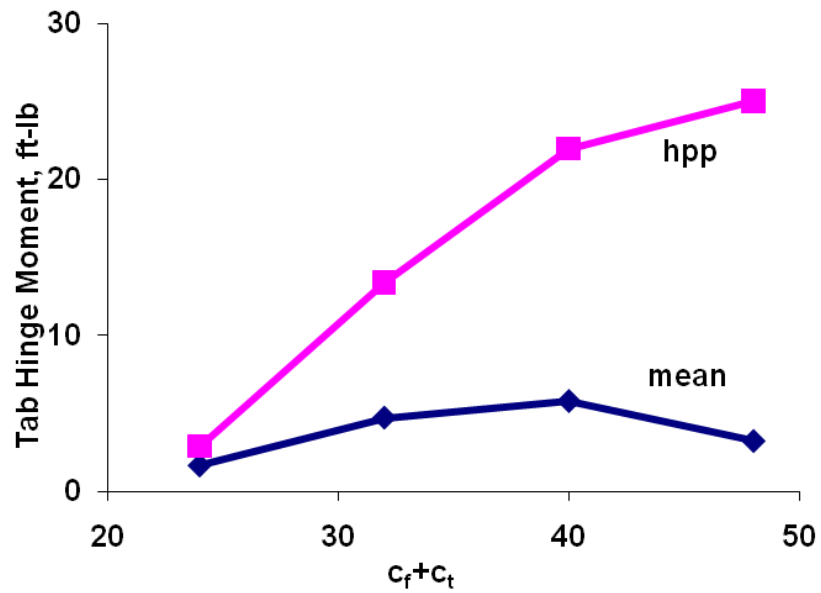
(b) Tab Hinge Moment

Figure 3.35: Effect of Combined Chord Ratio on Tab Control Angles and Hinge Moment, UH-60A Type Rotor, $\mu = 0.368$, $\theta_{idx} = 15°$, $C_T/\sigma = 0.084$
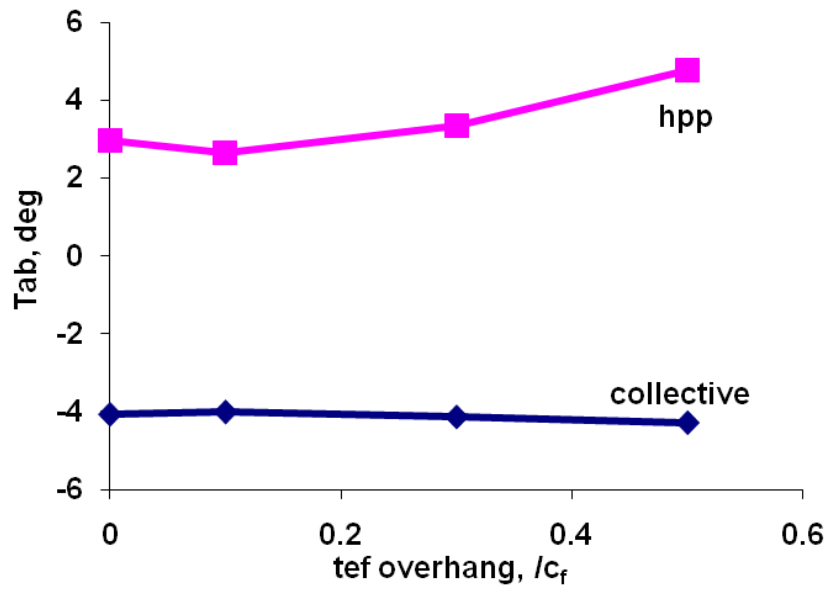
(a) Tab Control Angles
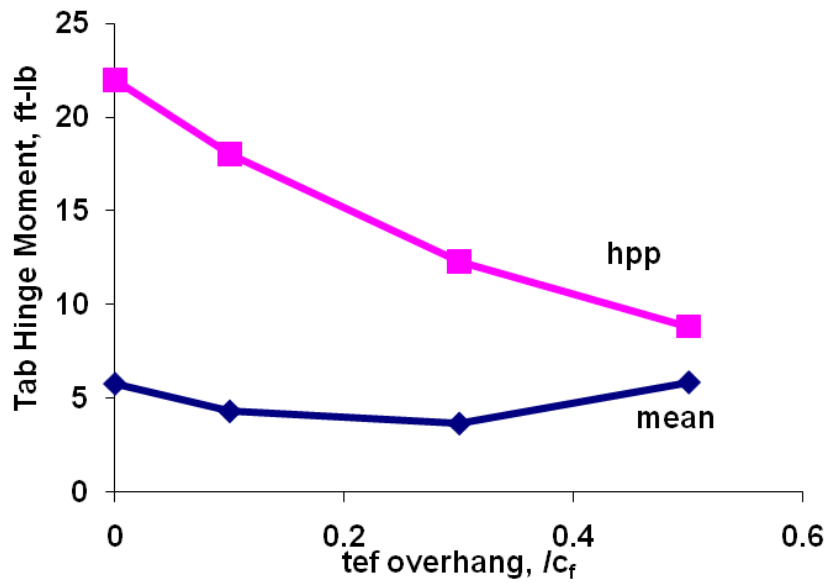
(b) Tab Hinge Moment

Figure 3.36: Effect of Flap Overhang on Tab Control Angles and Hinge Moment, UH-60A Type Rotor, $\mu = 0.368$, $\theta_{idx} = 15°$, $C_T/\sigma = 0.084$
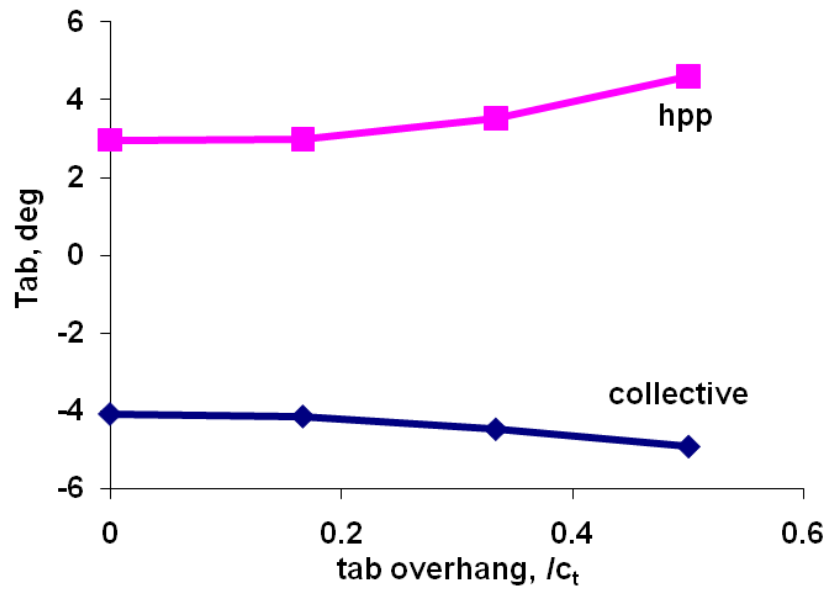
(a) Tab Control Angles
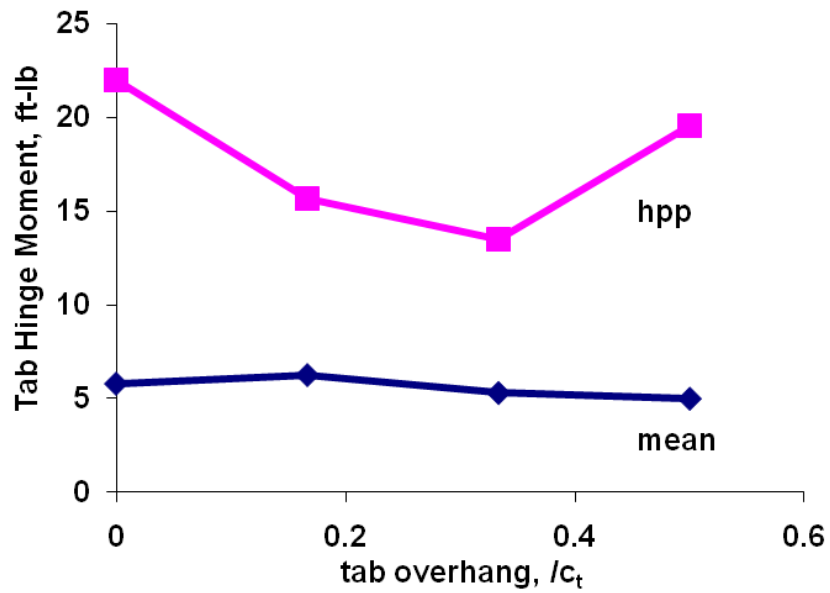
(b) Tab Hinge Moment

Figure 3.37: Effect of Tab Overhang on Tab Control Angles and Hinge Moment, UH-60A Type Rotor, $\mu = 0.368$, $\theta_{idx} = 15°$, $C_T/\sigma = 0.084$
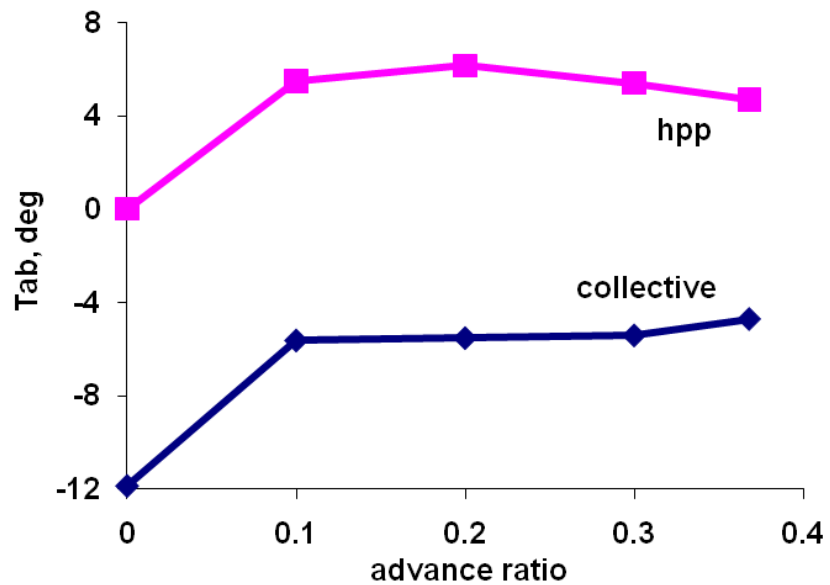
(a) Tab Control Angles
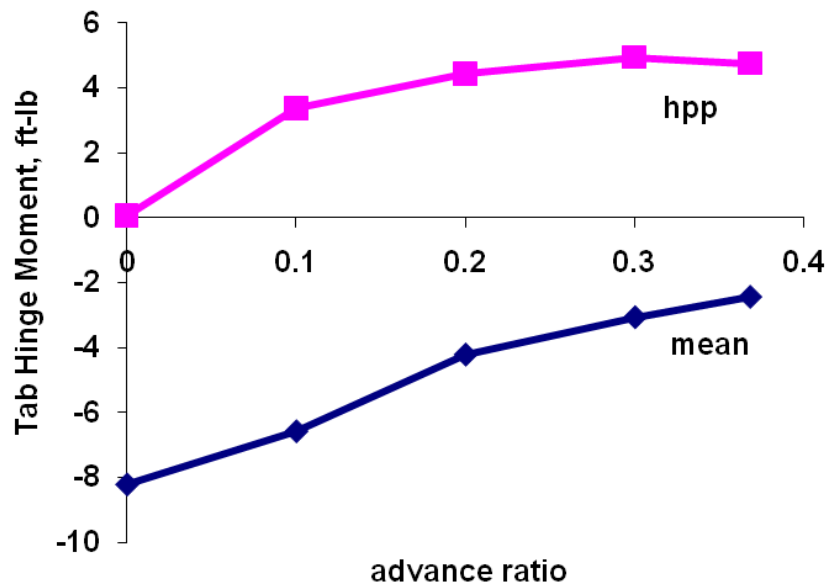
(b) Tab Hinge Moment

Figure 3.38: Effect of Advance Ratio on Improved Trailing Edge Flap and Tab Configuration, UH-60A Type Rotor, $\theta_{idx} = 18°$, $C_T/\sigma = 0.084$

Chapter 4

Performance Studies of Swashplateless Rotor

This chapter addresses the second central issue for the swashplateless rotor concept, which is the effect of the trailing edge controls on the main rotor performance. In this investigation, rotor performance is defined by rotor power and rotor lift-to-drag ratio, and only the UH-60A rotor is examined. The rotor is examined in hover and in forward flight, for both the baseline model and the swashplateless variant. Detailed structural and aerodynamic information is required to accurately assess rotor power. The structural model in the comprehensive analysis includes the inertial contributions of the flap and the tab to the blade. However, there are several aerodynamic models of differing fidelity. The parametric design study presented in the previous chapter used a quasi-steady thin airfoil model that allows aerodynamic overhang for airfoil sectional properties. The inflow distribution was calculated with a free wake model. The model was used to examine flap and tab design parameters, and to compare the flap and flap/tab configurations to each other. Since the model does not include airfoil drag, power can not be predicted accurately. The performance studies presented in this chapter use an aerodynamic model based on airfoil lookup tables, and three different inflow calculations. As described in Chapter 2, limited wind tunnel test data exists for flapped airfoils and even less has been published for airfoils with flap and tab. The tables for the flapped SC1094R8 airfoil

sections used on the swashplateless rotor were produced with computational fluid dynamics (CFD), and cover a range of angle of attack, Mach number and flap deflection. However, tables have not been produced for airfoils with flap and tab and the performance study therefore is confined to the swashplateless rotor with trailing edge flap, but no tab.

The performance of the swashplateless rotor is examined in hover and in forward flight. In hover, the inflow is assumed to be uniform for both the baseline and swashplateless rotors. The section on forward flight is divided into two major parts. In the first part, the swashplateless rotor is examined in wind tunnel trim, with the shaft angles and thrust prescribed to match the baseline rotor at each speed, and the hub moments set to zero. The inflow distribution is calculated with both uniform inflow and a relaxation method [123], single tip vortex, free wake model. This free wake model does not account for the trailing edge flap in any way. The effect of the inflow model is examined on the power prediction and the angle of attack distribution around the azimuth. Next, a modified free wake model is introduced to the analysis, which includes the influence of the trailing edge flap. The results using this model are compared to the results from the previous two inflow models. In the second part, the swashplateless rotor is examined in vehicle trim, using the newly refined free wake model. The effects of increasing vehicle weight and reducing parasite drag are studied for the swashplateless rotor.

The overall purpose of this study is to compare the performance of the swashplateless modification to the conventional rotor in hover and across the range of forward flight speed.

4.1 Baseline UH-60A Model

The UH-60A has been flight tested extensively, and data obtained from the NASA/Army UH-60A Airloads Program are stored in the NASA Ames Research Center database. Datta [124] separated the analysis of the helicopter into time-varying structural and aerodynamic parts. For the structural problem, the measured aerodynamic loads were used as input in blade dynamic analysis. Having established the accuracy of the structural model using measured airloads, the calculated blade deformations were then used to predict the airloads. It was shown that inaccuracies in the airloads predictions are due to errors in the aerodynamic model, rather than the structural model.

Yeo [127] compared flight test data to calculations of main rotor power, pitch control angles and shaft attitude produced with CAMRAD II. The study was performed for a range of gross weights, and showed good agreement with the flight test data for the power predictions and for the longitudinal control angles (collective and cyclic) and shaft angle (pitch attitude). In this section, the UH-60A flight test data are compared to power calculations from UMARC. This is to establish the baseline for comparison to the swashplateless rotor. The trim solution is for a nominal vehicle weight coefficient, C_W/σ, of 0.0783, which corresponds to a vehicle gross weight of 16500 lbs. The shaft angles are free to trim for the baseline (swashplate) rotor (see Figure 4.1). These predicted shaft angles compare well to flight test data at speeds above $\mu = 0.32$. Below that speed, the predicted angles follow the trend of the test data.

The prediction of required power, C_Q/σ is compared to flight test data across a range of flight speeds in Figure 4.2. The predicted results are accurate to within 2% of measured data. Removing the free wake from the model, and using uniform inflow only causes the power prediction to shift downward; however, the predictions with uniform inflow follow the trend of the test data for a conventional rotor, an indication that comparisons of predictions made with uniform inflow may yield correct trends for the swashplateless rotor too.

The prediction of required power in hover is compared to flight test data in Figure 4.9, for a range of thrust. Since the goal is to identify performance trends and focus on the effect of the airfoil tables, uniform inflow is used to study the hover performance. This ensures that differences between the swashplateless and the baseline rotors derive entirely from the trailing edge flaps and the index angle. The test data [128] is for a Mach scaled model of a UH-60A rotor in pure hover conditions, with nominal tip Mach number 0.628. Figure 4.10 shows the corresponding hover figure of merit for the UH-60A rotor. Below $C_T/\sigma = 0.06$, the rotor power is slightly over-predicted, resulting in a deviation in figure of merit of 5%. Above this thrust level, the power prediction corresponds well to the test data.

4.1.1 Pitch Control Angles and Elastic Twist

For the swashplateless rotor, flap authority is improved by maximizing the blade twist response to flap deflection. One of the key design requirements of this type of rotor is low torsional frequency, which facilitates blade twist. The response

of the baseline rotor to reduced torsional frequency can serve as a guide to the expected response from the swashplateless rotor. Figure 4.3 presents collective pitch across the range of forward flight speed for the rotor at two torsional frequencies: the baseline rotor at 4.3/rev and a variation at 2.7/rev. The torsional frequency is varied by adjusting the pitch link stiffness; in all other respects the rotors are identical. Reducing the torsional frequency by 40% increases the pitch collective by a similar amount across the range of advance ratios. The pitch cyclic in Fig. 4.4 increases moderately across the range of speed, but the softer root spring results in a maximum of 15% increase in the half peak-to-peak deflection. Although the pitch control angles are very sensitive to the torsional frequency, Figs. 4.5 and 4.6 show that the main rotor power and longitudinal shaft angle are less so. In response to the 40% reduction in torsion frequency, the rotor power decreases by a maximum of 10% at $\mu = 0.368$, while the shaft angle is unaffected by the variation. The elastic twist at the blade tip is presented in Fig. 4.7. The tip of the baseline rotor varies from $-1°$ twist at $30°$ azimuth to $-6°$ twist at $135°$ azimuth. By reducing the torsional frequency from 4.3/rev to 2.7/rev, the twist response increases 100% so that the half peak-to-peak measurement of the response increases from $2.5°$ to $5°$, and the entire twist distribution is offset to larger twist magnitudes.

The results of this study in hover are similar to those in forward flight. Figure 4.8 presents the variation in pitch collective with torsion frequency, for a range of thrust levels. As the torsional frequency decreases, the pitch collective required to hover increases linearly from 4.3/rev to 2.7/rev, then increases sharply as the root spring is softened further to 2/rev. This is the operating frequency for the

190

swashplateless rotor, and the collective ranges from $20°$ at $C_W/\sigma = 0.061$ to $25°$ at $C_W/\sigma = 0.101$. The collective pitch angles for the conventional rotor indicate the index angle that will allow the swashplateless rotor to operate with minimal flap deflections.

4.2 Swashplateless Rotor in Hover

The swashplateless rotor is trimmed to zero hub moments and the thrust level, C_T/σ, the same as the baseline rotor. The shaft angles for both the baseline and swashplateless rotor are set to zero, with the tail rotor collective at $6°$. The control pitch angles are replaced with control flap angles for the swashplateless rotor. The configuration used in this investigation is a TEF with chord of 0.15c and 0.40R span, with the midpoint located at the 75% radial station. The flap hinge is located at its leading edge, so that it has no aerodynamic overhang.

The hover analysis is conducted with uniform inflow, using lookup tables for both the main blade and the trailing edge flap aerodynamics. The TEF tables were produced with the CFD predictions for the flapped SC1095R8 airfoil for Mach numbers ranging from 0.3 to 0.8. The primary focus of the hover analysis is determining the effect of index angle on the predicted power. The baseline power and Figure of Merit (FM) for the UH-60A were shown in Figures 4.9 and 4.10. The range of index angle for the swashplateless rotor was varied from $5°$ to $19°$ and the thrust sweep, C_T/σ, was from 0.01 to 0.09. For each index angle, the swashplateless rotor was examined at increasing values of thrust, until blade deflection diverged and trim

solutions were no longer found. The maximum thrust level achieved at each index angle decreases as the index angle decreases.

For all results in this investigation, the index angle of the swashplateless rotor is not a degree of freedom, but is a prescribed value held constant for a range of thrust (in hover) or speed (in forward flight). By examining the effect of torsional frequency on the collective of the conventional rotor (see Fig. 4.8), it was shown that required pitch collective increased with thrust, for all torsional frequencies. From this it can be deduced that the swashplateless rotor requires lower index angles at low thrust, and higher index at high thrust. Since the index angle is held constant for all of the results presented in this investigation, an angle was selected to minimize the required control angles and hinge moments at high speed, and at the weight condition corresponding to $C_W/\sigma = 0.0783$. In less demanding conditions, the ideal index angle would decrease as the pitch collective does for the conventional rotor.

Figure 4.11 shows that the required power decreases as the index angle increases from 5° to 15°. From $C_T/\sigma = 0.01$ to 0.05, the power predictions for the baseline and swashplateless rotors are very similar, for all index angles. As the thrust increases above 0.05, differences can be seen. For 5° index, the predicted power increases rapidly from $C_T/\sigma = 0.05$ to 0.07, reaching a maximum at $C_T/\sigma = 0.07$. Above that level of thrust, a trim solution could not be found. At 10° index, the rapid increase in predicted power previously seen for the lower index angle does not occur until the thrust reaches 0.07. At 15° index angle, the power prediction is slightly lower than the baseline rotor for $C_T/\sigma = 0.05$ to 0.08. Finally, the highest index angle analyzed is 20°, where the power prediction dips below the conventional

rotor from $C_T/\sigma = 0.05$ to 0.10. As the thrust continues to increase, the power for 20° index begins to cross the baseline prediction, following a trend similar to that shown by the lower index angles. The curve is not fully expressed, however, as blade deflections diverged for this configuration above $C_T/\sigma = 0.10$.

Figure of merit (FM) offers another perspective on the trends of predicted power in Figure 4.12. The curve for 5° index follows the baseline prediction until $C_T/\sigma = 0.05$. Above that level of thrust, the FM decreases abruptly. At higher index angles, the FM of the swashplateless rotor exceeds that of the baseline, and the peak value of FM and the thrust at which it occurs increase with increasing index angle. For the 20° index, the most improvement in FM occurs at $C_T/\sigma = 0.08$, where the swashplateless rotor shows a 14% increase in efficiency.

It had been expected that as the thrust decreases, the optimal index angle would also decrease. This trend is discernible to a small degree, but significant differences are not shown in Figure 4.13 as a result of the index angle at low thrust. This result is supported by the predicted pitch collective angles for the conventional rotor at low torsional frequency in Figure 4.8. At 2/rev, the low torsional frequency which characterizes the swashplateless rotor, the predicted pitch collective for the conventional rotor is above 15° even at low thrust.

The blade angle of attack at 0.75R increases as the index angle decreases in Figure 4.14. As the thrust increases, the angle of attack increases more rapidly for the swashplateless rotor than for the conventional. The flap deflections corresponding to these predictions are shown in Figure 4.15. It can be seen that for every index angle, at all thrust levels above $C_T/\sigma = 0.03$, the flap angle needed to trim is neg-

ative (upward), and becomes more negative nearly linearly as the thrust increases. This flap deflection produces negative lift which is counteracted by the increased blade angle of attack.

4.3 Swashplateless Rotor in Forward Flight, in Wind Tunnel Trim

The forward flight analysis includes equivalent flat plate area as an estimate of the parasitic drag of the fuselage; in combination with the airfoil aerodynamics, this results in a required thrust for a given C_W/σ and flight speed. For each speed examined in this investigation, the swashplateless and baseline rotors are trimmed to matching thrust levels. By keeping the equivalent flat plate area the same for the baseline and swashplateless helicopter models, a disadvantage is conferred upon the swashplateless model, when in reality the absence of the swashplate would reduce the parasitic drag. An attempt has not yet been made to estimate the parasitic drag of the swashplate for this investigation.

4.3.1 Effect of Wake Model on Swashplateless Rotor Power Prediction

The free wake cases for the baseline rotor are solved with a six degree of freedom vehicle trim. All forward flight cases for the swashplateless rotor and the conventional rotor with uniform inflow use a moment trim targeted to zero hub moments. The shaft angles are prescribed, and match those of the baseline rotor at the same speed. The index angle of the swashplateless rotor is set to 15°. The aerody-

namic lookup tables for the trailing edge flaps contain properties for flap deflections of 0°, ±10° and ±15°, generated by the CFD analysis described previously. The lookup is based on linearly interpolated values of Mach number, angle of attack, and TEF deflection. Extrapolation up to 4° beyond the available TEF data is used in the prediction. The interpolation and extrapolation relies upon the assumption that the values of c_l, c_d, c_m, and c_h are close to linear between the existing data points. This appears to be an acceptable assumption for Mach number and angle of attack where many data points spanning a broad range are available; it may not be appropriate for the trailing edge flap at large flap deflections, where some effects of flow separation might be expected, but not captured. Solutions are found using both uniform inflow and the free wake. The free wake model has one vortex shed at the tip of the blade, with peak circulation strength at each azimuth angle.

Using uniform inflow, the predicted power for the swashplateless rotor with 15° index follows the baseline prediction from $\mu = 0.11$ to $\mu = 0.25$ (see Figure 4.16). As the advance ratio increases beyond 0.25, the swashplateless power prediction begins to diverge from the baseline, increasing rapidly until $\mu = 0.30$, where the swashplateless power is 33% higher than the baseline rotor. Beyond that speed, the trim solution diverges for the swashplateless rotor.

A similar divergence phenomenon is observed at low speed when the analysis incorporates the free wake. Figure 4.17 shows the swashplateless power prediction following the baseline within the range $\mu = 0.2$ to $\mu = 0.30$. The swashplateless power diverges from the baseline prediction at low speed ($\mu = 0.15$), where the 15° index angle requires 21% more in power. The prediction continues to increase as

the flight speed decreases; blade divergence occurred between $\mu = 0.11$ and hover. Above $\mu = 0.30$, blade deflection diverges again. The mean flap control angles corresponding to the predicted power are shown in Figures 4.18 and 4.19. The flap deflections required for trim are negative for the range of flight speed.

The swashplateless power predictions are very sensitive to the inflow model; omitting the free wake changes the required flap deflection for trim by up to 100%. For example, at low speed, $\mu = 0.11$, the flap deflection required for trim is -4° for uniform inflow, and -8.5° for free wake. Looking in the middle of the range, at $\mu = 0.25$, the TEF deflection is -6° for uniform inflow, and -7.5° for free wake. From this it can be concluded that neglecting the free wake in analysis produces an optimistic estimate of power and required flap deflection for a given thrust, in steady level flight.

4.3.1.1 Blade Angle of Attack Details

To understand the differences between the baseline and swashplateless rotors, the details of angle of attack are shown for azimuth, Mach number, and radial station at moderate and at low speeds. The speeds selected for investigation are $\mu = 0.30$ and $\mu = 0.11$, the high and low speeds at which the swashplateless and baseline power predictions diverge.

Significant differences appear at $\mu = 0.30$, where both inflow models are used, and comparisons can be made between the baseline and swashplateless rotors. In Figure 4.20, the angle of attack distribution is presented for the conventional rotor

at the 75% span position for two wake models. The angle of attack variation for the swashplateless rotor shows in Figure 4.21 similar phenomena in the second and fourth quadrants, but not the third. Wake induced effects begin to influence the predictions at this speed, as the shaft angle moves toward the vertical (from $7.68°$ at $\mu = 0.368$ to $5.07°$ at $\mu = 0.30$).

Viewing the angle of attack variation for both rotors clarifies the differences between the baseline and swashplateless solutions. The uniform inflow predictions are shown in Figure 4.22. The swashplateless rotor closely follows the trends of the baseline around the azimuth, but the angle of attack increases in magnitude by as much as $4°$ on the retreating side. Including free wake shows that the general trends remain the same, but the difference in magnitude becomes larger (see Fig. 4.23). The third quadrant (between $180°$ and $270°$ azimuth) in particular shows the greatest differences between the baseline and swashplateless rotors. The increase in angle of attack occurs in response to the large negative lift contribution from the trailing edge flap. Angle of attack and the Mach number vary at every azimuth angle, as the blade advances and then retreats through the four quadrants of the rotor disc. The highest Mach numbers occur on the advancing side (between $0°$ and $180°$ azimuth) where the forward speed of the blade combines with the forward speed of the vehicle. On the retreating side, where the flow of air over the blade is slower, the angles of attack increase. Stall becomes a concern as the angle of attack increases, and Figures 4.24 and 4.25 show that the sectional angle of attack for the swashplateless rotor at 0.75R approaches close to the stall boundary.

Breaking the angle of attack into its constituent components lends further

insight. The largest contributions to the angle of attack for the baseline rotor are provided by the control angles and twist, then the influence of the inflow and blade flexibility (see Fig. 4.26). Figure 4.27 shows that the largest contribution for the swashplateless rotor is provided by elastic twist. The torsional frequency was reduced from 4.38/rev to 1.92/rev to enable a 1/rev elastic twist as the driving mechanism of the swashplateless primary control. However, an unintentional 2/rev harmonic was also introduced, which may make the inflow a dominant contributor on the retreating side, leading to stall.

The lift and drag envelope shows important differences between the baseline and swashplateless rotors at $\mu = 0.30$. Figure 4.28 shows the lift coefficient of the baseline rotor ranges from -.05 to 0.2, with corresponding drag coefficients reaching a maximum of 0.0035 in the second quadrant. The lift and drag coefficients for the swashplateless rotor in Figure 4.29 include the effect of the trailing edge flap. The range of the lift coefficient has been extended down to -0.09 and up to 0.21, but the largest change is in drag coefficient, which reaches a maximum of 0.008 in the second quadrant, an increase of over 100% from the baseline. There is significant discontinuity seen in the second and third quadrants of the lift-drag envelope which may be caused by the similar discontinuity seen in the angle of attack. Figures 4.30 and 4.31 show the deflection of the trailing edge flap for both inflow models. The inclusion of the free wake decreases the range of TEF motion at the 0.75R station by 4°, from 18° to 14°, but results in the introduction of roughness to the TEF deflections that mimics the discontinuity seen in the angle of attack.

At low speed, $\mu = 0.11$, strong vortex interaction takes place and the free wake

is necessary for correct prediction of the angle of attack. The shaft angle at this speed is nearly vertical at -0.20°. The power prediction is affected by a large increase in angle of attack seen by the swashplateless rotor compared to the baseline. For uniform inflow, Figure 4.32 shows a maximum of 2° difference on the retreating side; when free wake is included in Figure 4.33, the difference increases to 5°. The trend of the angle of attack is similar for both the baseline and swashplateless rotors using uniform inflow, but the free wake predictions do not correlate well. The angle of attack envelope shows that the swashplateless prediction in Figure 4.35 is near or exceeds the airfoil stall boundary on the retreating side. The baseline rotor is well within the stall boundary at this section (see Figure 4.34).

When the angle of attack is separated into components in Figures 4.36 and 4.37, the difference between the baseline and swashplateless prediction is emphasized. As seen previously at $\mu = 0.30$, the elastic twist is the key contribution, and is influenced by unanticipated higher harmonics. Unlike the predictions at $\mu = 0.30$, the trends differ as much as the magnitude. This indicates that the uniform inflow model can provide neither trends nor magnitude for power prediction and angle of attack at low speed. For these cases, the prediction relies on a robust and valid free wake model.

In Figure 4.38 the lift-drag envelope for the baseline rotor is smooth, reaching a maximum c_d of 0.005 in the second quadrant. By comparison, Figure 4.39 shows that the swashplateless lift-drag envelope has more discontinuities, and the maximum c_d of 0.014 occurs on the retreating side where stall has occurred. Although the TEF deflections are continuous for both inflow models, seen in Figures 4.40 and 4.41,

the range of motion varies greatly. Uniform inflow predicts 6° of total deflection, while the free wake results in almost 19° of TEF deflection. The very large negative trailing edge flap deflection on the retreating side causes a lift decrement. For the swashplateless rotor to trim at the same thrust level as the baseline, there is a compensating large increase in blade angle of attack. As a result, the rotor performance is degraded.

4.3.2   Refining the Wake Model to Include Trailing Edge Flaps

The results discussed in the preceding sections use the baseline wake model without any modification for the trailing edge flap. This means that the sectional angles of attack do not include the effect of the flap, and the near and far wake are calculated as they would be for an unflapped blade. A revision to the wake model is proposed which includes the trailing edge flap in the near and far wake calculations by assuming small interruptions to the flow at the inboard and outboard bounds of the flap.

The trim solution for the swashplateless rotor is a three degree of freedom solution, with targeted thrust and zero hub moments; the longitudinal and lateral shaft angles, plus the tail rotor collective, match those of the conventional rotor at each advance ratio. The trim solution for the conventional rotor is full vehicle trim with six degrees of freedom. The power predicted with the TEF trailer wake model follows the trend of the baseline rotor power prediction for the range of advance ratio from $\mu = 0.11$ to $\mu = 0.30$, as shown in Fig.4.42. In Figure 4.42a, at low speed

transition ($\mu = 0.11$), the predicted power for the swashplateless rotor has decreased to 15% below the baseline rotor, using the refined wake model. As the advance ratio increases to $\mu = 0.25$, the swashplateless prediction approaches the baseline power. From $\mu = 0.25$ to $\mu = 0.30$, the swashplateless power prediction increases to 10% above the baseline rotor. This represents a large change from the swashplateless power predicted by the tip vortex model, particularly in the low speed range from $\mu = 0.25$ to $\mu = 0.11$. The trends of the power predictions from the two wake models are divergent at this speed. The tip vortex model is above the baseline at $\mu = 0.15$, and increases sharply to $\mu = 0.11$. In contrast, the TEF trailer model predicts power below the baseline at $\mu = 0.15$, and follows the trend of the baseline power prediction to $\mu = 0.11$. Figure 4.42b compares the swashplateless power predictions from the refined free wake model to uniform inflow and the baseline rotor. For both inflow models, the swashplateless power prediction follows the trend of the baseline rotor; however, the refined free wake model predicts higher rotor power from $\mu = 0.10$ to 0.25. To understand the differences between the free wake models, the details of angle of attack are shown for azimuth and Mach number at low speed ($\mu = 0.11$), where the swashplateless predictions from the tip vortex and TEF trailer models diverge.

At low speed, $\mu = 0.11$, strong vortex interaction takes place and the free wake is necessary for correct prediction of the angle of attack. The shaft angle at this speed is nearly vertical at -0.20°. Figure 4.43 shows the two free wake predictions for the swashplateless rotor and compares them to the baseline rotor. The power prediction from the tip vortex free wake model is affected by a 5° increase in angle

of attack seen by the swashplateless rotor compared to the baseline at 0.75R. The TEF trailer free wake model predicts no increase in maximum angle of attack at this station and a small decrease in the power prediction. Figure 4.44 shows the angle of attack vs. Mach number envelope for both wake models for the swashplateless rotor. The original wake model resulted in a trim solution where the angles of attack on the retreating side of the disk were near the stall boundary of the airfoil. The TEF trailer model prediction has reduced the angles of attack for the swashplateless rotor so that they remain within the static stall boundary at this section.

In Figure 4.45 the lift-drag envelope for the TEF trailer wake model is smooth and compact, reflecting the small range of angles of attack predicted for this section. The lift-drag envelope predicted by the tip vortex wake model has a maximum drag coefficient that is 5 times larger than the revised wake model, which contributes to the much larger power prediction. Although the trend of the TEF deflections are similar for both wake models, seen in Figure 4.46, the range of motion varies greatly. The tip vortex free wake results in more than 20° of TEF deflection, while the range of TEF deflection for the revised wake model is reduced to 7°. The very large negative trailing edge flap deflection predicted by the tip vortex model causes a lift decrement. For the swashplateless rotor to trim at the same thrust level as the baseline, there is a compensating large increase in blade angle of attack. As a result, the rotor performance is degraded. The reduction of TEF deflection that accompanies the TEF trailer wake model eliminates the increase in the blade angle of attack, and thus the performance prediction improves.

4.4 Swashplateless Rotor in Forward Flight, in Vehicle Trim

Having refined the wake model to reflect the probable physics of the flapped blade, the performance predictions in forward flight are re-evaluated using full vehicle (6 dof) trim for both the conventional and swashplateless rotors. For the swashplateless rotor, the six trim variables are: the flap collective (mean deflection), the two flap cyclics, the shaft roll and pitch positions, and the tail rotor collective. The effects of increasing rotor thrust and reducing fuselage drag are also examined for the swashplateless rotor.

First, the rotor torque and shaft angles were re-calculated for the baseline UH-60A, using the full refined wake model with the Weissinger-L near wake and free wake. With respect to the rotor power, the primary consequence of including the near wake model in the analysis is that the prediction improves slightly from $\mu = 0.30$ to $\mu = 0.40$, and is very close to the flight test data for $C_W/\sigma = 0.0783$ (See Figure 4.47). Figure 4.48 shows that the shaft angles undergo a very small change at the lower end of the speed range.

Next, the swashplateless rotor is compared to the baseline using vehicle trim. Figure 4.49 compares the power predictions for both rotors across the range of forward flight speeds. The swashplateless power follows the baseline prediction from $\mu = 0.16$ to $\mu = 0.30$ more closely than the results obtained using the 3dof trim. Compared to the baseline, there is a moderate increase in the swashplateless power prediction from $\mu = 0.25$ to $\mu = 0.30$, so that at $\mu = 0.30$, the predicted swashplateless power is 11% higher than the baseline. At low speed, the swashplateless

power is reduced 1% from the baseline prediction at $\mu = 0.16$. The predicted shaft angles are also nearly identical across the speed range, until $\mu = 0.27$, where the swashplateless shaft angles level off (see Figure 4.50). The change in the predicted power of the swashplateless rotor can be explained by the rotor hub moments, which were forced to zero for the previous 3 dof targetted thrust trim solutions. Despite the change in the trim procedure, the trend of the power prediction is not altered from that originally seen with the refined TEF trailer wake model (in Figure 4.42). At low speed, the swashplateless power prediction is lower than the baseline, and as the forward flight speed increases, the prediction increases above the baseline power calculation.

4.4.1 Effect of Increasing Rotor Thrust on Swashplateless Performance

The flight condition is changed so that the weight coefficient is increased, and the performance of the swashplateless rotor is compared to the baseline UH-60A across the range of flight speed. The predictions for the baseline rotor at higher thrust levels are validated against flight test data obtained from the NASA/Army UH-60A Airloads Program, and previously published in a performance analysis of the rotor [127]. The main rotor power is calculated for $C_W/\sigma = 0.0783$, $C_W/\sigma = 0.0891$ and $C_W/\sigma = 0.1000$; these conditions are also identified in the airloads program as flight 85, flight 84 and flight 88. They are steady level flights, and the measure power coefficient is based on the torque of the main rotor.

The predicted power for the baseline rotor is very close to the flight test data for all three weight coefficients. At $C_W/\sigma = 0.0891$, there is a small over-prediction at low speed ($0.1 \leq \mu < 0.20$), as shown in Figure 4.51. Figure 4.52 shows that at $C_W/\sigma = 0.1000$, the power is slightly under-predicted at higher speeds ($0.25 \leq \mu < 0.35$). In general, the trend is for the main rotor power to increase smoothly with increasing weight (Figure 4.53, while the rotor shaft angles decrease (Figure 4.54.

Trim solutions for the swashplateless rotor were obtained at two thrust levels, $C_W/\sigma = 0.0783$ and $C_W/\sigma = 0.0891$. Figure 4.55 compares the swashplateless and conventional rotor power predictions at $C_W/\sigma = 0.0891$. At low speed, $\mu = 0.13$, the prediction for the swashplateless rotor is 2% below that of the conventional rotor. As the forward flight speed increases, the predicted power rises with respect to the conventional rotor until at $\mu = 0.26$, there is a 13% increase. For the range of forward flight speed at this thrust level, the swashplateless rotor trim position is very similar to the conventional rotor, as shown in Figure 4.56. In the range $0.20 \leq \mu \leq 0.26$, the swashplateless rotor shaft angle decreases slightly with respect to the conventional rotor. At both thrust levels, $C_W/\sigma = 0.0783$ and $C_W/\sigma = 0.0891$, the flap control angles for the swashplatess rotor show a steady decrease in the mean flap angle as the advance ratio increases, and a corresponding increase in the half peak-to-peak (hpp) angles (See Figures 4.57 and 4.58.

Figure 4.59 and Figure 4.60 compare the swashplateless power predictions at the two different thrust levels. As the thrust increases, the predicted power curve increases at a nearly constant offset. This differs from the conventional rotor, for which the difference between the power curves decreases as the forward flight speed

205

increases. The predicted shaft angles for the swashplateless rotor show a similar trend as the advance ratio increases, where the swashplateless predictions fall below those for the conventional rotor. As the thrust increases, the flap control angles in Figure 4.59 show a similar trend to the power curves: there is a nearly constant offset between the curves for each thrust level. Note that as the thrust increased from $C_W/\sigma = 0.0783$ to $C_W/\sigma = 0.0891$, the maximum forward flight speed for which trim solutions were obtained decreased.

4.4.2 Effect of Fuselage Drag on Swashplateless Performance

The original UH-60A production vehicle had an equivalent flat plate area of 26 ft^2 for the fuselage drag. The sixth-year production vehicle tested in the Airloads Program is equipped with External Stores Support System (ESSS) fairings, accessories to the de-icing system and a wire-strike kit that increase the drag area significantly [127]. The addition of the additional stores and systems changed the UH-60A from a relatively "clean" drag profile to one that can better be described as "dusty" [3] for its gross weight. For this investigation, a value of 35 ft^2 has been used throughout as an estimate of the fuselage drag for both the conventional and swashplateless rotors.

Figure 4.62 shows the equivalent flat plate area for helicopters at a range of gross weights, along with a typical breakdown of the sources of parasite drag. The hub is assigned a value of 30% of the total fuselage drag; removing the swashplate should reduce the hub drag significantly. Accordingly, for this study the swash-

plateless rotor is examined for the effect of reducing the drag to 90% and 80% of the initial value. Reducing the drag by 10% or 20% simulates the removal of the swashplate, and may indicate a performance advantage achievable with the swashplateless configuration.

In Figure 4.63, each 10% decrease in the parasite drag results in a 2.5% decrease in the power prediction for the swashplateless rotor, so that the case with 80% drag has a power prediction 5% lower than the 100% drag case. This moderate reduction in predicted power is accompanied by a large change in the rotor shaft angle in Figure 4.64. At $\mu = 0.25$, the shaft angle of the 80% drag case has decreased 23% from the position for the 100% drag case. The flap control angles are not significantly affected by decreasing drag, as shown in Fig. 4.65. This is a consequence of the rotor trimming at different shaft angles. If the shaft angles were held constant and the thrust and hub moments prescribed, larger changes in flap control angles would result.

The swashplateless rotor used throughout this performance study is nearly identical to the UH-60A. The torsional frequency of the rotor was lowered by reducing the stiffness of the root pitch spring, and trailing edge flaps were added to the blades. The blade airfoils, selected to maximize the performance and maneuverability of the baseline rotor, are unchanged. It is seen that the swashplateless rotor, operating with a different distribution of angle of attack due to the lowered torsional frequency, uses these airfoils less efficiently. The rotor lift-to-drag ratio in Fig. 4.66 was calculated for the baseline rotor and for the swashplateless rotor at 100%, 90% and 80% parasite drag. For the range of forward flight speed from $\mu = 0.1$ to 0.25,

the lift-to-drag ratio of the swashplateless rotor is very close to the baseline rotor, regardless of decreases in parasite drag. However the baseline rotor sees a maximum lift-to-drag ratio near $\mu = 0.30$, while the ratio for the swashplateless rotor declines sharply after $\mu = 0.25$.

4.5   Concluding Remarks

The predictions of main rotor power and rotor lift-to-drag ratio are dependent on the accuracy of aerodynamic model of the comprehensive analysis. For the current work, the aerodynamic model was refined to include the effect of the trailing edge flap through airfoil table lookup and through the wake model. Tabs and aerodynamic balance were not included in this section of the current work because the difficulty and expense of producing either wind tunnel test data or thorough CFD simulation of these features for airfoil lookup tables is disproportionate to the scope of the investigation. The swashplateless rotor used in every performance study is a variant of the UH-60A, where the torsional frequency has been reduced from 4.3/rev to 2.0/rev by reducing the stiffness of the root pitch spring. The trailing edge flap on each blade is 0.15c in size, has no aerodynamic balance and spans 0.40 of the blade radius. This flap configuration was selected to facilitate actuator performance through the minimization of flap deflection and hinge moment. The purpose of the current study is to assess the impact of this configuration on rotor performance, and the focus is not on modifying the swashplateless rotor to improve performance.

4.5.1 Validation of Baseline Rotor

The power predictions of the comprehensive analysis were validated with flight test data from the UH-60A Airloads Program. The rotor power predictions for the baseline rotor model in vehicle trim showed very good correlation to test data in forward flight and in hover, for a range of vehicle thrust levels. The shaft angles predicted in forward flight show good agreement at advance ratios above $\mu = 0.3$, and fair agreement at slower speeds. The effect of the inflow distribution was demonstrated for the baseline rotor in forward flight; the two models used were uniform inflow and free wake with a single tip vortex. Since torsional frequency was identified as a key design parameter for swashplateless rotors, its effect on the baseline (swashplate) UH-60A rotor was examined.

4.5.2 Hover Performance of Swashplateless Rotor

This section of the performance study was conducted in wind tunnel trim with targeted thrust and zero first blade flap harmonics; the inflow distribution was uniform. For varying index angle, swashplateless rotor power, figure of merit, and angle of attack at the 0.75R radial station were compared to the baseline values across a range of thrust. The effect of index angle on trailing edge flap deflection was also shown for the swashplateless rotor.

4.5.3 Forward Flight Performance of Swashplateless Rotor

The swashplateless UH-60A was examined in forward flight using both isolated rotor and vehicle trim conditions. In the first case, isolated rotor trim was used to study the effect of the wake model on the power prediction. The targets of the trim solution were thrust and zero hub moments, and the rotor shaft angles were set to match those of the baseline rotor at the same speed in free flight. The wake models used were uniform inflow and a free wake model with a single tip vortex; these produce swashplateless rotor power predictions with very different magnitudes and trends across the range of forward flight speed. The free wake model was revised to include the effect of the trailing edge flap in both the near and far wake. The theory underlying the revision is that the flap deflection disrupts the flow at the trailing edge. Trailed vortices were added at the inboard and outboard ends of the flap to model the disruption. Results from the modified free wake model were compared to the two previous swashplateless rotor power predictions, and to the baseline rotor.

The torsional softness at the blade root of the swashplateless rotor allows the blade to easily twist in response to load. The result of this characteristic is that the swashplateless rotor generally operates with a different distribution of angle of attack than the conventional rotor. The 0.75R station of the blade was examined in detail at $\mu = 0.30$ and at $\mu = 0.11$, for the sectional angle of attack distribution, the lift-drag envelope and flap deflection. This information showed that at that radial station, the swashplateless rotor operates at a higher angle of attack compared to the baseline rotor; offsetting the increase in angle of attack is the large negative lift

contribution of the deflected trailing edge flap. For the nonlinear inflow distribution calculated by the free wake model, the angles of attack are close to or exceed the airfoil static stall boundary. The lift-drag envelope is large compared to the baseline rotor. The flap cyclic deflections are also large, both absolutely and relative to the deflections predicted by uniform inflow.

Finally, the swashplateless and baseline rotors were examined in free flight. The power predictions for the baseline rotor showed good correlation to the flight test data for a range of vehicle weights. For two vehicle weights, the swashplateless rotor was trimmed across the range of forward flight speed and compared to the baseline rotor. The trend of the swashplateless power prediction remains the same regardless of vehicle weight: at the low end of the speed range, the swashplateless rotor is predicted to require less power than the baseline rotor, and at the high end the requirement increases over baseline. The flap angles required to trim the rotor are moderately large. The range of forward flight speed over which the swashplateless rotor could be trimmed is limited. The comparison to the baseline rotor was repeated for several increments of parasite drag. The parasite drag used in the analysis is reduced by increments of 10%, to simulate the drag reduction that might be caused by the switch to a swashplateless configuration. In response, the rotor shaft angles experience a large decrease with each reduction in parasite drag, while the decreases to rotor power are small to moderate. The rotor lift-to-drag ratio was calculated for each level of parasite drag, and compared to the baseline rotor.

The following conclusions are drawn from the performance study:

1. Examination of the conventional (swashplate) UH-60A showed that rotor torsional frequency has a significant effect on blade elastic twist response and thus on the pitch trim angles at given thrust and forward flight speed. Reducing the torsional frequency by 40% leads to a large change in trim requirements, and a small to moderate decrease in the rotor power calculation; the predicted rotor shaft angles are unchanged. The decrease in rotor power predicted for the conventional rotor with torsional frequency between 2/rev and 3/rev is similar to the power reduction measured and predicted in other investigations of higher harmonic control (HHC) for rotors. The collective pitch required to trim the rotor when the torsional frequency is reduced offers an estimate of a suitable pitch index angle for a swashplateless rotor at a similarly low torsional frequency.

2. Index angle and torsional frequency are key design parameters for the swashplateless rotor: they act together to reduce the flap deflections required to trim the rotor, and produce a different blade twist distribution compared to the baseline (swashplate) rotor. Trailing edge flap deflections in combination with blade twisting redistribute lift and drag about the rotor disk to produce changes to rotor power across the range of forward flight speed.

   The TEF deflections required for trim increase with thrust in hover and with speed in forward flight, but can be reduced by increasing the index angle. In this study, using the flap aerodynamic lookup tables produced by CFD analysis, 15° was the highest index angle that produced trim solutions across

the range of flight speeds. The maximum index angle that can be used in this investigation was limited by blade deflection divergence; it is not clear whether this phenomenon is numerical or physical.

3. In hover, the swashplateless rotor requires less power than the conventional rotor, for a limited range of thrust at each index angle. A high index angle produces an increase in figure of merit (FM) compared to the baseline, at some thrust levels. Beyond the thrust level at which the maximum FM is produced, the predicted power increases rapidly compared to the baseline rotor and the figure of merit drops. This appears to limit the upper range of thrust at which the swashplateless rotor operates efficiently in hover.

4. The wake model used to analyze the swashplateless rotor has a significant effect on the prediction of rotor power in forward flight. A uniform inflow model produces a predicted power curve that follows the trend of the baseline (swashplate) rotor. This model might be sufficient for relative comparisons between rotors. A refined free wake model that accounts for the trailed vorticity from the trailing edge flap produces rotor power predictions that also follow the trend of the baseline rotor. The refined model indicates that the swashplateless rotor may require less power than the baseline at low speed, and more at high speed. This conclusion depends on the rotor models having identical configurations (and parasitic drag), except for torsional frequency and trailing edge flaps.

5. The flap deflections required to trim the swashplateless rotor in forward flight

vary with the inflow model used in the comprehensive analysis. Using 3 degree of freedom rotor trim and a target thrust level of $c_T/\sigma = 0.0783$, the three inflow models used required the following flap deflections to trim:

- Uniform inflow resulted in mean flap deflections of $-4°$ to $-10°$, and half peak-to-peak cyclic deflections of $3°$ to $11.5°$.

- The free wake model with a single tip vortex resulted in mean flap deflections of $-6°$ to $-9°$, and half peak-to-peak cyclic deflections of $7.5°$ to $11.5°$.

- The modified free wake model with trailers at the flap boundaries resulted in mean flap deflections of $-3°$ to $-6.5°$, and half peak-to-peak cyclic deflections of $3°$ to $8°$.

6. Solutions can be calculated for the swashplateless rotor in full vehicle trim across the range of forward flight speed. Trim solutions obtained for the rotor using the modified wake model result in power predictions that closely follow the power prediction of the baseline rotor. At low speed, $\mu = 0.16$, the swashplateless prediction is 1% lower than the baseline. The difference between the predictions increases slowly until at $\mu = 0.30$, the swashplateless power is 11% higher than the baseline. The predicted rotor shaft angles for the swashplateless rotor show good agreement with the predictions for the baseline rotor across the range of forward flight speed until $\mu = 0.30$. The mean trailing edge flap deflections range from $-3°$ to $-9°$. The half peak-to-peak flap deflections range from $4°$ to $11°$.

7. The swashplateless UH-60A rotor can be trimmed at a higher weight level, $C_W/\sigma = 0.0891$. The increase in predicted rotor power is similar to the trend seen for the baseline, but the maximum speed at which a solution could be obtained is reduced to $\mu = 0.26$. The flap control angles increase with the increased thrust, but follow the same trend as the solutions found for $C_W/\sigma = 0.0783$. Trim solutions could not be obtained for vehicle weights higher than $C_W/\sigma = 0.0891$.

8. Except where noted explicitly, the equivalent flat plate area is held constant in comparisons between the baseline and swashplateless rotors for most of this investigation. Accordingly, the power predictions shown for the swashplateless rotor are conservative. When the parasitic drag was reduced 20% from the baseline, the swashplateless power prediction decreased 5%, with a concurrent decrease of the rotor shaft angle of 23%.

9. The rotor lift-to-drag ratio was calculated for the swashplateless rotor at different increments of parasitic drag, and compared to the baseline rotor (with unchanged parasitic drag). For all increments of parasite drag, the maximum lift-to-drag ratio of the swashplateless rotor occurs at or below $\mu = 0.26$. This is in contrast to the baseline rotor, where the maximum lift-to-drag ratio occurs near $\mu = 0.35$. Up to $\mu = 0.26$, the swashplateless ratio follows the baseline rotor closely, then decreases rapidly. Beyond $\mu = 0.30$, trim solutions are difficult to obtain for the swashplateless rotor. These results indicate that at higher advance ratios, the swashplateless UH-60A operates less efficiently

than the baseline rotor.
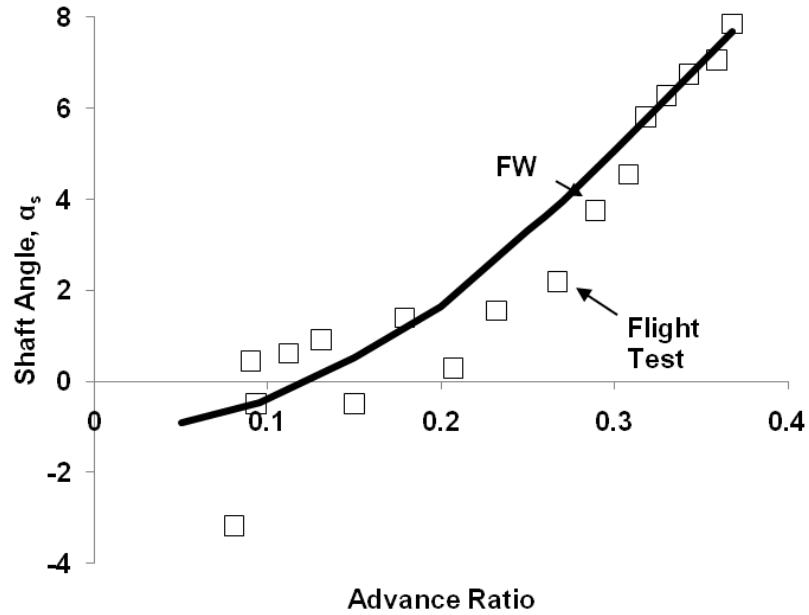
Figure 4.1: Predicted and Measured Shaft Angles for UH-60A in Forward Flight, $C_W/\sigma = 0.0783$ (FW: free wake)
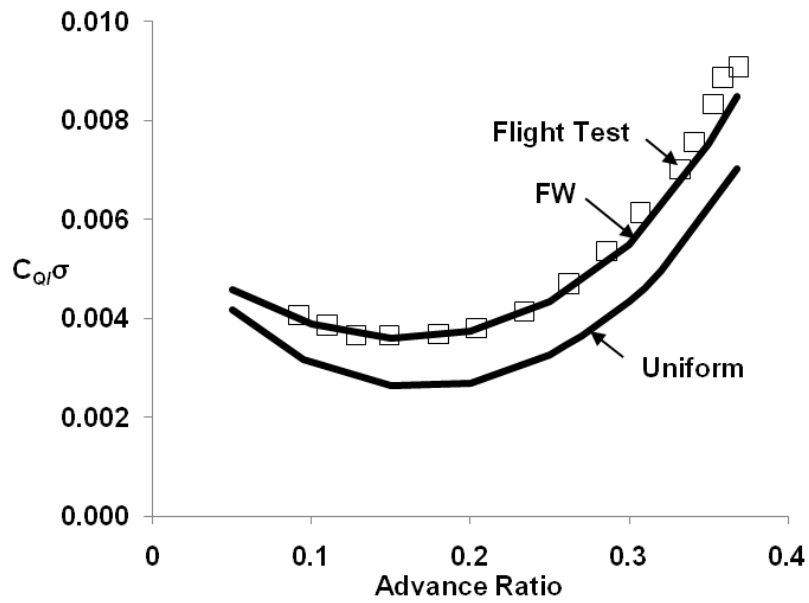
Figure 4.2: Predicted and Measured Power for UH-60A in Forward Flight, $C_W/\sigma = 0.0783$ (FW: free wake, Uniform: uniform inflow)
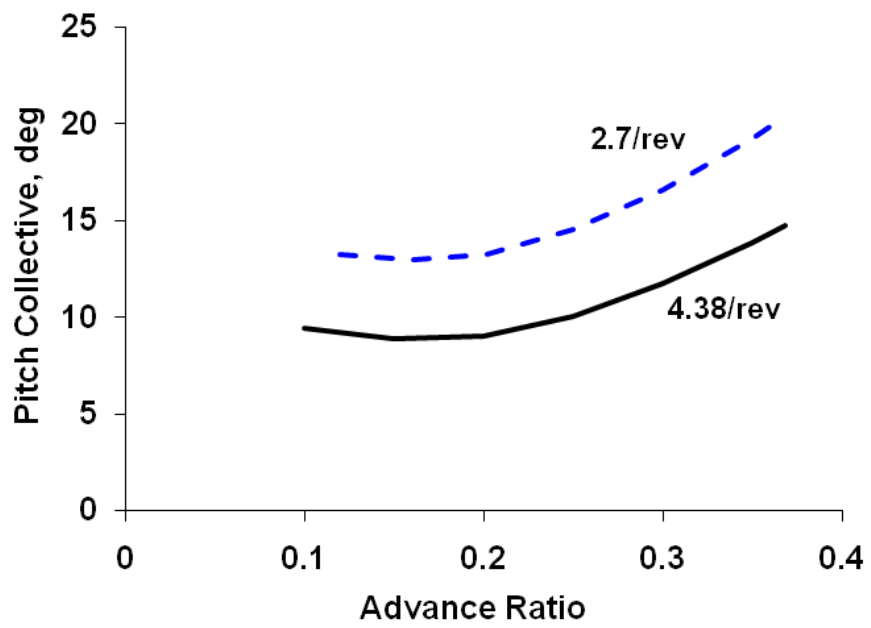
Figure 4.3: Effect of Reduced Torsional Frequency on Pitch Collective for Rotor in Forward Flight, $C_W/\sigma = 0.0783$
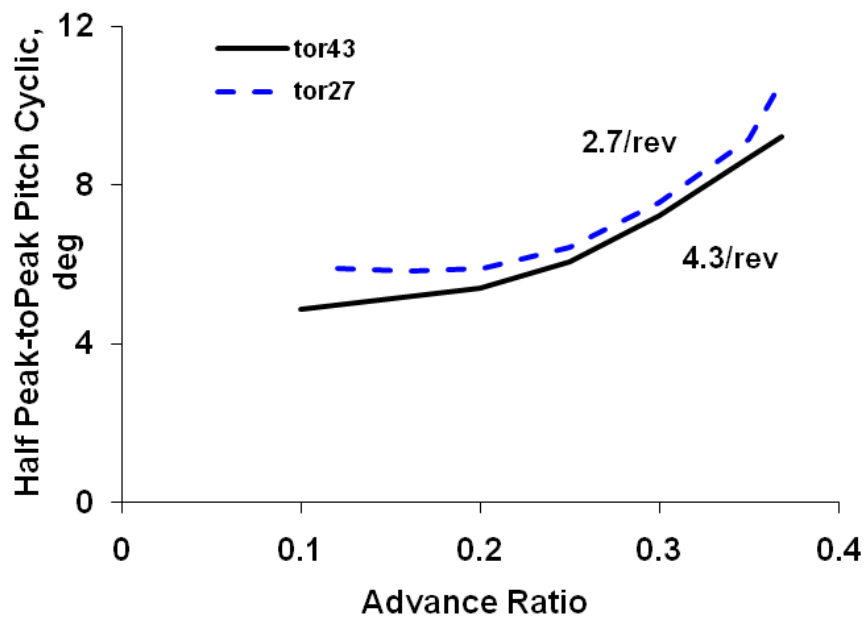
Figure 4.4: Effect of Reduced Torsional Frequency on Half Peak-to-Peak Pitch Cyclic for Rotor in Forward Flight, $C_W/\sigma = 0.0783$
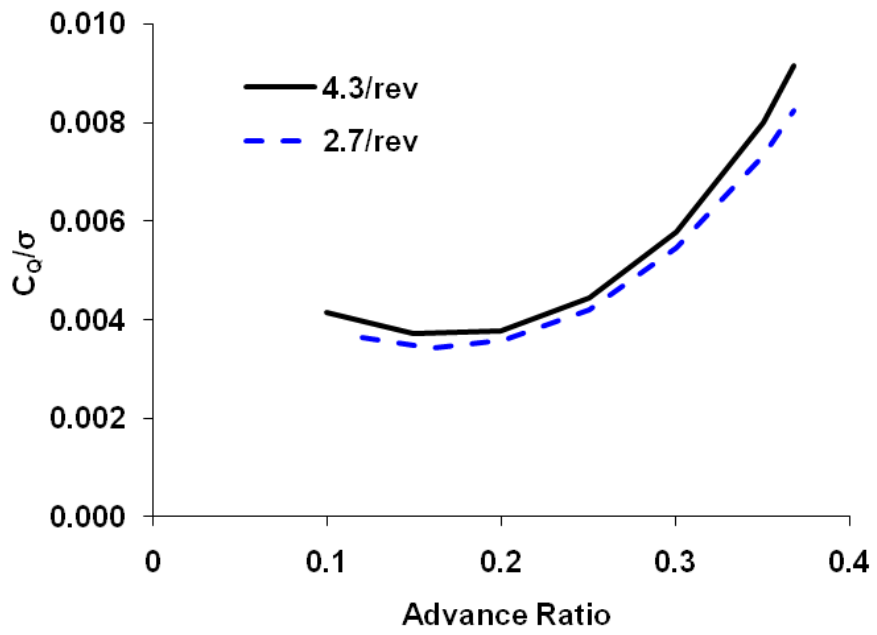
Figure 4.5: Effect of Reduced Torsional Frequency on Predicted Power for Rotor in Forward Flight, $C_W/\sigma = 0.0783$
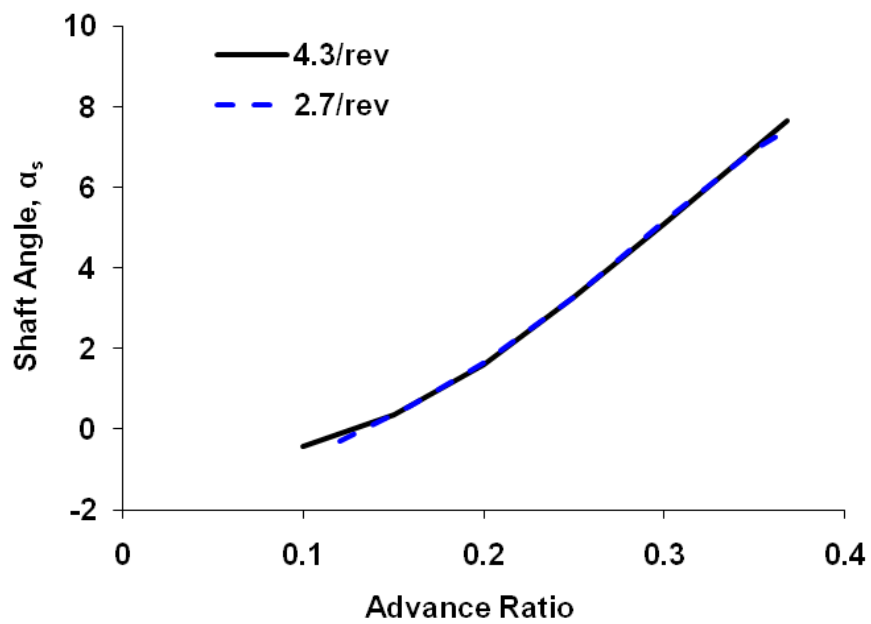
Figure 4.6: Effect of Reduced Torsional Frequency on Predicted Shaft Angles for Baseline in Forward Flight, $C_W/\sigma = 0.0783$
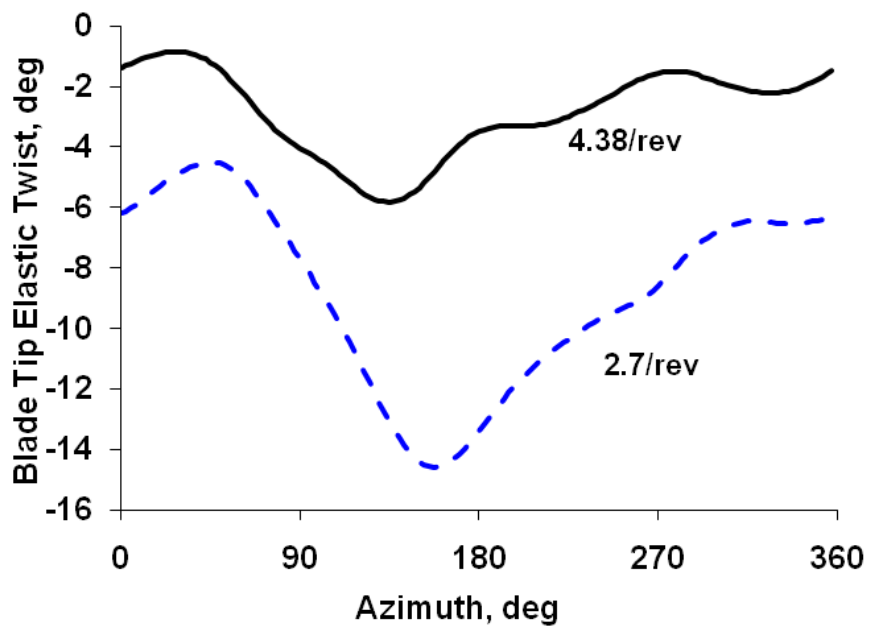
Figure 4.7: Effect of Reduced Torsional Frequency on Blade Tip Elastic Twist Distribution for Rotor in Forward Flight, $\mu = 0.368$, $C_W/\sigma = 0.0783$
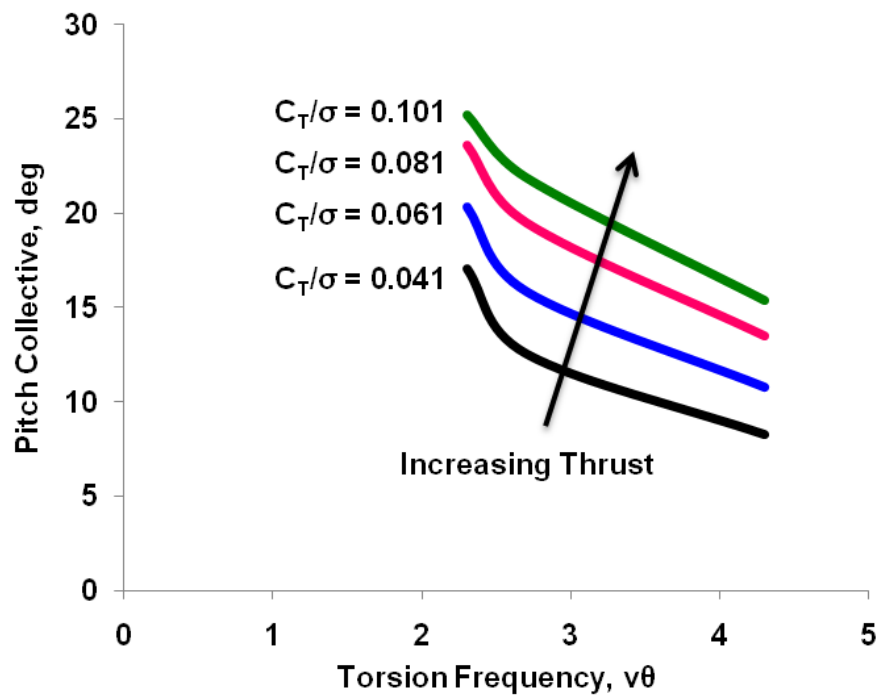
Figure 4.8: Variation of Pitch Collective with Torsional Frequency for a Range of Thrust in Hover
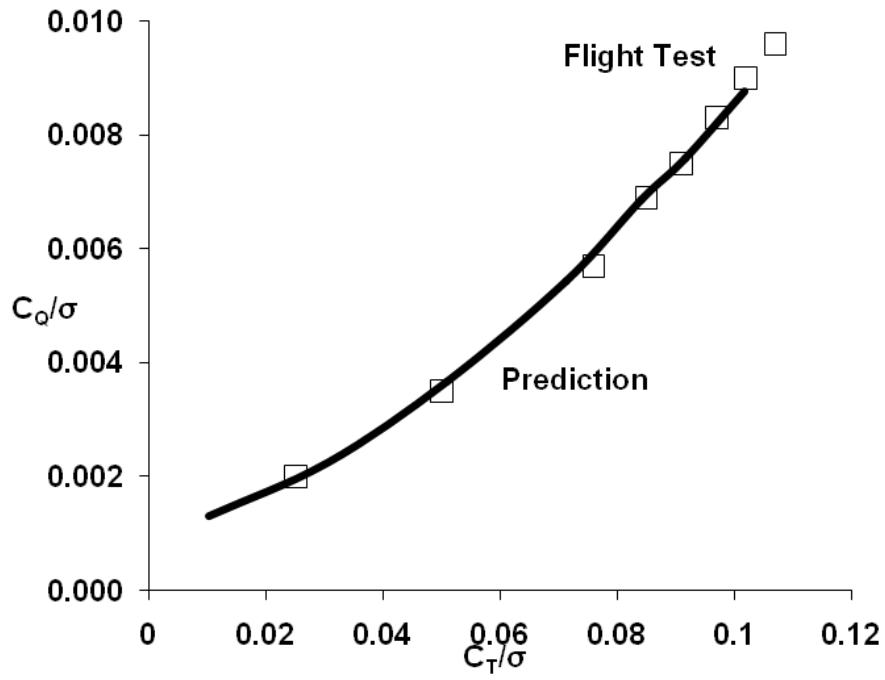
Figure 4.9: Predicted and Measured Power for UH-60A in Hover, Uniform Inflow
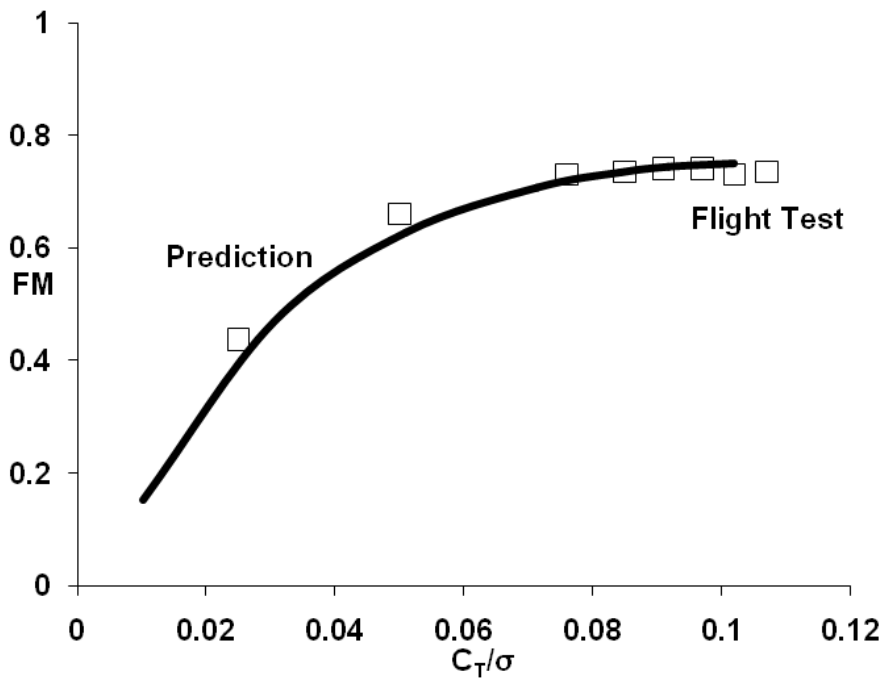
Figure 4.10: Predicted and Measured Figure of Merit for UH-60A in Hover, Uniform

Inflow
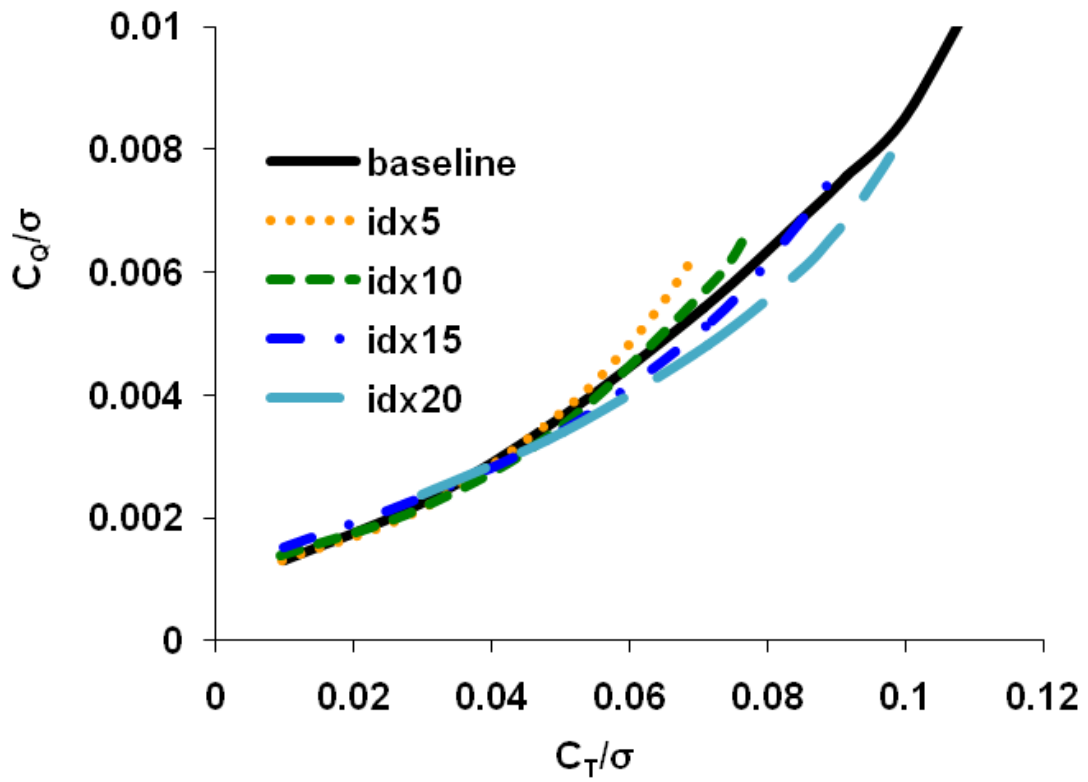
Figure 4.11: Effect of Index Angle (idx) on Predicted Power, in Hover
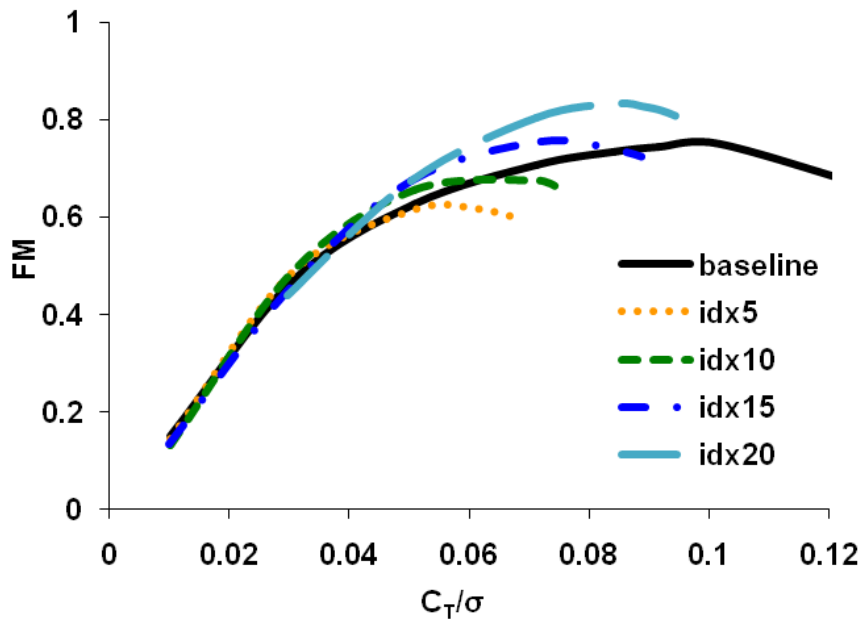
Figure 4.12: Effect of Index Angle on Figure of Merit
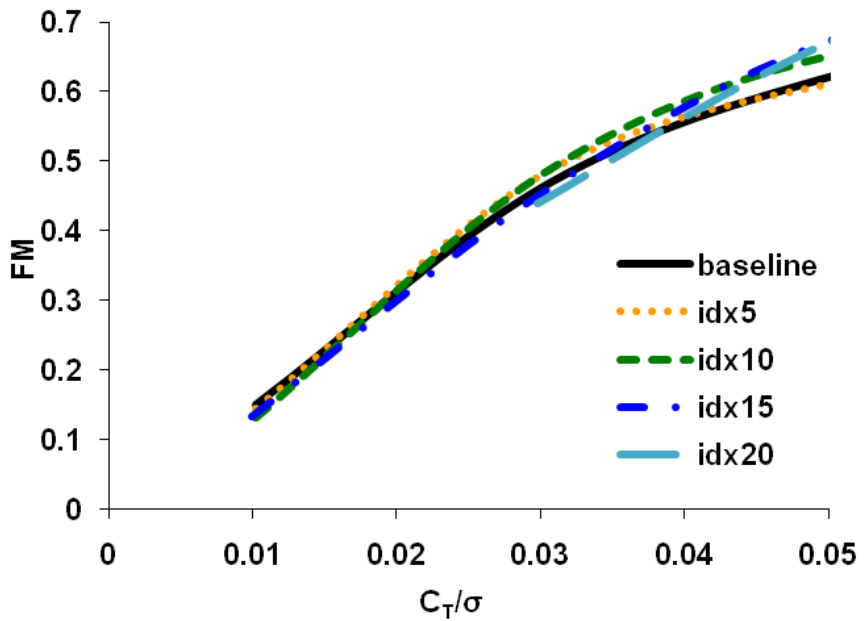
Figure 4.13: Effect of Index Angle on Figure of Merit at Low Thrust
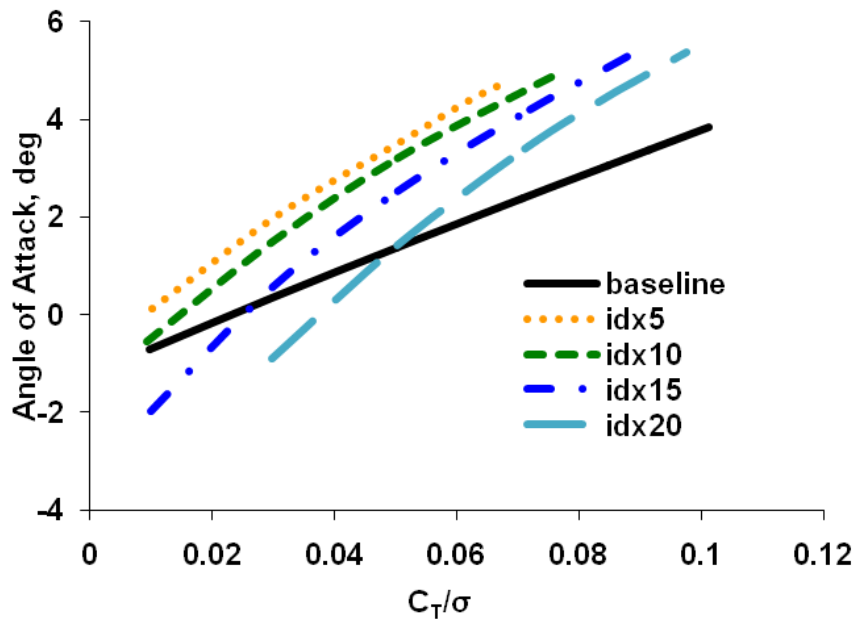
Figure 4.14: Effect of Index Angle on Blade Angle of Attack at 75%R, in Hover
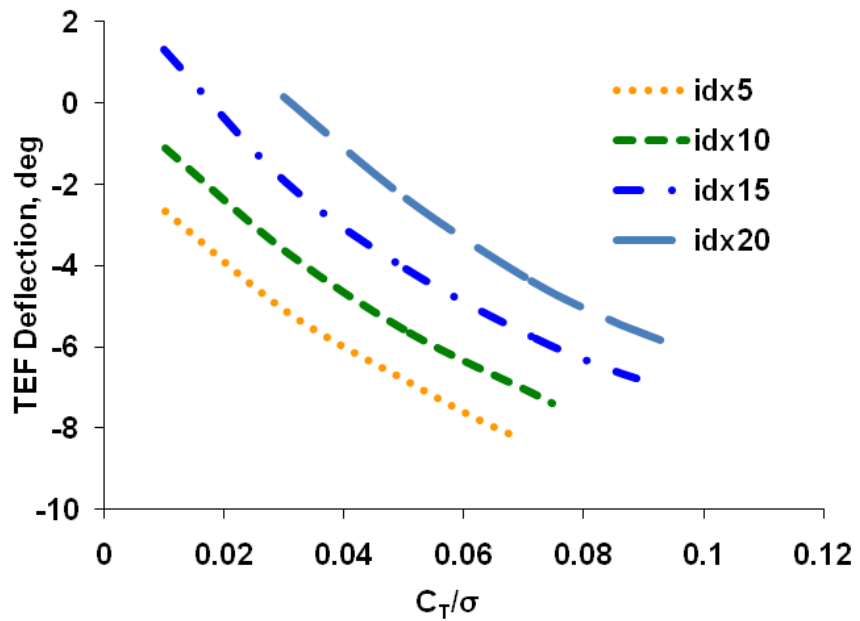
Figure 4.15: Effect of Index Angle on Required TEF Deflection, in Hover
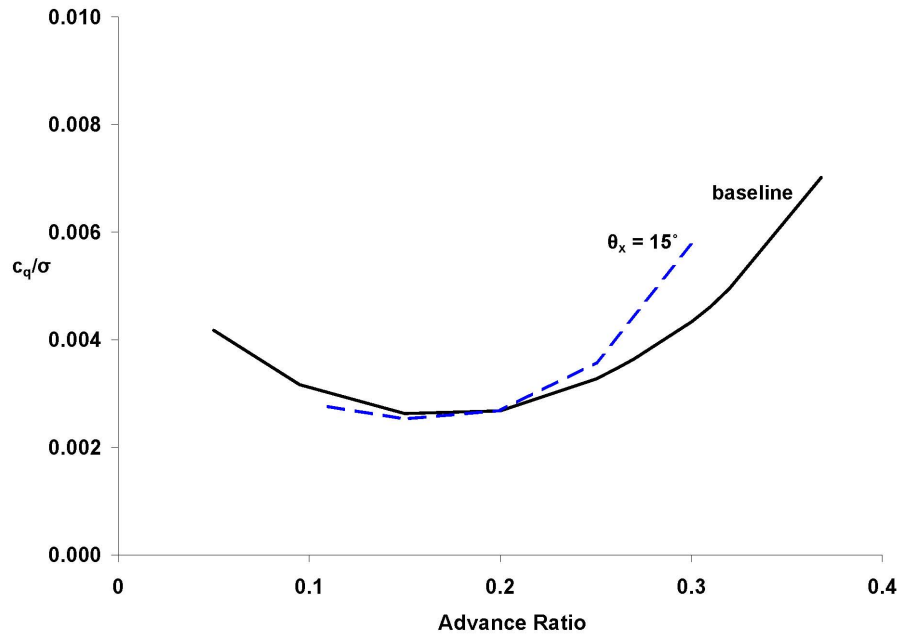
Figure 4.16: Predicted Power in Forward Flight, $C_W/\sigma = 0.0783$, Uniform Inflow
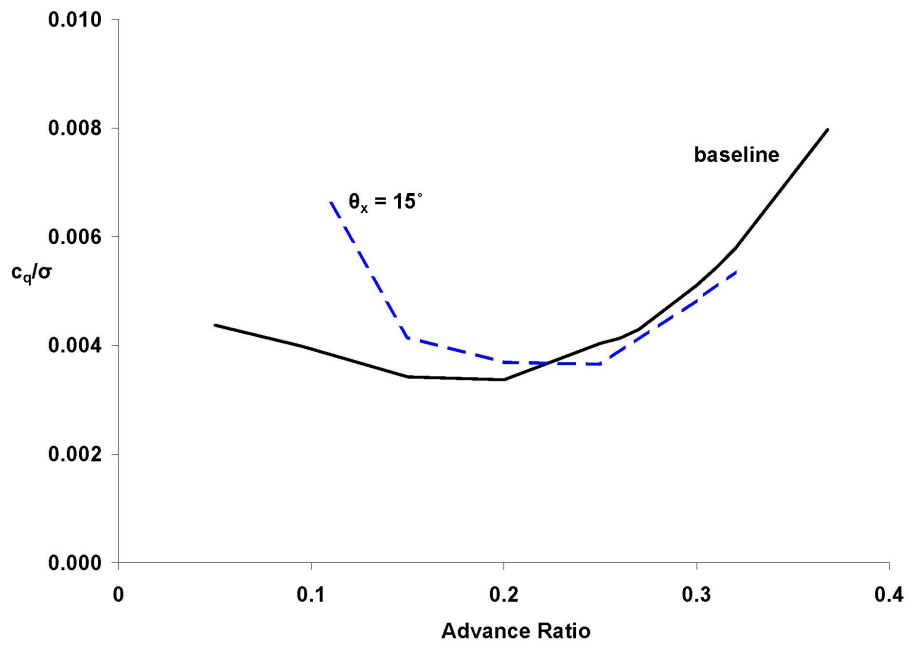
Figure 4.17: Predicted Power in Forward Flight, $C_W/\sigma = 0.0783$, Free Wake
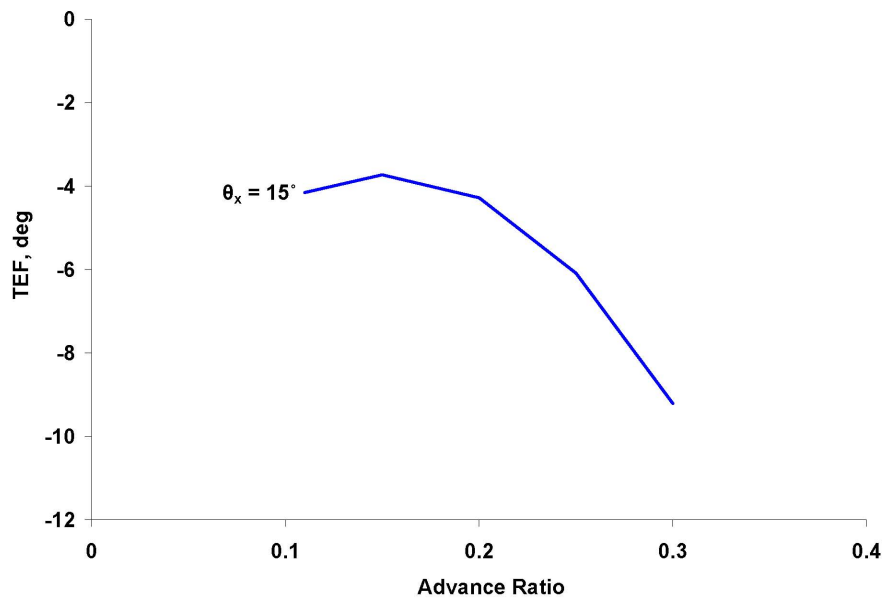
Figure 4.18: Mean Flap Control Angles in Forward Flight, $C_W/\sigma = 0.0783$, Uniform Inflow
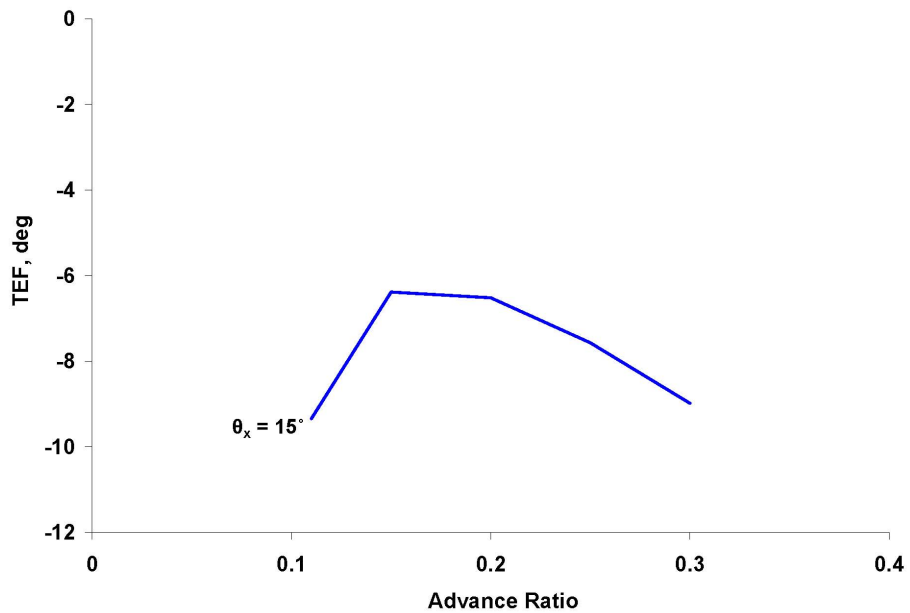
Figure 4.19: Mean Flap Control Angles in Forward Flight, $C_W/\sigma = 0.0783$, Free Wake
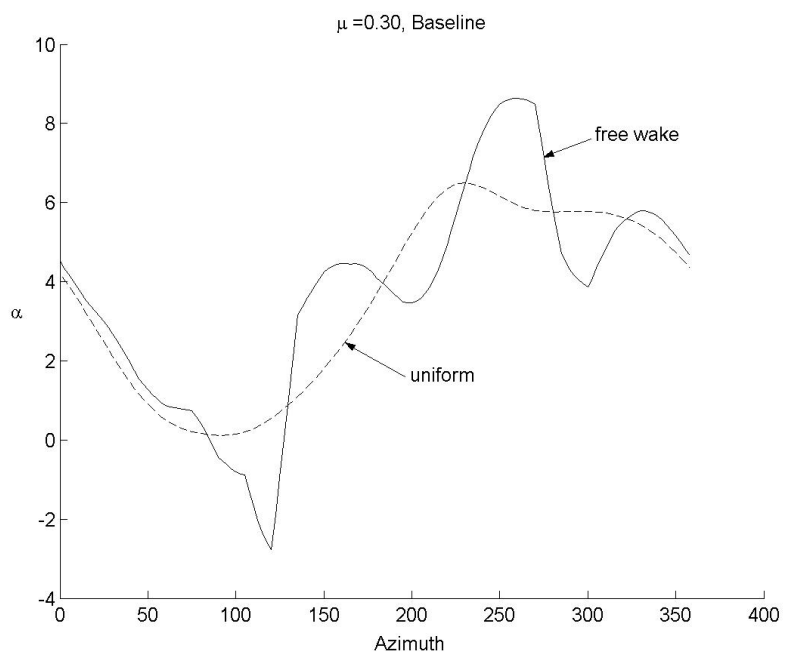
Figure 4.20: Angle of Attack vs Azimuth, Baseline Rotor, for $\mu = 0.30$ at 0.75R
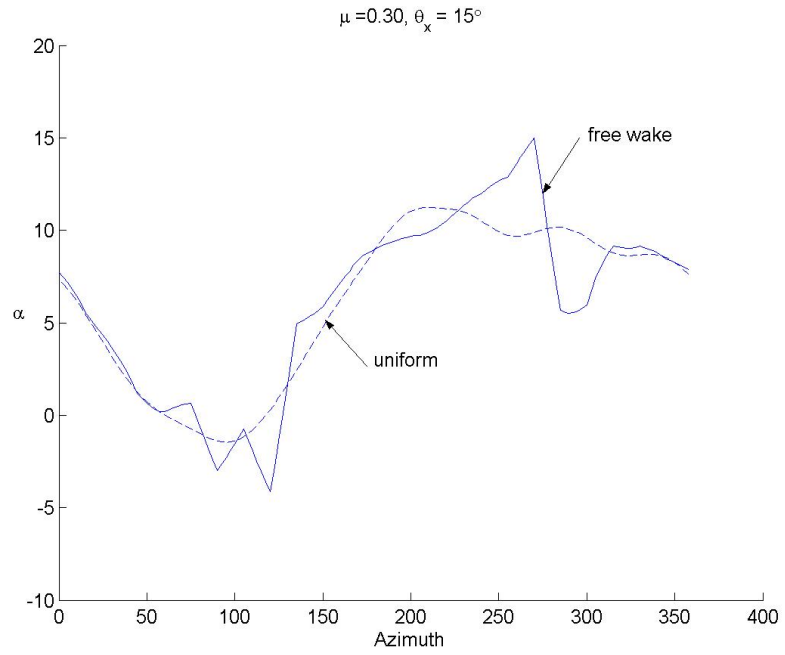
Figure 4.21: Angle of Attack vs Azimuth, Swashplateless, for $\mu = 0.30$ at 0.75R
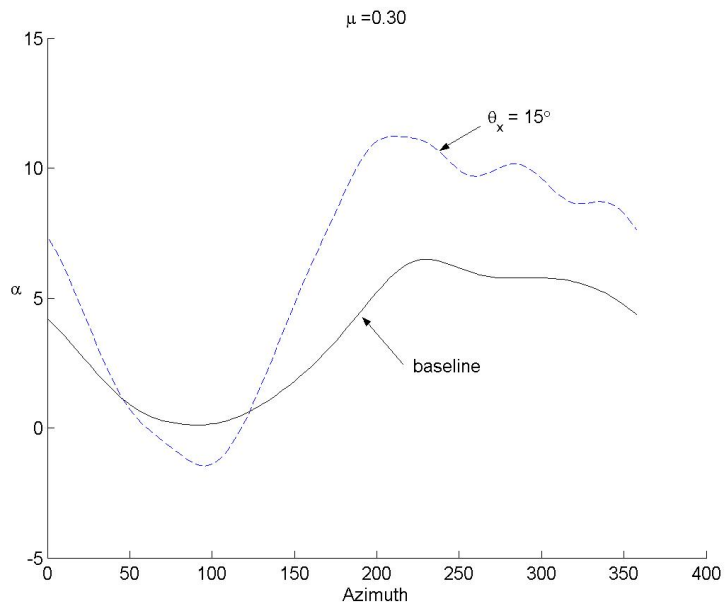
Figure 4.22: Angle of Attack vs Azimuth, Baseline and Swashplateless Rotors, Uniform Inflow, for $\mu = 0.30$ at 0.75R
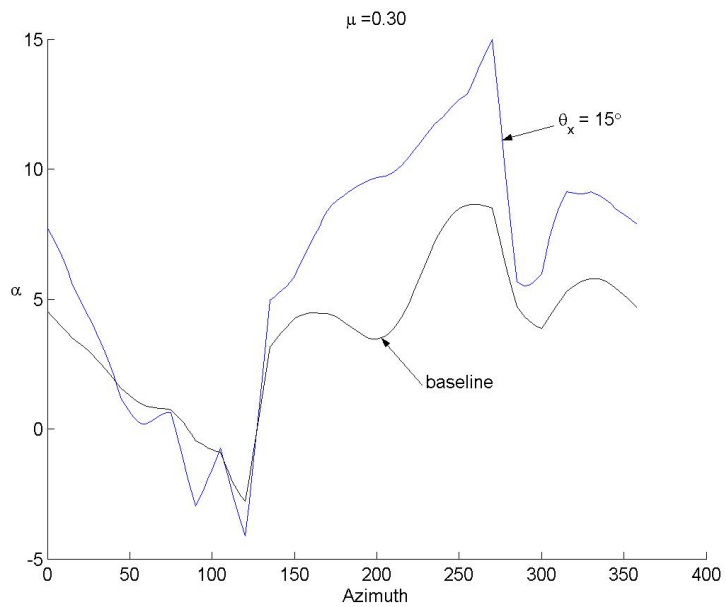
Figure 4.23: Angle of Attack vs Azimuth, Baseline and Swashplateless Rotors, Free Wake, for $\mu = 0.30$ at 0.75R
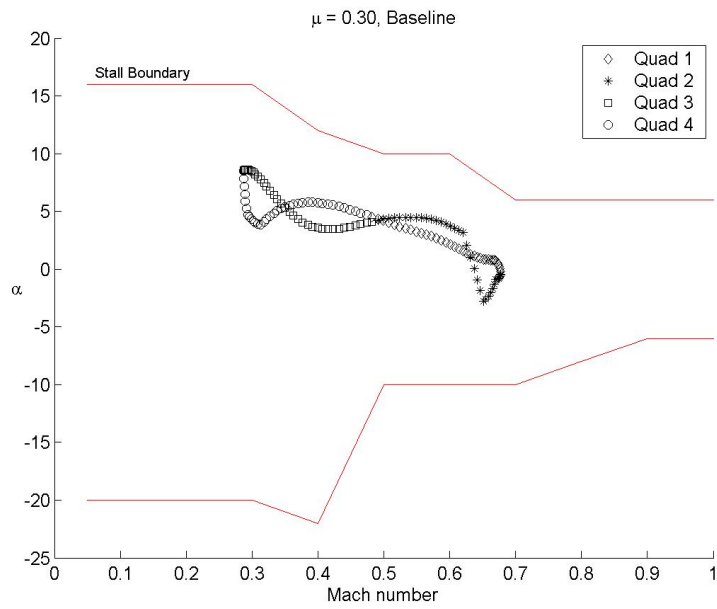
Figure 4.24: Angle of Attack vs Mach Number, Baseline Rotor, Free Wake, for $\mu = 0.30$ at 0.75R
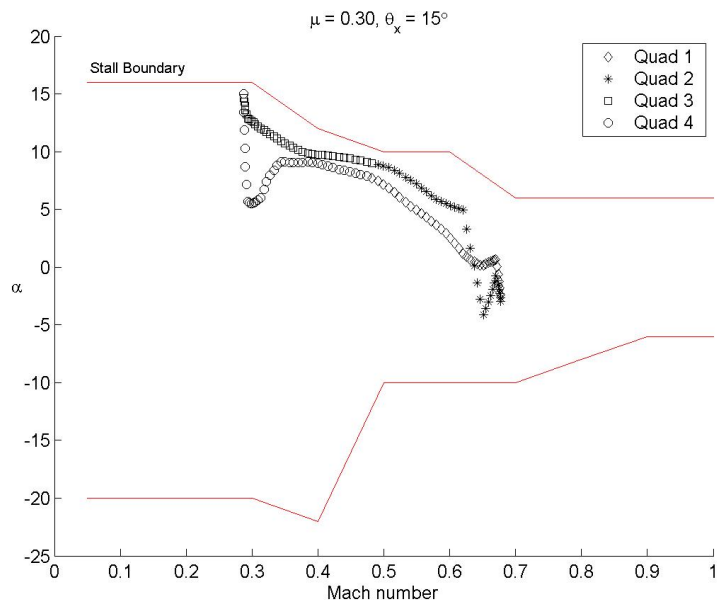
Figure 4.25: Angle of Attack vs Mach Number, Swashplateless Rotor, Free Wake, for $\mu = 0.30$ at 0.75R
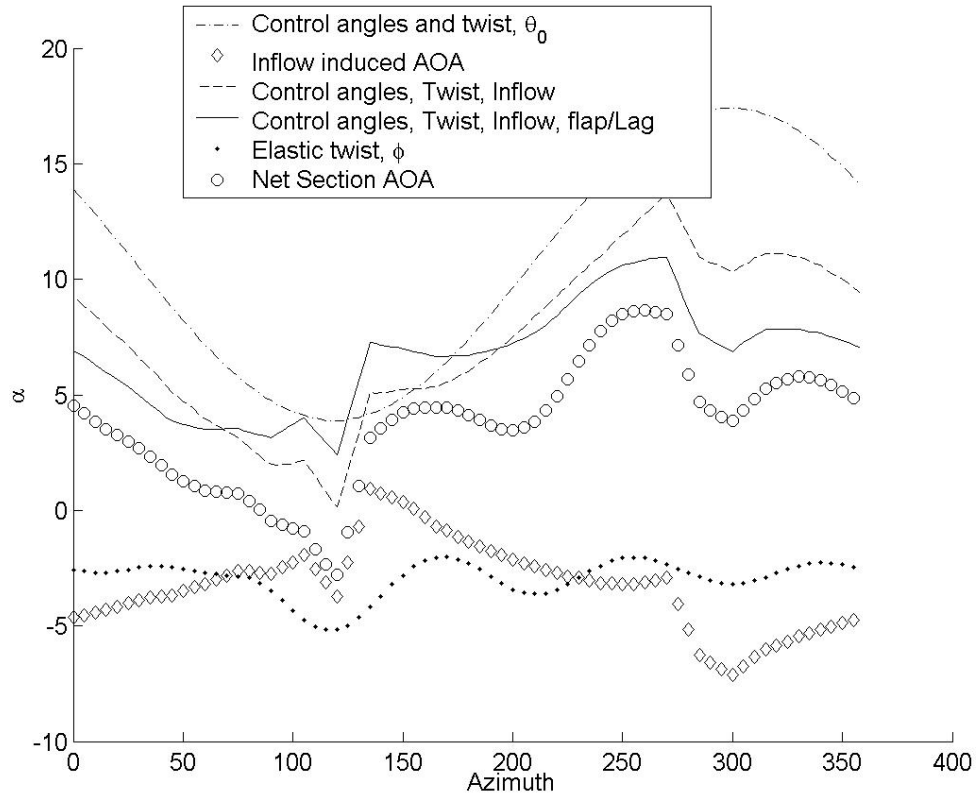
Figure 4.26: Angle of Attack Components, Baseline Rotor, Free Wake, for $\mu = 0.30$ at 0.75R

μ = 0.30, θ_x = 15°
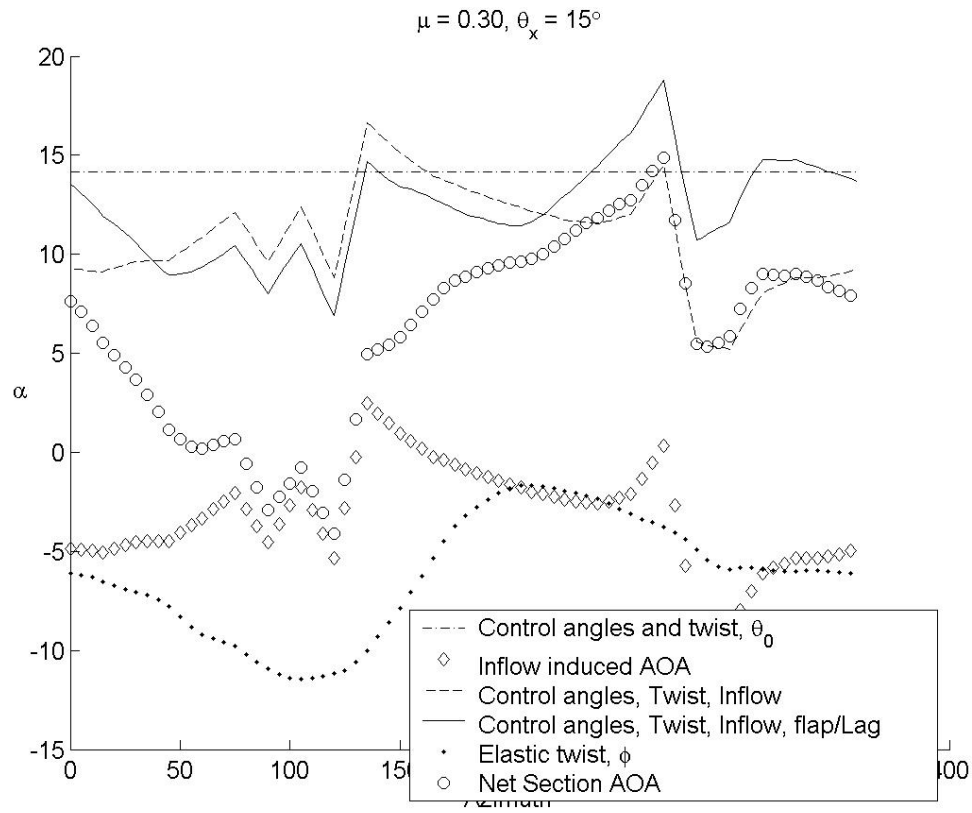
Figure 4.27: Angle of Attack Components, Swashplateless Rotor, Free Wake, for μ = 0.30 at 0.75R
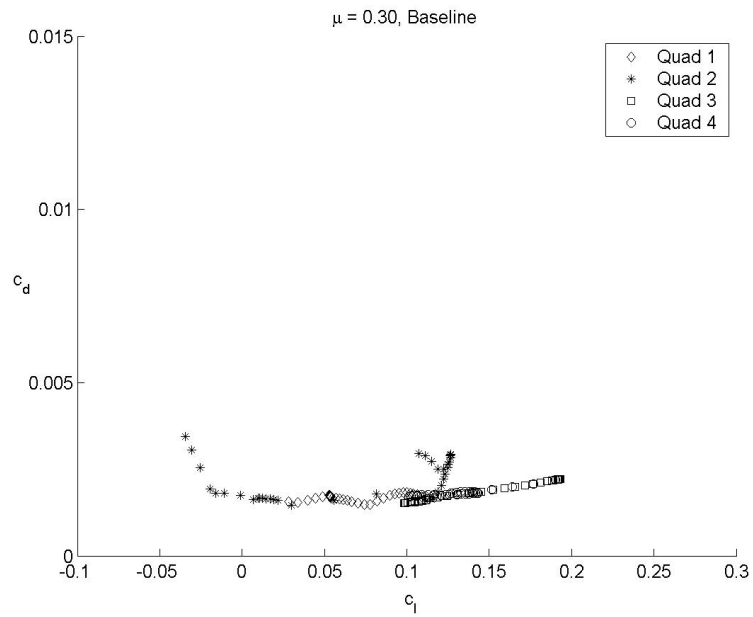
Figure 4.28: Lift and Drag Envelope, Baseline Rotor, Free Wake, for $\mu = 0.30$ at 0.75R
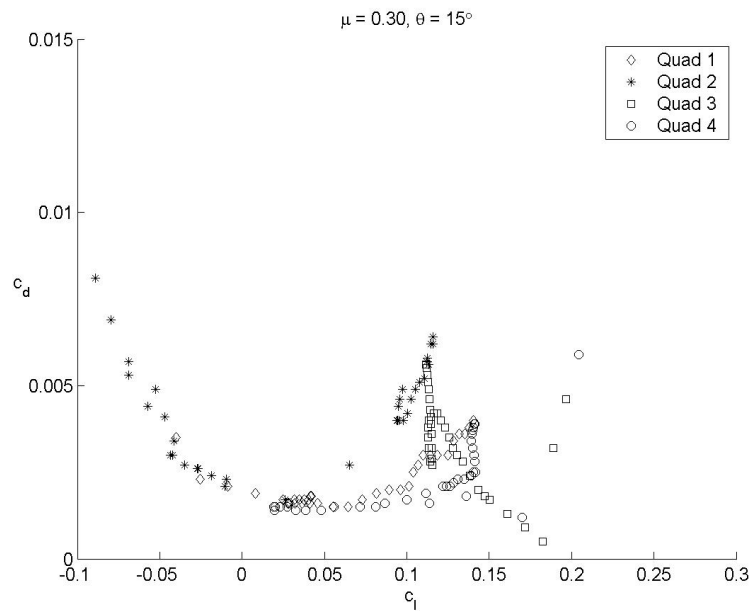
Figure 4.29: Lift and Drag Envelope, Swashplateless Rotor, Free Wake, for $\mu = 0.30$ at 0.75R
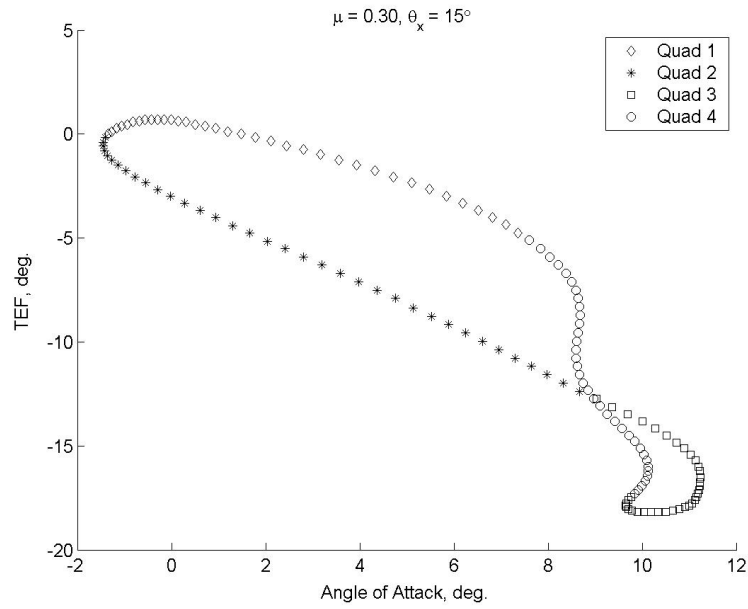
Figure 4.30: TEF vs. Angle of Attack, Swashplateless Rotor, Uniform Inflow, for μ = 0.30 at 0.75R

Figure 4.31: TEF vs. Angle of Attack, Swashplateless Rotor, Free Wake, for μ = 0.30 at 0.75R
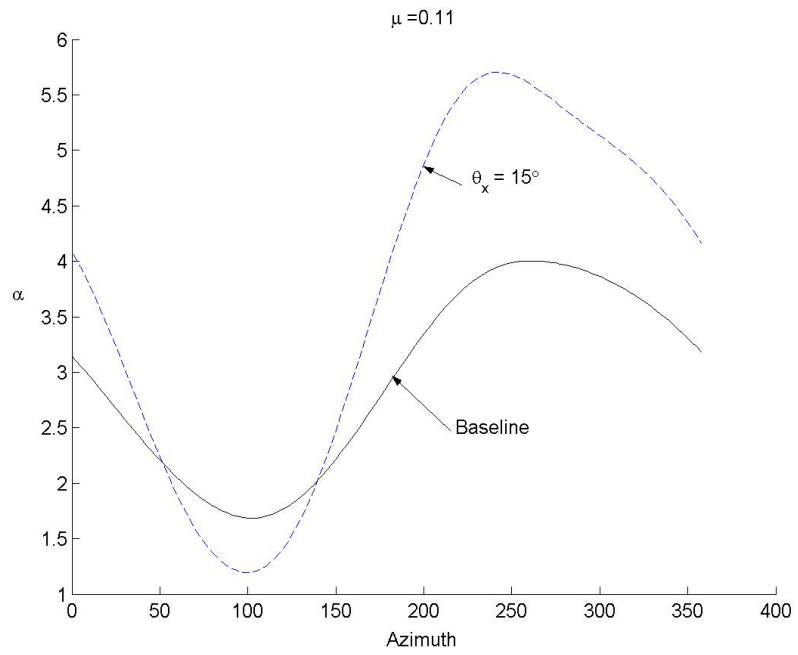
Figure 4.32: Angle of Attack vs Azimuth, Baseline and Swashplateless Rotors, Uniform Inflow, for $\mu = 0.11$ at 0.75R
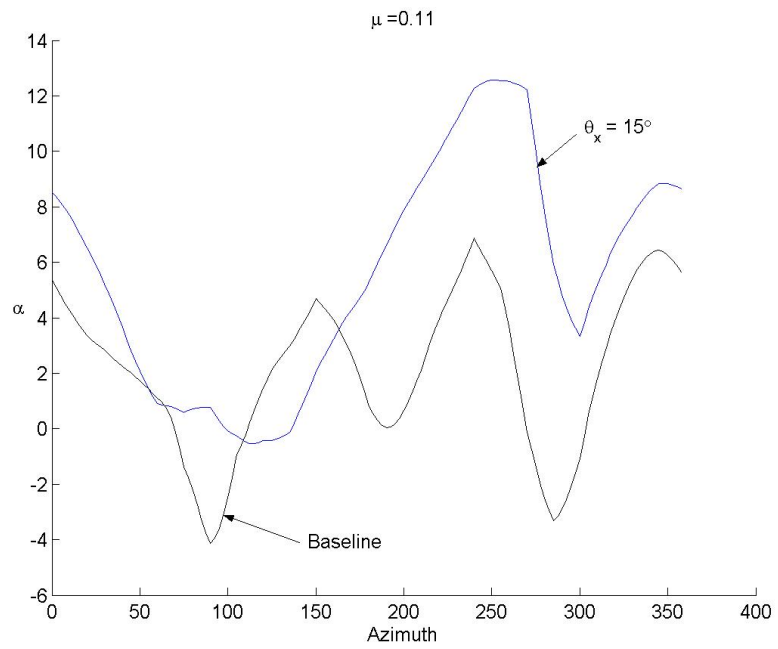
Figure 4.33: Angle of Attack vs Azimuth, Baseline and Swashplateless Rotors, Free
Wake, for $\mu = 0.11$ at 0.75R
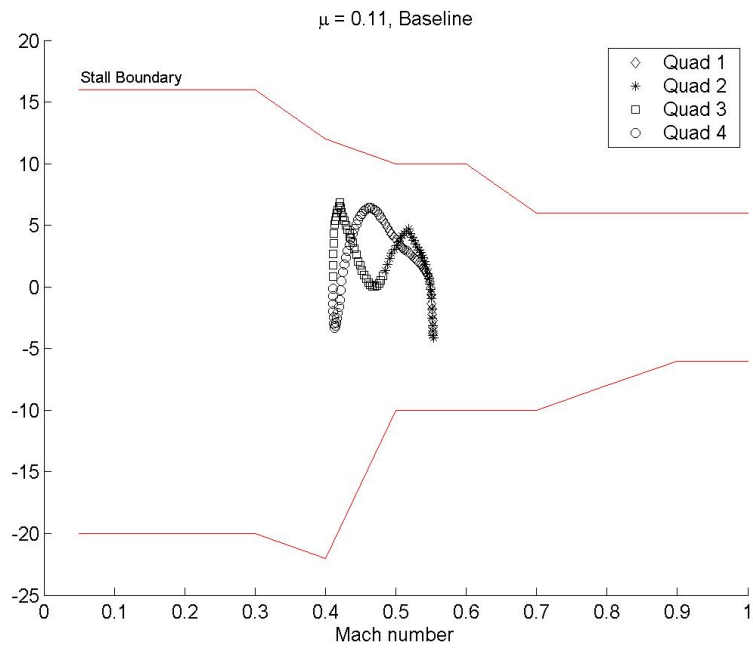
Figure 4.34: Angle of Attack vs Mach Number, Baseline Rotor, Free Wake, for $\mu = 0.11$ at 0.75R
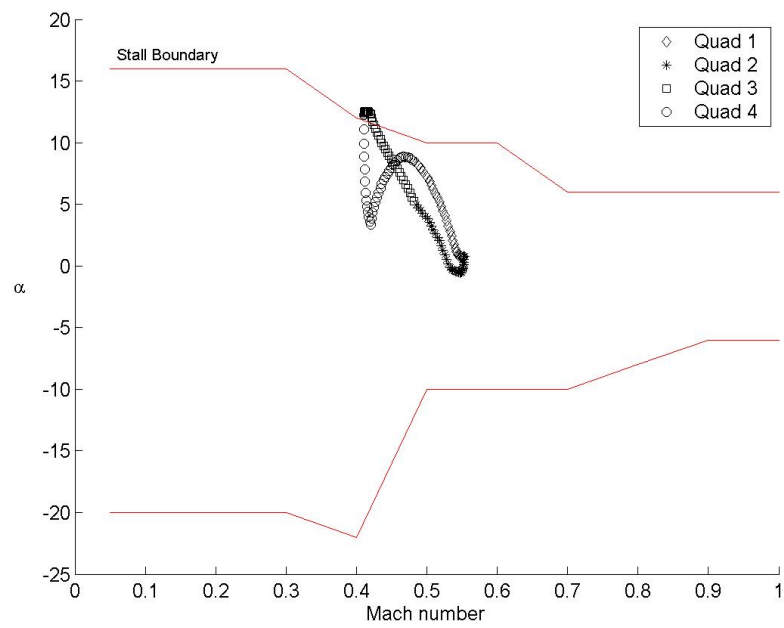
Figure 4.35: Angle of Attack vs Mach Number, Swashplateless Rotor, Free Wake, for $\mu = 0.11$ at 0.75R
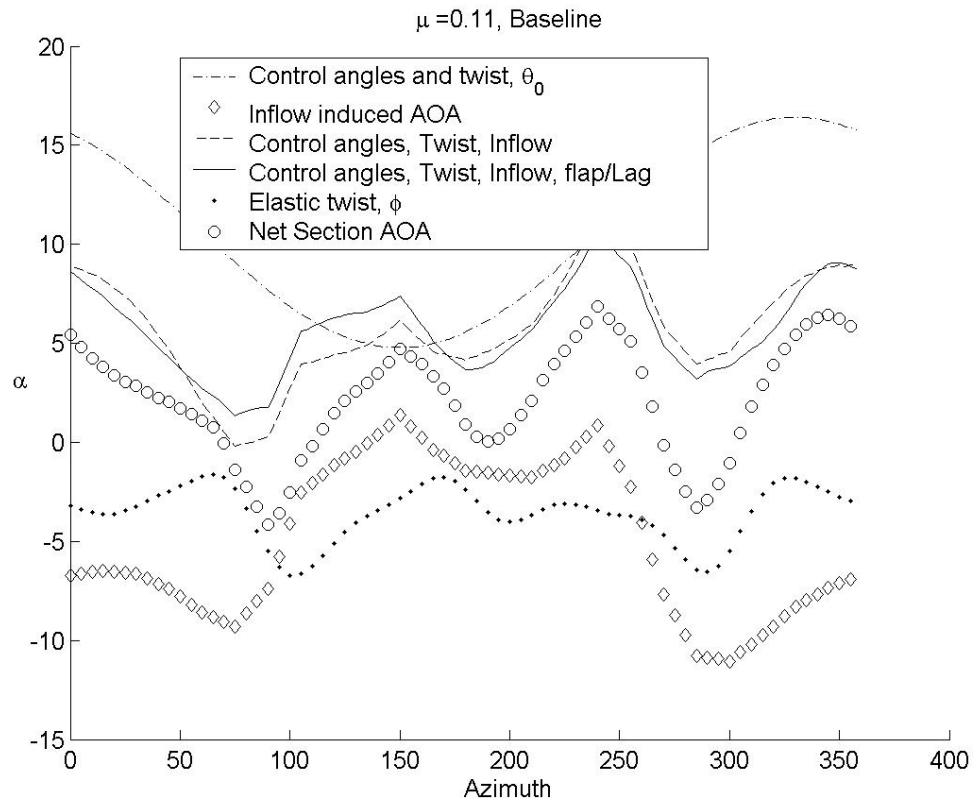
Figure 4.36: Angle of Attack Components, Baseline Rotor, Free Wake, for $\mu = 0.11$ at 0.75R
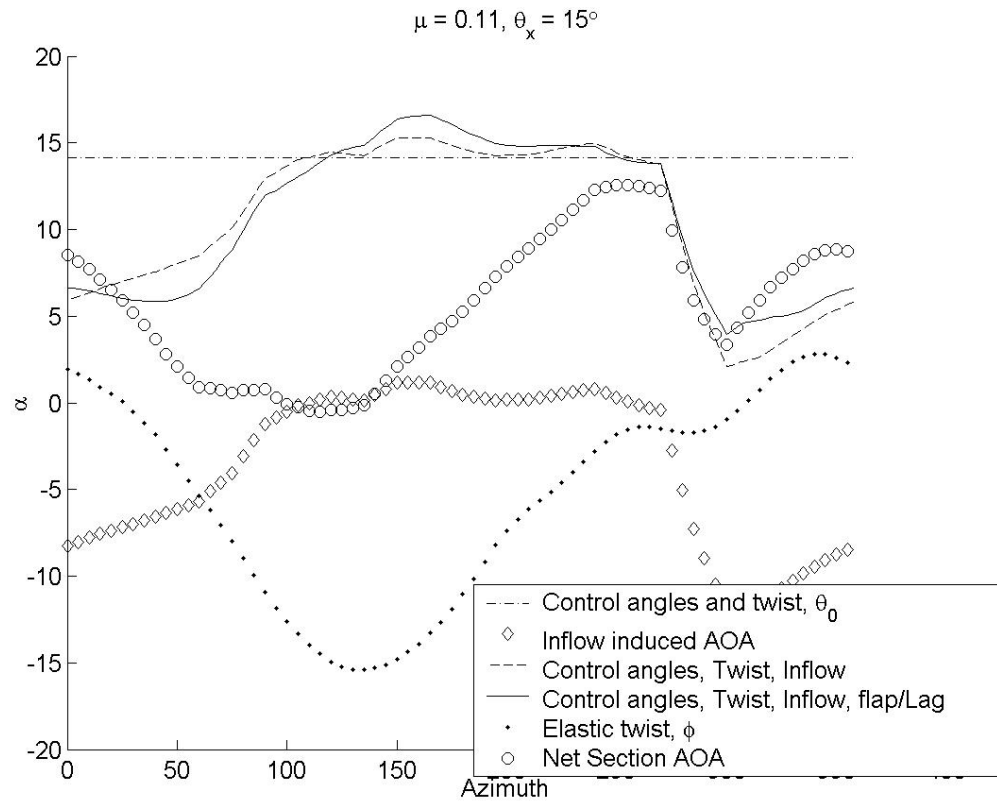
Figure 4.37: Angle of Attack Components, Swashplateless Rotor, Free Wake, for μ = 0.11 at 0.75R
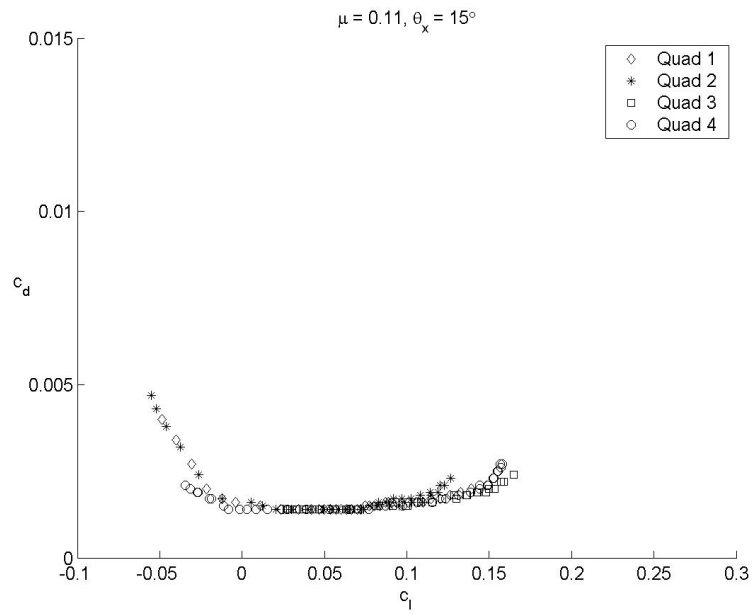
Figure 4.38: Lift and Drag Envelope, Baseline Rotor, Free Wake, for $\mu = 0.11$ at 0.75R
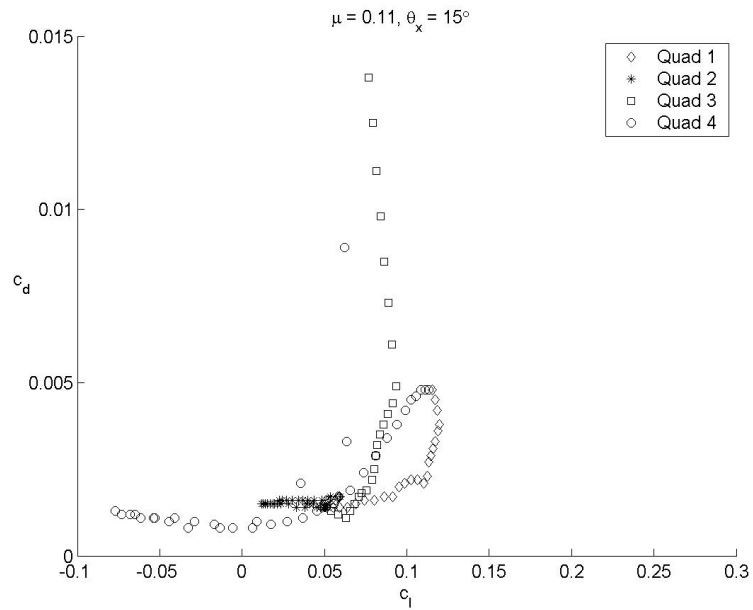
Figure 4.39: Lift and Drag Envelope, Swashplateless Rotor, Free Wake, for $\mu = 0.11$ at 0.75R

244
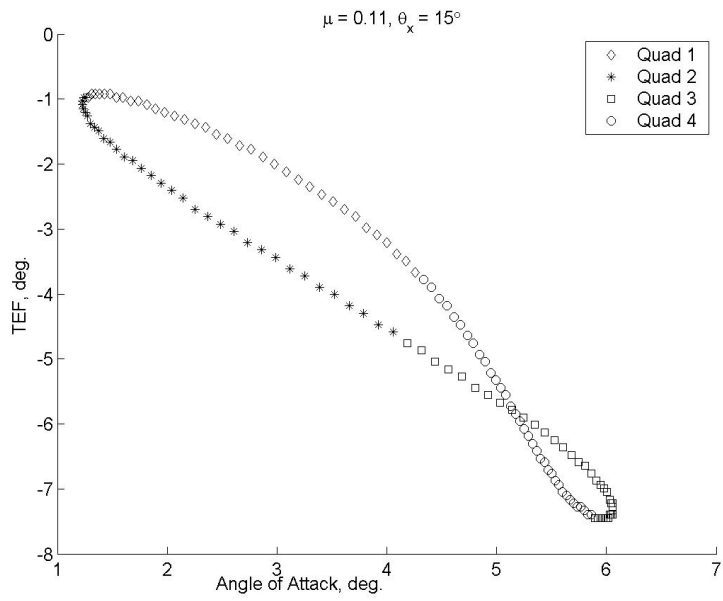
Figure 4.40: TEF vs. Angle of Attack, Swashplateless Rotor, Uniform Inflow, for μ = 0.11 at 0.75R

Figure 4.41: TEF vs. Angle of Attack, Swashplateless Rotor, Free Wake, for μ = 0.11 at 0.75R
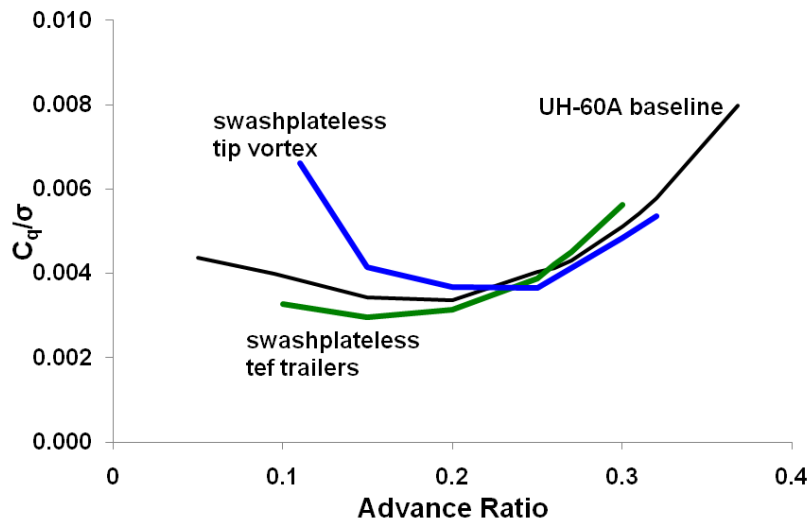
(a) TEF Trailers Compared to Tip Vortex Model
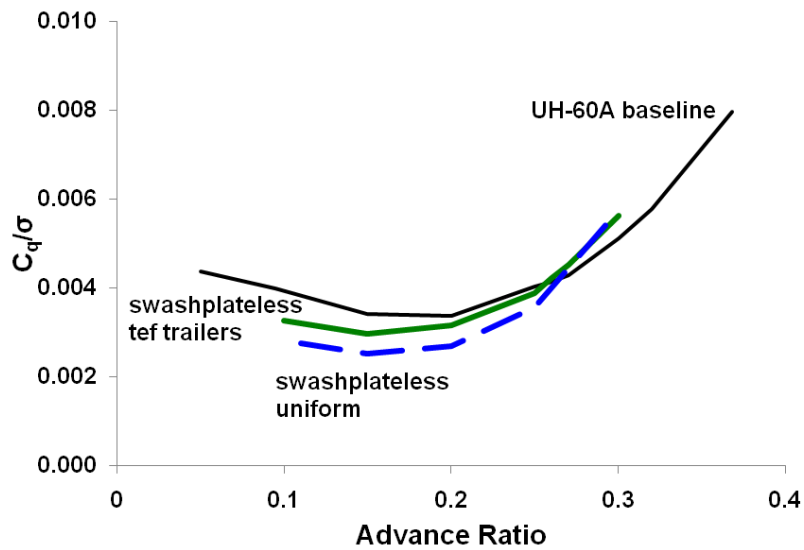
(b) TEF Trailers Compared to Uniform Inflow

Figure 4.42: Effect of Free Wake Model on Predicted Power in Forward Flight, $C_W/\sigma = 0.0783$
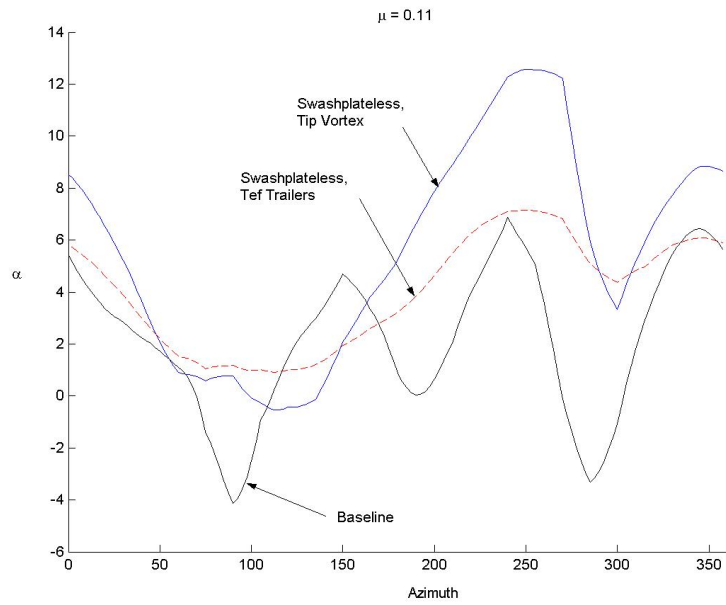
Figure 4.43: Angle of Attack vs. Azimuth, Baseline and Swashplateless Rotors, Tip Vortex and TEF Trailer Wake Models, for $\mu = 0.11$ at 0.75R
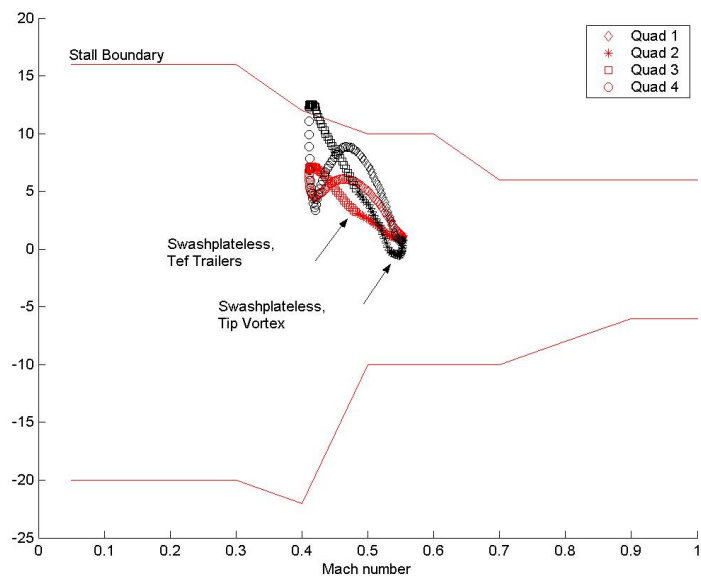
Figure 4.44: Angle of Attack vs Mach Number, Swashplateless Rotor, TEF Trailer Wake Model, for $\mu = 0.11$ at 0.75R
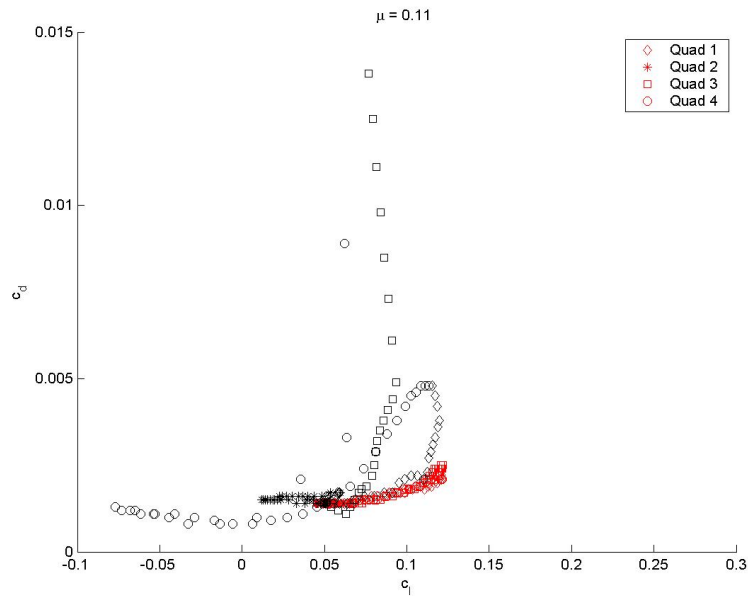
Figure 4.45: Lift and Drag Envelope, Swashplateless Rotor, TEF Trailer Wake Model, for $\mu = 0.11$ at 0.75R
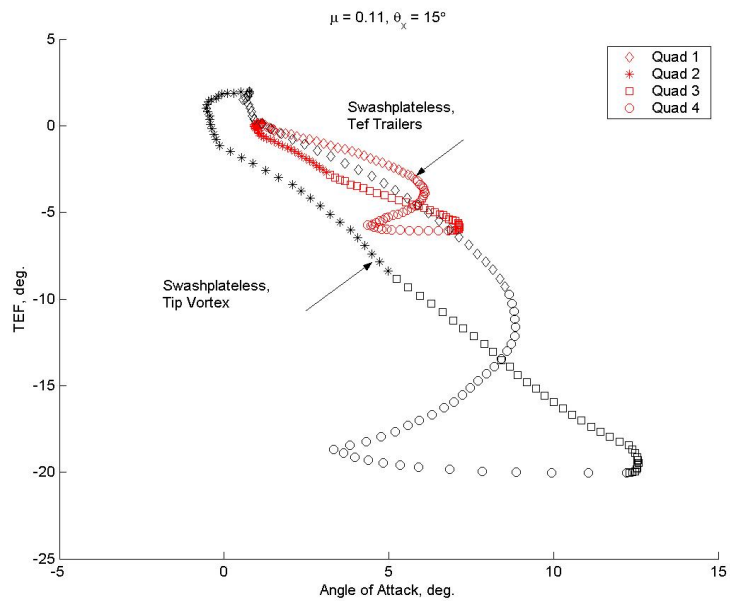
Figure 4.46: TEF vs. Angle of Attack, Swashplateless Rotor, Tip Vortex and TEF Trailer Wake Models, for $\mu = 0.11$ at 0.75R
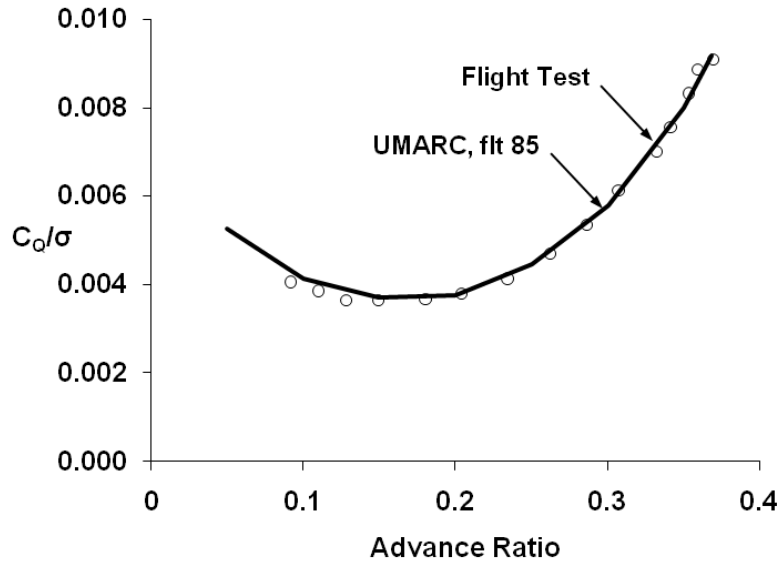
Figure 4.47: Predicted and Measured Power for UH-60A in Forward Flight, $C_W/\sigma = 0.0783$, W-L Near Wake and Free Wake
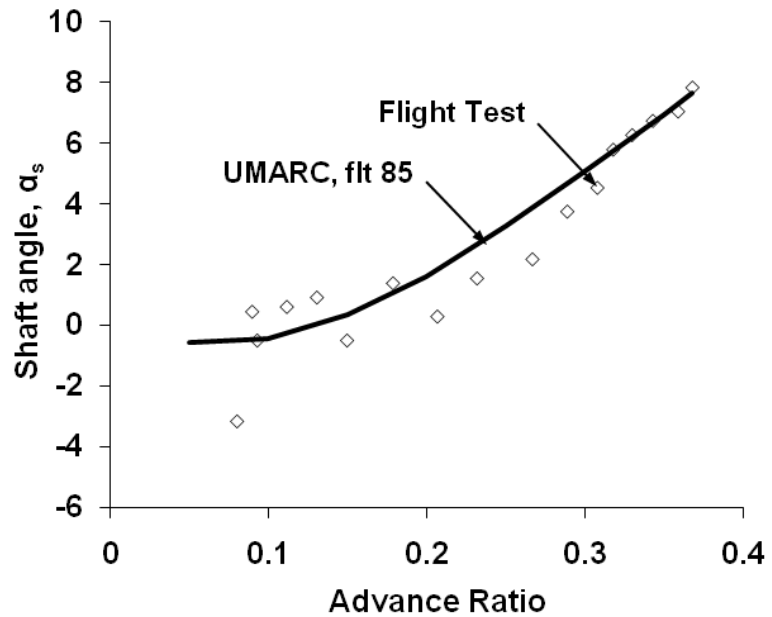
Figure 4.48: Predicted and Measured Rotor Shaft Angles for UH-60A in Forward Flight, $C_W/\sigma = 0.0783$
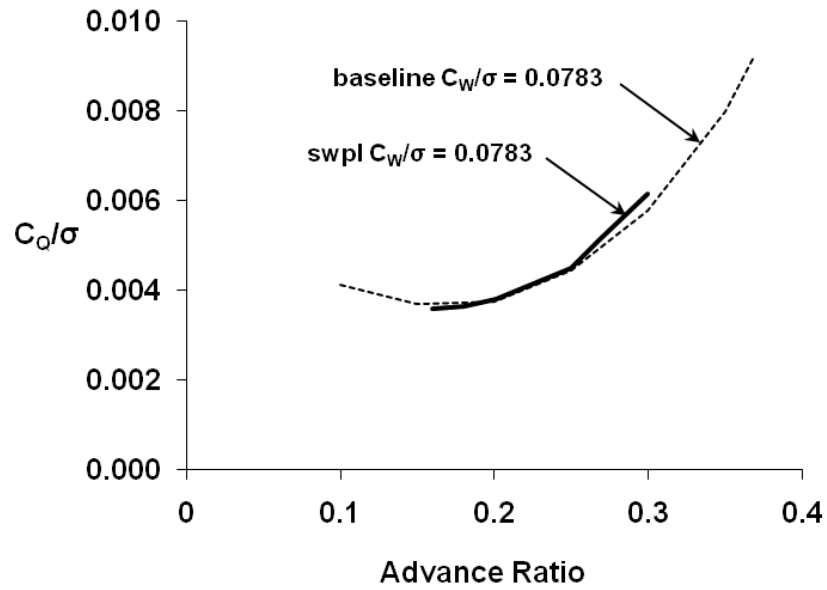
Figure 4.49: Predicted Power of Swashplateless Rotor in Forward Flight, TEF Trailer Wake Model, Vehicle Trim, $C_W/\sigma = 0.0783$
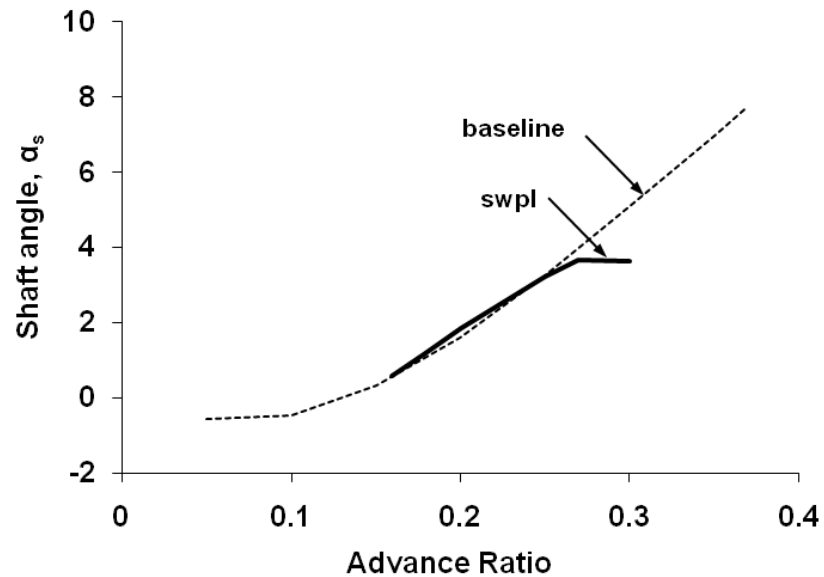
Figure 4.50: Predicted Shaft Angles of Swashplateless Rotor in Forward Flight, TEF Trailer Wake Model, Vehicle Trim, $C_W/\sigma = 0.0783$
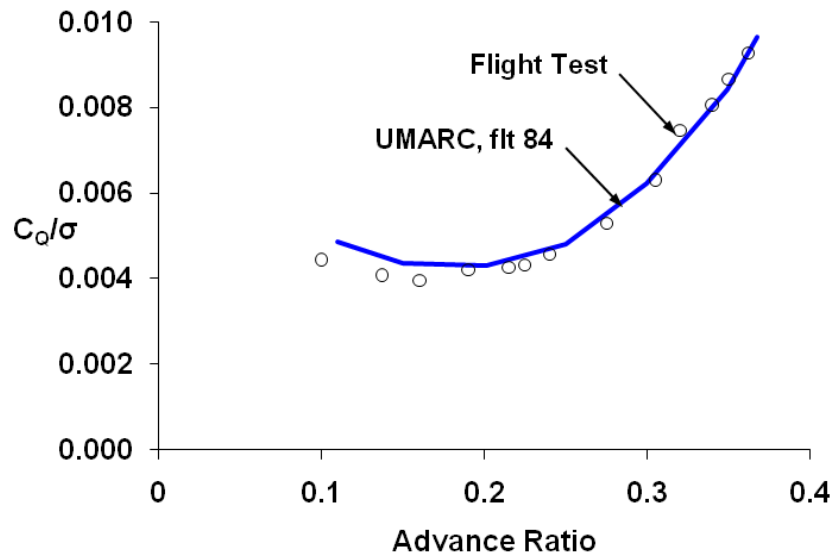
Figure 4.51: Predicted and Measured Power for UH-60A in Forward Flight, $C_W/\sigma = 0.0891$, W-L Near Wake and Free Wake
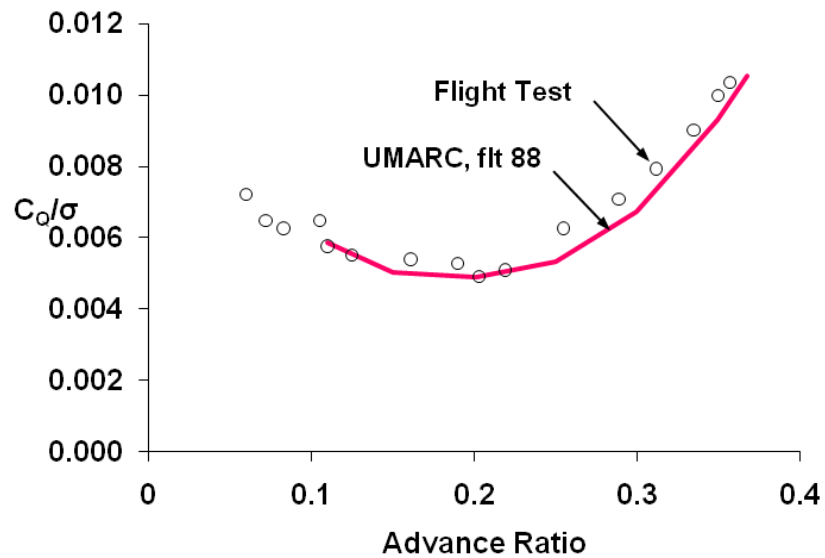
Figure 4.52: Predicted and Measured Power for UH-60A in Forward Flight, $C_W/\sigma = 0.1000$, W-L Near Wake and Free Wake
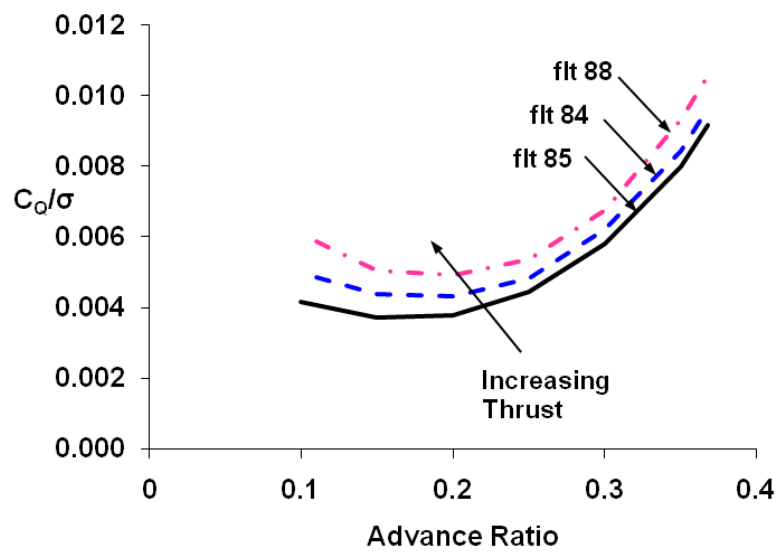
Figure 4.53: Effect of Increasing Thrust on Predicted Power for UH-60A in Forward

Flight. (Flt 85: $C_W/\sigma = 0.0783$; Flt 84: $C_W/\sigma = 0.0891$; Flt 88: $C_W/\sigma = 0.1000$)
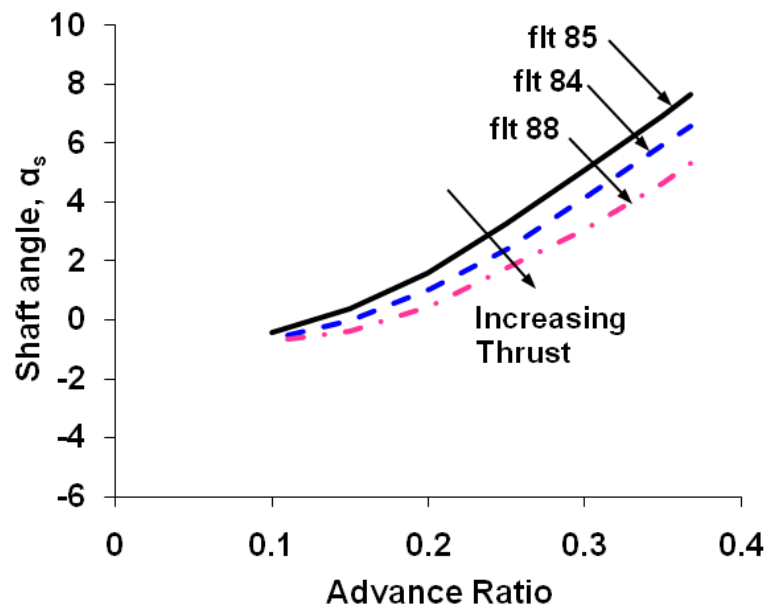
Figure 4.54: Effect of Increasing Thrust on Predicted Rotor Shaft Angles for UH-60A in Forward Flight. (Flt 85: $C_W/\sigma = 0.0783$; Flt 84: $C_W/\sigma = 0.0891$; Flt 88: $C_W/\sigma = 0.1000$)
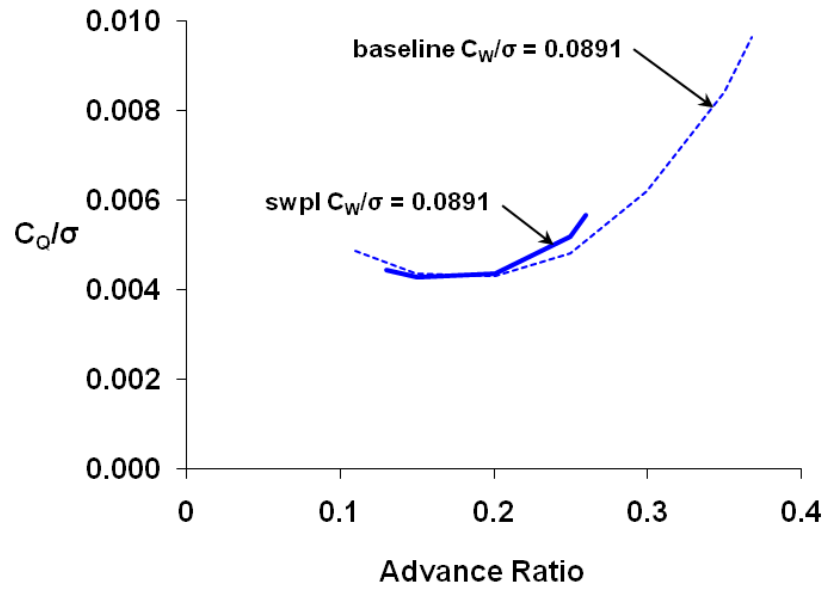
Figure 4.55: Predicted Power of Swashplateless Rotor in Forward Flight, TEF Trailer Wake Model, Vehicle Trim, $C_W/\sigma = 0.0891$
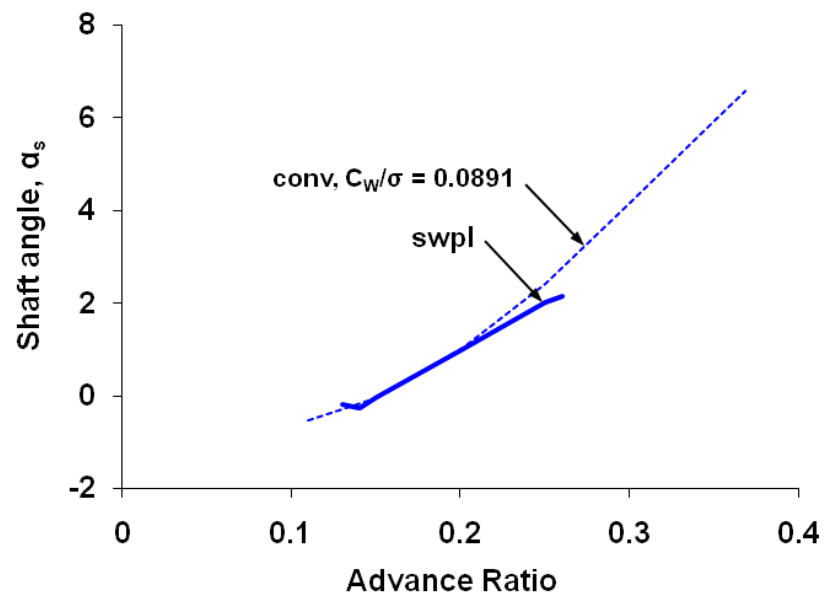
Figure 4.56: Predicted Shaft Angles of Swashplateless Rotor in Forward Flight, TEF Trailer Wake Model, Vehicle Trim, $C_W/\sigma = 0.0891$
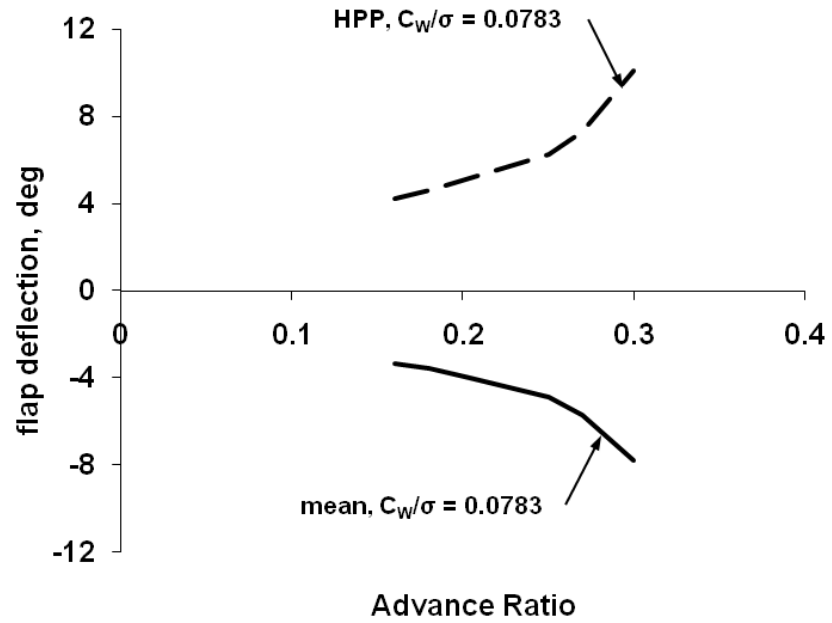
Figure 4.57: Flap Control Angles of Swashplateless Rotor in Forward Flight, TEF
Trailer Wake Model, Vehicle Trim, $C_W/\sigma = 0.0783$
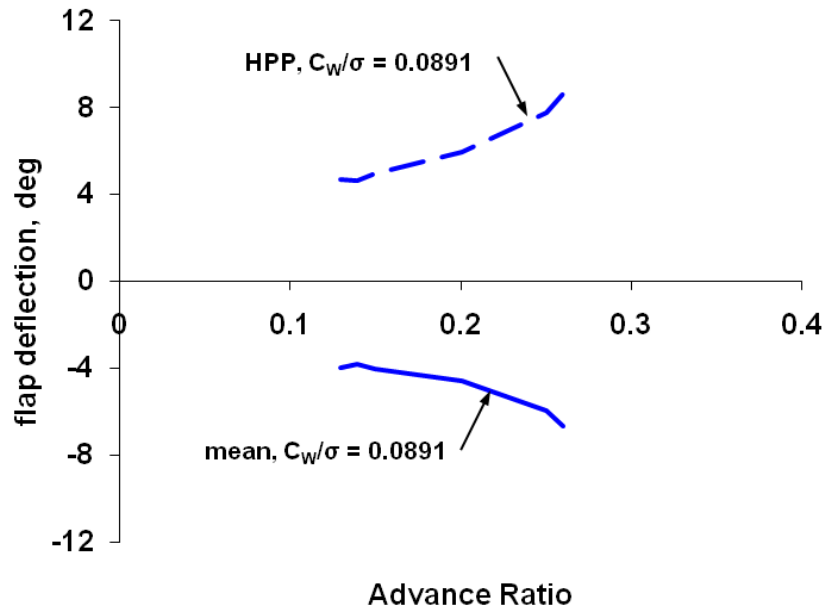
Figure 4.58: Flap Control Angles of Swashplateless Rotor in Forward Flight, TEF

Trailer Wake Model, Vehicle Trim, $C_W/\sigma = 0.0891$
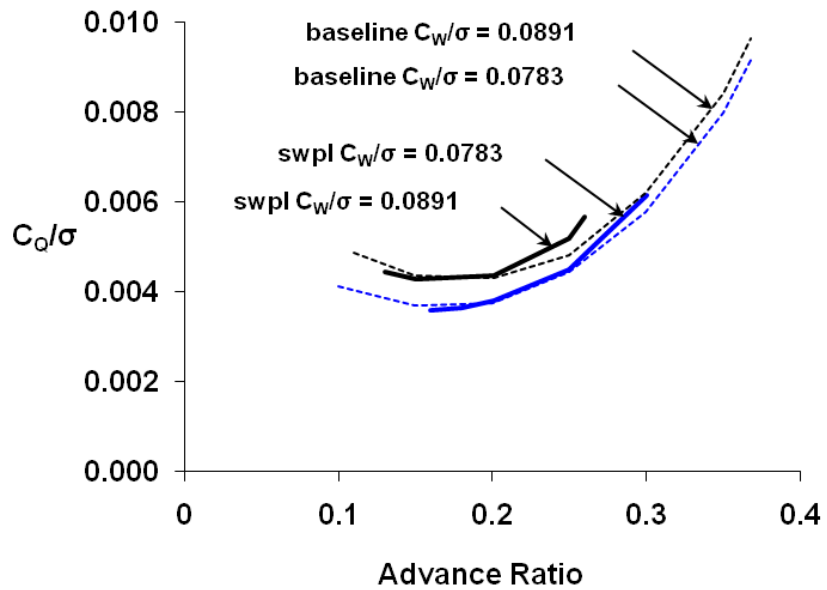
Figure 4.59: Effect of Increasing Thrust on Predicted Power of Swashplateless Rotor

in Forward Flight, TEF Trailer Wake Model, Vehicle Trim
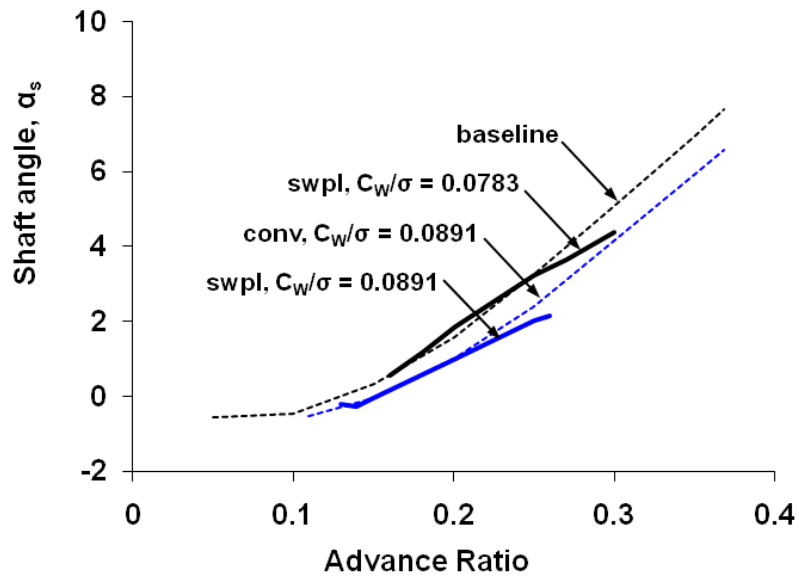
Figure 4.60: Effect of Increasing Thrust on Predicted Shaft Angles of Swashplateless Rotor in Forward Flight, TEF Trailer Wake Model, Vehicle Trim
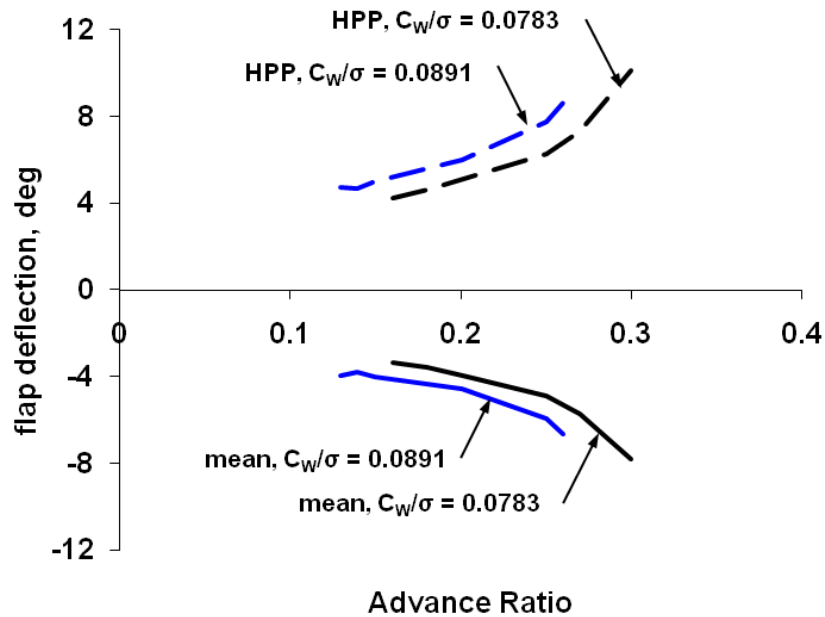
Figure 4.61: Effect of Increasing Thrust on Flap Control Angles of Swashplateless Rotor in Forward Flight, TEF Trailer Wake Model, Vehicle Trim
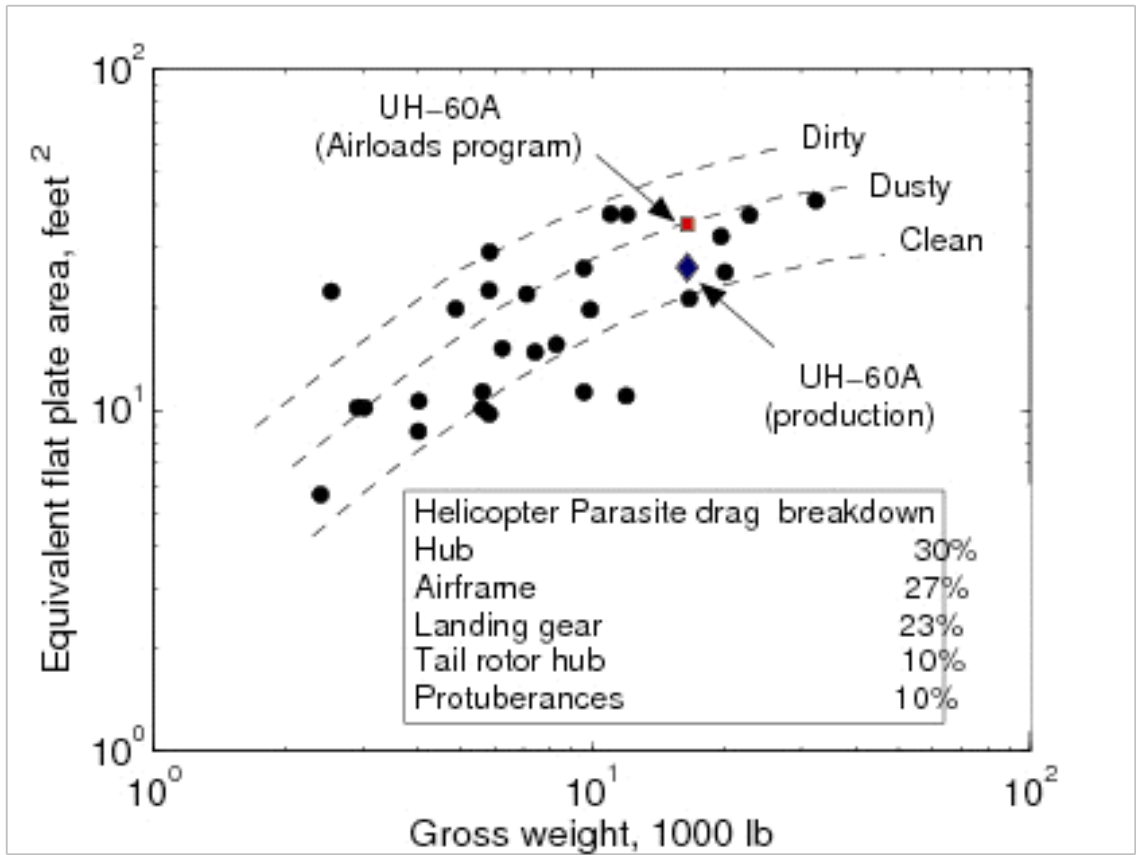
Figure 4.62: Distribution of Parasite Drag (Ref. [3])
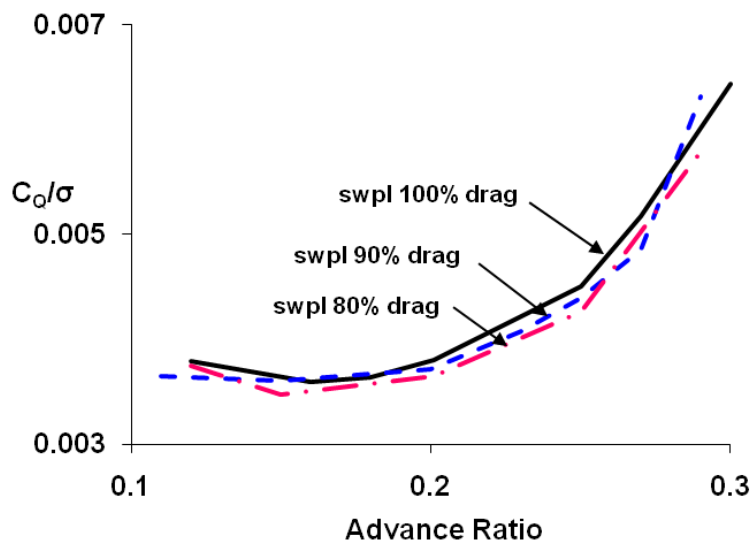
Figure 4.63: Effect of Decreasing Parasite Drag on Predicted Power of Swashplate-less Rotor in Forward Flight, TEF Trailer Wake Model, Vehicle Trim, $C_W/\sigma = 0.0783$
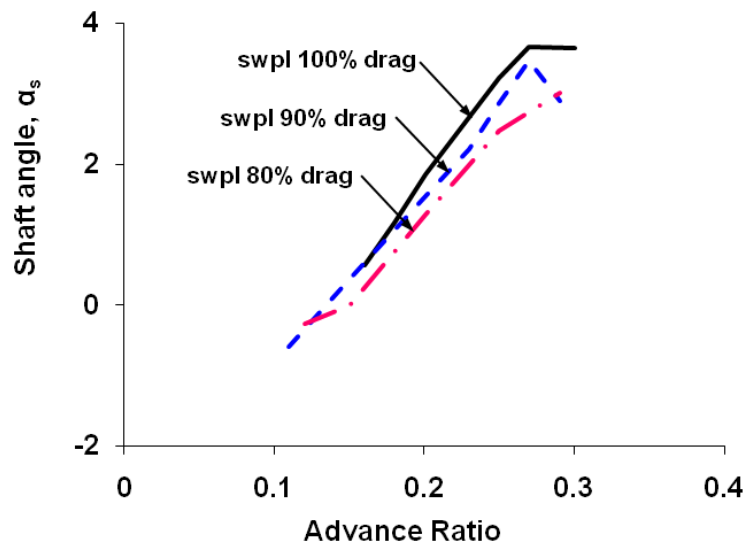
Figure 4.64: Effect of Decreasing Parasite Drag on Predicted Shaft Angles of Swashplateless Rotor in Forward Flight, TEF Trailer Wake Model, Vehicle Trim, $C_W/\sigma = 0.0783$
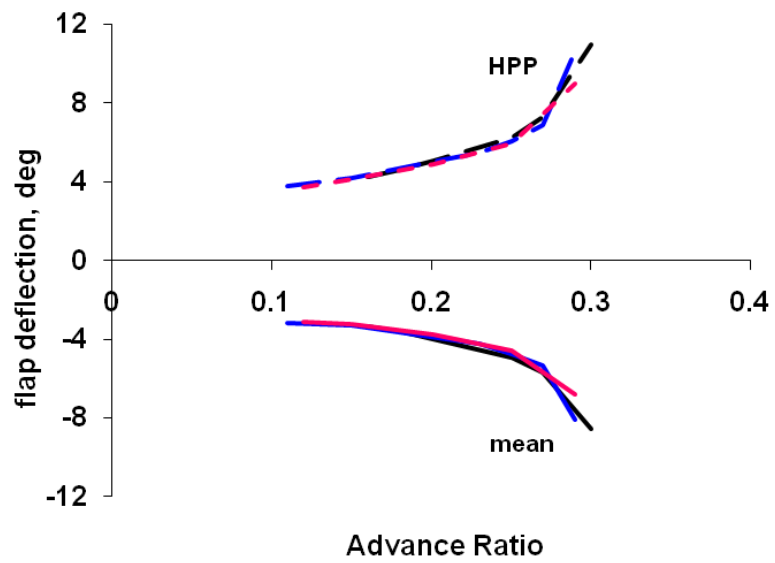
Figure 4.65: Effect of Decreasing Parasite Drag on Flap Control Angles of Swash-plateless Rotor in Forward Flight, TEF Trailer Wake Model, Vehicle Trim, $C_W/\sigma = 0.0783$
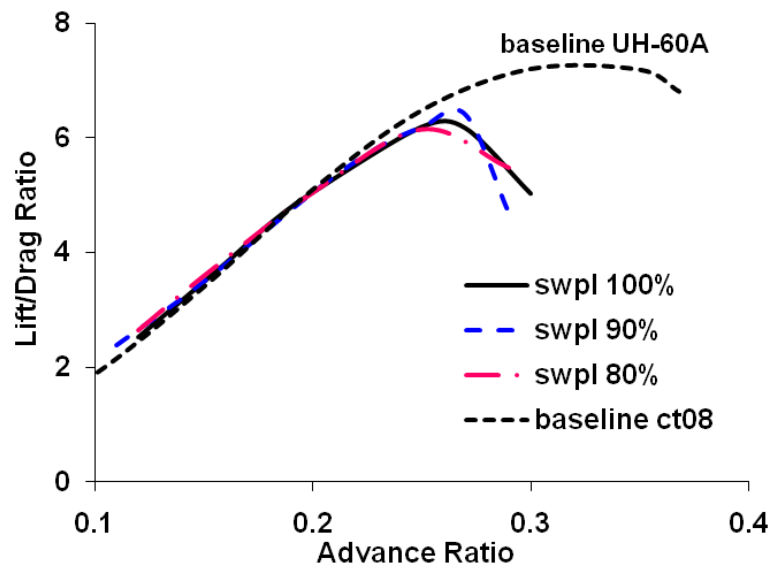
Figure 4.66: Effect of Decreasing Parasite Drag on Lift-to-Drag Ratio of Swash-plateless Rotor in Forward Flight, TEF Trailer Wake Model, Vehicle Trim, $C_W/\sigma = 0.0783$

Chapter 5

Conclusions

The summary and the key conclusions of this investigation are presented in this chapter. This investigation addressed the analysis, design and performance evaluation of swashplateless rotors controlled with trailing edge flaps and tabs. The objective was to understand the fundamental responses of such a rotor, and develop an analytical method that can accurately represent them.

Two rotors were used in the course of the investigation. A conceptual rotor based on the work of the Kaman Aerospace Group was used with an initial, linear analysis using rigid blades to establish basic behavior of the swashplateless rotor system with trailing edge flaps and tabs. The conceptual rotor was characterized by moderate, linear twist of $-10°$, a rectangular planform and very low blade torsional stiffness which facilitates blade elastic twist in response to the aerodynamic pitching moments generated by the deflections of the trailing edge flap and tab. The UH-60A Black Hawk rotor was used to validate the predictions of a refined comprehensive analysis and as a testbed for the design and evaluation of swashplateless primary control. The UH-60A is a modern, mission optimized rotor, characterized by nonlinear blade twist of $-16°$, tip sweep and sectional center of gravity offsets. The elastic blade deformations of the baseline rotor are large, and there are nonlinear couplings between the flap, lag and torsion modes. These two rotors represent the opposite

extremes that can be considered in the design of the swashplateless primary control concept: the one a new rotor that could be design optimized for trailing edge flap control, and the other an existing production rotor that could be retro-fitted with a new control system.

This investigation was conducted in two major parts. In the first section, trailing edge flap and tab control systems were designed for the rotors using parametric studies. The linear, rigid blade analysis was developed with four degrees of freedom: blade flap, blade pitch, flap deflection and tab deflection; the inflow distribution was uniform. The comprehensive analysis was refined to include the contributions of the flap and the tab in both the structural and aerodynamic models; the inflow distribution was calculated with a free wake model. For both analyses, the aerodynamic model was based on quasi-steady thin airfoil theory. The baseline test condition for both rotors was steady level flight at high advance ratio ($\mu \geq 0.35$) and at constant blade loading, c_t/σ. Each flap configuration parameter was varied across a range of values, while the others were held constant, and the sensitivity of the system to the parameter was established. The results of the parameter studies were used to produce flap-tab designs which minimized both control angles and hinge moments. This minimization is key for on-blade smart actuators, which deliver limited stroke and force, but have the light weight, compact size, and high bandwidth necessary for the practical implementation of swashplateless primary control. The second section focused on the evaluation of the swashplateless rotor derived from the UH-60A. Flight test data from the UH-60A Airloads Program were used to validate the performance predictions of the comprehensive analysis. The aerodynamic model was

further refined to include airfoil table lookup for flapped airfoils and the effect of the trailing edge flaps in the near and far wake. The swashplateless rotor power and rotor lift-to-drag ratio predictions from the comprehensive analysis were compared to the baseline rotor in hover and in forward flight for several levels of thrust and parasitic drag. These performance metrics provide necessary information to compare the swashplateless primary control concept to existing rotors.

5.1 Key Conclusions

Detailed discussion of the conclusions for each section of this investigation are at the end of each chapter. The principal conclusions of the entire work are summarized here:

1. A swashplateless derivative of a modern heavy utility (UH-60A) rotor can be trimmed across the range of forward flight speed with tab-actuated trailing edge flaps. Compared to controlling the rotor with trailing edge flaps only, at high speed ($\mu = 0.368$) with fixed shaft angles and zero hub moments, the required tab control angles are less than half the deflections required by a flap only system. The tab hinge moment is larger than the flap hinge moment of an equivalent system, but it still small in absolute magnitude. The low stroke and force required for the tab-actuated trailing edge flap concept make it a good candidate for on-blade smart actuators.

2. Index angle and torsional frequency are key design parameters for the swashplateless rotor: they act together to reduce the flap deflections required to

trim the rotor, and produce a different blade twist distribution compared to the baseline (swashplate) rotor. Trailing edge flap deflections in combination with blade twisting redistribute lift and drag about the rotor disk to produce changes to rotor power across the range of forward flight speed.

The TEF deflections required for trim increase with thrust in hover and with speed in forward flight, but can be reduced by increasing the index angle. In this study, using the flap aerodynamic lookup tables produced by CFD analysis, 15° was the highest index angle that produced trim solutions across the range of flight speeds. The maximum index angle that can be used in this investigation was limited by blade deflection divergence; it is not clear whether this phenomenon is numerical or physical.

3. In hover, the swashplateless rotor requires less power than the conventional rotor, for a limited range of thrust at each index angle. A high index angle produces an increase in figure of merit (FM) compared to the baseline, at some thrust levels. Beyond the thrust level at which the maximum FM is produced, the predicted power increases rapidly compared to the baseline rotor and the figure of merit drops. This appears to limit the upper range of thrust at which the swashplateless rotor operates efficiently in hover.

4. The wake model used to analyze the swashplateless rotor has a significant effect on the prediction of rotor power in forward flight. A uniform inflow model produces a predicted power curve that follows the trend of the baseline (swashplate) rotor. This model might be sufficient for relative comparisons

between rotors. A refined free wake model that accounts for the trailed vorticity from the trailing edge flap produces rotor power predictions that also follow the trend of the baseline rotor. The refined model indicates that the swashplateless rotor may require less power than the baseline at low speed, and more at high speed. This conclusion depends on the rotor models having identical configurations (and parasitic drag), except for torsional frequency and trailing edge flaps.

5. Except where noted explicitly, the equivalent flat plate area is held constant in comparisons between the baseline and swashplateless rotors for most of this investigation. Accordingly, the power predictions shown for the swashplateless rotor are conservative. When the parasitic drag was reduced 20% from the baseline, the swashplateless power prediction decreased 5%, with a concurrent decrease of the rotor shaft angle of 23%.

6. The rotor lift-to-drag ratio was calculated for the swashplateless rotor at different increments of parasitic drag, and compared to the baseline rotor (with unchanged parasitic drag). For all increments of parasite drag, the maximum lift-to-drag ratio of the swashplateless rotor occurs at or below $\mu = 0.26$. This is in contrast to the baseline rotor, where the maximum lift-to-drag ratio occurs near $\mu = 0.35$. Up to $\mu = 0.26$, the swashplateless ratio follows the baseline rotor closely, then decreases rapidly. Beyond $\mu = 0.30$, trim solutions are difficult to obtain for the swashplateless rotor. These results indicate that at higher advance ratios, the swashplateless UH-60A operates less efficiently

267

than the baseline rotor.

5.2 Future Work

The following suggestions are made for future research of swashplateless rotors with trailing edge flaps. In the current investigation, it has been shown that adding actuated tabs to trailing edge flaps for primary control results in smaller trim control angles and hinge moments than flaps alone. The performance of the trailing edge flap controlled rotor has been studied and compared to a baseline rotor with a swashplate. Two parts of the aerodynamic analysis are key to the accurate prediction of trim requirements and rotor performance: sectional properties and inflow distribution. Additional research to improve the model and to advance the design and analysis of swashplateless rotors is suggested below.

1. Experimental data are required to validate the prediction of trim requirements and rotor power for the swashplateless rotor in hover and in forward flight. Sectional aerodynamic data for airfoils with flaps and/or tabs remains limited. Computational fluid dynamics can be used to produce properties for different flap and tab configurations with aerodynamic balance and hinge gaps. Both static and dynamic flap/tab deflections, at $\pm 15°$, for a wide range of angles of attack and Mach numbers, are required to validate and improve the aerodynamic model.

   Investigation of the effect of trailing edge flaps on the rotor wake is required to confirm the correct inflow model for comprehensive analysis. Flow visualiza-

tion can be used to identify the generation and evolution of the vortices trailed at the flap boundaries and at the blade tip. Wake measurements are needed to confirm the strengths of the vortices and how the tip vortex is modified by the deflecting flap.

Wind tunnel tests of a rotor with and without flaps can be used to study the effect of torsional frequency on rotor power (for flapped and unflapped rotors), and on trailing edge flap effectiveness.

2. Steady level flight has been assumed throughout this investigation. More demanding conditions, such as maneuvering and autorotation, must be studied for proper design of swashplateless rotors controlled with trailing edge flaps.

3. The index angle, or pre-collective, of the blade was identified as a key design parameter that minimizes the flap angles required to trim the rotor. However, the index angle chosen by a parameter study at high advance ratio is not optimum at all speeds. To improve the design and performance of the swashplateless rotor, variable indexing should be included in the analysis, so that the optimum index angle is identified for each flight condition.

4. Airfoil selection is an important aspect of rotor performance. In the present investigation, flaps and tabs were added to the SC1094R8 airfoil, which was selected for the UH-60A rotor in response to particular performance criteria. The resulting lift-to-drag ratio for the swashplateless variant of the rotor followed the baseline up to moderate advance ratio ($\mu = 0.25$). A thorough investigation of airfoils suited for the operating conditions of the swashplateless

rotor is required to determine if the rotor lift-to-drag ratio can be improved at faster forward flight speeds.

5. The major advantage of the swashplateless control system lies in the potential for simultaneous primary control, vibration reduction, noise suppression and performance enhancement. Multiple flaps per blade and flexible flaps should be implemented in the comprehensive analysis to facilitate investigations of multi-use flaps. In addition, this modification would allow other concepts such as deformable trailing edges to be examined.

Bibliography

[1] M. Ames and R. Sears. Wind tunnel investigation of two airfoils with 25-percent-chord gwinn and plain flaps. Technical Report TN 763, NACA, 1940.

[2] A. Hassan, F. Straub, and K. Noonan. Experimental/numerical evaluation of integral trailing edge flaps for helicopter rotor applications. *Journal of the American Helicopter Society*, 50(1):3–17, January 2005.

[3] R.M. Carlson. Helicopter performance - transportation's latest chromosome: The 21st annual Alexander A. Nikolsky lecture. *Journal of the American Helicopter Society*, 47(1):3–17, January 2002.

[4] A. Datta, M. Nixon, and I. Chopra. Review of rotor loads prediction with the emergence of rotorcraft CFD. *Journal of the American Helicopter Society*, 52(4):287–317, 2007. doi: 10.4050/JAHS.52.287. URL http://link.aip.org/link/?JHS/52/287/1.

[5] J. Hobbs. *Bristol Helicopters: A Tribute to Raoul Hafner*. Frenchay Publications, Bristol, UK, 1 edition, 1984.

[6] W. Johnson. *Helicopter Theory*. Dover Publications, Inc., New York, 1994.

[7] J.G. Leishman. *Principles of Helicopter Aerodynamics*. Cambridge University Press, Cambridge, UK, 1 edition, 2000.

[8] A.Z. Lemnios and R. Jones. The servo-flap - an advanced rotor control system. In *Proceedings of AHS and NASA Ames Research Center Vertical Lift Aircraft Design Conference*, San Francisco, January 1990. AHS.

[9] F.S. Wei and F. Gallagher. Servo-flap rotor performance flight testing and data identification. In *American Helicopter Society 57th Annual Forum Proceedings* AHS [129].

[10] B. Rocconella and F.S. Wei. Wind tunnel model testing of the improved K-MAX servo-flap blade section. In *American Helicopter Society 57th Annual Forum Proceedings* AHS [129].

[11] F.S. Wei. Design of soft torsion rotor systems at Kaman Aerospace Corporation. In *American Helicopter Society 58th Annual Forum Proceedings* AHS [130].

[12] R.P. Pescara. Screw propeller of helicopter flying machines. U.S. Patent Office, March 1923. Patent No. 1,449,129.

[13] C. d'Ascanio. Helicopter. U.S. Patent Office, May 1934. Patent No. 1,960,141.

[14] C.H. Kaman. Aircraft of rotary wing type. U.S. Patent Office, May 1948. Patent No. 2,455,866.

[15] A.Z. Lemnios and A.F. Smith. An analytical evaluation of the controllable twist rotor performnce and dynamic behavior. Technical Report TR 72-16, USAAMRDL, May 1972.

[16] A.Z. Lemnios and F.K. Dunn. Theoretical study of multicyclic control of a controllable twist rotor. Technical Report NASA-CR-151959, NASA, May 1976.

[17] J.L McCloud. An analytical study of a multicyclic controllable twist rotor. In *American Helicopter Society 31st Annual National Forum*, Washington, D.C., May 1975. AHS.

[18] J.L McCloud and A.L. Weisbrich. Wind-tunnel test results of a full-scale multicyclic controllable twist rotor. In *American Helicopter Society 34th Annual National Forum*, Washington, D.C., May 1978. AHS.

[19] F.-S. Wei and A.L. Weisbrich. Multicyclic controllable twist rotor data analysis. Technical Report NASA-CR-152251, NASA, 1979.

[20] F.-S. Wei and R. Jones. Correlation and analysis for sh-2f 101 rotor. *Journal of Aircraft*, 25(7):647–652, July 1988.

[21] F.-S. Wei. Advanced servo flap rotor using variable blade index angle control. In *38th AIAA/ASME/ASCE/AHS/ASC Structures, Structural Dynamics and Materials Conference*, pages 876–884, Kissimmee, FL, April 1997. AIAA.

[22] F.-S. Wei, J.P. Basile, and R. Jones. Vibration reduction on servo flap controlled rotor using HHC. In *American Helicopter Society National Specialists' Meeting on Rotorcraft Dynamics*, Arlington, TX, November 1989. AHS.

[23] F.-S. Wei. Active trailing edge tab control for helicopter rotor vibration reduction. In *AIAA Dynamics Specialists Conference*, Salt Lake City, UT, April 1996. AIAA.

[24] T. Ning, F.-S. Wei, and A. Suen. Servo-flap rotor design parameters indentification via spectral analysis of flight data. In *46th AIAA Aerospace Sciences Meeting and Exhibit*, Reno, NV, January 2008. AIAA.

[25] F.S. Wei. Design of an integrated servo-flap main rotor. In *American Helicopter Society 59th Annual Forum Proceedings* AHS [131].

[26] P.R. Payne. Higher harmonic rotor control: The possibilities of third and higher harmonic feathering for delaying the stall limit in helicopters. *Aircraft Engineering and Aerospace Technology*, 30(8):222–226, 1958.

[27] P.J. Arcidiacono. Theoretical performance of helicopters having second and higher harmonic feathering control. *Journal of the American Helicopter Society*, 6(2):8–19, 1961. doi: 10.4050/JAHS.6.8. URL http://link.aip.org/link/?JHS/6/8/1.

[28] J. Shaw and N. Albion. Active control of the helicopter rotor for vibration reduction. *Journal of the American Helicopter Society*, 26(3):32–39, July 1981.

[29] J. Shaw, N. Albion, E. Hanker, and R. Teal. Higher harmonic control: Wind tunnel demonstration of fully effective vibratory hub force suppression. In *American Helicopter Society 41st Annual Forum Proceedings*, Fort Worth, TX, May 1985. AHS.

[30] K. Nguyen and I. Chopra. Application of higher harmonic control to rotors operating at high speed and thrust. *Journal of the American Helicopter Society*, 35(3):78–89, July 1990.

[31] K. Nguyen. Active control of helicopter blade stall. *Journal of Aircraft*, 35 (1):91–98, January-February 1998.

[32] K. Nguyen. Active suppression of stall on helicopter rotors. In *25th European Rotorcraft Forum*, Rome, Italy, 1999. ERF.

[33] W. R. Splettstoesser, R. Kube, W. Wagner, U. Seelhorst, A. Boutier, F. Micheli, E. Mercker, and K. Pengel. Key results from a higher harmonic control aeroacoustic rotor test (HART). *Journal of the American Helicopter Society*, 42(1):58–78, 1997. doi: 10.4050/JAHS.42.58. URL `http://link.aip.org/link/?JHS/42/58/1`.

[34] R. Kube, W. Splettstoesser, W. Wagner, U. Seelhorst, Y. Yu, C. Tung, P. Beaumier, J. Prieur, G. Rahier, P. Spiegel, A. Boutier, T. Brooks, C. Burley, D. Boyd, E. Mercker, and K. Pengel. Hhc aeroacoustic rotor tests in the german dutch wind tunnel: Improving physical understanding and prediction codes. In *American Helicopter Society 52nd Annual Forum Proceedings*, Washington, D.C., June 1996. AHS.

[35] Y. Yu, C. Tung, B. van der Wall, H. Pausder, C. Burley, T. Brooks, P. Beaumier, Y. Delrieux, and E. Mercker. The HART-II test: Rotor wakes and aeroacoustics with higher-harmonic pitch control (hhc) inputs - the joint german/french/dutch/us project. In *American Helicopter Society 58th Annual Forum Proceedings* AHS [130].

[36] B. Van der Wall, C. Burley, Y. Yu, H. Richard, K. Pengel, and P. Beaumier. The HART II test - measurement of helicopter rotor wakes. *Aerospace Science and Technology*, 8(4):273–284, June 2004.

[37] R.P. Cheng, C.R. Theodore, and R. Celi. Effects of two/rev higher harmonic control on rotor performance. *Journal of the American Helicopter Society*, 48(1):18–27, 2003. doi: 10.4050/JAHS.48.18. URL `http://link.aip.org/link/?JHS/48/18/1`.

[38] R. Cheng and R. Celi. Optimum two-per-revolution inputs for improved rotor performance. *Journal of Aircraft*, 42(6):1409–1417, November-December 2005.

[39] D. Wachspress, T. Quackenbush, and C. Solomon. On minimum induced power of the helicopter rotor. In *American Helicopter Society 61st Annual Forum Proceedings* AHS [132].

[40] K.F. Guinn. Individual blade control independent of a swashplate. *Journal of the American Helicopter Society*, 27(3):25–31, 1982. doi: 10.4050/JAHS.27.25. URL `http://link.aip.org/link/?JHS/27/25/1`.

[41] N.D. Ham. Helicopter individual-blade-control and its applications. In *American Helicopter Society 39th Annual Forum Proceedings*, St. Louis, MO, May 1983.

[42] I. Chopra. Status of application of smart structures technology to rotorcraft systems. *Journal of the American Helicopter Society*, 45(4):228–252, 2000. doi: 10.4050/JAHS.45.228. URL `http://link.aip.org/link/?JHS/45/228/1`.

[43] N.D. Ham. Helicopter individual-blade-control research at MIT 1977-1985. *Vertica*, 11(1):109–122, 1987.

[44] D. Teves, V. Kloppel, and P. Richter. Development of active control technology in the rotating system, flight testing and theoretical investigations. In *18th European Rotorcraft Forum*, Avignon, France, September 1992.

[45] P. Richter and T. Schreiber. Theoretical investigations and windtunnel tests with HHC-IBC. In *20th European Rotorcraft Forum*, Amsterdam, Netherlands, October 1994.

[46] D. Roth. Advanced vibration reduction by ibc technology. In *30th European Rotorcraft Forum*, Munchen, Germany, September 2004.

[47] S. John, N. Wereley, and J. Sirohi. Development of a piezohydraulic active pitch link for a swashplateless helicopter rotor. *Journal of Aircraft*, 46(1): 328–331, January 2009.

[48] P. Chen and I. Chopra. Wind tunnel test of a smart rotor model with individual blade twist control. *Journal of Intelligent Material Systems and Structures*, 8(5):414–425, May 1997.

[49] W. Wilkie, M. Wilbur, P. Mirick, C. Cesnik, and S. Shin. Aeroelastic analysis of the NASA/Army/MIT active twist rotor. In *American Helicopter Society 55th Annual Forum Proceedings*, Montreal, Canada, May 1999. AHS.

[50] M. Wilbur, P. Mirick, W. Yeager, C. Langston, C. Cesnik, and S. Shin. Vibratory loads reduction testing of the NASA/Army/MIT active twist rotor. In *American Helicopter Society 57th Annual Forum Proceedings* AHS [129].

[51] S. Shin, C. Cesnik, and S. Hall. Closed-loop control test of the NASA/Army/MIT active twist rotor for vibration reduction. *Journal of the American Helicopter Society*, 50(2):178–194, April 2005.

[52] J. Kim, N. Koratkar, and A. Messac. Optimal design of a swash-plateless main rotor featuring active control of blade twist. In *43rd AIAA/ASME/ASCE/AHS/ASC Structures, Structural Dynamics and Materials Conference*, Denver, CO, April 2002. AIAA.

[53] L. Dadone, J. Cowan, and F. Mchugh. Variable camber rotor study. Technical Report NASA-CR-166382, NASA, 1982.

[54] P. Anusonti-Inthra, R. Sarjeant, M. Frecker, and F. Gandhi. Design of a conformable rotor airfoil using distributed piezoelectric actuators. *AIAA Journal*, 43(8):1684–1695, August 2005.

[55] P. Janker, F. Hermle, S. Friedl, K. Lentner, B. Enenkl, and C. Muller. Advanced piezoelectric servoflap system for rotor active control. In *32nd European Rotorcraft Forum*, Maastricht, The Netherlands, September 2006.

[56] C. Maucher, B. Grohmann, P. Janker, A. Altmikus, F. Jensen, and H. Baier. Actuator design for the active trailing edge of a helicopter rotor blade. In *33rd European Rotorcraft Forum*, Kazan, Russia, September 2007.

[57] F. Straub and A. Hassan. Aeromechanic considerations in the design of a rotor with smart material actuated trailing edge flaps. In *American Helicopter Society 52nd Annual Forum Proceedings*, Washington, D.C, June 1996. AHS.

[58] F. Straub and B. Charles. Aeroelastic analysis of rotors with trailing edge flaps using comprehensive codes. *Journal of the American Helicopter Society*, 46(3):192–199, July 2001.

[59] F. Straub, D. Kennedy, D. Domzalski, A. Hassan, H. Ngo, V. Anand, and T. Birchette. Smart material-actuated rotor technology - SMART. *Journal of Intelligent Material Systems and Structures*, 15:249–260, April 2004.

[60] F. Straub and D. Kennedy. Design, development, fabrication and testing of an active flap rotor system. In *American Helicopter Society 61st Annual Forum Proceedings* AHS [132].

[61] F. Toulmay, V. Kloppel, F. Lorin, B. Enenki, and J. Gaffiero. Active blade flaps - the needs and current capabilities. In *American Helicopter Society 57th Annual Forum Proceedings* AHS [129].

[62] O. Dieterich, B. Enenkl, and D. Roth. Trailing edge flaps for active rotor control aeroelastic characteristics of the ADASYS rotor system. In *American Helicopter Society 62nd Annual Forum Proceedings*, Phoenix, AZ, May 2006. AHS.

[63] P. Konstanzer, B. Enenkl, P. Auborg, and P. Cranga. Recent advances in eurocopter's passive and active vibration control. In *American Helicopter Society 64th Annual Forum Proceedings* AHS [133].

[64] K. Noburu, S. Saito, M. Kosaka, and H. Fuse. A study of closed loop control with BVI detection method for helicopter noise reduction. In *Proceedings of the 44th Aircraft Symposium*, Japan, 2006.

[65] K. Noboru and S. Saito. Performance evaluation of full scale on-board active flap system in transonic wind tunnel. In *American Helicopter Society 64th Annual Forum Proceedings* AHS [133].

[66] R. Spangler and S. Hall. Piezoelectric actuators for helicopter rotor control. In *31st AIAA/ASME/ASCE/AHS/ASC Structures, Structural Dynamics and Materials Conference*, Long Beach, CA, 1990. AIAA.

[67] M. Fulton and R. Ormiston. Hover testing of a small-scale rotor with on-blade elevons. *Journal of the American Helicopter Society*, 46(2):96–106, April 2001.

[68] N. Koratkar and I. Chopra. Wind tunnel testing of a smart rotor model with trailing-edge flaps. *Journal of the American Helicopter Society*, 47(4):263–272, October 2002.

[69] B. Roget and I. Chopra. Individual blade control methodology for a rotor with dissimilar blades. *Journal of the American Helicopter Society*, 48(3):176–185, July 2003.

[70] T. Millott and P. Friedmann. Vibration reduction in helicopter rotors using an active control surface located on the blade. In *33rd AIAA/ASME/ASCE/AHS/ASC Structures, Structural Dynamics and Materials Conference*, Dallas, TX, April 1992. AIAA.

[71] P. Friedmann and T. Millott. Vibration reduction in rotorcraft using active control: A comparison of various approaches. *Journal of Guidance, Control and Dynamics*, 18(4):664–673, July-August 1995.

[72] J. Milgram, I. Chopra, and F. Straub. Rotors with trailing edge flaps: Analysis and comparison with experimental data. *Journal of the American Helicopter Society*, 43(4):319–332, October 1998. Analysis compared to test data from MDD AFR, indicial aero.

[73] T. Myrtle and P. Friedmann. Application of a new compressible time domain aerodynamic model to vibration reduction in helicopters using an actively controlled flap. *Journal of the American Helicopter Society*, 46(1):32–43, January 2001.

[74] T. Theodorsen. General theory of aerodynamic instability and the mechanism of flutter. Technical Report 496, NACA, 1935.

[75] J. Zhang, E.C. Smith, and K.W. Wang. Active-passive hybrid optimization of rotor blades with trailing edge flaps. *Journal of the American Helicopter Society*, 49(1):54–65, 2004. doi: 10.4050/JAHS.49.54. URL `http://link.aip.org/link/?JHS/49/54/1`.

[76] G. Depailler and P. Friedmann. Alleviation of dynamic stall induced vibrations using actively controlled flaps. In *American Helicopter Society 58th Annual Forum Proceedings* AHS [130].

[77] M. Fulton. Aeromechanics of the active elevon rotor. In *American Helicopter Society 61st Annual Forum Proceedings* AHS [132].

[78] D. Patt, L. Liu, and P. Friedmann. Simultaneous vibration and noise reduction in rotorcraft using aeroelastic simulation. *Journal of the American Helicopter Society*, 51(2):127–140, April 2006. doi: 10.4050/JAHS.51.127. URL http://link.aip.org/link/?JHS/51/127/1.

[79] R.A. Ormiston. Aeroelastic considerations for rotorcraft primary control with on-blade elevons. In *American Helicopter Society 57th Annual Forum Proceedings* AHS [129].

[80] J. Shen. *Comprehensive Aeroelastic Analysis of Helicopter Rotor with Trailing-Edge Flap for Primary Control and Vibration Control*. PhD thesis, University of Maryland, College Park, 2003.

[81] J. Shen, I. Chopra, and W. Johnson. Performance of swashplateless ultralight helicopter rotor with trailing-edge flaps for primary flight control. In *American Helicopter Society 59th Annual Forum Proceedings* AHS [131].

[82] J. Shen and I. Chopra. Swashplateless helicopter rotor with trailing-edge flaps. *Journal of Aircraft*, 41(2):208–214, March-April 2004.

[83] J. Shen and I. Chopra. Aeroelastic modeling of trailing-edge-flap helicopter rotors including actuator dynamics. *Journal of Aircraft*, 41(6):1465–1472, November-December 2004.

[84] J. Shen, M. Yang, and I. Chopra. Swashplateless helicopter rotor with trailing-edge flaps for flight and vibration control. *Journal of Aircraft*, 43(2):346–352, March-April 2006.

[85] R. Ganguli, B. Jehnert, J. Wolfram, and P. Voersmann. Survivability of helicopter with individual blade primary control failure. *The Aeronautical Journal*, 111(1124):645–658, October 2007.

[86] R. Ganguli, B. Jehnert, J. Wolfram, and P. Voersmann. Optimal location of centre of gravity for swashplateless helicopter UAV and MAV. *Aerospace Engineering and Aircraft Technology*, 79(4):335–345, 2007.

[87] I. Abbott and A. von Doenhoff. *Theory of Wing Sections*. Dover Publications, New York, NY, 1949.

[88] I. Abbott and H. Greenberg. Tests in the variable-density wind tunnel of the NACA 23012 airfoil with plain and split flaps. Technical Report TN 661, NACA, 1939.

[89] I. Abbott, A. von Doenhoff, and L. Stivers. Summary of airfoil data. Technical Report TN 824, NACA, 1945.

[90] C. Wenzinger and M. Ames. Wind tunnel investigation of rectangular and tapered NACA 23012 wings with plain ailerons and full-span split flaps. Technical Report TN 661, NACA, 1938.

[91] C. Wenzinger and T. Harris. Wind tunnel investigation of an NACA 23012 airfoil with various arrangements of slotted flaps. Technical Report TN 664, NACA, 1939.

[92] W. Street and M. Ames. Pressure-distribution investigation of a naca 0009 airfoil with a 50-percent-chord plain flap and three tabs. Technical Report TN 734, NACA, 1939.

[93] M. Ames and R. Sears. Pressure-distribution investigation of a naca 0009 airfoil with a 30-percent-chord plain flap. Technical Report TN 759, NACA, 1940.

[94] M. Ames and R. Sears. Pressure-distribution investigation of a naca 0009 airfoil with an 80-percent-chord plain flap and three tabs. Technical Report TN 761, NACA, 1940.

[95] M. Ames and R. Sears. Determination of control-surface characteristics from naca plain-flap and tab data. Technical Report TN 721, NACA, 1940.

[96] R. Sears and P. Purser. Wind tunnel investigation of control-surface characteristics XIV- NACA 0009 airfoil with a 20-percent-chord double plain flap. Technical Report 3F29, NACA, 1943.

[97] R. Liddell. Wind tunnel investigation of control-surface characteristics XIX- a double flap with an overhang and an internal aerodynamic balance. Technical Report L4F23, NACA, December 1946.

[98] E. A. Mayda and C. P. van Dam. Automated generation of airfoil performance tables using a two-dimensional navier—stokes solver. *Journal of the American Helicopter Society*, 50(4):338–348, 2005. doi: 10.4050/JAHS.50.338. URL `http://link.aip.org/link/?JHS/50/338/1`.

[99] W. Bousman. Aerodynamic characteristics of sc1095 and sc1094r8 airfoils. Technical Report TP-2003-212265, NASA, December 2003.

[100] M. Smith, M. Potsdam, T.-C. Wong, J. Baeder, and S. Phanse. Evaluation of computational fluid dynamics to determine two-dimensional airfoil characteristics for rotorcraft applications. *Journal of the American Helicopter Society*, 51(1):70–79, January 2006.

[101] A. Shelton, J. Abras, R. Jurenko, and M. Smith. Improving the CFD predictions of airfoils in stall. In *43rd AIAA Aerospace Sciences Meeting and Exhibit*, Reno, NV, January 2005. AIAA. 2005-1227.

[102] A. Jose and J. Baeder. An investigation into the aerodynamics of trailing edge flaps using CFD and analytical methods. In *American Helicopter Society 61st Annual Forum Proceedings* AHS [132].

[103] A. Jose, A. Mishra, and J. Baeder. An investigation into the aerodynamics of trailing edge flaps with overhang and gap. In *American Helicopter Society Specialists Conference on Aeromechanics Proceedings*, San Francisco, CA, January 2008. AHS.

[104] P. Purser and J. Riebe. Wind tunnel investigation of control-surface characteristics XV- various contour modifications of a 0.30-airfoil-chord plain flap on an NACA 66(215)-014 airfoil. Technical Report 3L20, NACA, 1943.

[105] P. Gerontakos and T. Lee. Active trailing-edge flap control of oscillating-wing tip vortex. *AIAA Journal*, 44(11):2746–2754, November 2006.

[106] A. Panagakos and T. Lee. Tip vortex control via an active trailing-edge tab. *Journal of Aircraft*, 43(4):1152–1158, July-August 2006.

[107] T. Lee and J. Pereira. Tip vortex control via a tab deflecting at higher harmonic frequencies. *AIAA Journal*, 46(6):1342–1350, June 2008.

[108] K. Noonan, W. Yeager, J. Singleton, M. Wilbur, and P. Mirick. Wind tunnel evaluation of a helicopter main-rotor blade with slotted airfoils at the tips. Technical Report NASA-TP-2001-211260, NASA Langley Research Center, Hampton, VA, December 2001.

[109] A. Gagliardi and G.N. Barakos. Analysis and design of a flap-equipped low-twist rotor for hover. *Journal of Aircraft*, 46(1):74–84, January-February 2009.

[110] B. Glaz, P. Friedmann, and L.Liu. Active/passive vibration reduction and performance enhancement of helicopter rotors at high advance ratios. In *American Helicopter Society 64th Annual Forum Proceedings* AHS [133].

[111] L. Liu, P. Friedmann, I. Kim, and D. Bernstein. Rotor performance enhancement and vibration reduction in presence of dynamic stall using actively controlled flaps. *Journal of the American Helicopter Society*, 53(4):338–350, October 2008.

[112] H. Yeo. Assessment of active controls for rotor performance enhancement. *Journal of the American Helicopter Society*, 53(2):152–163, April 2008.

[113] S. Gai and R. Palfrey. Influence of trailing-edge flow control on airfoil performance. *Journal of Aircraft*, 40(2):332–337, March-April 2003.

[114] K. J. Standish and C. P. van Dam. Computational analysis of a microtab-based aerodynamic load control system for rotor blades. *Journal of the American Helicopter Society*, 50(3):249–258, 2005. doi: 10.4050/JAHS.50.249. URL `http://link.aip.org/link/?JHS/50/249/1`.

[115] M.S. Chandrasekhara, P.B. Martin, and C. Tung. Compressible dynamic stall performance of a variable droop leading edge airfoil with a gurney flap. *Journal of the American Helicopter Society*, 53(1):18–25, 2008. doi: 10.4050/JAHS.53.18. URL `http://link.aip.org/link/?JHS/53/18/1`.

[116] M.P. Kinzel, M.D. Maughmer, and G. A. Lesieutre. Miniature trailing-edge effectors for rotorcraft performance enhancement. *Journal of the American Helicopter Society*, 52(2):146–158, April 2007. doi: 10.4050/JAHS.52.146. URL `http://link.aip.org/link/?JHS/52/146/1`.

[117] R. Loewy and S.P. Tseng. Smart structures stabilized unstable control surfaces. In *34th AIAA/ASME/ASCE/AHS/ASC Structures, Structural Dynamics and Materials Conference*, La Jolla, CA, 1993. AIAA.

[118] S. Heinze and M. Karpel. Analysis and wind tunnel testing of a piezoelectric tab for aeroelastic control applications. *Journal of Aircraft*, 43(6):1799–1804, November-December 2006.

[119] T. Theodorsen and I.E. Garrick. Nonstationary flow about a wing-aileron-tab combination including aerodynamic balance. Technical Report 736, NACA, 1942.

[120] N. Hariharan and J.G. Leishman. Unsteady aerodynamics of a flapped airfoil in subsonic flow by indicial concepts. *Journal of Aircraft*, 33(5):855–868, September-October 1996.

[121] G. Bir and I. Chopra. University of Maryland advanced rotor code (UMARC) theory manual. Technical Report UM AERO 94-18, Center for Rotorcraft Education and Research, July 1994.

[122] A. Datta and I. Chopra. Validation and understanding of UH-60A vibratory loads in steady level flight. *Journal of the American Helicopter Society*, 49(3): 271–287, July 2004.

[123] A. Bagai and J. Leishman. Rotor free-wake modeling using a pseudo-implicit technique - including comparisons with experimental data. *Journal of the American Helicopter Society*, 40(3):29–41, July 1995.

[124] A. Datta and I. Chopra. Validation of structural and aerodynamic modeling using UH-60A airloads program data. *Journal of the American Helicopter Society*, 51(1):43–58, January 2006.

[125] D.H. Hodges and E. Dowell. Nonlinear equations of motion for the elastic bending and torsion of twisted nonuniform rotor blades. Technical Report TN D-7818, NASA, 1974.

[126] D.H. Hodges, R. Ormiston, and D. Peters. On the nonlinear deformation geometry of euler-bernoulli beams. Technical Report TR 1566, NASA, 1980.

[127] H. Yeo, W.G. Bousman, and W. Johnson. Performance analysis of a utility helicopter with standard and advanced rotors. *Journal of the American Helicopter Society*, 49(3):250–270, July 2004.

[128] P. Lorber, R. Stauter, and A. Landgrebe. A comprehensive hover test of the airloads and airflow of an extensively instrumented model helicopter rotor. In *American Helicopter Society 45th Annual Forum Proceedings*, Boston, MA, May 1989.

[129] *American Helicopter Society 57th Annual Forum Proceedings*, Washington, D.C., May 2001. AHS.

[130] *American Helicopter Society 58th Annual Forum Proceedings*, Montreal, Canada, June 2002. AHS.

[131] *American Helicopter Society 59th Annual Forum Proceedings*, Phoenix, AZ, May 2003. AHS.

[132] *American Helicopter Society 61st Annual Forum Proceedings*, Grapevine, TX, June 2005. AHS.

[133] *American Helicopter Society 64th Annual Forum Proceedings*, Montreal, Canada, May 2008. AHS.